Smart Masks for *in situ* Exhaled Breath Condensate Harvesting and Analysis

Thesis by

Wenzheng Heng

In Partial Fulfillment of the Requirements for

the degree of

Doctor of Philosophy

CALIFORNIA INSTITUTE OF TECHNOLOGY

Pasadena, California

2025

(Defended March 14, 2025)

Wenzheng Heng
ORCID: 0009-0009-5278-0727

ACKNOWLEDGEMENTS

I wish to express my profound appreciation to everyone who played a role in bringing this thesis to fruition. This achievement stands as a collective effort made possible by countless forms of assistance and inspiration.

To my advisor, Wei Gao, I owe an immeasurable debt for his steadfast guidance, intellectual rigor, and unwavering faith in this project. His mentorship fundamentally shaped both the trajectory of this research and my growth as a scholar.

I am equally grateful to my thesis committee members—Prof. Yu-Chong Tai, Prof. Changhuei Yang, and Prof. Anqi Zhang—for their rigorous evaluation, thoughtful critiques, and willingness to invest time in refining this work. Their perspectives elevated the scholarly rigor of this endeavor.

I would also like to extend my heartfelt thanks to Prof. Harry Rossiter from the UCLA Lundquist Institute for his invaluable contributions. His expertise in patient recruitment and clinical testing was instrumental to this research. His insightful clinical suggestions and guidance not only improved the quality of our work but also deepened our understanding of the clinical aspects of this study.

I am deeply grateful to Prof. Martin Kaltenbrunner from JKU for his collaboration in the preparation of perovskite solar cells and his expert guidance on energy-related improvements. His profound knowledge and constructive advice in the field of energy significantly enhanced the scope and impact of this research.

The California Institute of Technology provided not just an intellectual home but also state-of-the-art facilities critical to this investigation. Equally indispensable were the contributions of those who participated in this study; their insights formed the empirical foundation of this research.

To my family, I extend eternal gratitude for their unconditional support and enduring patience. Their emotional anchor sustained me through moments of doubt and celebrated every milestone along this journey.

My colleagues and friends deserve special recognition for their intellectual camaraderie and moral sustenance. Their collaborative spirit transformed challenges into opportunities for growth.

While words fall short of capturing the depth of my gratitude, I hope these acknowledgments serve as a humble testament to the village that nurtured this work.

ABSTRACT

With the growing focus on personalized breath health management and early detection of chronic pulmonary diseases, there is an urgent demand for noninvasive wearable technologies capable of continuous breath molecular monitoring during daily activities. Existing respiratory monitoring systems remain limited to physical signal tracking and lack the capability for real-time biochemical analysis of exhaled biomarkers. To address this critical gap, we developed EBCare, a fully integrated smart mask platform for automated in situ analysis of exhaled breath condensate (EBC) biomarkers. The system combines tandem passive cooling strategies (hydrogel evaporation and radiative metamaterials) with bioinspired microfluidics to enable sustainable breath condensation and efficient sample transport under real-world conditions. A multiplexed electrochemical sensor array functionalized with nanoengineered interfaces achieves selective detection of key inflammatory markers (nitrite, pH) and metabolic indicators (ammonia, alcohol), while an embedded wireless module facilitates continuous data transmission. System validation through controlled breathing experiments and field trials demonstrates reliable operation across diverse environments (10-35°C, 30-80% humidity). Clinical evaluations involving healthy subjects, COPD/asthma patients, and post-COVID cohorts reveal EBCare's ability to dynamically track airway inflammation patterns and metabolic shifts during daily tasks. This wearable EBC analysis platform bridges the gap between laboratory-based breath testing and real-world respiratory monitoring, offering a scalable solution for home-based management of chronic respiratory conditions and post-infection recovery tracking. The modular design and automated operation framework further support future expansion to monitor airborne pathogens and systemic metabolic disease biomarkers through exhaled breath.

PUBLISHED CONTENT AND CONTRIBUTIONS

1. Heng, W.; Yin, S.; Min, J.; Wang, C.; Han, H.; Sani, E. S.; Li, J.; Song, Y.; Rossiter, H. B.; Gao, W. A smart mask for exhaled breath condensate harvesting and analysis. Science 385, 954–961 (2024). https://doi.org/10.1126/science.adn6471.

Conceptualization: W.G. and W.H. Methodology: W.G. and W.H. Investigation: W.H., S.Y., J.M., C.W., H.H., E.S.S., J.L., and H.B.R. Visualization: W.H. and Y.S. Funding acquisition: W.G. and H.B.R. Supervision: W.G. Writing – original draft: W.G. and W.H. Writing – review & editing: all authors.

2. Heng, W.; Solomon, S.; Gao, W. Flexible electronics and devices as human–machine interfaces for medical robotics. Advanced Materials 34, 2107902 (2022). https://doi.org/10.1002/adma.202107902.

W.H. prepared the figures and the manuscript.

3. Heng, W.; Yin, S.; Chen, Y.; Gao, W. Exhaled breath analysis: From laboratory test to wearable sensing. IEEE Reviews in Biomedical Engineering 1–25 (2024). https://doi.org/10.1109/RBME.2024.3481360.

W.H. prepared the figures and the manuscript.

TABLE OF CONTENTS

LIST OF ILLUSTRATIONS AND/OR TABLES

ABBREVIATIONS

AA - Arachidonic Acid

ADC - Analog-to-Digital Converter

Ag/AgCl - Silver/Silver Chloride

AgNPs - Silver Nanoparticles

Al_2O_3 - Aluminum Oxide

ARDS - Acute Respiratory Distress Syndrome

ATCC - American Type Culture Collection

ATP - Adenosine Triphosphate

ATS - American Thoracic Society

BAC - Blood Alcohol Concentration

BLE - Bluetooth Low Energy

BMI - Body Mass Index

BrAC - Breath Alcohol Concentration

BSA - Bovine Serum Albumin

CEA - Carcinoembryonic Antigen

CFU - Colony Forming Units

CNN - Convolutional Neural Network

COPD - Chronic Obstructive Pulmonary Disease

COVID-19 - Coronavirus Disease 2019

CRISPR - Clustered Regularly Interspaced Short Palindromic Repeats

CRP - C-Reactive Protein

CT - Computed Tomography

DAC - Digital-to-Analog Converter

DAQ - Data Acquisition

DI - Deionized

DLCO - Lung Diffusion Testing

DMF - Dimethylformamide

DOS - Dioctyl Sebacate

DUI - Driving Under the Influence

EBA - Exhaled Breath Aerosol

EBC - Exhaled Breath Condensate

eCO - Exhaled Carbon Monoxide

EIA - Enzyme Immunoassay

EIT - Electrical Impedance Tomography

ELISA - Enzyme-Linked Immunosorbent Assay

ERS - European Respiratory Society

FDA - Food and Drug Administration

FEA - Finite Element Analysis

FEF - Forced Expiratory Flow

FeNO/FENO - Fractional Exhaled Nitric Oxide

FEV_1 - Forced Expiratory Volume in the First Second

FITC - Fluorescein Isothiocyanate

FPCB - Flexible Printed Circuit Board

FVC - Forced Vital Capacity

GC - Gas Chromatography

GC-MS - Gas Chromatography-Mass Spectrometry

GOLD - Global Initiative for Chronic Obstructive Lung Disease

H1N1 - Influenza A Virus Subtype H1N1

H_2O_2 - Hydrogen Peroxide

H_2S - Hydrogen Sulfide

HMI - Human-Machine Interaction

INA - Instrumentation Amplifier

IPA - Isopropyl Alcohol

IRB - Institutional Review Board

LC-MS - Liquid Chromatography-Mass Spectrometry

LTs - Leukotrienes

MCU - Microcontroller Unit

MDR - Multidrug-Resistant

MERS - Middle East Respiratory Syndrome

MIR - Mid Infrared

MRI - Magnetic Resonance Imaging

MRSA - Methicillin-Resistant Staphylococcus Aureus

MS - Mass Spectrometry

MV - Minute Ventilation

MVV - Maximal Voluntary Ventilation

N95 - A type of respirator mask

NDIR - Non-Dispersive Infrared

NH_3 - Ammonia

NH_4/NH_4^+ - Ammonium/Ammonium Ion

NIH - National Institutes of Health

NIR - Near Infrared

NMR - Nuclear Magnetic Resonance

NO_2/NO_2^- - Nitrite/Nitrite Ion

NO_3 - Nitrate

$PaCO_2$ - Partial Pressure of Carbon Dioxide in Arterial Blood

PANI - Polyaniline

PaO_2 - Partial Pressure of Oxygen in Arterial Blood

PBS - Phosphate-Buffered Saline

PCA - Principal Component Analysis

PCR - Polymerase Chain Reaction

PDMS - Polydimethylsiloxane

PEF - Peak Expiratory Flow

PEG - Polyethylene Glycol

PET - Polyethylene Terephthalate

$PetCO_2$ - End-Tidal Carbon Dioxide

$PetO_2$ - End-Tidal Oxygen

POC - Point of Care

PPG - Photoplethysmography

$PtcCO_2$ - Transcutaneous Carbon Dioxide

$PtcO_2$ - Transcutaneous Oxygen

PtNPs - Platinum Nanoparticles

PU - Polyurethane

PVC - Polyvinyl Chloride

RH - Relative Humidity

RIA - Radioimmunoassay

RNN - Recurrent Neural Network

SaO_2 - Oxygen Saturation in Arterial Blood

SARS - Severe Acute Respiratory Syndrome

SARS-CoV-2 - Severe Acute Respiratory Syndrome Coronavirus 2

sEBC - Simulated Exhaled Breath Condensate

SEBS - Styrene-Ethylene-Butylene-Styrene

SEM - Scanning Electron Microscope

SIBO - Small Intestinal Bacterial Overgrowth

SIFT-MS - Selected Ion Flow Tube Mass Spectrometry

SLA - Stereolithography/Stereolithography Apparatus

SPI - Serial Peripheral Interface

TCM - Transcutaneous Monitoring

THF - Tetrahydrofuran

TIA - Trans-Impedance Amplifier

TLC - Total Lung Capacity

TV - Tidal Volume

USB - Universal Serial Bus

UV - Ultraviolet

UV-vis - Ultraviolet-Visible Spectroscopy

VC - Vital Capacity

VO_2 - Oxygen Uptake

VOC/VOCs - Volatile Organic Compound(s)

VSCs - Volatile Sulfur Compounds

WHO - World Health Organization

XPS - X-ray Photoelectron Spectroscopy

Chapter 1

INTRODUCTION

Materials from this chapter appear in "Heng, W.; Yin, S.; Chen, Y.; Gao, W. Exhaled breath analysis: From laboratory test to wearable sensing. IEEE Reviews in Biomedical Engineering 1–25 (2024). https://doi.org/10.1109/RBME.2024.3481360."

1.1 Introduction

Breath is a complex and intricate physiological process that facilitates gas exchange among the internal milieu, the airway lumen of the human organism, and the external environment. This process is precisely regulated by the central nervous system through the coordinated movement of respiratory muscles, including the diaphragm and intercostal muscles, causing periodic volume changes in the thoracic cavity and lungs [1]. The continuous, autonomous activity of respiratory muscles and cardiac muscles constitutes the core mechanism for maintaining basic life functions. Under normal physiological conditions, adults breathe approximately 12-20 times per minute, providing about 250 mL of oxygen for metabolism while expelling about 200 mL of carbon dioxide. This cyclic gas exchange not only meets cellular metabolic demands but also plays a crucial role in maintaining blood pH balance [2]. The physiological significance of respiration extends far beyond gas exchange. Research indicates that the respiratory process has significant influences on olfactory signal processing [3], circadian rhythm regulation [4], emotional modulation [5], and cognitive function [6]. Given the fundamental role of respiration in maintaining life and its broader impacts on various physiological and psychological processes, the importance of understanding and addressing respiratory health cannot be overstated.

Respiratory-related diseases are also a cause for serious concern. Over the past five years, coronavirus disease (COVID-19) has emerged as a representative global infectious disease, directly claiming ~7 million lives, and indirectly contributing to a death toll surpassing 15 million [7]. This emergence, coupled with other respiratory epidemics (SARS, MERS) and pandemics (H1N1) underscore the urgent and critical necessity for extensive research into the respiratory system [8]. As a key research field in modern medicine, respiratory diseases, such as pneumonia, chronic obstructive pulmonary disease (COPD), and lung cancer, among other diseases, are serious threats to human health and major burdens on global public health expenditures. COPD, as an irreversible and progressive pulmonary disease, annually causes >3 million deaths, ranking as the third leading single cause of death globally and posing a significant threat to the health of billions worldwide [9]. According to data from the WHO, approximately 262 million people globally suffer from asthma [10]. Lung cancer, with

an annual diagnosis rate exceeding 2.2 million and a death toll of 1.8 million, is equally serious [11]. Even relatively minor respiratory issues, such as Obstructive Sleep Apnea Syndrome (commonly known as snoring), can significantly impact the quality of life for patients and their partners, increasing the risk of cardiovascular diseases and cognitive impairments [12]. The prevalence of respiratory infectious diseases and the prominence of respiratory diseases further highlight the imperative to propel research efforts aimed at addressing the multifaceted challenges in breath analysis.

Significant value of breath analysis in the diagnosis and monitoring of various non-respiratory diseases are also demonstrated. Studies have shown that breath analysis can be used to assess diabetes. Patients with diabetic ketoacidosis are often described as smelling like rotten apples because changes in the levels of acetone and other ketone bodies in their breath can reflect lipid metabolism. In renal dysfunction, blood urea nitrogen levels can be non-invasively evaluated by measuring ammonia concentrations in exhaled breath. Thus, a "urine" odor in the breath often implies problems with kidney function. Furthermore, breath analysis is gaining importance in liver disease diagnosis, as evidenced by elevated sulfide concentrations in the exhaled breath of cirrhosis patients. These applications showcase the potential of breath analysis as a non-invasive diagnostic tool in the management of multi-system disorders [13].

Routine examinations in respiratory medicine include radiological examinations, bronchoscopy, pulmonary function tests, and symptom analysis, each with its specific clinical significance. Despite significant advancements in respiratory system research over the past decades, all these examinations have inherent limitations. Imaging techniques such as X-rays and computed tomography (CT) are limited by their inability to discern subtle structural changes and their radiation exposure. Bronchoscopy is restricted in its routine application due to its invasive nature. Pulmonary physiological tests, such as respiratory rate and tidal volume measurements, are hindered by measurement instability and lack of specificity. Symptom analysis is subjective, varies between individuals, and is often not apparent in early stages. Moreover, compared to routinely monitored physiological

parameters like heart rate, blood pressure, and body temperature, physical respiratory monitoring and assessment have not received due attention in clinical and daily health management [14]. The primary reason for this is the lack of economical, portable, and accurate respiratory monitoring devices. Existing high-precision respiratory function testing equipment is typically expensive, complex to operate, and challenging to be widely applied in daily health monitoring. Therefore, at present, one of the few breath parameters that people often pay attention to is respiratory rate, but the recording of it in clinical settings still relies mainly on manual operation. One the other hand, changes in biochemical molecular are crucial triggers, manifestations, and primary diagnostic criteria for many diseases, underscoring the importance of biochemical information. However, breath analysis and monitoring often lacks detailed biochemical detection in routine clinical and everyday practice. Considering these limitations of existing physical respiratory monitoring technologies and the lack of detailed biochemical information in breath analysis, non-invasive, quantitative, and daily monitoring of physical and biochemical information of respiration has the potential to revolutionize our understanding of breath process [15].

This review aims to systematically explore the physical and chemical information related to breath, relevant biological and clinical background, advanced laboratory-based test methodology, and wearable breath monitoring devices. (**Fig. 1-1**). Specifically, we first conduct an in-depth analysis of the physical information of respiration, like respiratory rate, volume, etc., examining the patterns of changes in these parameters under different physiological and pathological conditions and their clinical significance. Secondly, we provide a detailed overview of the gaseous chemical information in exhaled breath, for example, dynamic changes in oxygen and carbon dioxide concentrations, as well as the application prospects of volatile organic compounds (VOCs) in disease diagnosis and health monitoring. Afterwards, we explore the biochemical characteristics of non-volatile substances and their potential value in non-invasive disease diagnosis and metabolic state tracking. Finally, we present breathomics related data processing methods, the use of breath in human- machine interaction (HMI), and we outline our outlook for a future in which such

various analysis and monitoring technologies are embedded in the non-invasive breath healthcare landscape.

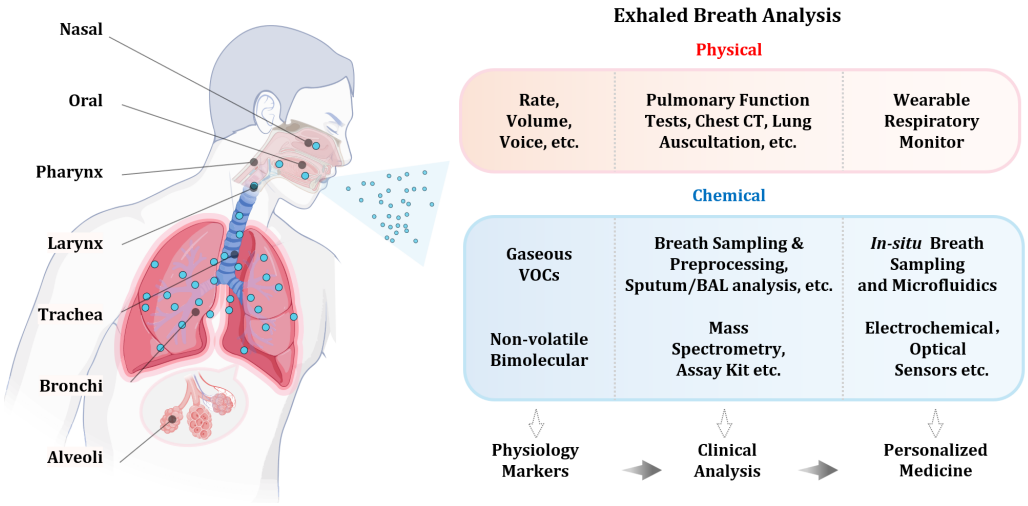

Figure 1-1. Overview of exhaled breath analysis - from Physiological markers to clinical and personalized medicine. BAL, Bronchoalveolar Lavage; CT, Computer Tomography.

1.2 Physical monitoring

In respiratory monitoring, the measurement and analysis of physical parameters are key to assessing respiratory health and overall health (see **Fig. 1-2**). These parameters include respiratory rate, volume, flow rate, breath sounds, breath temperature, and humidity. These parameters are well established with a lengthy history of research, extensive data support, and clinical validation, and are widely recognized for their use in clinical and daily health monitoring.

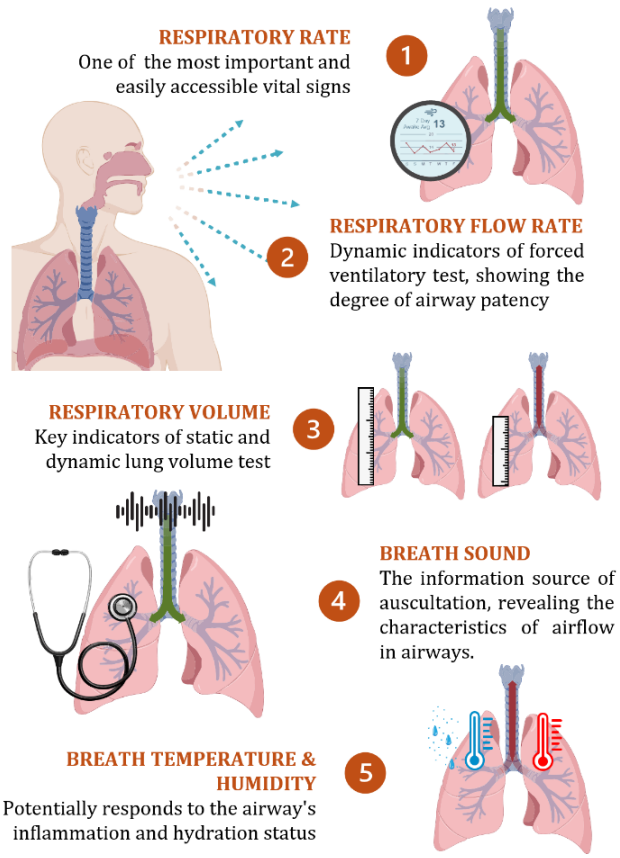

Figure 2-2. Physical breath monitoring in the precision medicine via emerging wearable devices.

1.2.1 Respiratory rate, volume & flow rate

Rate

Respiratory rate is the most widely used, simple to measure, and medically important physiological parameter. As one of the vital signs, it is, together with heart rate, blood pressure, and body temperature, a basic indicator for assessing the health status of the human body [16]. The normal respiratory rate for adults is usually between 12 and 20 breaths per minute, but this range may vary depending on age, physical condition, and environmental factors. When the respiratory rate is outside the normal range, such as more than 25 breaths per minute (rapid breathing) or less than 8 breaths per minute (bradypnea), it often means

that the subject may be in a pathological state. This abnormality may be an early warning sign of several serious diseases, including lung infections, heart failure, metabolic disorders, or neurological disorders [17]. Therefore, in clinical practice, monitoring of respiratory rate is of key importance to timely detection and evaluation of critically ill patients [17]. More specifically, there is a complex interaction between respiratory rate and the cardiopulmonary and cardiovascular systems [5,18]. This relationship is manifested primarily through cardiopulmonary coupling mechanisms, in which respiratory activity can directly influence heart rate variability and blood pressure fluctuations [19–21]. Further studies have shown that conscious regulation of breathing rhythm, especially the use of slow, deep, and long breaths, can significantly affect the activity of the autonomic nervous system [22]. In addition, breathing rate is closely related to an individual's mental state and emotional experience. In a state of stress or anxiety, the human body tends to adopt a rapid, shallow breathing pattern and the respiratory rate increases significantly. Conversely, in a relaxed or calm state, breathing tends to become slow and deep [23]. This phenomenon not only reflects the current mental state, but also offers the possibility of active emotional regulation. Based on the close correlation between breathing and physical and mental states, many psychological relaxation techniques and meditation practices include breathing regulation as a central element. For example, various breathing exercises in yoga (e.g., abdominal breathing, alternate nostril breathing, etc.) aim to influence the autonomic nervous system by adjusting breathing patterns, thereby achieving physical and mental relaxation and stress relief [24]. These techniques are not only useful in the field of mental health but have also shown positive results in the adjunctive treatment of certain diseases. For example, in asthma patients, specific breathing exercises can help improve lung function, reduce the frequency of exacerbations, and improve quality of life [25].

Volume

Respiratory volumetric indices play a key role in medical diagnosis and treatment and can be categorized into static and dynamic categories, also known as lung volume and pulmonary

ventilation function [26]. These two types of indicators can reflect the health and performance of the lungs.

The key indicators of static lung function mainly include total lung volume (TLC) and lung capacity (VC). Total lung volume is an important indicator for the assessment of restrictive lung diseases such as pulmonary fibrosis. Decreased lung volumes are usually seen in parenchymal lung lesions, thoracic deformities, and neuromuscular diseases [26]. In addition, spirometry is used to assess growth and development in children [27] and physical fitness in athletes [28,29]. In mechanical ventilation of critically ill patients, tidal volume (TV) is a key parameter used to assess and guide the patient's ventilatory status. In patients with acute respiratory distress syndrome (ARDS), a low tidal volume ventilation strategy is thought to help improve prognosis [30].

Dynamic lung function mainly consists of metrics such as forceful lung volume (FVC) and forceful expiratory volume in the first second (FEV1). These indices are very sensitive to most of the diseases involving the lungs. The FEV1/FVC ratio is the most used index for determining how good or bad airway patency is, and it is also one of the most important reference parameters for the diagnosis of obstructive lung disease. The FEV1/FVC ratio is greater than 80% in normal subjects [26]. Bronchodilator testing to observe changes in FEV1/FVC can be used to differentiate reactive reversible changes in the airways and is often used in the diagnosis and differentiation of COPD and asthma [31,32].

Flow rate

Respiratory flow rate primarily reflects airway patency and respiratory muscle strength. Commonly used indicators include Peak Expiratory Flow (PEF) [33] and Forced Expiratory Flow (FEF) at different percentages of vital capacity (FEFXX%) [34,35]. These parameters are crucial for assessing airway obstruction and pulmonary function impairment. Due to the simplicity of peak flow meters, they are widely used in the basic diagnosis and management of asthma [36]. Furthermore, the velocity of exhaled breath is closely related to gas exchange and viral transmission, which is of significant importance to public health [37,38].

Interrelationship

There exists a close interrelationship among respiratory rate, volume, and flow rate. Collectively, these parameters constitute the foundation for numerous areas of respiratory science research and clinical applications. In a single breath, the velocity-volume relationship forms a flow-volume loop that is clinically intuitive and diagnostic [39]. In multiple breaths, the rate-volume relationship is reflected in the volume of ventilation per minute. Resting and maximal ventilation (MV or MVV) reflect the volume of air breathed over a period of time in the resting and forced states, respectively. Minute ventilation is an important guide in assessing metabolic and cardiopulmonary capacity [40].

The inseparable interplay of these respiratory parameters guides clinical respiratory strategies, varied with different types of lung diseases. Patients with restrictive lung disease (e.g., pulmonary fibrosis, asbestosis, morbid obesity, etc.) usually breathe rapidly and shallowly because their lungs require higher pressures to expand. In contrast, patients with obstructive lung disease (e.g., asthma, COPD) are best served by deep and slow breathing because the airway obstruction causes the lungs to require higher pressures to overcome the resistance to flow, and therefore the volume of each breath becomes smaller [41].

Measurement methods

These three respiratory parameters monitoring methods can be broadly categorized into direct and indirect measurement techniques. Direct measurement involves analyzing airflow parameters, while indirect methods focus on measuring changes in body or thoracic volume during respiration [42,43]. Direct measurement methods include mechanical, pressure differential, and thermosensitive approaches [44]. Mechanical methods, once common in spirometry, have fallen out of favor due to their low sensitivity and the complex structure of their equipment. Pressure differential and thermosensitive methods offer higher sensitivity and easier integration, making them more suitable for modern electronic applications [45]. However, these methods are often sensitive to ambient temperature and humidity, requiring real-time compensation [46]. Recent advancements in ultrasonic flow meters have led to more

sensitive measurements by eliminating interference from temperature and humidity fluctuations in the airflow [47,48]. Direct measurement techniques provide high accuracy and are ideal for detailed flow measurements, but they often require the use of breath inlets or masks, which may cause discomfort for wearer.

Indirect respiratory measurements primarily focus on changes in body or thoracic volume during breathing. Body plethysmography, a common clinical method, estimates various respiratory parameters by measuring air pressure at different positions within a sealed space. This technique is particularly useful for measuring airway resistance and is often employed in the diagnosis and management of obstructive lung diseases [49]. Electromagnetic [50], optical [51], and acoustic[52] respiratory measurements analyze thoracic movement using radar technology, image processing, or sound analysis. These methods offer comfortable and non-invasive solutions, making them suitable for monitoring children and critically ill patients. However, they typically require fixed equipment locations and professional guidance [53].

Wearable devices

While some of the aforementioned methods and instruments offer high-precision respiratory monitoring capabilities, unfortunately they are often expensive and bulky, rendering them impractical for everyday use. In recent years, wearable smart devices for respiratory monitoring have gained increasing popularity [54], as shown in **Fig. 1-3**. Although these devices may have slight limitations in terms of time resolution and accuracy, they are exceptionally well-suited for long-term, real-time monitoring in daily environments.

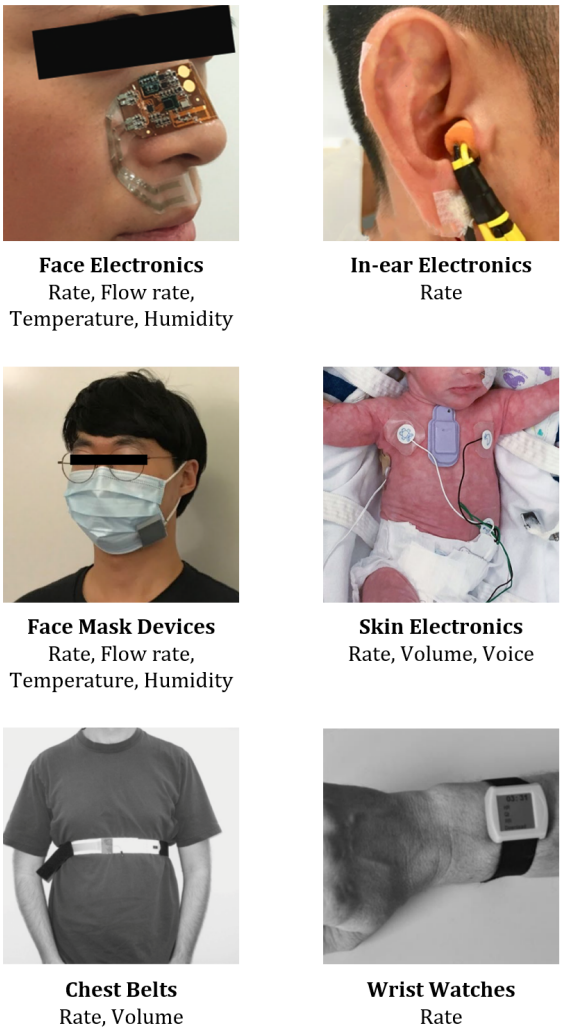

Figure 1-3 Physical breath monitoring in the precision medicine via emerging wearable devices.

Intuitively, directly attaching respiratory monitoring devices to the face is the most effective method for monitoring respiratory parameters, as they have direct access to the airflow [55,56]. Additionally, face masks, as everyday wearable items, serve as an ideal monitoring platform [57,58]. These research focuses is on measuring airflow vibrations [59], pressure [60], humidity [61], and temperature [62] to infer respiratory parameters. However, the spontaneous nasal cycle during human respiration and variations in device placement and non-enclosed respiratory mask spaces have led to predominantly qualitative research on respiration (mostly about

respiratory rate), lacking accurate quantitative studies (respiratory velocity and volume). Some devices utilize enclosed masks for qualitative respiratory analysis, but the complexity of these systems makes them unsuitable for daily use [63,64]. Chest strips utilizing electrical analysis techniques, such as electrical impedance tomography (EIT) [65] and strain [66–68] measurements, allow for respiratory analysis (rate and volume) and monitoring during sleep or exercise. Motion detection [69] and photoplethysmography (PPG) devices [70], like smart wristbands [71] and earphones [72,73], show promise in estimating respiratory rates through algorithm-based approaches. However, these wearable devices often focus on qualitative measurements of respiratory rate or relative intensity, with limited quantitative information[74].

1.2.2 Breath voice

Respiratory sounds, including both distant breath sounds and those heard through a stethoscope, are crucial physical parameters in clinical assessment. These sounds originate from mechanical vibrations produced as air flows through various chest shapes. Careful auscultation and analysis of respiratory sounds enable physicians to identify early signs of numerous conditions, including pneumonia, asthma, lung infections, and obstructive sleep apnea [75]. Different types of respiratory sounds provide valuable diagnostic information. Wheezes are associated with asthma, crackles with pneumonia, pulmonary fibrosis, and pulmonary edema, while stridor indicates upper airway obstruction outside the chest cavity [76,77]. Moreover, cough sounds, characterized by sudden expulsion of air accompanied by distinctive sounds, are important symptoms in over 100 diseases and medically significant conditions [78]. As an example, breath and cough sounds can be used to distinguish and diagnose COVID-19 [79].

Clinically, the assessment of respiratory sounds primarily relies on the use of stethoscopes to auscultate different areas of the chest, enabling the acquisition of acoustic information from various lung structures. However, accurate interpretation of these acoustic signals often requires significant clinical experience and can be highly subjective [77]. In recent years, the development of digital stethoscopes and artificial intelligence has initiated revolutionary changes in auscultation techniques [80,81]. For instance, a flexible wireless auscultation device,

incorporating miniature wireless chips and filtering functions, has demonstrated the feasibility for remote respiratory monitoring. This technology has been successfully applied in monitoring respiratory sounds of premature infants to prevent airway obstruction and in patients with pulmonary surgical conditions [82].

1.2.3 Breath temperature & humidity

Exhaled breath temperature has shown potential correlations with airway inflammation, particularly in asthma and COPD [83]. Two primary parameters are considered: temperature rise time and plateau temperature [83]. These parameters may reflect microvascular function, inflammation status, or airway remodeling in the small airways [84]. In asthma, elevated exhaled breath temperatures may be associated with bronchial congestion due to inflammation or increased microvasculature resulting from airway remodeling [85]. Conversely, in COPD, lower exhaled breath temperatures might indicate reduced bronchial vascular function [86,87]. However, it's important to note that monitoring methods and devices can significantly influence temperature results, necessitating standardized measurement protocols [88].

The typical relative humidity of exhaled breath ranges from 60-80% [89]. Some studies suggest a potential link between breath humidity and body hydration status, with factors such as alcohol consumption and physical exercise potentially influencing these measurements [90]. Other research implies that breath humidity may reflect certain pulmonary inflammations or diseases [91,92]. However, overall, medical research on the humidity of exhaled breath remains limited in its clinic promise and application.

Wearable temperature and humidity sensors have experienced remarkable growth, primarily due to their simple system structure and extremely fast response times, making them suitable for measuring respiratory rate or intensity [93,94]. Common fast-response temperature and humidity sensors typically output four types of signals: impedance, light, frequency, and voltage. Owing to the unique properties of their microstructures, nanomaterial-based sensors

have emerged as a promising direction for respiratory temperature and humidity monitoring [95,96].

1.3 Exhaled gaseous detection

Respiration serves as a gaseous medium for continuous molecular exchange between the internal milieu and the external environment. With technological advancements, non-invasive research on respiratory gaseous molecules has become a new focal area of interest. From the fundamental basis of breathing—the inhalation of oxygen and expulsion of carbon dioxide—to everyday oral odors and alcohol breath, to the apple-like scent in patients and ammonia odor in urine, the human body continuously manifests its health status through the composition of gaseous molecules it exhales (**Fig. 1-4**).

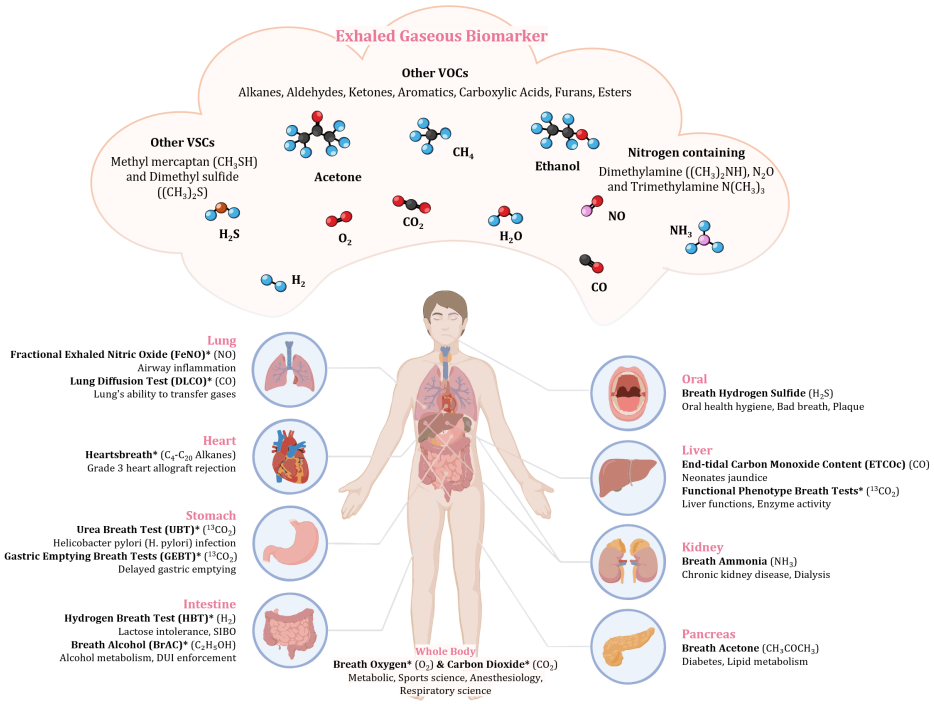

Figure 1-4 Representative gaseous chemical biomarkers in human exhaled breath and corresponding organ disorders. * means approved by U.S. Food and Drug Administration (FDA); SIBO, Small intestinal bacterial overgrowth; DUI, Driving Under the Influence.

1.3.1 Sampling methods

Breath gas monitoring can generally be divided into offline monitoring and online real-time monitoring. The former typically involves collecting exhaled breath in polymer bags, followed by preprocessing techniques such as drying or concentration, before entering the analysis platform [97]. Although offline collection and detection often imply more reliable and precise results, they lack many of the advantages and conveniences of real-time detection in terms of dynamic changes and long-term monitoring. Generally, online real-time breath monitoring often has extremely high requirements for the response time of the monitoring method (much less than one respiratory cycle of ~4 s) [98]. Additionally, some online monitoring devices are equipped with air pumping systems to effectively control the gas in the detection chamber [99]. It is important to note that the airway is a semi-open gas environment composed of alveolar end-tidal air and dead space air. The composition of these two types of gases can, to some extent, influence the concentration levels of gases from different sources [100].

1.3.2 Detection methods

Various methods are available for the detection of breathing gases. As shown in **Fig. 1-5**, sensors based on electromagnetism, chemistry, optics, etc. all possess distinct advantages and specific application domains, thereby offering a comprehensive spectrum of solutions for exhaled gas analysis.

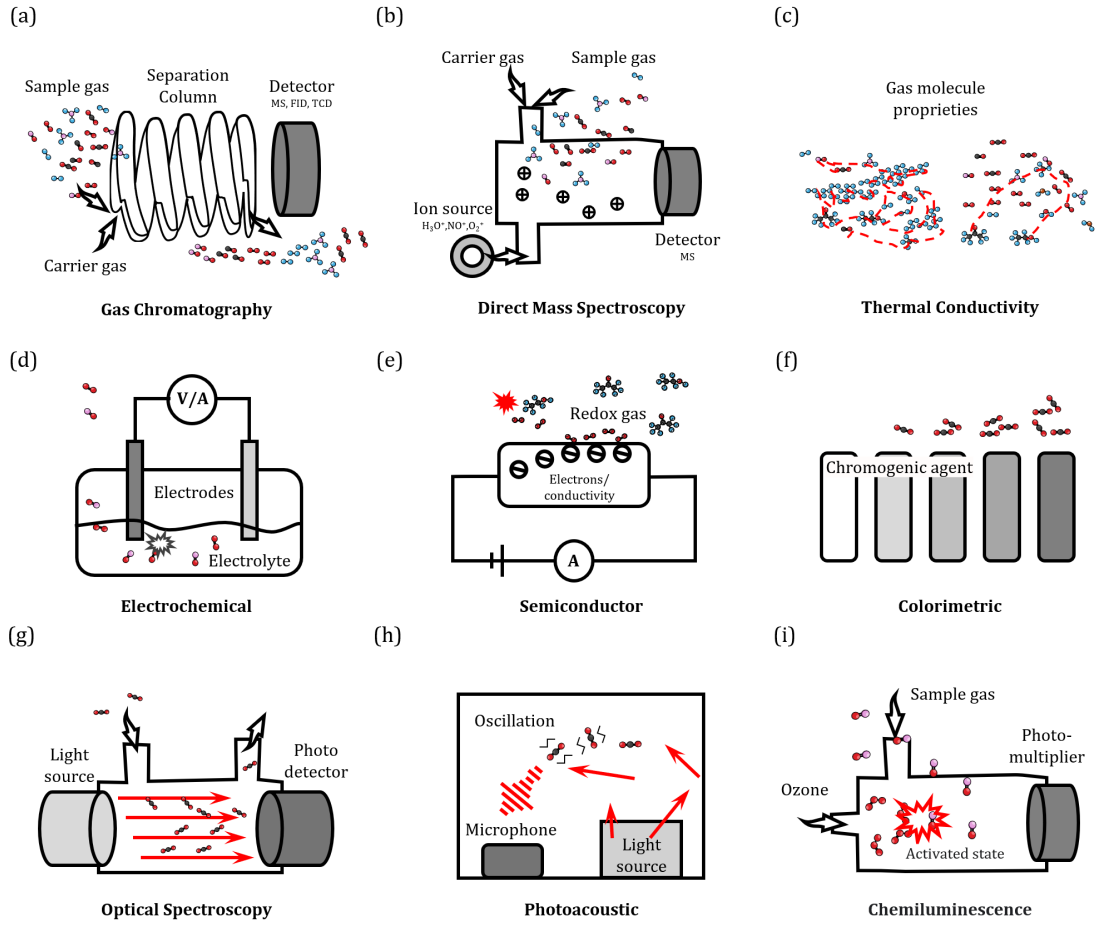

Figure 1-5. Emerging gas sensing strategies in breath analysis. Thermionic Ionization Detector (TID), and Thermal conductivity detector (TCD).

Gas chromatography

Gas chromatography (GC) is a widely used separation and detection technique. The principle is to utilize the difference in partition coefficients of different components between the stationary phase and the mobile phase for separation. The sample is injected through a syringe and enters a column coated with a liquid or solid stationary phase with a carrier gas. Each component interacts with the stationary phase to a different extent, resulting in unequal migration rates through the column and thus realizing the separation. GC is often coupled with detection techniques such as mass spectrometry (MS) and flame ionization, and ion migration spectrometry [101], and it's often considered as the gold standard for the detection of

exhaled volatile gases because of its ability to accurately measure them with high sensitivity and specificity. However, this method requires more complicated sample preparation and introduction procedures, smaller detection throughput, longer analysis cycle time, and is not conducive to real-time measurement [102,103].

Direct mass spectroscopy

Direct MS technologies like proton transfer reaction mass spectrometry (PTR-MS) and selected ion flow tube mass spectrometry (SIFT-MS) techniques have gained broad attention and applications in the field of breath gas analysis with their online real-time detection of VOCs [104] by direct ionization of the compounds in the exhaled gases and measurement of their mass-to-charge ratios. Compared with traditional GC-MS, these techniques do not require pre-enrichment or pre-separation and have advantages such as low fragmentation ionization. Although there are some shortcomings in molecular identification and complex sample analysis capability, they are gradually developing as ideal alternative of traditional MS and complementary technologies in the field of breath gas analysis by virtue of their rapid response and capability of online detection. PTR-MS has some limitations in detecting molecules with low proton affinity due to its inherent H_3O^+ ionization mechanism, whereas SIFT-MS provides a board selection of ion sources such as H_3O^+, NO^+, and O_2^+, expanding the detection range. However, the high cost of the equipment and the relatively complex operation limit their applications in daily life to some extent [105].

Electrochemical

Electrochemical sensors represent one of the earliest developed methodologies for breath analysis [106]. These devices function by detecting either the redox reactions of electroactive gaseous substances on electrode surfaces or the pH alterations in electrolytes resulting from gas dissolution [107]. The advantages of electrochemical sensors include low cost and operational portability, rendering them suitable for real-time and wearable monitoring in both daily life and clinical settings [108], see **Fig. 1-6A**. Recent advancements in solid electrolyte research have enabled certain electrochemical sensors to operate at ambient temperatures for

prolonged periods [109]. However, these sensors face limitations such as dependence on specific gas types, the need for frequent calibration and maintenance, relatively low sensitivity, and limited suitability for detecting trace gas concentrations.

Semiconductor

Semiconductor sensors exploit the interaction between gas molecules and semiconductor surfaces (e.g., metal oxides, carbon-based materials) for target gas detection. The reaction between the gas molecule and the semiconductor surface induce changes in carrier concentration or produce adsorption effects, inducing alteration in conductivity [110]. These sensors offer advantages such as low cost, rapid response, and facile integration, making them the most extensively researched category of wearable gas sensors. However, their detection principle, mostly based on the redox properties of gas molecules, renders them susceptible in many occasions, leading to poor selectivity and challenges in accurately distinguishing types of specific gas molecule [111]. Furthermore, certain semiconductor materials necessitate high-temperature gas detection and are prone to humidity interference [112,113]. Consequently, as depicted in **Fig. 1-6B**, pre-removal of interfering components from exhaled gas prior to detection appears to be a viable option.

Optical Spectroscopy

Spectroscopy is based on the absorption of specific wavelengths of light by target gas molecules. As light passes through a gas-containing medium, molecules absorb light at frequencies matching their characteristic vibrations, producing absorption peaks in the incident light's energy spectrum [114]. This technique offers real-time analysis and simplicity [115]. Recent advancements in semiconductor laser diodes and photodetectors have led to the miniaturization of spectrometric equipment, including portable devices [116]. However, the requirement for a sufficiently long effective gas path length to achieve high sensitivity poses challenges for further miniaturization, limiting its application in wearable devices.

Photoacoustic

Photoacoustic spectroscopy is a gas detection method based on spectroscopic principles. It utilizes the photothermal effect, which is produced when laser radiation interacts with gas molecules and triggers oscillatory collision sounds for gas detection. This technique eliminates the reliance on optical detectors, overcomes limitations associated with laser wavelengths, and avoids the need for long optical absorption paths, thereby enabling miniaturization [117,118]. However, turbulence from gas flow can interfere with measurements, and its sensitivity is lower compared to optical spectroscopy methods [119].

Chemiluminescent

Chemiluminescence is a detection technique predicated on the emission of light resulting from energy transitions and releases during specific chemical processes. The quantification of analyte concentration is achieved indirectly through the measurement of chemiluminescent signal intensity. Critical to this methodology is the judicious selection of chemical reaction systems or sensor materials that catalyze the luminescent reaction [120]. This analytical approach is characterized by operational simplicity, high sensitivity, and excellent specificity, with the notable advantage of not requiring external excitation sources. Chemiluminescence finds particular utility in the analysis of exhaled breath, specifically for the detection of nitric oxide in medical diagnostics [121,122]. However, the requirement for additional chemical substances, such as ozone, presents challenges for miniaturization.

Others

In addition to the aforementioned methodologies, a diverse array of techniques has been applied for exhaled gas sensing, including colorimetric methods [123–125], thermal conductivity sensors [126], and surface plasmon resonance techniques [127,128] etc. Colorimetric methods are among the simplest and most stable sensor technologies available, making them particularly well-suited for the construction of wearable devices (**Fig. 1-6C**). However, it is important to acknowledge that their selectivity and sensitivity are relatively limited compared to other techniques.

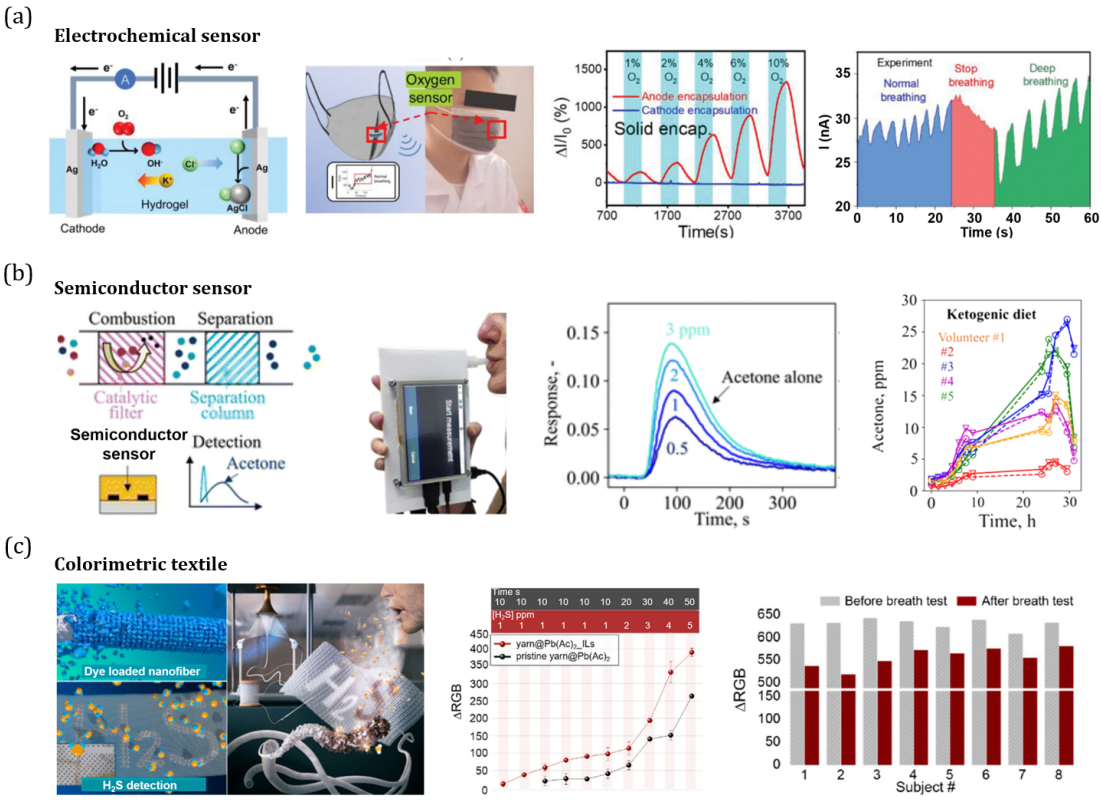

Figure 1-6. Miniaturized gas sensing system development for in situ breath analysis. (a). Hydrogel material-based electrochemical oxygen sensor for breath oxygen measurement in a mask device. (b). A portable semiconductor sensor based on interferon filtering and separation for exhaled acetone analysis. (c). A colorimetric textile based H_2S sensor for halitosis breath detection.

1.3.3 Biomarkers

Oxygen and carbon dioxide

Oxygen represents a fundamental element essential for the maintenance of biological processes. During the respiratory cycle, atmospheric oxygen enters the pulmonary system and diffuses across the alveolar-capillary membrane into the circulatory system. Erythrocyte hemoglobin binds oxygen, forming oxyhemoglobin, which facilitates the systemic distribution of oxygen to diverse tissues and organs. Within these tissues, oxygen dissociates

from hemoglobin and participates in cellular respiration. Specifically, oxygen serves as the terminal electron acceptor in the mitochondrial electron transport chain, enabling oxidative phosphorylation. This process culminates in the synthesis of adenosine triphosphate (ATP), the primary energy currency of the cell, which is subsequently utilized by various cellular functions [129].

Oxygen uptake (VO_2) is an important measure of the amount of oxygen absorbed and utilized by the body. In exercise physiology, oxygen uptake reflects the consumption of oxygen by exercising muscles. Oxygen uptake can be measured by gas analysis of the oxygen content in inhaled and exhaled air. Within seconds to minutes after the onset of intense intensity exercise, pulmonary oxygen consumption may rise rapidly from about 0.25 L/min at rest to an individual maximum that may exceed 5 to 6 L/min, known as maximal oxygen uptake [130,131]. Maximum oxygen uptake has a close correlation with exercise capacity and metabolic capacity [132,133]. The kinetics of oxygen uptake changes are also commonly used to analyze cardiopulmonary function in patients with pathologically slowed VO_2 kinetics, such as COPD and other obstructive lung diseases [134].

Oxygen utilization is not just a one-way process. While cells utilize oxygen for metabolic reactions, they also produce the metabolic waste product, which is carbon dioxide. After carbon dioxide is produced during cellular metabolism, it needs to be transported through the bloodstream to the lungs for removal. Carbon dioxide is transported in the blood in three main forms: dissolved in plasma, combined with hemoglobin to form bicarbonate hemoglobin, and converted to bicarbonate. In the capillaries, carbon dioxide diffuses into the erythrocytes, where it partially combines with water to form carbonic acid, which is rapidly dissociated into hydrogen ions and bicarbonate by the enzyme called carbonic anhydrase. This process plays a key role in maintaining the acid-base balance of the blood [135]. Ultimately, carbon dioxide is transported to the alveolar capillaries, diffuses from the bloodstream into the alveoli, and is expelled from the body through exhalation. Through this complex mechanism of transportation and elimination, carbon dioxide levels in the body are regulated

and are directly related to the maintenance of acid-base balance and overall metabolic homeostasis in the body.

Interestingly, the core function of human respiration is not to directly regulate arterial partial pressure of oxygen but to facilitate carbon dioxide removal [136]. Because oxygenation and ventilation are independent physiologic processes, monitoring oxygenation by pulse oximetry alone is not a suitable means of monitoring ventilatory function. The value of carbon dioxide, instead, happens to reflect ventilation more clearly [137]. The study of carbon dioxide is important in the context of hypoventilation due to lung diseases, such as hypercapnia due to failure to remove carbon dioxide in time [138] and hypocapnia due to hyperventilation [139]. Important applications of exhaled carbon dioxide monitoring in clinical practice include its role as a decisive method of confirming endotracheal intubation and its role in harm reduction by recognizing the serious consequences of mistaken esophageal intubation [140]. The field of synergistic oxygen and carbon dioxide research also includes indirect calorimetry. Indirect calorimetry estimates the form and rate of receptor utilization and energy metabolism in the body by measuring gas exchanges (oxygen consumption and carbon dioxide production during rest and steady exercise), providing an important data reference for human metabolic studies [141]. The monitoring of exhaled carbon dioxide has another significant medical application in the form of the Breath $^{13}CO_2$ test. This technology involves administering a substance labeled with a stable isotope of carbon (^{13}C) to the subject, which, upon metabolism, produces $^{13}CO_2$. The ratio of $^{13}CO_2$ to $^{12}CO_2$ in the exhaled breath is then measured, providing valuable information about metabolic processes in the body [142]. For instance, the Breath $^{13}CO_2$ test can be used to assess liver function [143], diagnose Helicobacter pylori infections [144], and monitor metabolic disorders [145]. This non-invasive technique offers a safe and efficient means of gaining insights into the patient's metabolic state, making it a valuable tool in both clinical diagnostics and research.

Four prevalent clinical monitoring methods are employed for the in vivo assessment of oxygen and carbon dioxide: 1) arterial blood gas analysis (PaO_2, $PaCO_2$), 2) end-tidal breath analysis ($PetO_2$ $PetCO_2$), 3) pulse oximetry (SaO_2), and 4) transcutaneous gas analysis ($PtcO_2$,

$PtcCO_2$). Blood gas analysis serves as the gold standard for evaluating respiratory function and blood acid-base balance, but its invasive nature presents challenges for continuous monitoring [146,147]. The other three non-invasive methods can reflect blood gas parameters under certain conditions [148]. End-tidal analysis directly analyzes exhaled gas composition, which offer superior real-time capabilities and richer information, facilitating the calculation of metabolic rates and oxygen consumption, albeit requiring cumbersome equipment. Pulse oximetry is a non-invasive method that measures the oxygen saturation ratio in arterial blood by analyzing light absorption changes during pulsatile blood flow. Transcutaneous gas measurements provide a more comprehensive assessment of tissue gas content. This technique involves locally heating the skin to induce vasodilation and enhance gas diffusion. By doing so, it more accurately reflects blood gas values, including not only oxygen but also carbon dioxide levels. Consequently, transcutaneous gas monitoring offers broader applicability in clinical settings, enabling continuous assessment of both ventilation efficiency and tissue oxygenation status [149].

Measurements

Clinical oxygen and carbon dioxide sensing systems typically consist of sampling devices and sensing units. Sampling devices can be categorized based on medical applications and wear locations, including blood gas analyzers [150], Douglas bags [151], respiratory masks [152], transdermal patches [153], and indirect calorimetry hoods [152]. There are diverse measurement forms and associated commercial products, ranging from invasive blood gas analysis for critical care patient monitoring to end-tidal oxygen and carbon dioxide monitoring. For athletic monitoring, commercial wearable metabolic systems like COSMED K5 are used, while single-breath analysis devices such as Microlife MedGem are employed for home indirect calorie measurement. Devices like TCM CombiM are used for transcutaneous gas monitoring.

Regarding gas sensing units, current CO_2 sensors for respiratory gas analysis are based on Non-dispersive infrared (NDIR) principles [154], offering rapid response but requiring certain gas chamber space and air pump systems for gas renewal. For blood gas and transcutaneous

analysis of dissolved gases and miniaturized devices, CO_2 analysis techniques rely on electrochemical technology using Severinghaus electrodes [155]. Oxygen analysis across various forms is based on electrochemical Clark electrodes [156]. While these technologies have achieved most functionalities, barriers to wearable and long-term monitoring of human-related oxygen and carbon dioxide in daily life remain unbroken.

Recent research has focused on wearable analytical devices, such as NDIR-based masks or skin electronic systems for CO_2 concentration measurement [157,158]. Some oxygen sensing devices utilize colorimetric [159,160] or electrochemical methods [161]. These sensor principles are conducive to miniaturization and integration, but their performance in practical use still falls short in key indicators, including response speed, measurement accuracy, frequency of calibration, membrane replacement, and duration time. From a systematic perspective, minimizing the size of wearable sensors while maintaining measurement precision is crucial for realizing the value of this field.

Nitric oxide

Biological meaning

Fractional exhaled nitric oxide (FeNO) is an important biomarker that plays a crucial role in diagnosing and managing airway inflammation. Nitric oxide is a gas molecule produced by airway epithelial cells under the influence of specific enzymes such as inducible nitric oxide synthase (iNOS). Its concentration accurately reflects the inflammatory level of the airways, providing clinicians with a non-invasive, rapid, and reliable assessment method.

FeNO measurement is widely used in the diagnosis and treatment of inflammatory airway diseases such as asthma. Due to chronic airway inflammation, asthma patients typically have higher FeNO levels than healthy individuals. Through regular FeNO measurements, doctors can dynamically assess the severity of airway inflammation and adjust treatment plans accordingly, particularly the dosage of anti-inflammatory treatments like inhaled corticosteroids, thereby optimizing therapeutic effects and improving disease control [162].

Besides asthma, FeNO measurement is also applicable to other eosinophil-related inflammatory airway diseases such as COPD, allergic rhinitis, and eosinophilic bronchitis [163]. In these conditions, changes in FeNO levels can reflect disease activity and treatment efficacy, providing an important reference for clinical decision-making.

The main advantages of FeNO measurement lie in its non-invasiveness and real-time nature. Patients only need to perform specific exhalation maneuvers without any invasive procedures, greatly improving patient compliance and comfort. The entire measurement process is quick, and results are immediately available, aiding clinicians in timely decision-making and treatment adjustments. However, FeNO measurement also has some limitations and issues to consider. Firstly, FeNO levels are influenced by various factors such as smoking, diet, and exhalation flow rate. Therefore, measurements need to be conducted under standardized conditions, considering the potential impact of these factors on results [164]. Secondly, while elevated FeNO usually indicates airway inflammation, it cannot fully differentiate between different types of inflammation or identify their specific causes. Doctors need to interpret results in conjunction with other clinical information. Additionally, baseline FeNO levels vary among individuals, requiring doctors to consider patients' individual characteristics and medical records when interpreting results. Furthermore, since the paranasal sinuses also produce high concentrations of NO, NO exhaled from the nasal cavity does not accurately reflect NO concentrations in the small airways of the lungs. Therefore, to exclude nasal NO interference, FeNO measurements are typically performed during oral breathing. Despite these limitations, FeNO measurement remains a valuable clinical tool.

Measurements

There are two main methods for detecting exhaled nitric oxide. One is the ozone chemiluminescence method, considered as the gold standard. In this method, ozone (O_3) reacts with nitric oxide (NO) to produce nitrogen dioxide (NO_2) and oxygen (O_2). During the formation of nitrogen dioxide, some NO_2 molecules are in an excited state (NO_2*). As these excited NO_2 molecules return to their ground state, they emit photons (i.e., luminescence) [165]. This principle is used in commercial instruments, like the model 280i by Sievers.

With electrochemical technological advancements, FeNO measuring devices are becoming more portable and suitable for a broader range of clinical and home environments. Electrochemical devices (such as NIOX MINO) have made personal, independent measurements possible [166]. These devices measure NO concentration by oxidizing NO at a platinum electrode at 0.8V, correlating the oxidation current with NO concentration after removing interfering gases and other components [167]. However, NO concentrations obtained through commercial electrochemical devices are generally slightly lower than those from chemiluminescence devices [168].

Ammonia

Ammonia in exhaled breath is closely related to protein metabolism in the body, primarily originating from the breakdown of proteins and amino acids. The metabolism and excretion of ammonia is a complex physiological process involving the coordinated action of multiple organ systems [169,170]. Notably, the ammonia content in the oral cavity may be more substantial than other sources. Research shows that urea in saliva is broken down by urease produced by oral bacteria, generating substantial amounts of ammonia. This process has important physiological implications: the produced ammonia helps neutralize acidic substances from food and bacterial metabolism, thereby protecting the oral mucosa and teeth from acid erosion [171]. This natural buffering mechanism plays a crucial role in maintaining oral health. In certain disease states, the concentration of ammonia in exhaled breath can change significantly, thus holding potential diagnostic value. For instance, patients with renal insufficiency have markedly elevated urea levels in blood and saliva due to impaired urea excretion. This leads to the production of large amounts of ammonia in the oral cavity, giving the patients' breath a characteristic ammoniacal odor. This phenomenon is not only a clinical manifestation of renal insufficiency but also offers possibilities for non-invasive kidney function assessment [172]. Furthermore, researchers have found that levels of exhaled ammonia are associated with Helicobacter pylori (HP) infection in the stomach, suggesting potential applications of ammonia detection in gastrointestinal disease diagnosis. Studies have shown that without urea ingestion, HP-positive individuals have lower exhaled ammonia levels

compared to normal subjects. However, upon urea ingestion, HP-positive individuals show significantly elevated ammonia levels due to the large amount of urease produced by HP in the stomach, which breaks down urea into ammonia that enters the bloodstream and is subsequently exhaled through the lungs. In contrast, normal individuals show little change [173]. This difference provides a theoretical basis for developing HP infection diagnostic methods based on exhaled ammonia detection [174].

For the detection of breath ammonia, a crucial point to consider is that ammonia is highly soluble in water. Therefore, humidity measurement or dehumidification is necessary before detecting gaseous ammonia. Numerous methods can achieve breath ammonia detection [175]. However, most methods rely on complex systems and are not suitable for daily monitoring. Various wearable devices based on chemiresistive [176] or colorimetric [177] principles have been developed, but there are still lack of in situ quantitative ammonia measurement methods on the human body.

Acetone

Acetone is a prominent gas molecule for biological analysis, primarily produced through fat metabolism in the body. When carbohydrate supply is insufficient, the body turns to fat reserves for energy production. In this process, fatty acids are broken down into acetyl-CoA, which then generates ketone bodies such as acetone, β-hydroxybutyrate, and acetoacetate through ketogenesis. Acetone is released into the bloodstream, with a portion expelled through respiration [178]. In certain specific conditions, the concentration of acetone in exhaled breath can increase significantly, such as in diabetic ketoacidosis, prolonged fasting states, or ketogenic diets [179]. In healthy individuals, the concentration of exhaled acetone is relatively low, typically ranging from 0.1 to 2 ppm. Mild fasting or low-carbohydrate diets may elevate acetone concentrations to between 2 and 10 ppm, while in cases of diabetic ketoacidosis or strict ketogenic diets, the concentration of acetone in exhaled breath may exceed 100 ppm, demonstrating a wide range of concentrations [180]. Due to this variability, breath acetone analysis shows great promise in the fields of diabetes management [181], metabolic nutrition [182], and liver function assessment [183]. The wide varied concentration

range of breath acetone corresponding to different physiological and pathological conditions makes it a versatile biomarker with significant potential for clinical applications.

For offline measurement of exhaled acetone content, Gas Chromatography-Mass Spectrometry (GC-MS) can be considered the gold standard. From the perspective of portable, wearable online measurements, chemiresistive and electrochemical sensors are hot research areas [180]. Chemiresistive sensors utilize various nanomaterials to enhance sensitivity and selectivity for acetone gas. However, they cannot eliminate interference from other gases. Consequently, some research focuses on preprocessing exhaled breath to remove interfering components [184,185]. The challenge for electrochemical sensors in detecting acetone gas lies in constructing the chemical reaction system. Some approaches are based on enzyme systems, but the selectivity of enzymes requires further evaluation [186,187]. Other sensors are based on strong acid electrolytes, which significantly limits their potential for wearable applications [188,189].

Hydrogen and methanol

Hydrogen-producing bacteria, especially anaerobic bacteria, are present in the intestines of both healthy people and patients suffering from lactulose intolerance or small intestinal bacterial overgrowth. These bacteria produce hydrogen by fermenting unabsorbed carbohydrates. When small intestinal carbohydrates are malabsorbed or small intestinal bacteria are overpopulated, large amounts of unabsorbed carbohydrates reach the colon, leading to the production of hydrogen in large quantities. The hydrogen produced is absorbed through the intestinal wall into the circulation and eventually released from the lungs and exhaled with the breath [190]. Although the sensitivity of hydrogen breath test is only 30-40%, it is still popular due to its non-invasiveness [191].

Measurements of methane are closely related to hydrogen concentrations. Approximately 15-30% of the human intestinal flora contains Pseudomonas smithi, a bacterium that converts four hydrogen atoms into one methane molecule [192]. In addition, studies have shown that methane concentration is positively correlated with the severity of constipation, providing

new ideas for the diagnosis of intestinal dysfunction [193,194]. Thus, combined measurements of hydrogen and methane can significantly improve diagnostic accuracy for malabsorption syndromes and small intestinal bacterial overgrowth [195].

In recent years, with the development of electrochemical [196] and chemiresistive sensing technology [197], the cost of hydrogen testing equipment has gradually decreased, making this noninvasive breath hydrogen test more popular. Additionally, due to the significant difference in thermal conductivity between hydrogen and other gases, sensors based on thermal conductivity measurements are commonly used for hydrogen detection [198]. Furthermore, under the influence of catalytic elements, trace amounts of hydrogen can undergo combustion reactions, raising the temperature at the reaction interface. This change in temperature can be converted into measurable electrical signals through the Seebeck effect, enabling the assessment of hydrogen content [199,200]. Methane monitoring is primarily based on optical methods, such as photoacoustic and optical absorption [201,202]. However, there is currently no mature technology for wearable devices capable of monitoring both hydrogen and methane in breath.

Ethanol and acetaldehyde

Breath ethanol testing is the most successful example of commercialization in breath analysis field. Breath ethanol levels show a good linear relationship with blood ethanol levels, making it one of the gold standards for alcohol detection, widely used in legal and medical fields [203]. Research indicates that ethanol can be produced in the intestines even without alcohol consumption, which may be associated with the development of obesity and fatty liver disease. This finding provides a new perspective for understanding the pathological mechanisms of obesity-related diseases [204,205]. Acetaldehyde, the first metabolite of ethanol, is primarily produced in the liver. The concentration of acetaldehyde in exhaled breath is typically lower than that of ethanol and can be used to assess alcohol metabolism status [206]. Furthermore, as an aldehyde, endogenous acetaldehyde is also important in cancer metabolism research [207].

Breath Alcohol Concentration (BrAC) measurement has been conducted using various techniques. Among the reported technologies, electrochemical methods have proven particularly suitable, with fuel cell-based sensors garnering the most attention. Indeed, commercial breathalyzers typically employ fuel cell chemistry technology. The prevalence of electrochemical methods stems from their simplicity, portability, cost-effectiveness, rapid detection, acceptable accuracy, data linearity, sensitivity, and alcohol selectivity. These attributes facilitate real-time measurements, handheld device applications, and overall efficacy in both research and practical BrAC assessment scenarios [208]. Enzyme-based alcohol sensors offer alternative approaches to BrAC measurement. Sensors utilizing alcohol oxidase (AOx) and alcohol dehydrogenase (ADH) enzymes provide cost-effective solutions for ethanol detection [209]. Additionally, for measuring acetaldehyde, the metabolite of ethanol, sensors based on aldehyde dehydrogenase enzymatic reactions demonstrate good performance [206]. These enzyme-based sensors complement existing technologies, offering potential advantages in terms of cost and specificity for both ethanol and its metabolites in breath analysis applications.

Sulfide containing

Exhaled sulfur compounds provide a non-invasive, rapid, and effective method for health monitoring, with applications in oral hygiene assessment and airway inflammation detection. In oral health, bacteria in the mouth produce sulfur compounds such as hydrogen sulfide (H_2S), methyl mercaptan (CH_3SH), and dimethyl sulfide (CH_3SCH_3) when breaking down sulfur-containing amino acids. Detection of volatile sulfur compounds (VSCs) enables evaluation of halitosis severity and periodontal disease status [210,211]. In airway inflammation, sulfur compound detection aids in diagnosing and monitoring inflammatory conditions like asthma and COPD. Patients with these conditions typically exhibit elevated concentrations of sulfur compounds in their exhaled breath, making this approach a valuable tool for respiratory health assessment [212].

Semiconductive chemiresistor are the most extensively studied devices for detecting exhaled volatile sulfur compounds (VSCs). Particularly when material dimensions are restricted to

the nanoscale, these gas sensors exhibit advantages such as structural stability, high sensitivity, rapid dynamic processes, and low cost, which effectively meet the requirements for biomarker detection [213]. Additionally, some carbon-based materials enable VSC measurements at room temperature, facilitating integration into wearable devices [214].

Carbon monoxide

Carbon monoxide (CO) is an important exhaled gas biomarker for assessing subjects' smoking status [215]. Additionally, exhaled carbon monoxide (eCO) has been evaluated as an indicator for various pathophysiological conditions, including inflammatory diseases of the lungs and other organs. eCO levels have shown potential value in assessing inflammation in asthma, COPD, cystic fibrosis, and lung cancer [216–218]. Furthermore, CO is commonly used in Lung Diffusion Testing (DLCO) to measure the lung's capacity for oxygen absorption [219].

Electrochemical sensors are the mainstream commercial devices for CO monitoring, capable of distinguishing the commonly used 6 ppm threshold for smokers [220]. However, for lower physiologically relevant endogenous CO levels, MS or NDIR method is required for measurement [221,222].

Other VOCs

The volatile substances mentioned above are relatively characteristic elements, possessing distinct physiological properties or present in high concentrations. However, breath still contains over 200 other VOCs of significant medical value, though clinical trial data based on these have not yet been fully integrated into our understanding of functional and mechanistic physiology [223]. Relevant medical fields include cancer [224], gastrointestinal digestion [225], pulmonary inflammation [226], cardiovascular disease [227], diabetes metabolism [228], and liver metabolism [229]. The types of compounds encompass alkanes, aldehydes, ketones, aromatics, carboxylic acids, furans, and esters. The relationships between these compounds and clinical physiology are complex, and consensus on the efficacy of individual compounds in identifying specific diseases and/or disease-related metabolism has not been

reached. Consequently, studies on numerous VOCs often employ omics approaches for analysis. For instance, furans, cyclic hydrocarbons, aromatic compounds, and benzene derivatives have been consistently identified as cancer markers across various types of cancer (including lung, breast, or oral and upper digestive tract cancers). The pathophysiology of COVID-19 includes inflammatory responses characterized by oxidative stress, which has been linked to aldehydes and hydrocarbons [230].

For the study of these multiple trace VOCs, most detection methods lack sufficient sensitivity and selectivity. Many semiconductor-based VOC sensors, while capable of measuring the equivalent total amount of VOCs, generally lack selectivity and thus cannot be directly used for precise classification and measurement of VOCs [231]. Therefore, MS remains the only viable method for clinical detection of volatile organic compounds at present.

1.4 Chemical non-volatile substances test

Breath non-volatile substances originate from the microdroplets of the respiratory tracts. The alveolar surface is covered with surfactant and a fluid layer containing various bioactive molecules. The epithelial cells lining the airways (bronchioles) are covered with airway surface liquid. During exhalation, these fluids are disturbed by airflow, forming aerosols and droplets of varying sizes. As shown in **Fig. 1-7**, these substances contain a broad range of components from small molecules like ions to macromolecules such as proteins. Their composition reflects the origin and chemical environment within the respiratory tract, making them highly promising non-invasive samples for assessing human health status.

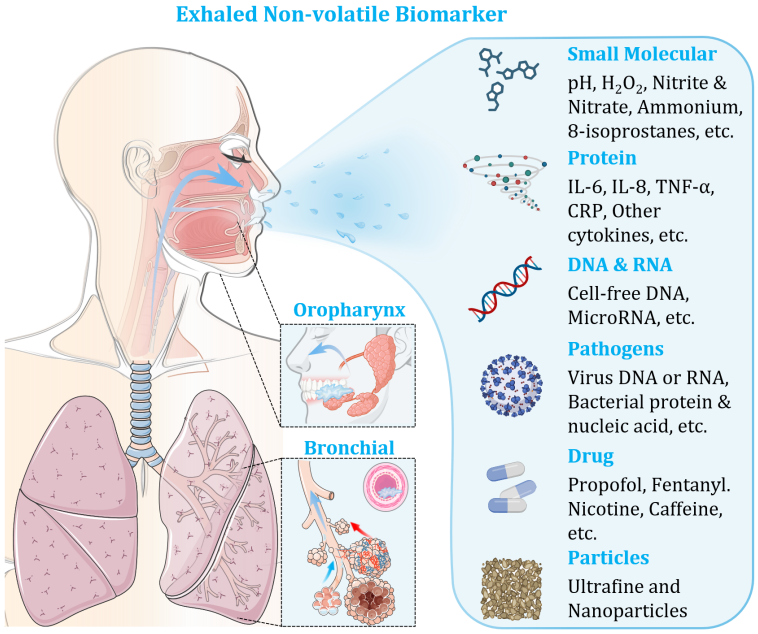

Figure 1-7. Non-volatile composition in human exhaled breath.

1.4.1 Sampling methods

Sampling methods for non-volatile substances can be classified into two categories: exhaled breath aerosol (EBA) and exhaled breath condensate (EBC). As illustrated in the **Fig. 1-8A**, EBA collection primarily relies on collection film based on wearable breath platforms such as face masks. Through wearing for a specified duration, sufficient EBA samples are collected. Subsequently, a solvent is added to dissolve and extract the aerosol particles on the collection media for further biochemical analysis. This method features simple construction and low cost. However, its dependence on external solvent for sample extraction leads to stability and reproducibility issues, limiting its applicability in quantitative detection and continuous monitoring. EBC is a liquid matrix containing non-volatile substances and soluble gases. It is generated when high-

temperature, high-humidity exhaled air comes into contact with a cold interface, causing water vapor to condense into liquid while trapping aerosols and droplets. According to the **Fig. 1-8B**, two common clinical collection methods include: 1) utilizing collection tubes in

temporary low-temperature environments created by ice buckets or frozen metal cylinders, and 2) employing thermoelectric cooling devices to form condensation interfaces. The former has a cooling duration of less than 1 hour at approximately 0°C, but the condensation temperature fluctuates over time. The latter maintains a stable temperature but is constrained by high energy consumption. Both methods suffer from bulkiness, impeding long-term monitoring, and wearable applications. Moreover, they overemphasize extremely low temperatures (<0°C, while the actual dew point is only about 5°C lower than breath temperature, ~30°C), resulting in excessive EBC sample production, which contradicts the current trend in microfluidic analysis. Low temperatures also result in high EBC dilution ratios and therefore lower biomarker concentrations, complicating the detection. Recently, with the emerging of passive cooling technologies, hydrogel cooling and radiative cooling have been applied to the condensation process of EBC, achieving desirable detection volume and continuous monitoring. These passive cooling methods do not require external energy supply, and are compact in size, low in cost, and suitable for wearable devices. Additionally, in the sampling of non-volatile substances in exhaled breath, several critical factors must be considered. Primarily, the coating material of the condensing surface at the sampling interface must possess non-adhesive properties towards biomarkers [232]. To mitigate oral saliva contamination, nasal exhaled breath collection methods can be employed, or salivary amylase tests can be utilized to verify contamination levels. Furthermore, attention must be paid to the potential degradation of active substances and the dilution ratio of samples to ensure the accuracy and reliability of collected data [233].

1.4.2 Detection methods

Spectrometry

Spectrometric technologies employing MS [234], nuclear magnetic resonance (NMR) [235], and ion mobility spectrometry (IMS) [236] can be categorized into offline detection and online monitoring methodologies (see **Fig. 1-8C**). Liquid chromatography-mass spectrometry (LC-MS) systems are predominantly utilized for offline analysis of non-volatile breath metabolites and proteins. Breath analytes typically undergo preprocessing steps, including

extraction, centrifugation, and concentration, prior to spectrometric analysis [237]. In contrast, online spectrometric analysis involves direct, real-time, and efficient ionization of molecules from exhaled breath to achieve the requisite high sensitivity. Electrospray ionization (ESI) is among the common ionization techniques employed in this context [238]. These spectrometric methods facilitate high-throughput and accurate measurements, often regarded as the gold standard in breath analysis. However, it is noteworthy that these systems are generally characterized by their complexity and substantial cost.

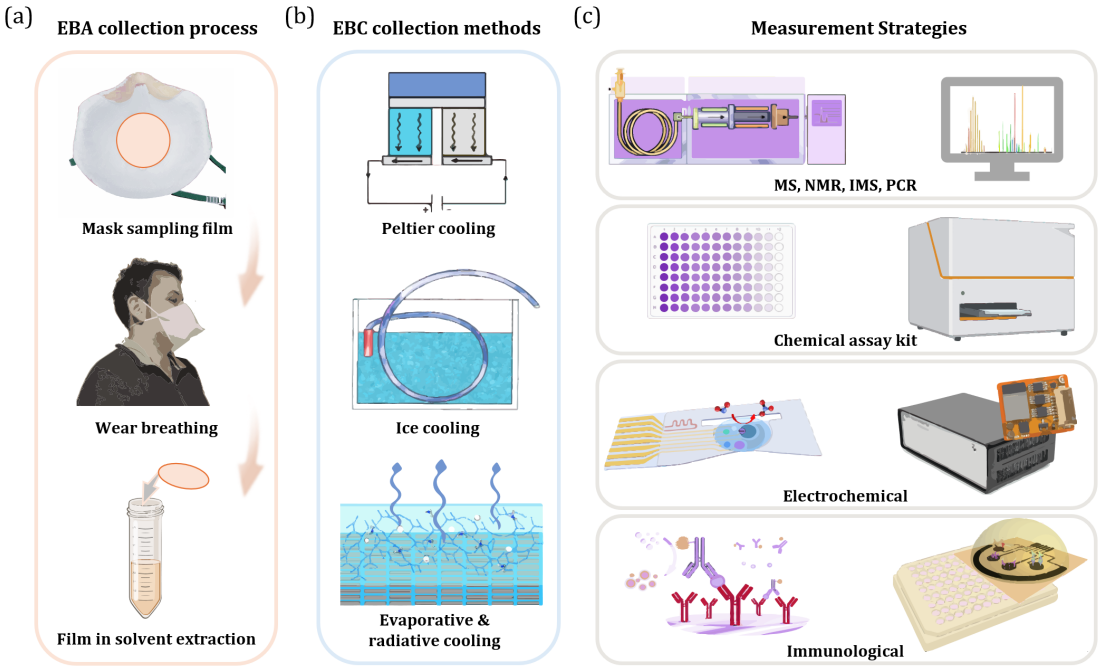

Figure 1-8 Collection and detection procedures for non-volatile substance in exhaled breath analysis. (a). EBA collection process. (b). EBC collection methods. (c). Measurements strategies for nonvolatile substance in breath analysis. EBA, Exhaled breath aerosol; EBC, Exhaled breath condensate; MS, Mass spectrometry; NMR, Nuclear magnetic resonance spectroscopy; IMS, Ion mobility spectrometry; PCR, Polymerase chain reaction.

Electrochemical

Electrochemical sensors offer significant advantages for measuring electroactive biomarkers in exhaled breath. These sensors are characterized by their low cost, operational simplicity,

and ease of integration into compact devices [239]. Furthermore, they can be effectively combined with other biotechnologies, like immunology [240], aptamer [241], etc., to create sensors based on multiple measurement principles. Consequently, several studies have explored EBC bioanalysis using electrochemical sensors, including the analysis of ions [242], reactive oxygen species [243], and proteins [244]. The ease of integration makes electrochemical sensors the most promising technological solution for portable and wearable devices in detecting breath non-volatile substances.

Chemical assay kit

Chemical assay kits are common tools for analyzing small molecules in EBC. These kits typically contain pre-formulated reagents and detailed protocols, enabling researchers to perform specific analyses quickly and in a standardized manner. Due to its predominantly aqueous composition and minimal content of interfering and biofouling substances, EBC typically requires no pretreatment and can be directly analyzed using assay kits. The advantages of chemical assay kits lie in their convenience, consistency, and reproducibility. Many kits utilize techniques such as colorimetry or fluorescence detection. Chemical assay kits play a crucial role in simplifying experimental procedures, improving efficiency, and standardizing EBC analysis [245].

Immunology

Immunological methods are widely used tools for studying biomacromolecules in EBC. These techniques, based on the principle of specific antigen-antibody binding, enable efficient and sensitive detection and quantification of proteins [246], cytokines [247], and other biomarkers in EBC [248]. Common immunoassay techniques include enzyme-linked immunosorbent assay (ELISA), immunofluorescence, and electrochemical sensing. These methods offer high specificity and sensitivity, and can achieve multiplexed analysis, detecting multiple target molecules simultaneously. In recent years, with the advancement of microfluidic technologies and nanomaterials, novel immunosensors have shown promising prospects in EBC analysis [249].

Wearable systems

Wearable devices are gaining increasing attention in the field of non-volatile respiratory substance analysis. These devices aim to achieve non-invasive, portable, and real-time monitoring of respiratory biomarkers. Research in this area primarily focuses on two aspects: aerosol studies and EBC analysis. In EBA research, researchers are developing technologies to capture and analyze minute particles in exhaled breath. These particles may contain important biomarkers such as inflammation biomarkers[243] (**Fig. 1-9A**), virus [250,251] (**Fig. 1-9B**), or bacterial [252]. Mask-based platforms are of particular interest as they can be seamlessly integrated into daily life without additional burden on users. These "smart masks" are typically equipped with miniature sensors and sampling media, capable of in situ collecting and analyzing exhaled aerosols during wearing [253,254].

The smart mask-based EBC analysis system, depicted in **Fig. 1-9C** [255], integrates mini-condensers, microfluidic devices, and diverse sensing elements to detect multiple biomarkers in EBC. The primary challenge in EBC analysis revolves around the feasibility, stability, and continuous collection of EBC using wearable devices. Key factors influencing this process include the condensation of exhaled breath and the material characteristics that impact droplet nucleation and accumulation. Passive cooling methods, such as hydrogel evaporation and radiative cooling, are considered ideal solutions to overcome these challenges. Another critical aspect is the miniaturization of sensor-based devices, where electrochemical sensors excel due to their exceptional compactness. By focusing on these areas, the field of wearable EBC devices can advance significantly [256,257]. All aforementioned technologies are characterized by low power consumption, which significantly mitigates the challenge of power supply in wearable devices.

Given the convenience and cost-effectiveness of these wearable devices, extensive clinical validation is a crucial step in the transition of novel breath analysis devices from laboratory to practical applications. This validation process aims to assess the accuracy, reliability, and practicality of these devices in diagnosing and monitoring various health conditions. With ongoing advancements in materials science, electronics, and biosensing technologies,

wearable breath analysis devices show great promise in the analysis of non-volatile substances for early disease diagnosis, chronic disease management, and personalized medicine.

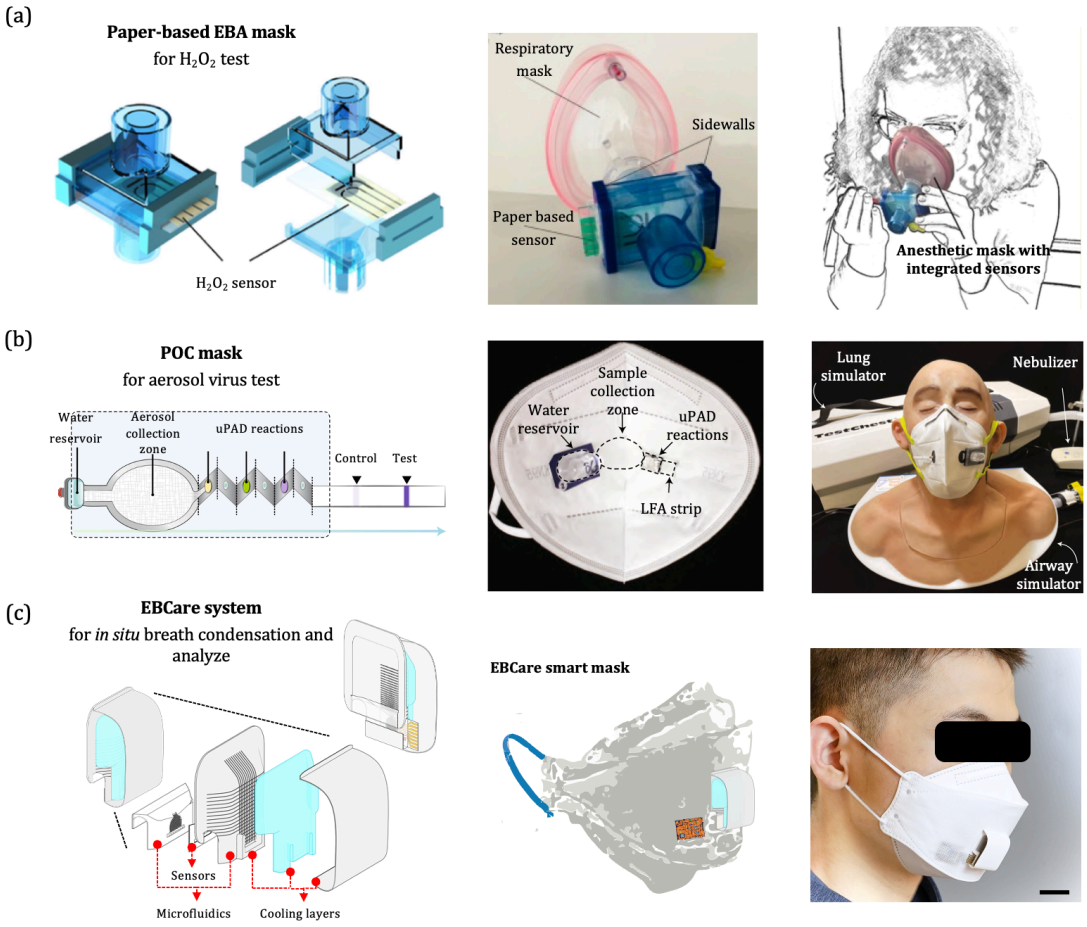

Figure 1-9 Wearable smart mask system development for in situ breath aerosol and condensate analysis. (a). A paper-based electrochemical sensor in a mask for H_2O_2 detection in exhaled breath aerosol. (b). A POC mask with microfluidics for COVID-19 test base crisper technology.(c). A smart mask system integrated with in situ condensation, microfluidics, and sensing function for real-time exhaled breath condensation analysis. EBA, exhaled breath aerosol; EBC, exhaled breath condensate; POC, point of care.

1.4.3 Biomarkers

A. Small molecules

pH

pH serves as a robust and reproducible biomarker in EBC, reflecting airway acidity [258]. In healthy individuals, the airways maintain a slightly alkaline environment [259]. However, in patients with obstructive airway diseases such as asthma [260], COPD [261], and cystic fibrosis [262], the airways often become acidified. This acidification process enhances the production of acidic droplets in the airway lining fluid (ALF), which are then more readily captured in the EBC, contributing to its acidic nature [258]. However, the measurement of EBC pH, while informative, presents technical challenges. It necessitates the exclusion of volatile carbon dioxide (imparting EBC carbonic acid properties), typically achieved by bubbling an inert gas (e.g., argon) through the sample or by controlling carbon dioxide partial pressure [263]. This requirement complicates in situ pH monitoring of EBC.

Hydrogen peroxide

Elevated levels of H_2O_2 in EBC have been frequently observed in patients with airway inflammation [264,265]. This increase is attributed to the activation of various cells in the respiratory system during inflammatory processes, including airway epithelial cells, endothelial cells, neutrophils, alveolar macrophages, and eosinophils. These activated cells produce superoxide radicals, which subsequently generate H_2O_2. However, the origin of H_2O_2 in EBC remains a subject of debate. Some researchers propose that water vapor might spontaneously generate hydrogen peroxide at the condensation interface, raising questions about the source of H_2O_2 in EBC samples [266,267]. Regardless of its origin, the reactive nature of H_2O_2 necessitates immediate monitoring for optimal detection and quantification [243].

Most clinical studies rely on H_2O_2 assay kits that utilize peroxidase enzymes (such as horseradish peroxidase, HRP) to catalyze the reaction between H_2O_2 and specific substrates, producing detectable fluorescent or colored products. The intensity of these products is

proportional to the H_2O_2 in the sample [268]. The advent of electrochemical sensors has enabled real-time analysis of H_2O_2 in EBC, based on the redox current of H_2O_2 at Prussian blue or platinum electrodes in microfluidics [269,270]. However, both H_2O_2 assay kits and electrochemical sensors exhibit relatively low sensitivity, with H_2O_2 levels in EBC often approaching their lower limits of detection.

Nitrite/nitrate

NO_2^- and NO_3^- play dual roles as both products and precursors in the NO metabolic cycle [271]. In healthy individuals, their levels in EBC are typically low. However, these levels can increase significantly in conditions such as respiratory infections, asthma, and COPD [272,273]. This elevation generally indicates inflammatory responses in the respiratory tract, reflecting increased NO production. Additionally, levels of NO derivatives such as S-nitrosothiols and nitrotyrosine may also be elevated in these conditions [274].

NO_2^- and NO_3^- assay kits utilize NO_3^- reductase enzymes to convert NO_3^- to NO_2^- (alternatively only NO_2^- detection without the enzyme), followed by the Griess reaction to detect total NO_2^-. This reaction produces a colored azo dye, with intensity proportional to the concentration of NO_2^- and NO_3^- in the sample [275,276]. The advent of ion-selective or carbon-based redox electrodes has enabled real-time analysis of NO_2^- and NO_3^- in EBC, based on the potentiometric and amperometric response of these ions at specific membrane electrodes or electrode potential (~0.7V) [242,277].

Ammonium

NH_4^+ is the dominant ion in the EBC, primarily originating from the dissolution of NH_3 [278]. This relationship is governed by Henry's law for soluble gas-solution ion equilibrium, offering a potentially effective method for indirectly monitoring NH_3 gas levels in breath. The quantification of NH_4^+ in EBC presents several advantages over conventional NH_3 gas monitoring, particularly in addressing challenges such as real-time measurements and

humidity interference. This approach may prove more suitable for long-term wearable measurements in breath monitoring.

NH_4^+ assay kits typically utilize the Berthelot reaction, where NH_4^+ reacts with phenol and hypochlorite to form indophenol blue, with light intensity proportional to NH_4^+ concentration. The development of ion-selective electrodes has enabled real-time analysis of NH_4^+ in EBC, based on the potentiometric response of these ions at specific ion-selective membranes (Nonactin-based) on electrodes [279].

Arachidonic acid derivatives (8-isoprostane and Leukotrienes)

Arachidonic acid (AA), a polyunsaturated omega-6 fatty acid predominantly found in cell membrane phospholipids, serves as a precursor for various biologically active substances. Through diverse enzymatic pathways, AA is metabolized to produce compounds such as 8-isoprostane [280], prostaglandins [281], and leukotrienes (LTs) [282]. These metabolites exhibit potent inflammatory bioeffects on airway epithelial cells and other airway cells. The ALF serves as a crucial medium for these effects, containing substantial amounts of AA and its derivatives [283,284]. EBC, being a non-invasive sample of ALF components, allows for the detection of 8-isoprostane, LTs, and prostaglandins. These compounds have emerged as important biomarkers for oxidative stress and respiratory inflammation. Most pulmonary diseases demonstrate elevated concentrations of these derivatives in EBC, reflecting oxidative stress conditions [285].

Methods for detecting AA derivatives in EBC include GC/MS, LC/MS, radioimmunoassay (RIA), and enzyme immunoassay (EIA). By integrating immunosensing techniques [286] or molecularly imprinted polymer (MIP) [287] technologies, electrochemical sensors can effectively detect biomarkers such as 8-isoprostane and leukotrienes [288].

Others

Electrolytes, trace metals, adenosine, glucose, and lactate represent a significant class of small molecule biomarkers that reflect the ionic balance, metabolic state, and redox

environment of the respiratory tract. Electrolytes (such as sodium, potassium, and chloride) potentially indicate the dilution ratio of EBC to ALF [289]. Trace metals (like iron and zinc) are involved in the regulation of airway inflammation or serve as monitors for specific occupational environments [290].

Adenosine acts as a signaling molecule regulating airway reactivity [291], while glucose [292–294] and lactate [295,296] reflect the glucose content and energy metabolism status of the pulmonary fluid environment. Encouragingly, several studies have reported on the quantification of glucose and lactate in EBC using electrochemical devices. This suggests the potential for continuous, wearable monitoring of these biomarkers [297,298]. Concentration changes of these molecules may indicate various respiratory diseases, including asthma, COPD, and cystic fibrosis. These small molecules are relatively stable in EBC, easily detectable, and often respond rapidly to physiological and pathological changes. Their comprehensive analysis can provide multidimensional information about the respiratory tract microenvironment, aiding in early disease diagnosis, condition monitoring, and treatment response evaluation, thus offering crucial insights for personalized precision medicine in respiratory system diseases.

B. Proteins

EBC proteins, primarily cytokines, play a central role in the immune and inflammatory response of the host defense system. Based on their ability to either promote or inhibit inflammatory responses, these cytokines can be divided into three categories: pro-inflammatory cytokines (e.g., IL-1β, IL-2, IL-6, IL-8, IL-12, IL-17, IFN-γ, and TNF-α), anti-inflammatory cytokines (e.g., IL-4, IL-5, IL-10, IL-13, and TGF-β), and chemokines (e.g., IL-8, MCP-1 and MIP-1ß). Systematic cytokine analysis is important for the diagnosis and treatment of airway diseases [299]. Furthermore, the C-reactive protein (CRP) content in EBC is considered to provide another useful diagnostic tool for detecting and monitoring low-grade inflammation in asthma patients [300].

Proteins in EBC can be detected by using ELISA. Studies have reported that the levels of several cytokines in EBC ranging from approximately 1-50 pg/mL [247,301]. However, the accuracy of these values remains challenging due to cytokine levels in EBC are typically near the lower limit of the assay methodology. Combining immunological and electrochemical methods shows significant potential. This approach allows sensing elements to induce electrical signals upon capturing large target molecules like proteins [244,302]. In addition, surface acoustic wave (SAW) sensors can be incorporated into immunosensing technologies to enable miniaturized detection of carcinoembryonic antigen (CEA) in EBCs [249].

C. DNA/RNA

Nucleic acid detection in EBC is promising in lung cancer research [303], with investigators focusing on various genetic and epigenetic markers such as mutation hotspot [304], microsatellite alterations [305], mitochondrial genes [306], cell-free DNA [307], and microRNA [308]. These genetic and epigenetic markers are utilized not only in lung cancer research but also in studies of other respiratory diseases such as COPD [309].

D. Pathogens

Respiratory infections, caused by pathogens such as viruses and bacteria, are a major global health concern. Traditional diagnostic methods like sputum culture or swabs may be limited by sample collection difficulties and sensitivity. EBC allows for non-invasive sampling, suitable for children and patients unable to provide sputum. Pathogen detection can be categorized into endogenous and exogenous biomarkers. Endogenous markers result from abnormal metabolic patterns due to infection, manifesting as changes in VOCs [310] or biomolecules [311]. Exogenous markers primarily involve detecting pathogen-specific substances [302,311]. Analysis of EBC components using MS, immunoassays, and other techniques can identify specific pathogens. Viral pathogens such as *SARS-CoV-2* [312,313], *Torque teno* virus [314], *H1N1* [315], and *influenza* virus [250,316] are primarily identified by detecting viral nucleic acid. For bacterial pathogens, like *Methicillin-resistant*

Staphylococcus aureus (MRSA), *Mycobacterium tuberculosis*, and *Pseudomonas aeruginosa* [317], detection methods may simultaneously target their specific proteins [302], lipids [318], and nucleic acid [317] to enhance diagnostic accuracy and reliability. This method offers the advantages of being non-invasive, simple, and high throughput, aiding in early diagnosis and control of respiratory infections.

Respiratory infectious diseases primarily spread through droplets or aerosols, making face masks the most effective personal protective equipment in daily life [319,320]. The wearable, low-cost nature of masks and their direct contact with respiration make them an ideal platform for collecting and detecting respiratory pathogens [321]. Mask-based devices have shown promising applications in large-scale pathogen screening and collection in less developed regions [252,318]. Additionally, some real-time point-of-care (POC) systems using microfluidics have enabled on-site virus screening during the COVID-19 pandemic based on immunoelectrochemical sensors or CRISPR sensing technology [251,253]. These advancements demonstrate the significant potential of masks as tools for personal respiratory pathogen assessment.

E. Drugs

Personalized treatment is increasingly vital, with multiple factors affecting drug dosage. Therapeutic drug monitoring is crucial for narrow therapeutic range medications. Real-time breath sampling provides immediate pharmacokinetic information, particularly beneficial for emergency, anesthesia, and intensive care patients, enabling precise medication adjustments [238]. Various drugs such as propofol [322], fentanyl [323], methadone [324], nicotine [325], and caffeine [326] can be detected in breath, with some showing excellent correlation to blood concentrations. This indicates the value of investigating non-invasive monitoring of exhaled drugs through breath.

Due to low drug concentrations in EBC and complex molecular structures, detection techniques require high sensitivity and resolution. For rapid and accurate drug concentration measurement, fast, sensitive, and user-friendly instruments are needed. MS, as one of the

most sensitive and versatile analytical tools, may play a crucial role in measuring levels of drugs and metabolites for future personalized patient treatment [238]. Drugs that can be recognized by immune elements may also be measured electrochemically, making at-home monitoring easier [327].

F. Exogenous particles

Ultrafine particles and nanoparticles depositing in the deep lungs pose high health risks, potentially causing respiratory and cardiovascular diseases. While the causal link between mineral particle inhalation and pneumoconiosis is established, the role of nanoparticles in interstitial lung diseases remains unclear. Bronchoalveolar lavage fluid and EBC are important diagnostic tools for studying lung pathology. Recent studies show that EBC can assess occupational exposure and lung function impairment, but whether its particle load accurately reflects deep lung conditions requires further investigation [328–330].

Bibliography of Chapter 1

1. Smith, J. C., Ellenberger, H. H., Ballanyi, K., Richter, D. W. & Feldman, J. L. Pre-Bötzinger Complex: a Brainstem Region that May Generate Respiratory Rhythm in Mammals. *Science* **254**, 726–729 (1991).
2. Del Negro, C. A., Funk, G. D. & Feldman, J. L. Breathing matters. *Nat Rev Neurosci* **19**, 351–367 (2018).
3. Moore, J. D. *et al.* Hierarchy of orofacial rhythms revealed through whisking and breathing. *Nature* **497**, 205–210 (2013).
4. Engelen, T., Solcà, M. & Tallon-Baudry, C. Interoceptive rhythms in the brain. *Nat Neurosci* **26**, 1670–1684 (2023).
5. Zaccaro, A. *et al.* How Breath-Control Can Change Your Life: A Systematic Review on Psycho-Physiological Correlates of Slow Breathing. *Front Hum Neurosci* **12**, 353 (2018).
6. Zelano, C. *et al.* Nasal Respiration Entrains Human Limbic Oscillations and Modulates Cognitive Function. *J. Neurosci.* **36**, 12448–12467 (2016).
7. Schumacher, A. E. *et al.* Global age-sex-specific mortality, life expectancy, and population estimates in 204 countries and territories and 811 subnational locations, 1950–2021, and the impact of the COVID-19 pandemic: a comprehensive demographic analysis for the Global Burden of Disease Study 2021. *The Lancet* **403**, 1989–2056 (2024).
8. Abdelrahman, Z., Li, M. & Wang, X. Comparative Review of SARS-CoV-2, SARS-CoV, MERS-CoV, and Influenza A Respiratory Viruses. *Front. Immunol.* **11**, (2020).

9. Chronic obstructive pulmonary disease (COPD). https://www.who.int/news-room/fact-sheets/detail/chronic-obstructive-pulmonary-disease-(copd).

10. Asthma. https://www.who.int/news-room/fact-sheets/detail/asthma.

11. Thai, A. A., Solomon, B. J., Sequist, L. V., Gainor, J. F. & Heist, R. S. Lung cancer. *The Lancet* **398**, 535–554 (2021).

12. Yaggi, H. K. *et al.* Obstructive Sleep Apnea as a Risk Factor for Stroke and Death. *New England Journal of Medicine* **353**, 2034–2041 (2005).

13. Shirasu, M. & Touhara, K. The scent of disease: volatile organic compounds of the human body related to disease and disorder. *The Journal of Biochemistry* **150**, 257–266 (2011).

14. Scott, J. B. & Kaur, R. Monitoring Breathing Frequency, Pattern, and Effort. *Respiratory Care* **65**, 793–806 (2020).

15. Ates, H. C. & Dincer, C. Wearable breath analysis. *Nat Rev Bioeng* **1**, 80–82 (2023).

16. Elliott, M. & Coventry, A. Critical care: the eight vital signs of patient monitoring. *Br J Nurs* **21**, 621–625 (2012).

17. Smith, G. B., Prytherch, D. R., Meredith, P., Schmidt, P. E. & Featherstone, P. I. The ability of the National Early Warning Score (NEWS) to discriminate patients at risk of early cardiac arrest, unanticipated intensive care unit admission, and death. *Resuscitation* **84**, 465–470 (2013).

18. Russo, M. A., Santarelli, D. M. & O'Rourke, D. The physiological effects of slow breathing in the healthy human. *Breathe* **13**, 298–309 (2017).

19. Schäfer, C., Rosenblum, M. G., Abel, H.-H. & Kurths, J. Synchronization in the human cardiorespiratory system. *Phys. Rev. E* **60**, 857–870 (1999).

20. Dick, T. E. *et al.* Chapter 10 - Cardiorespiratory Coupling: Common Rhythms in Cardiac, Sympathetic, and Respiratory Activities. in *Progress in Brain Research* (eds. Holstege, G., Beers, C. M. & Subramanian, H. H.) vol. 209 191–205 (Elsevier, 2014).

21. Hirsch, J. A. & Bishop, B. Respiratory sinus arrhythmia in humans: how breathing pattern modulates heart rate. *American Journal of Physiology-Heart and Circulatory Physiology* **241**, H620–H629 (1981).

22. Bernardi, L. *et al.* Effects of controlled breathing, mental activity and mental stress with or without verbalization on heart rate variability. *Journal of the American College of Cardiology* **35**, 1462–1469 (2000).

23. Giannakakis, G. *et al.* Review on Psychological Stress Detection Using Biosignals. *IEEE Transactions on Affective Computing* **13**, 440–460 (2022).

24. Gerritsen, R. J. S. & Band, G. P. H. Breath of life: The respiratory vagal stimulation model of contemplative activity. *Frontiers in Human Neuroscience* **12**, (2018).

25. Singh, V., Wisniewski, A., Britton, J. & Tattersfield, A. Effect of yoga breathing exercises (pranayama) on airway reactivity in subjects with asthma. *The Lancet* **335**, 1381–1383 (1990).

26. Quanjer, P. H. *et al.* Lung volumes and forced ventilatory flows. *European Respiratory Journal* **6**, 5–40 (1993).

27. Jat, K. R. Spirometry in children. *Prim Care Respir J* **22**, 221–229 (2013).

28. Cordain, L., Tucker, A., Moon, D. & Stager, J. M. Lung Volumes and Maximal Respiratory Pressures in Collegiate Swimmers and Runners. *Research Quarterly for Exercise and Sport* **61**, 70–74 (1990).

29. Doherty, M. & Dimitriou, L. Comparison of lung volume in Greek swimmers, land based athletes, and sedentary controls using allometric scaling. *Br J Sports Med* **31**, 337–341 (1997).

30. null, null. Ventilation with Lower Tidal Volumes as Compared with Traditional Tidal Volumes for Acute Lung Injury and the Acute Respiratory Distress Syndrome. *New England Journal of Medicine* **342**, 1301–1308 (2000).

31. Janson, C. *et al.* Bronchodilator reversibility in asthma and COPD: findings from three large population studies. *European Respiratory Journal* **54**, (2019).

32. Calverley, P. M., Albert, P. & Walker, P. P. Bronchodilator reversibility in chronic obstructive pulmonary disease: use and limitations. *The Lancet Respiratory Medicine* **1**, 564–573 (2013).

33. Gregg, I. & Nunn, A. J. Peak Expiratory Flow in Normal Subjects. *Br Med J* **3**, 282–284 (1973).

34. Kwon, D. S. *et al.* $FEF_{25-75\%}$ Values in Patients with Normal Lung Function Can Predict the Development of Chronic Obstructive Pulmonary Disease . *COPD* **15**, 2913–2921 (2020).

35. Simon, M. R. *et al.* Forced expiratory flow between 25% and 75% of vital capacity and FEV1/forced vital capacity ratio in relation to clinical and physiological parameters in asthmatic children with normal FEV1 values. *Journal of Allergy and Clinical Immunology* **126**, 527-534.e8 (2010).

36. Adeniyi, B. O. & Erhabor, G. E. The peak flow meter and its use in clinical practice. *African Journal of Respiratory Medicine* **6**, 5–8 (2011).

37. Gupta, J. K., Lin, C.-H. & Chen, Q. Characterizing exhaled airflow from breathing and talking. *Indoor Air* **20**, 31–39 (2010).

38. Tang, J. W. *et al.* Airflow Dynamics of Human Jets: Sneezing and Breathing - Potential Sources of Infectious Aerosols. *PLOS ONE* **8**, e59970 (2013).

39. Miller, M. R. Standardisation of spirometry. *European Respiratory Journal* **26**, 319–338 (2005).

40. Albouaini, K., Egred, M. & Alahmar, A. Cardiopulmonary exercise testing and its application. *Postgrad Med J* **83**, 675–682 (2007).

41. Tobin, M. J. *et al.* Breathing Patterns. *Chest* **84**, 286–294 (1983).

42. Berg, S., Haight, J. S. J., Yap, V., Hoffstein, V. & Cole, P. Comparison of Direct and Indirect Measurements of Respiratory Airflow: Implications for Hypopneas. *Sleep* **20**, 60–64 (1997).

43. AL-Khalidi, F. q., Saatchi, R., Burke, D., Elphick, H. & Tan, S. Respiration rate monitoring methods: A review. *Pediatric Pulmonology* **46**, 523–529 (2011).

44. Lamb, K., Theodore, D. & Bhutta, B. S. Spirometry. in *StatPearls* (StatPearls Publishing, Treasure Island (FL), 2024).

45. Jiang, T. *et al.* Wearable breath monitoring via a hot-film/calorimetric airflow sensing system. *Biosensors and Bioelectronics* **163**, 112288 (2020).

46. Perks, W. H., Sopwith, T., Brown, D., Jones, C. H. & Green, M. Effects of temperature on Vitalograph spirometer readings. *Thorax* **38**, 592–594 (1983).

47. Afandi, A., Khasani, Deendarlianto, Catrawedarma, I. G. N. B. & Wijayanta, S. The development of the ultrasonic flowmeter sensors for mass flow rate measurement: A comprehensive review. *Flow Measurement and Instrumentation* **97**, 102614 (2024).

48. Walters, J. A. E., Wood-Baker, R., Walls, J. & Johns, D. P. Stability of the EasyOne ultrasonic spirometer for use in general practice. *Respirology* **11**, 306–310 (2006).

49. Criée, C. P. *et al.* Body plethysmography – Its principles and clinical use. *Respiratory Medicine* **105**, 959–971 (2011).

50. Li, W., Tan, B. & Piechocki, R. J. Non-contact breathing detection using passive radar. in *2016 IEEE International Conference on Communications (ICC)* 1–6 (2016). doi:10.1109/ICC.2016.7511389.

51. Shao, D. *et al.* Noncontact Monitoring Breathing Pattern, Exhalation Flow Rate and Pulse Transit Time. *IEEE Transactions on Biomedical Engineering* **61**, 2760–2767 (2014).

52. Min, S. D. *et al.* Noncontact Respiration Rate Measurement System Using an Ultrasonic Proximity Sensor. *IEEE Sensors Journal* **10**, 1732–1739 (2010).

53. Ali, M., Elsayed, A., Mendez, A., Savaria, Y. & Sawan, M. Contact and Remote Breathing Rate Monitoring Techniques: A Review. *IEEE Sensors Journal* **21**, 14569–14586 (2021).

54. Shen, S. *et al.* Advances in wearable respiration sensors. *Materials Today* **72**, 140–162 (2024).

55. Chen, Y., Liu, F., Lu, B., Zhang, Y. & Feng, X. Skin-Like Hybrid Integrated Circuits Conformal to Face for Continuous Respiratory Monitoring. *Advanced Electronic Materials* **6**, 2000145 (2020).

56. Liao, F. *et al.* Ultrafast response flexible breath sensor based on vanadium dioxide. *J. Breath Res.* **11**, 036002 (2017).

57. Kim, J.-H. *et al.* A conformable sensory face mask for decoding biological and environmental signals. *Nat Electron* **5**, 794–807 (2022).

58. Adeel, M., Cotur, Y., Naik, A., Gonzalez-Macia, L. & Güder, F. Face masks as a platform for wearable sensors. *Nat Electron* **5**, 719–720 (2022).

59. Fang, Y. *et al.* A Deep-Learning-Assisted On-Mask Sensor Network for Adaptive Respiratory Monitoring. *Advanced Materials* **34**, 2200252 (2022).

60. Zhong, J. *et al.* Smart Face Mask Based on an Ultrathin Pressure Sensor for Wireless Monitoring of Breath Conditions. *Advanced Materials* **34**, 2107758 (2022).

61. Cui, S. *et al.* Laser direct writing of Ga_2O_3/liquid metal-based flexible humidity sensors. *OEA* **6**, 220172–220172 (2023).

62. Ye, L. *et al.* Face mask integrated with flexible and wearable manganite oxide respiration sensor. *Nano Energy* **112**, 108460 (2023).

63. Tipparaju, V. V. *et al.* Reliable Breathing Tracking With Wearable Mask Device. *IEEE Sensors Journal* **20**, 5510–5518 (2020).

64. Perez-Suarez, I. *et al.* Accuracy and Precision of the COSMED K5 Portable Analyser. *Front Physiol* **9**, 1764 (2018).

65. Frerichs, I. *et al.* Chest electrical impedance tomography examination, data analysis, terminology, clinical use and recommendations: consensus statement of the TRanslational EIT developmeNt stuDy group. *Thorax* **72**, 83–93 (2017).

66. Chu, M. *et al.* Respiration rate and volume measurements using wearable strain sensors. *npj Digital Med* **2**, 1–9 (2019).

67. Merritt, C. R., Nagle, H. T. & Grant, E. Textile-Based Capacitive Sensors for Respiration Monitoring. *IEEE Sensors Journal* **9**, 71–78 (2009).

68. Cotur, Y. *et al.* Bioinspired Stretchable Transducer for Wearable Continuous Monitoring of Respiratory Patterns in Humans and Animals. *Advanced Materials* **34**, 2203310 (2022).

69. Hernandez, J., McDuff, D. & Picard, R. W. Biowatch: Estimation of heart and breathing rates from wrist motions. in *2015 9th International Conference on Pervasive Computing Technologies for Healthcare (PervasiveHealth)* 169–176 (2015). doi:10.4108/icst.pervasivehealth.2015.259064.

70. Iqbal, T., Elahi, A., Ganly, S., Wijns, W. & Shahzad, A. Photoplethysmography-Based Respiratory Rate Estimation Algorithm for Health Monitoring Applications. *J. Med. Biol. Eng.* **42**, 242–252 (2022).

71. Renevey, Ph. *et al.* Validation of a wrist monitor for accurate estimation of RR intervals during sleep. in *2013 35th Annual International Conference of the IEEE Engineering in Medicine and Biology Society (EMBC)* 5493–5496 (2013). doi:10.1109/EMBC.2013.6610793.

72. Röddiger, T., Wolffram, D., Laubenstein, D., Budde, M. & Beigl, M. Towards Respiration Rate Monitoring Using an In-Ear Headphone Inertial Measurement Unit. in *Proceedings of the 1st International Workshop on Earable Computing* 48–53 (ACM, London United Kingdom, 2019). doi:10.1145/3345615.3361130.

73. Goverdovsky, V. *et al.* Hearables: Multimodal physiological in-ear sensing. *Sci Rep* **7**, 6948 (2017).

74. Charlton, P. H. *et al.* Breathing Rate Estimation From the Electrocardiogram and Photoplethysmogram: A Review. *IEEE Reviews in Biomedical Engineering* **11**, 2–20 (2018).

75. Fouzas, S., Anthracopoulos, M. B. & Bohadana, A. Clinical Usefulness of Breath Sounds. in *Breath Sounds: From Basic Science to Clinical Practice* (eds. Priftis, K. N., Hadjileontiadis, L. J. & Everard, M. L.) 33–52 (Springer International Publishing, Cham, 2018). doi:10.1007/978-3-319-71824-8_3.

76. Kim, Y. *et al.* Respiratory sound classification for crackles, wheezes, and rhonchi in the clinical field using deep learning. *Sci Rep* **11**, 17186 (2021).

77. Sarkar, M., Madabhavi, I., Niranjan, N. & Dogra, M. Auscultation of the respiratory system. *Ann Thorac Med* **10**, 158–168 (2015).

78. Korpás, J., Sadlonová, J. & Vrabec, M. Analysis of the cough sound: an overview. *Pulm Pharmacol* **9**, 261–268 (1996).

79. Manzella, F., Pagliarini, G., Sciavicco, G. & Stan, I. E. The voice of COVID-19: Breath and cough recording classification with temporal decision trees and random forests. *Artificial Intelligence in Medicine* **137**, 102486 (2023).

80. Bohadana, A., Izbicki, G. & Kraman, S. S. Fundamentals of Lung Auscultation. *New England Journal of Medicine* **370**, 744–751 (2014).

81. Lee, S. H. *et al.* Fully portable continuous real-time auscultation with a soft wearable stethoscope designed for automated disease diagnosis. *Science Advances* **8**, eabo5867 (2022).

82. Yoo, J.-Y. *et al.* Wireless broadband acousto-mechanical sensing system for continuous physiological monitoring. *Nat Med* **29**, 3137–3148 (2023).

83. Popov, T. A., Kralimarkova, T. Z. & Dimitrov, V. D. Measurement of exhaled breath temperature in science and clinical practice. *Breathe* **8**, 186–192 (2012).

84. Paredi, P., Kharitonov, S. A. & Barnes, P. J. Correlation of exhaled breath temperature with bronchial blood flow in asthma. *Respir Res* **6**, 15 (2005).

85. Piacentini, G. L. *et al.* Relationship between exhaled air temperature and exhaled nitric oxide in childhood asthma. *European Respiratory Journal* **20**, 108–111 (2002).

86. Paredi, P. *et al.* Slower rise of exhaled breath temperature in chronic obstructive pulmonary disease. *Eur Respir J* **21**, 439–443 (2003).

87. Lázár, Z. *et al.* Exhaled breath temperature in patients with stable and exacerbated COPD. *J Breath Res* **8**, 046002 (2014).

88. Popov, T. A. *et al.* Development of an Individual Device for Exhaled Breath Temperature Measurement. *IEEE Sensors Journal* **10**, 110–113 (2010).

89. Mansour, E. *et al.* Measurement of temperature and relative humidity in exhaled breath. *Sensors and Actuators B: Chemical* **304**, 127371 (2020).

90. Mogera, U., Sagade, A. A., George, S. J. & Kulkarni, G. U. Ultrafast response humidity sensor using supramolecular nanofibre and its application in monitoring breath humidity and flow. *Sci Rep* **4**, 4103 (2014).

91. Noble, D. D., McCafferty, J. B., Greening, A. P. & Innes, J. A. Respiratory heat and moisture loss is associated with eosinophilic inflammation in asthma. *European Respiratory Journal* **29**, 676–681 (2007).

92. Cherrie, J. W., Wang, S., Mueller, W., Wendelboe-Nelson, C. & Loh, M. In-mask temperature and humidity can validate respirator wear-time and indicate lung health status. *J Expo Sci Environ Epidemiol* **29**, 578–583 (2019).

93. Shin, J. *et al.* Sensitive Wearable Temperature Sensor with Seamless Monolithic Integration. *Advanced Materials* **32**, 1905527 (2020).

94. Chen, J. *et al.* Breathable Strain/Temperature Sensor Based on Fibrous Networks of Ionogels Capable of Monitoring Human Motion, Respiration, and Proximity. *ACS Appl Mater Interfaces* **13**, 51567–51577 (2021).

95. Kano, S. *et al.* Respiratory Monitoring by Ultrafast Humidity Sensors with Nanomaterials: A Review. *Sensors* **22**, 1251 (2022).

96. Yao, S., Swetha, P. & Zhu, Y. Nanomaterial-Enabled Wearable Sensors for Healthcare. *Advanced Healthcare Materials* **7**, 1700889 (2018).

97. Lawal, O., Ahmed, W. M., Nijsen, T. M. E., Goodacre, R. & Fowler, S. J. Exhaled breath analysis: a review of 'breath-taking' methods for off-line analysis. *Metabolomics* **13**, 110 (2017).

98. Tai, H., Wang, S., Duan, Z. & Jiang, Y. Evolution of breath analysis based on humidity and gas sensors: Potential and challenges. *Sensors and Actuators B: Chemical* **318**, 128104 (2020).

99. Miekisch, W. *et al.* Construction and Evaluation of a Versatile \hbox CO_2 Controlled Breath Collection Device. *IEEE Sensors Journal* **10**, 211–215 (2010).

100. Miekisch, W. *et al.* Impact of sampling procedures on the results of breath analysis. *J Breath Res* **2**, 026007 (2008).

101. Xu, M., Tang, Z., Duan, Y. & Liu, Y. GC-Based Techniques for Breath Analysis: Current Status, Challenges, and Prospects. *Crit Rev Anal Chem* **46**, 291–304 (2016).

102. Kim, K.-H., Jahan, S. A. & Kabir, E. A review of breath analysis for diagnosis of human health. *TrAC Trends in Analytical Chemistry* **33**, 1–8 (2012).

103. Van den Velde, S., Nevens, F., Van hee, P., van Steenberghe, D. & Quirynen, M. GC–MS analysis of breath odor compounds in liver patients. *Journal of Chromatography B* **875**, 344–348 (2008).

104. Zhang, X. *et al.* Direct mass spectrometry analysis of exhaled human breath in real-time. *Mass Spectrom Rev* (2023) doi:10.1002/mas.21855.

105. Smith, D. & Španěl, P. Direct, rapid quantitative analyses of BVOCs using SIFT-MS and PTR-MS obviating sample collection. *TrAC Trends in Analytical Chemistry* **30**, 945–959 (2011).

106. Elliott, S. E., Segger, F. J. & Osborn, J. J. A modified oxygen gauge for the rapid measurement of Po2 in respiratory gases. *Journal of Applied Physiology* **21**, 1672–1674 (1966).

107. Tierney, M. J. & Kim, H. O. L. Electrochemical gas sensor with extremely fast response times. *Anal. Chem.* **65**, 3435–3440 (1993).

108. Gao, W. *et al.* Fully integrated wearable sensor arrays for multiplexed in situ perspiration analysis. *Nature* **529**, 509–514 (2016).

109. Wei, D. & Ivaska, A. Applications of ionic liquids in electrochemical sensors. *Analytica Chimica Acta* **607**, 126–135 (2008).

110. Nikolic, M. V., Milovanovic, V., Vasiljevic, Z. Z. & Stamenkovic, Z. Semiconductor Gas Sensors: Materials, Technology, Design, and Application. *Sensors* **20**, 6694 (2020).

111. Röck, F., Barsan, N. & Weimar, U. Electronic Nose: Current Status and Future Trends. *Chem. Rev.* **108**, 705–725 (2008).

112. Kwak, C.-H. *et al.* Humidity-Independent Oxide Semiconductor Chemiresistors Using Terbium-Doped SnO2 Yolk–Shell Spheres for Real-Time Breath Analysis. *ACS Appl. Mater. Interfaces* **10**, 18886–18894 (2018).

113. Cho, H.-J., Kim, S.-J., Choi, S.-J., Jang, J.-S. & Kim, I.-D. Facile synthetic method of catalyst-loaded ZnO nanofibers composite sensor arrays using bio-inspired protein cages for pattern recognition of exhaled breath. *Sensors and Actuators B: Chemical* **243**, 166–175 (2017).

114. Wang, C. & Sahay, P. Breath Analysis Using Laser Spectroscopic Techniques: Breath Biomarkers, Spectral Fingerprints, and Detection Limits. *Sensors* **9**, 8230–8262 (2009).

115. Liang, Q. *et al.* Ultrasensitive multispecies spectroscopic breath analysis for real-time health monitoring and diagnostics. *Proceedings of the National Academy of Sciences* **118**, e2105063118 (2021).

116. Blaikie, T. P. J. *et al.* Portable Device for Measuring Breath Acetone Based on Sample Preconcentration and Cavity Enhanced Spectroscopy. *Anal. Chem.* **88**, 11016–11021 (2016).

117. Wang, F. *et al.* Techniques to enhance the photoacoustic signal for trace gas sensing: A review. *Sensors and Actuators A: Physical* **345**, 113807 (2022).

118. Zhao, X. *et al.* Dense Multibutterfly Spots-Enhanced Miniaturized Optical Fiber Photoacoustic Gas Sensor. *Anal. Chem.* **96**, 5554–5559 (2024).

119. Dervieux, E., Théron, M. & Uhring, W. Carbon Dioxide Sensing—Biomedical Applications to Human Subjects. *Sensors* **22**, 188 (2022).

120. Zhang, L., Hu, J., Lv, Y. & Hou, X. Recent Progress in Chemiluminescence for Gas Analysis. *Applied Spectroscopy Reviews* **45**, 474–489 (2010).

121. Zhang, Z., Cang, H., Xie, Y., Li, H. & Li, H. A miniaturized photodiode-based chemiluminescence sensor for measurement of fractional exhaled nitric oxide. *Sensors and Actuators B: Chemical* **394**, 134402 (2023).

122. Hunter, R. A., Storm, W. L., Coneski, P. N. & Schoenfisch, M. H. Inaccuracies of Nitric Oxide Measurement Methods in Biological Media. *Anal. Chem.* **85**, 1957–1963 (2013).

123. Mazzone, P. J. *et al.* Diagnosis of lung cancer by the analysis of exhaled breath with a colorimetric sensor array. *Thorax* **62**, 565–568 (2007).

124. Wang, D. *et al.* Colorimetric Sensor for Online Accurate Detection of Breath Acetone. *ACS Sens.* **6**, 450–453 (2021).

125. Kim, D.-H. *et al.* Colorimetric Dye-Loaded Nanofiber Yarn: Eye-Readable and Weavable Gas Sensing Platform. *ACS Nano* **14**, 16907–16918 (2020).

126. Tardy, P., Coulon, J.-R., Lucat, C. & Menil, F. Dynamic thermal conductivity sensor for gas detection. *Sensors and Actuators B: Chemical* **98**, 63–68 (2004).

127. Mehaney, A., Alrowaili, Z. A., Elsayed, H. A., Taha, T. A. & Ahmed, A. M. Theoretical investigations of Tamm plasmon resonance for monitoring of isoprene traces in the exhaled breath: Towards chronic liver fibrosis disease biomarkers. *Physics Letters A* **413**, 127610 (2021).

128. Usman, F., Dennis, J. O. & Meriaudeau, F. Development of a surface plasmon resonance acetone sensor for noninvasive screening and monitoring of diabetes. *IOP Conf. Ser.: Mater. Sci. Eng.* **383**, 012024 (2018).

129. Rossiter, H. B. Exercise: Kinetic Considerations for Gas Exchange. in *Comprehensive Physiology* 203–244 (John Wiley & Sons, Ltd, 2010). doi:10.1002/cphy.c090010.

130. Boone, T. *Introduction to Exercise Physiology*. (Jones & Bartlett Publishers, 2014).

131. Poole, D. C. & Jones, A. M. Oxygen uptake kinetics. *Compr Physiol* **2**, 933–996 (2012).

132. Burnley, M. & Jones, A. M. Oxygen uptake kinetics as a determinant of sports performance. *European Journal of Sport Science* **7**, 63–79 (2007).

133. Bassett, D. R. & Howley, E. T. Limiting factors for maximum oxygen uptake and determinants of endurance performance. *Med Sci Sports Exerc* **32**, 70–84 (2000).

134. Chae, G. *et al.* Stronger correlation of peak oxygen uptake with distance of incremental shuttle walk test than 6-min walk test in patients with COPD: a systematic review and meta-analysis. *BMC Pulmonary Medicine* **22**, 102 (2022).

135. Geers, C. & Gros, G. Carbon dioxide transport and carbonic anhydrase in blood and muscle. *Physiol Rev* **80**, 681–715 (2000).

136. *Clinical Methods: The History, Physical, and Laboratory Examinations*. (Butterworths, Boston, 1990).

137. Siobal, M. S. Monitoring Exhaled Carbon Dioxide. *Respiratory Care* **61**, 1397–1416 (2016).

138. Jubran, A., Grant, B. J. B. & Tobin, M. J. Effect of Hyperoxic Hypercapnia on Variational Activity of Breathing. *Am J Respir Crit Care Med* **156**, 1129–1139 (1997).

139. Corfield, D. R., Morrell, M. J. & Guz, A. The nature of breathing during hypocapnia in awake man. *Respir Physiol* **101**, 145–159 (1995).

140. Goldberg, J. S., Rawle, P. R., Zehnder, J. L. & Sladen, R. N. Colorimetric End-Tidal Carbon Dioxide Monitoring for Tracheal Intubation. *Anesthesia & Analgesia* **70**, 191 (1990).

141. Lam, Y. Y. & Ravussin, E. Indirect calorimetry: an indispensable tool to understand and predict obesity. *Eur J Clin Nutr* **71**, 318–322 (2017).

142. Braden, B., Lembcke, B., Kuker, W. & Caspary, W. F. 13C-breath tests: Current state of the art and future directions. *Digestive and Liver Disease* **39**, 795–805 (2007).

143. Armuzzi, A. Non-Invasive Assessment of Human Hepatic Mitochondrial Function through the 13C-Methionine Breath Test. *Scandinavian Journal of Gastroenterology* **35**, 650–653 (2000).

144. Gisbert, J. P. & Pajares, J. M. Review article: 13C-urea breath test in the diagnosis of Helicobacter pylori infection – a critical review. *Alimentary Pharmacology & Therapeutics* **20**, 1001–1017 (2004).

145. Yazbeck, R., Howarth, G. S., Kosek, M., Davidson, G. P. & Butler, R. N. Breath 13CO2—evidence for a noninvasive biomarker to measure added refined sugar uptake. *Journal of Applied Physiology* **130**, 1025–1032 (2021).

146. Severinghaus, J. W., Astrup, P. & Murray, J. F. Blood Gas Analysis and Critical Care Medicine. *Am J Respir Crit Care Med* **157**, S114–S122 (1998).

147. Sood, P., Paul, G. & Puri, S. Interpretation of arterial blood gas. *Indian J Crit Care Med* **14**, 57–64 (2010).

148. Hoffmann, U., Eßfeld, D. & Stegemann, J. Comparison of arterial, end-tidal and transcutaneous PCO2 during moderate exercise and external C02 loading in humans. *Eur J Appl Physiol* **61**, 1–4 (1990).

149. Umeda, A. *et al.* Recent Insights into the Measurement of Carbon Dioxide Concentrations for Clinical Practice in Respiratory Medicine. *Sensors* **21**, 5636 (2021).

150. Severinghaus, J. W. The Invention and Development of Blood Gas Analysis Apparatus. *Anesthesiology* **97**, 253–256 (2002).

151. Shephard, R. J. Open-circuit respirometry: a brief historical review of the use of Douglas bags and chemical analyzers. *Eur J Appl Physiol* **117**, 381–387 (2017).

152. Schoffelen, P. F. M. & Plasqui, G. Classical experiments in whole-body metabolism: open-circuit respirometry—diluted flow chamber, hood, or facemask systems. *Eur J Appl Physiol* **118**, 33–49 (2018).

153. Ochoa, M. *et al.* Integrated sensing and delivery of oxygen for next-generation smart wound dressings. *Microsyst Nanoeng* **6**, 1–16 (2020).

154. Jha, R. K. Non-Dispersive Infrared Gas Sensing Technology: A Review. *IEEE Sensors Journal* **22**, 6–15 (2022).

155. Lunn, J. N. & Mapleson, W. W. THE SEVERINGHAUS Pco2 ELECTRODE: A THEORETICAL AND EXPERIMENTAL ASSESSMENT. *British Journal of Anaesthesia* **35**, 666–678 (1963).

156. Clark, L. C. J. & Clark, E. W. A Personalized History of the Clark Oxygen Electrode. *International Anesthesiology Clinics* **25**, 1 (1987).

157. Feng, L. *et al.* An ultra-small integrated CO2 infrared gas sensor for wearable end-tidal CO2 monitoring. *iScience* **26**, 108293 (2023).

158. Angelucci, A. *et al.* A Wearable Device to Monitor the Partial Pressure of Transcutaneous Carbon Dioxide. *IEEE Transactions on Instrumentation and Measurement* **73**, 1–12 (2024).

159. Cascales, J. P. *et al.* Wireless Wearable Sensor Paired With Machine Learning for the Quantification of Tissue Oxygenation. *IEEE Internet of Things Journal* **8**, 17557–17567 (2021).

160. Lopez-Ruiz, N., Lopez-Torres, J., Rodriguez, M. A. C., De Vargas-Sansalvador, I. P. & Martinez-Olmos, A. Wearable System for Monitoring of Oxygen Concentration in Breath Based on Optical Sensor. *IEEE Sensors J.* **15**, 4039–4045 (2015).

161. Wu, Z. *et al.* A Humidity-Resistant, Sensitive, and Stretchable Hydrogel-Based Oxygen Sensor for Wireless Health and Environmental Monitoring. *Advanced Functional Materials* **34**, 2308280 (2024).

162. Smith, A. D., Cowan, J. O., Brassett, K. P., Herbison, G. P. & Taylor, D. R. Use of Exhaled Nitric Oxide Measurements to Guide Treatment in Chronic Asthma. *New England Journal of Medicine* **352**, 2163–2173 (2005).

163. Dweik, R. A. *et al.* An official ATS clinical practice guideline: interpretation of exhaled nitric oxide levels (FENO) for clinical applications. *American journal of respiratory and critical care medicine* **184**, 602–615 (2011).

164. American, T. S. & European, R. S. ATS/ERS recommendations for standardized procedures for the online and offline measurement of exhaled lower respiratory nitric oxide and nasal nitric oxide, 2005. *Am. J. Respir. Crit. Care Med.* **171**, 912–930 (2005).

165. N. Clough, P. & A. Thrush, B. Mechanism of chemiluminescent reaction between nitric oxide and ozone. *Transactions of the Faraday Society* **63**, 915–925 (1967).

166. Brown, M. D. & Schoenfisch, M. H. Electrochemical Nitric Oxide Sensors: Principles of Design and Characterization. *Chem. Rev.* **119**, 11551–11575 (2019).

167. Zajda, J., Schmidt, N. J., Zheng, Z., Wang, X. & Meyerhoff, M. E. Performance of Amperometric Platinized-Nafion Based Gas Phase Sensor for Determining Nitric Oxide (NO) Levels in Exhaled Human Nasal Breath. *Electroanalysis* **30**, 1610–1615 (2018).

168. Maniscalco, M. *et al.* Fractional exhaled nitric oxide-measuring devices: technology update. *MDER* 151 (2016) doi:10.2147/MDER.S91201.

169. Mohiuddin, S. S. & Khattar, D. Biochemistry, Ammonia. in *StatPearls* (StatPearls Publishing, Treasure Island (FL), 2024).

170. Rath, R. J. *et al.* Ammonia detection: A pathway towards potential point-of-care diagnostics. *Biosensors and Bioelectronics* **251**, 116100 (2024).

171. Carpenter, G. H. Salivary Factors that Maintain the Normal Oral Commensal Microflora. *J Dent Res* **99**, 644–649 (2020).

172. Narasimhan, L. R., Goodman, W. & Patel, C. K. N. Correlation of breath ammonia with blood urea nitrogen and creatinine during hemodialysis. *Proceedings of the National Academy of Sciences* **98**, 4617–4621 (2001).

173. Kearney, D. J., Hubbard, T. & Putnam, D. Breath Ammonia Measurement in Helicobacter pylori Infection. *Dig Dis Sci* **47**, 2523–2530 (2002).

174. Song, G. *et al.* An ultrasensitive fluorescent breath ammonia sensor for noninvasive diagnosis of chronic kidney disease and helicobacter pylori infection. *Chemical Engineering Journal* **440**, 135979 (2022).

175. Hibbard, T. & Killard, A. J. Breath Ammonia Analysis: Clinical Application and Measurement. *Critical Reviews in Analytical Chemistry* **41**, 21–35 (2011).

176. Wu, G. *et al.* A wearable mask sensor based on polyaniline/CNT nanocomposites for monitoring ammonia gas and human breathing. *Sensors and Actuators B: Chemical* **375**, 132858 (2023).

177. Wang, J. *et al.* Machine Learning-Assisted Janus Colorimetric Face Mask for Breath Ammonia Analysis. *Anal. Chem.* **96**, 381–387 (2024).

178. Wang, Z. & Wang, C. Is breath acetone a biomarker of diabetes? A historical review on breath acetone measurements. *J. Breath Res.* **7**, 037109 (2013).

179. Anderson, J. C. Measuring breath acetone for monitoring fat loss: Review. *Obesity (Silver Spring)* **23**, 2327–2334 (2015).

180. Obeidat, Y. The Most Common Methods for Breath Acetone Concentration Detection: A Review. *IEEE Sensors Journal* **21**, 14540–14558 (2021).

181. Wang, C., Mbi, A. & Shepherd, M. A Study on Breath Acetone in Diabetic Patients Using a Cavity Ringdown Breath Analyzer: Exploring Correlations of Breath Acetone With Blood Glucose and Glycohemoglobin A1C. *IEEE Sensors Journal* **10**, 54–63 (2010).

182. Španěl, P., Dryahina, K., Rejšková, A., Chippendale, T. W. E. & Smith, D. Breath acetone concentration; biological variability and the influence of diet. *Physiol. Meas.* **32**, N23–N31 (2011).

183. Alkhouri, N. *et al.* Analysis of breath volatile organic compounds as a noninvasive tool to diagnose nonalcoholic fatty liver disease in children. *European Journal of Gastroenterology & Hepatology* **26**, 82 (2014).

184. Bastide, G. M. G. B. H. *et al.* Handheld device quantifies breath acetone for real-life metabolic health monitoring. *Sens. Diagn.* **2**, 918–928 (2023).

185. Weber, I. C. *et al.* Monitoring Lipolysis by Sensing Breath Acetone down to Parts-per-Billion. *Small Science* **1**, 2100004 (2021).

186. Landini, B. E. & Bravard, S. T. Breath Acetone Concentration Measured Using a Palm-Size Enzymatic Sensor System. *IEEE Sensors Journal* **9**, 1802–1807 (2009).

187. Obeidat, Y. M., Bany Hamad, N. & Rawashdeh, A. M. A solid state electrolyte based enzymatic acetone sensor. *Sci Rep* **14**, 15461 (2024).

188. Obeidat, Y. *et al.* Acetone sensing in liquid and gas phases using cyclic voltammetry. *Sci Rep* **12**, 11010 (2022).

189. Motsegood, P. & Leddy, J. Detection of Acetone on Human Breath Using Cyclic Voltammetry. *ECS Trans.* **41**, 1–7 (2012).

190. Rana, S. V. & Malik, A. Hydrogen Breath Tests in Gastrointestinal Diseases. *Ind J Clin Biochem* **29**, 398–405 (2014).

191. Ghoshal, U. C. How to Interpret Hydrogen Breath Tests. *J Neurogastroenterol Motil* **17**, 312–317 (2011).

192. Levitt, M. D., Furne, J. K., Kuskowski, M. & Ruddy, J. Stability of Human Methanogenic Flora Over 35 Years and a Review of Insights Obtained From Breath Methane Measurements. *Clinical Gastroenterology and Hepatology* **4**, 123–129 (2006).

193. Kunkel, D. *et al.* Methane on breath testing is associated with constipation: a systematic review and meta-analysis. *Dig Dis Sci* **56**, 1612–1618 (2011).

194. Chatterjee, S., Park, S., Low, K., Kong, Y. & Pimentel, M. The degree of breath methane production in IBS correlates with the severity of constipation. *Am J Gastroenterol* **102**, 837–841 (2007).

195. Rezaie, A. *et al.* Hydrogen and Methane-Based Breath Testing in Gastrointestinal Disorders: The North American Consensus. *Am J Gastroenterol* **112**, 775–784 (2017).

196. Korotcenkov, G., Han, S. D. & Stetter, J. R. Review of Electrochemical Hydrogen Sensors. *Chem. Rev.* **109**, 1402–1433 (2009).

197. Nguyen, K. *et al.* Low-temperature prototype hydrogen sensors using Pd-decorated SnO2 nanowires for exhaled breath applications. *Sensors and Actuators B: Chemical* **253**, 156–163 (2017).

198. Berndt, D. *et al.* MEMS-based thermal conductivity sensor for hydrogen gas detection in automotive applications. *Sensors and Actuators A: Physical* **305**, 111670 (2020).

199. Shin, W. *et al.* Planar catalytic combustor film for thermoelectric hydrogen sensor. *Sensors and Actuators B: Chemical* **108**, 455–460 (2005).

200. Nishibori, M., Shin, W., Izu, N., Itoh, T. & Matsubara, I. Sensing performance of thermoelectric hydrogen sensor for breath hydrogen analysis. *Sensors and Actuators B: Chemical* **137**, 524–528 (2009).

201. Kong, R., Huang, J., Liu, P. & Zhou, X. Real-time breath gas analysis of methane using a multipass cell-based near-infrared gas sensor. *Biomed. Opt. Express, BOE* **15**, 4207–4219 (2024).

202. Mao, X., Zheng, P., Wang, X. & Yuan, S. Breath methane detection based on all-optical photoacoustic spectrometer. *Sensors and Actuators B: Chemical* **239**, 1257–1260 (2017).

203. Hlastala, M. P. The alcohol breath test—a review. *Journal of Applied Physiology* **84**, 401–408 (1998).

204. Cope, K., Risby, T. & Diehl, A. M. Increased gastrointestinal ethanol production in obese mice: implications for fatty liver disease pathogenesis. *Gastroenterology* **119**, 1340–1347 (2000).

205. Nair, S., Cope, K., Terence, R. H. & Diehl, A. M. Obesity and Female Gender Increase Breath Ethanol Concentration: Potential Implications for The Pathogenesis of Nonalcoholic Steatohepatitis. *Official journal of the American College of Gastroenterology | ACG* **96**, 1200 (2001).

206. Mitsubayashi, K., Matsunaga, H., Nishio, G., Toda, S. & Nakanishi, Y. Bioelectronic sniffers for ethanol and acetaldehyde in breath air after drinking. *Biosensors and Bioelectronics* **20**, 1573–1579 (2005).

207. Fuchs, P., Loeseken, C., Schubert, J. K. & Miekisch, W. Breath gas aldehydes as biomarkers of lung cancer. *Int J Cancer* **126**, 2663–2670 (2010).

208. Ozoemena, K. I. *et al.* Fuel cell-based breath-alcohol sensors: Innovation-hungry old electrochemistry. *Current Opinion in Electrochemistry* **10**, 82–87 (2018).

209. Mitsubayashi, K. *et al.* Bio-sniffer sticks for breath analysis after drinking. *Sensors and Actuators B: Chemical* **108**, 660–664 (2005).

210. Suarez, F. L., Furne, J. K., Springfield, J. & Levitt, M. D. Morning Breath Odor: Influence of Treatments on Sulfur Gases. *J Dent Res* **79**, 1773–1777 (2000).

211. Van den Velde, S., van Steenberghe, D., Van hee, P. & Quirynen, M. Detection of Odorous Compounds in Breath. *J Dent Res* **88**, 285–289 (2009).

212. Chen, Y. & Wang, R. The message in the air: Hydrogen sulfide metabolism in chronic respiratory diseases. *Respiratory Physiology & Neurobiology* **184**, 130–138 (2012).

213. Yang, S. *et al.* Au@ZnO functionalized three–dimensional macroporous WO3: A application of selective H2S gas sensor for exhaled breath biomarker detection. *Sensors and Actuators B: Chemical* **324**, 128725 (2020).

214. Wu, G. *et al.* Polyaniline/Graphene-Functionalized Flexible Waste Mask Sensors for Ammonia and Volatile Sulfur Compound Monitoring. *ACS Appl. Mater. Interfaces* **14**, 56056–56064 (2022).

215. Middleton, E. T. & Morice, A. H. Breath Carbon Monoxide as an Indication of Smoking Habit. *Chest* **117**, 758–763 (2000).

216. Kharitonov, S. A. & Barnes, P. J. Exhaled markers of inflammation. *Current Opinion in Allergy and Clinical Immunology* **1**, 217 (2001).

217. Montuschi, P., Kharitonov, S. A. & Barnes, P. J. Exhaled Carbon Monoxide and Nitric Oxide in COPD. *Chest* **120**, 496–501 (2001).

218. Ryter, S. W. & Choi, A. M. K. Carbon monoxide in exhaled breath testing and therapeutics. *J. Breath Res.* **7**, 017111 (2013).

219. Graham, B. L. *et al.* 2017 ERS/ATS standards for single-breath carbon monoxide uptake in the lung. *European Respiratory Journal* **49**, (2017).

220. Meredith, S. E. *et al.* A mobile-phone-based breath carbon monoxide meter to detect cigarette smoking. *Nicotine Tob Res* **16**, 766–773 (2014).

221. Mitlyng, B. L., Singh, J. A., Furne, J. K., Ruddy, J. & Levitt, M. D. Use of breath carbon monoxide measurements to assess erythrocyte survival in subjects with chronic diseases. *American Journal of Hematology* **81**, 432–438 (2006).

222. Vreman, H. J. *et al.* Semiportable electrochemical instrument for determining carbon monoxide in breath. *Clinical Chemistry* **40**, 1927–1933 (1994).

223. Phillips, M. *et al.* Variation in volatile organic compounds in the breath of normal humans. *Journal of Chromatography B: Biomedical Sciences and Applications* **729**, 75–88 (1999).

224. Sun, X., Shao, K. & Wang, T. Detection of volatile organic compounds (VOCs) from exhaled breath as noninvasive methods for cancer diagnosis. *Anal Bioanal Chem* **408**, 2759–2780 (2016).

225. Rondanelli, M. *et al.* Volatile Organic Compounds as Biomarkers of Gastrointestinal Diseases and Nutritional Status. *Journal of Analytical Methods in Chemistry* **2019**, 7247802 (2019).

226. van de Kant, K. D., van der Sande, L. J., Jöbsis, Q., van Schayck, O. C. & Dompeling, E. Clinical use of exhaled volatile organic compounds in pulmonary diseases: a systematic review. *Respir Res* **13**, 117 (2012).

227. Cikach, F. S. & Dweik, R. A. Cardiovascular Biomarkers in Exhaled Breath. *Progress in Cardiovascular Diseases* **55**, 34–43 (2012).

228. Minh, T. D. C., Blake, D. R. & Galassetti, P. R. The clinical potential of exhaled breath analysis for diabetes mellitus. *Diabetes Research and Clinical Practice* **97**, 195–205 (2012).

229. Dadamio, J. *et al.* Breath biomarkers of liver cirrhosis. *Journal of Chromatography B* **905**, 17–22 (2012).

230. Issitt, T. *et al.* Volatile compounds in human breath: critical review and meta-analysis. *J. Breath Res.* **16**, 024001 (2022).

231. Xu, H. *et al.* Multifunctional Wearable Sensing Devices Based on Functionalized Graphene Films for Simultaneous Monitoring of Physiological Signals and Volatile Organic Compound Biomarkers. *ACS Appl. Mater. Interfaces* **10**, 11785–11793 (2018).

232. Rosias, P. P. *et al.* Breath condenser coatings affect measurement of biomarkers in exhaled breath condensate. *European Respiratory Journal* **28**, 1036–1041 (2006).

233. Horváth, I., Hunt, J. & Barnes, P. J. Exhaled breath condensate: methodological recommendations and unresolved questions. *Eur Respir J* **26**, 523–548 (2005).

234. Esther, C. R. *et al.* Mass spectrometric analysis of biomarkers and dilution markers in exhaled breath condensate reveals elevated purines in asthma and cystic fibrosis. *American Journal of Physiology-Lung Cellular and Molecular Physiology* **296**, L987–L993 (2009).

235. Sofia, M. *et al.* Exploring Airway Diseases by NMR-Based Metabonomics: A Review of Application to Exhaled Breath Condensate. *J Biomed Biotechnol* **2011**, 403260 (2011).

236. Zang, X. *et al.* Comparison of Ambient and Atmospheric Pressure Ion Sources for Cystic Fibrosis Exhaled Breath Condensate Ion Mobility-Mass Spectrometry Metabolomics. *J. Am. Soc. Mass Spectrom.* **28**, 1489–1496 (2017).

237. Hu, B. Mass spectrometric analysis of exhaled breath: Recent advances and future perspectives. *TrAC Trends in Analytical Chemistry* **168**, 117320 (2023).

238. Berchtold, C., Bosilkovska, M., Daali, Y., Walder, B. & Zenobi, R. Real-time monitoring of exhaled drugs by mass spectrometry. *Mass Spectrometry Reviews* **33**, 394–413 (2014).

239. Yang, Y. & Gao, W. Wearable and flexible electronics for continuous molecular monitoring. *Chem. Soc. Rev.* **48**, 1465–1491 (2019).

240. Tu, J. *et al.* A wireless patch for the monitoring of C-reactive protein in sweat. *Nat. Biomed. Eng* 1–14 (2023) doi:10.1038/s41551-023-01059-5.

241. Ye, C. *et al.* A wearable aptamer nanobiosensor for non-invasive female hormone monitoring. *Nat. Nanotechnol.* 1–8 (2023) doi:10.1038/s41565-023-01513-0.

242. Gholizadeh, A. *et al.* Toward point-of-care management of chronic respiratory conditions: Electrochemical sensing of nitrite content in exhaled breath condensate using reduced graphene oxide. *Microsyst Nanoeng* **3**, 17022 (2017).

243. Maier, D. *et al.* Toward Continuous Monitoring of Breath Biochemistry: A Paper-Based Wearable Sensor for Real-Time Hydrogen Peroxide Measurement in Simulated Breath. *ACS Sens.* **4**, 2945–2951 (2019).

244. Bhide, A., Pali, M., Muthukumar, S. & Prasad, S. EBC-SURE (exhaled breath condensate- scanning using rapid electro analytics): A non-faradaic and non-invasive electrochemical assay to screen for pro-inflammatory biomarkers in human breath condensate. *Biosensors and Bioelectronics* **206**, 114117 (2022).

245. Corradi, M. *et al.* Comparison between exhaled and bronchoalveolar lavage levels of hydrogen peroxide in patients with diffuse interstitial lung diseases. *Acta Biomed* **79 Suppl 1**, 73–78 (2008).

246. Hayes, S. A. *et al.* Exhaled breath condensate for lung cancer protein analysis: a review of methods and biomarkers. *J. Breath Res.* **10**, 034001 (2016).

247. Sack, U. *et al.* Multiplex analysis of cytokines in exhaled breath condensate. *Cytometry Part A* **69A**, 169–172 (2006).

248. Ryan, D. J. *et al.* Exhaled Breath Condensate (EBC) analysis of circulating tumour DNA (ctDNA) using a lung cancer specific UltraSEEK oncogene panel. *Lung Cancer* **168**, 67–73 (2022).

249. Zhang, X. *et al.* A miniaturized immunosensor platform for automatic detection of carcinoembryonic antigen in EBC. *Sensors and Actuators B: Chemical* **205**, 94–101 (2014).

250. Li, X. *et al.* Rapid and on-site wireless immunoassay of respiratory virus aerosols via hydrogel-modulated resonators. *Nat Commun* **15**, 4035 (2024).

251. Nguyen, P. Q. *et al.* Wearable materials with embedded synthetic biology sensors for biomolecule detection. *Nat Biotechnol* **39**, 1366–1374 (2021).

252. Williams, C. M. *et al.* Exhaled Mycobacterium tuberculosis output and detection of subclinical disease by face-mask sampling: prospective observational studies. *The Lancet Infectious Diseases* **20**, 607–617 (2020).

253. Li, H. *et al.* Wireless, battery-free, multifunctional integrated bioelectronics for respiratory pathogens monitoring and severity evaluation. *Nat Commun* **14**, 7539 (2023).

254. Wallace, M. A. G., Pleil, J. D. & Madden, M. C. Identifying organic compounds in exhaled breath aerosol: Non-invasive sampling from respirator surfaces and disposable hospital masks. *Journal of Aerosol Science* **137**, 105444 (2019).

255. Heng, W. *et al.* A smart mask for exhaled breath condensate harvesting and analysis. *Science* **385**, 954–961 (2024).

256. Cao, Y. *et al.* Polyaniline/Prussian blue nanolayer enhanced electrochemical sensing of H2O2 in EBC using an integrated condensation facemask. *Sensors and Actuators B: Chemical* **393**, 134189 (2023).

257. Daniels, J. *et al.* A mask-based diagnostic platform for point-of-care screening of Covid-19. *Biosensors and Bioelectronics* **192**, 113486 (2021).

258. Vaughan, J. *et al.* Exhaled breath condensate pH is a robust and reproducible assay of airway acidity. *European Respiratory Journal* **22**, 889–894 (2003).

259. Paget-Brown, A. O. *et al.* Normative Data for pH of Exhaled Breath Condensate. *Chest* **129**, 426–430 (2006).

260. Hunt, J. F. *et al.* Endogenous Airway Acidification. *Am J Respir Crit Care Med* **161**, 694–699 (2000).

261. Kostikas, K. *et al.* pH in Expired Breath Condensate of Patients with Inflammatory Airway Diseases. *Am J Respir Crit Care Med* **165**, 1364–1370 (2002).

262. Tate, S., MacGregor, G., Davis, M., Innes, J. A. & Greening, A. P. Airways in cystic fibrosis are acidified: detection by exhaled breath condensate. *Thorax* **57**, 926–929 (2002).

263. Kullmann, T. *et al.* Exhaled breath condensate pH standardised for CO2 partial pressure. *European Respiratory Journal* **29**, 496–501 (2007).

264. Antczak, A. *et al.* Increased hydrogen peroxide and thiobarbituric acid-reactive products in expired breath condensate of asthmatic patients. *European Respiratory Journal* **10**, 1235–1241 (1997).

265. Kietzmann, D., Kahl, R., Müller, M., Burchardi, H. & Kettler, D. Hydrogen peroxide in expired breath condensate of patients with acute respiratory failure and with ARDS. *Intensive Care Med* **19**, 78–81 (1993).

266. Kakeshpour, T., Metaferia, B., Zare, R. N. & Bax, A. Quantitative detection of hydrogen peroxide in rain, air, exhaled breath, and biological fluids by NMR spectroscopy. *Proceedings of the National Academy of Sciences* **119**, e2121542119 (2022).

267. Lee, J. K. *et al.* Condensing water vapor to droplets generates hydrogen peroxide. *Proc Natl Acad Sci U S A* **117**, 30934–30941 (2020).

268. Corradi, M. *et al.* Biomarkers of oxidative stress after controlled human exposure to ozone. *Toxicology Letters* **134**, 219–225 (2002).

269. Wiedemair, J., van Dorp, H. D. S., Olthuis, W. & van den Berg, A. Developing an amperometric hydrogen peroxide sensor for an exhaled breath analysis system. *ELECTROPHORESIS* **33**, 3181–3186 (2012).

270. Chen, Y.-C. & O'Hare, D. Exhaled breath condensate based breath analyser – a disposable hydrogen peroxide sensor and smart analyser. *Analyst* **145**, 3549–3556 (2020).

271. Lundberg, J. O., Weitzberg, E. & Gladwin, M. T. The nitrate–nitrite–nitric oxide pathway in physiology and therapeutics. *Nat Rev Drug Discov* **7**, 156–167 (2008).

272. Corradi, M. *et al.* Nitrate in exhaled breath condensate of patients with different airway diseases. *Nitric Oxide* **8**, 26–30 (2003).

273. Rihák, V. *et al.* Nitrite in exhaled breath condensate as a marker of nitrossative stress in the airways of patients with asthma, COPD, and idiopathic pulmonary fibrosis. *J Clin Lab Anal* **24**, 317–322 (2010).

274. Donnelly, L. Exhaled breath condensate: Nitric oxide-related compounds. *European Respiratory Monograph (Exhaled Biomakers)* **49**, (2009).

275. Stefanska, J. *et al.* Hydrogen peroxide and nitrite reduction in exhaled breath condensate of COPD patients. *Pulmonary Pharmacology & Therapeutics* **25**, 343–348 (2012).

276. Dziedzic, B., Mazanowska-Gajdowicz, J., Walczewska, A., Sarniak, A. & Nowak, D. Comparison of cadmium and enzyme-catalyzed nitrate reduction for determination of NO2−/NO3− in breath condensate. *Clinica Chimica Acta* **335**, 65–74 (2003).

277. Soares, R. R. A. *et al.* Ion-selective electrodes based on laser-induced graphene as an alternative method for nitrite monitoring. *Microchim Acta* **190**, 43 (2023).

278. Effros, R. M. *et al.* The Effects of Volatile Salivary Acids and Bases on Exhaled Breath Condensate pH. *Am J Respir Crit Care Med* **173**, 386–392 (2006).

279. MacGregor, G. *et al.* Breath condensate ammonium is lower in children with chronic asthma. *European Respiratory Journal* **26**, 271–276 (2005).

280. Shoman, Y. *et al.* Reference Ranges of 8-Isoprostane Concentrations in Exhaled Breath Condensate (EBC): A Systematic Review and Meta-Analysis. *Int J Mol Sci* **21**, 3822 (2020).

281. Montuschi, P., Kharitonov, S. A., Ciabattoni, G. & Barnes, P. J. Exhaled leukotrienes and prostaglandins in COPD. *Thorax* **58**, 585–588 (2003).

282. Carraro, S. *et al.* Exhaled breath condensate cysteinyl leukotrienes are increased in children with exercise-induced bronchoconstriction. *Journal of Allergy and Clinical Immunology* **115**, 764–770 (2005).

283. Janicka, M., Kot-Wasik, A., Kot, J. & Namieśnik, J. Isoprostanes-Biomarkers of Lipid Peroxidation: Their Utility in Evaluating Oxidative Stress and Analysis. *International Journal of Molecular Sciences* **11**, 4631–4659 (2010).

284. Konstan, M. W., Walenga, R. W., Hilliard, K. A. & Hilliard, J. B. Leukotriene B4 Markedly Elevated in the Epithelial Lining Fluid of Patients with Cystic Fibrosis. *Am Rev Respir Dis* **148**, 896–901 (1993).

285. Liang, Y., Yeligar, S. M. & Brown, L. A. S. Exhaled Breath Condensate: A Promising Source for Biomarkers of Lung Disease. *The Scientific World Journal* **2012**, 217518 (2012).

286. Lee, G. *et al.* Single Microfluidic Electrochemical Sensor System for Simultaneous Multi-Pulmonary Hypertension Biomarker Analyses. *Sci Rep* **7**, 7545 (2017).

287. Gamero, B., Bebe, S. & Prakash, R. Molecularly Imprinted Electroimpedance Sensor for Detection of 8-Isoprostane in Exhaled Breath Condensate. *IEEE Sensors Letters* **5**, 1–4 (2021).

288. Lütkecosmann, S., Warsinke, A., Tschöpe, W., Eichler, R. & Hanack, K. A novel monoclonal antibody suitable for the detection of leukotriene B4. *Biochemical and Biophysical Research Communications* **482**, 1054–1059 (2017).

289. Effros, R. M. *et al.* A Simple Method for Estimating Respiratory Solute Dilution in Exhaled Breath Condensates. *Am J Respir Crit Care Med* **168**, 1500–1505 (2003).

290. Ghio, A. J., Madden, M. C. & Esther, C. R. Transition and post-transition metals in exhaled breath condensate. *J. Breath Res.* **12**, 027112 (2018).

291. Huszár, É. *et al.* Adenosine in exhaled breath condensate in healthy volunteers and in patients with asthma. *Eur Respir J* **20**, 1393–1398 (2002).

292. Monge, M. E. *et al.* Ion mobility and liquid chromatography/mass spectrometry strategies for exhaled breath condensate glucose quantitation in cystic fibrosis studies. *Rapid Communications in Mass Spectrometry* **27**, 2263–2271 (2013).

293. Baker, E. H. *et al.* Hyperglycemia and cystic fibrosis alter respiratory fluid glucose concentrations estimated by breath condensate analysis. *Journal of Applied Physiology* **102**, 1969–1975 (2007).

294. Zhou, Y.-Y. *et al.* A non-invasive method for the detection of glucose in human exhaled breath by condensation collection coupled with ion chromatography. *Journal of Chromatography A* **1685**, 463564 (2022).

295. Marek, E. M. *et al.* Measurements of lactate in exhaled breath condensate at rest and after maximal exercise in young and healthy subjects. *J. Breath Res.* **4**, 017105 (2010).

296. Kubáň, P., Kobrin, E.-G. & Kaljurand, M. Capillary electrophoresis – A new tool for ionic analysis of exhaled breath condensate. *Journal of Chromatography A* **1267**, 239–245 (2012).

297. Chu, B. H. *et al.* Wireless Detection System for Glucose and pH Sensing in Exhaled Breath Condensate Using AlGaN/GaN High Electron Mobility Transistors. *IEEE Sensors Journal* **10**, 64–70 (2010).

298. Zhang, S. *et al.* Rapid Measurement of Lactate in the Exhaled Breath Condensate: Biosensor Optimization and In-Human Proof of Concept. *ACS Sens.* **7**, 3809–3816 (2022).

299. Ghelli, F. *et al.* Inflammatory Biomarkers in Exhaled Breath Condensate: A Systematic Review. *Int J Mol Sci* **23**, 9820 (2022).

300. Zietkowski, Z. *et al.* High-sensitivity C-reactive protein in the exhaled breath condensate and serum in stable and unstable asthma. *Respir Med* **103**, 379–385 (2009).

301. Schumann, C. *et al.* Detection of Erythropoietin in Exhaled Breath Condensate of Nonhypoxic Subjects Using a Multiplex Bead Array. *Mediators Inflamm* **2006**, 18061 (2006).

302. Ma, J. *et al.* Rapid detection of airborne protein from Mycobacterium tuberculosis using a biosensor detection system. *Analyst* **147**, 614–624 (2022).

303. Youssef, O. *et al.* Exhaled breath condensate as a source of biomarkers for lung carcinomas. A focus on genetic and epigenetic markers—A mini-review. *Genes, Chromosomes and Cancer* **55**, 905–914 (2016).

304. Chen, J.-L. *et al.* Analysis of p16 gene mutations and their expression using exhaled breath condensate in non-small-cell lung cancer. *Oncol Lett* **10**, 1477–1480 (2015).

305. Carpagnano, G. E. *et al.* 3p microsatellite alterations in exhaled breath condensate from patients with non-small cell lung cancer. *Am J Respir Crit Care Med* **172**, 738–744 (2005).

306. Yang Ai, S. S. *et al.* Mitochondrial DNA mutations in exhaled breath condensate of patients with lung cancer. *Respiratory Medicine* **107**, 911–918 (2013).

307. Koc, A. *et al.* cfDNA in exhaled breath condensate (EBC) and contamination by ambient air: toward volatile biopsies. *J Breath Res* **13**, 036006 (2019).

308. Pérez-Sánchez, C. *et al.* Clinical Utility of microRNAs in Exhaled Breath Condensate as Biomarkers for Lung Cancer. *J Pers Med* **11**, 111 (2021).

309. Carpagnano, G. E. *et al.* Study of mitochondrial DNA alteration in the exhaled breath condensate of patients affected by obstructive lung diseases. *J. Breath Res.* **10**, 026005 (2016).

310. Gould, O., Ratcliffe, N., Król, E. & de Lacy Costello, B. Breath analysis for detection of viral infection, the current position of the field. *J. Breath Res.* **14**, 041001 (2020).

311. Nwanochie, E. & Linnes, J. C. Review of non-invasive detection of SARS-CoV-2 and other respiratory pathogens in exhaled breath condensate. *J. Breath Res.* **16**, 024002 (2022).

312. Sawano, M., Takeshita, K., Ohno, H. & Oka, H. SARS-CoV-2 RNA load and detection rate in exhaled breath condensate collected from COVID-19 patients infected with Delta variant. *J. Breath Res.* **16**, 036006 (2022).

313. Ryan, D. J. *et al.* Use of exhaled breath condensate (EBC) in the diagnosis of SARS-COV-2 (COVID-19). *Thorax* **76**, 86–88 (2021).

314. Chikasue, K. *et al.* Detection of Torque teno virus DNA in exhaled breath by polymerase chain reaction. *Acta Med Okayama* **66**, 387–397 (2012).

315. Shen, F. *et al.* Rapid Flu Diagnosis Using Silicon Nanowire Sensor. *Nano Lett.* **12**, 3722–3730 (2012).

316. Li, X., Wang, M., Chen, J., Lin, F. & Wang, W. Nucleic acid detection and quantitative analysis of influenza virus using exhaled breath condensate. *J. Breath Res.* **15**, 026001 (2021).

317. Zheng, Y., Chen, H., Yao, M. & Li, X. Bacterial pathogens were detected from human exhaled breath using a novel protocol. *Journal of Aerosol Science* **117**, 224–234 (2018).

318. Mosquera-Restrepo, S. F. *et al.* A Mycobacterium tuberculosis fingerprint in human breath allows tuberculosis detection. *Nat Commun* **13**, 7751 (2022).

319. Leung, N. H. L. *et al.* Respiratory virus shedding in exhaled breath and efficacy of face masks. *Nat Med* **26**, 676–680 (2020).

320. Cheng, Y. *et al.* Face masks effectively limit the probability of SARS-CoV-2 transmission. *Science* **372**, 1439–1443 (2021).

321. Liu, X. & Hu, B. Mask device as a new wearable sampler for breath analysis: what can we expect in the future? *Anal Bioanal Chem* **415**, 3759–3768 (2023).

322. Colin, P. *et al.* Propofol Breath Monitoring as a Potential Tool to Improve the Prediction of Intraoperative Plasma Concentrations. *Clin Pharmacokinet* **55**, 849–859 (2016).

323. Wang, C. *et al.* Determination of fentanyl in human breath by solid-phase microextraction and gas chromatography–mass spectrometry. *Microchemical Journal* **91**, 149–152 (2009).

324. Beck, O., Sandqvist, S., Eriksen, P., Franck, J. & Palmskog, G. Method for determination of methadone in exhaled breath collected from subjects undergoing methadone maintenance treatment. *Journal of Chromatography B* **878**, 2255–2259 (2010).

325. Colard, S., O'Connell, G. & Cahours, X. An Experimental Method to Determine the Concentration of Nicotine in Exhaled Breath and its Retention Rate Following Use of an Electronic Cigarette. *Environmental Analytical Chemistry*

326. Chen, X. *et al.* Breath analysis: Harnessing its potential for non-volatile drug caffeine monitoring in human body. *Microchemical Journal* **198**, 110130 (2024).

327. Ates, H. C. *et al.* Biosensor-Enabled Multiplexed On-Site Therapeutic Drug Monitoring of Antibiotics. *Advanced Materials* **34**, 2104555 (2022).

328. Benor, S. *et al.* Ultrafine particle content in exhaled breath condensate in airways of asthmatic children. *J. Breath Res.* **9**, 026001 (2015).

329. Marie-Desvergne, C. *et al.* Characterization of the elemental and particle load of patient exhaled breath condensate and comparison with pulmonary lavages. *J. Breath Res.* **17**, 016008 (2023).

330. Sauvain, J.-J., Hohl, M. S. S., Wild, P., Pralong, J. A. & Riediker, M. Exhaled Breath Condensate as a Matrix for Combustion-Based Nanoparticle Exposure and Health Effect Evaluation. *Journal of Aerosol Medicine and Pulmonary Drug Delivery* **27**, 449–458 (2014).

331. Yang, Y. *et al.* Artificial intelligence-enabled detection and assessment of Parkinson's disease using nocturnal breathing signals. *Nat Med* (2022) doi:10.1038/s41591-022-01932-x.

332. Ibrahim, W. *et al.* Visualization of exhaled breath metabolites reveals distinct diagnostic signatures for acute cardiorespiratory breathlessness. *Science translational medicine* **14**, eabl5849 (2022).

333. Smolinska, A. *et al.* Current breathomics—a review on data pre-processing techniques and machine learning in metabolomics breath analysis. *J. Breath Res.* **8**, 027105 (2014).

334. Nakhleh, M. K. *et al.* Diagnosis and Classification of 17 Diseases from 1404 Subjects via Pattern Analysis of Exhaled Molecules. *ACS Nano* **11**, 112–125 (2017).

335. Sinha, A. *et al.* Exhaled breath condensate metabolome clusters for endotype discovery in asthma. *J Transl Med* **15**, 262 (2017).

336. Barberis, E. *et al.* Metabolomics Diagnosis of COVID-19 from Exhaled Breath Condensate. *Metabolites* **11**, 847 (2021).

337. Kurova, V. S. *et al.* Proteomics of exhaled breath: methodological nuances and pitfalls. *Clinical Chemistry and Laboratory Medicine* **47**, 706–712 (2009).

338. Bloemen, K. *et al.* A new approach to study exhaled proteins as potential biomarkers for asthma. *Clinical & Experimental Allergy* **41**, 346–356 (2011).

339. Sakumura, Y. *et al.* Diagnosis by Volatile Organic Compounds in Exhaled Breath from Lung Cancer Patients Using Support Vector Machine Algorithm. *Sensors* **17**, 287 (2017).

340. Hakim, M. *et al.* Diagnosis of head-and-neck cancer from exhaled breath. *Br J Cancer* **104**, 1649–1655 (2011).

341. Peng, G. *et al.* Diagnosing lung cancer in exhaled breath using gold nanoparticles. *Nature Nanotech* **4**, 669–673 (2009).

342. Alkhalifah, Y. *et al.* VOCCluster: Untargeted Metabolomics Feature Clustering Approach for Clinical Breath Gas Chromatography/Mass Spectrometry Data. *Anal. Chem.* **92**, 2937–2945 (2020).

343. Lee, B. *et al.* Breath analysis system with convolutional neural network (CNN) for early detection of lung cancer. *Sensors and Actuators B: Chemical* **409**, 135578 (2024).

344. Hsu, F.-S. *et al.* Benchmarking of eight recurrent neural network variants for breath phase and adventitious sound detection on a self-developed open-access lung sound database—HF_Lung_V1. *PLoS One* **16**, e0254134 (2021).

345. Heng, W., Solomon, S. & Gao, W. Flexible Electronics and Devices as Human–Machine Interfaces for Medical Robotics. *Advanced Materials* **34**, 2107902 (2022).

346. Pang, G. *et al.* CoboSkin: Soft Robot Skin With Variable Stiffness for Safer Human–Robot Collaboration. *IEEE Trans. Ind. Electron.* **68**, 3303–3314 (2021).

347. Pang, Y. *et al.* Self-Powered Multifunctional Human–Machine Interfaces for Respiratory Monitoring and Smart System Control. *Advanced Materials Interfaces* **9**, 2201202 (2022).

348. Xu, K. *et al.* Laser Direct Writing of Flexible Thermal Flow Sensors. *Nano Lett.* **23**, 10317–10325 (2023).

349. Tang, K. *et al.* Respiration-based human-machine interface for aphasic patients with limited physical mobility. *Chemical Engineering Journal* **487**, 150507 (2024).

350. Zhang, B. *et al.* Breath-based human–machine interaction system using triboelectric nanogenerator. *Nano Energy* **64**, 103953 (2019).

351. Kim, J.-H. & Lee, J. Controlling your contents with the breath: Interactive breath interface for VR, games, and animations. *PLOS ONE* **15**, e0241498 (2020).

352. Liu, Y. *et al.* Soft, miniaturized, wireless olfactory interface for virtual reality. *Nat Commun* **14**, 2297 (2023).

Chapter 2

A SMART MASK FOR EXHALED BREATH CONDENSATE HARVESTING AND ANALYSIS

Materials from this chapter appear in Heng, W.; Yin, S.; Min, J.; Wang, C.; Han, H.; Sani, E. S.; Li, J.; Song, Y.; Rossiter, H. B.; Gao, W. A smart mask for exhaled breath condensate harvesting and analysis. Science 385, 954–961 (2024). https://doi.org/10.1126/science.adn6471.

Respiratory epidemics and pandemics have prompted an urgent and critical need for comprehensive research on the respiratory system. A number of clinically meaningful molecular analytes such as volatile organic compounds (VOCs) (e.g., acetone and alkanes), inorganic substances (e.g., nitric oxide and ammonia), cytokines, and pathogens (e.g., SARS-CoV-2) are exhaled in the form of gases, aerosols, or droplets [1–3]. Instinctively, the real-time and continuous analysis of exhaled breath biomarkers could provide immense potential for offering valuable insights into the early diagnosis, monitoring, and management of a variety of respiratory and metabolic health conditions including asthma [4], chronic obstructive pulmonary disease (COPD) [5], COVID-19 [6], lung cancer [7], tuberculosis [8], and beyond [3]. Despite this promise, the tools available for studying human breath remain severely restricted. Existing methods of real-time and wireless monitoring of exhaled breath molecular biomarkers are primarily limited to breath alcohol tests while "electronic noses" based on gas sensors, though actively researched, are limited by inadequate selectivity for practical exhaled breath analysis [9–11].

Exhaled breath condensate (EBC) is a highly promising noninvasive aqueous matrix in which soluble gaseous and non-volatile biomarkers can be measured selectively for personalized healthcare (**Fig. 2-1A**) [2, 12]. Clinically, EBC is collected using commercial condenser [13] or specialized condensation instruments [12, 14, 15] and subsequently analyzed in laboratory conditions using mass spectrometry or photometric assays to assess airway inflammation and substance metabolism (**Fig. A-1**) [16–18]. However, the implementation of these approaches for at-home remote sensing is hindered by challenges related to labor, time, money, and energy costs. Furthermore, issues such as the degradation of reactive substances (e.g., NO_2^- and H_2O_2) during the sample process and storage, interference of oral ingredients, and the absence of continuous dynamic information impede the practical and widespread application of EBC testing [2]. The recent development of wearable biosensors has ushered the door in a new era of telehealth, enabling continuous and wireless molecular monitoring of biomarkers in sweat, saliva, and interstitial fluid [19–21]. The exploration of wearable EBC analysis has been limited, primarily due to the challenges in condensing exhaled breath, EBC sampling, and in situ analysis during an individual's daily activities [22]. Face masks serve as

an ideal wearable platform for personal protection [6, 23, 24] and breath sampling [25, 26]. Recent advances in exhaled breath aerosol (EBA) devices based on masks have shown some promise in point-of-care analysis, but their reliance on external media for sample extraction has introduced challenges with stability and reproducibility, which limits their suitability for continuous monitoring (**Fig. A-1** and **table A-1**) [27-29].

We introduce a mechanically soft microfluidic smart mask system, EBCare (Exhaled Breath Condensate Analysis and Respiratory Evaluation), designed for continuous exhaled breath condensation, automatic EBC capturing and transport, and real-time in situ EBC biomarkers analysis (**Fig. 2-1A**–**C**, **Fig. A-2** and **table A-2**). Compared to traditional bulky EBC collection devices that rely heavily on ice buckets or refrigeration, EBCare is capable of effective condensation of breath vapor under indoor-outdoor environments via tandem passive cooling technologies that integrate hydrogel evaporative cooling, metamaterial radiative cooling, and a device framework with high thermal conductivity. A bioinspired microfluidic module substantially enhances EBC harvesting and transport efficiency by leveraging the capillary action driven by surface hydrophilicity and microengineerd graded pillar array (**Fig. 2-1B**,**C** and **Fig. A-3**). EBCare supports high-temporal-resolution EBC harvesting and transport, making it ideal for real-time continuous in situ analysis (**table A-1**). EBCare system enables highly sensitive, selective, and continuous EBC biomarkers analysis, facilitated by a nanoengineered electrochemical sensor array coupled with a flexible printed circuit board (FPCB) for signal processing and wireless communication (**Fig. 2-1D** and **E**). The post-analysis EBC efflux was absorbed by cooling hydrogel, ensuring a continuous water replenishment for sustainable evaporative cooling.

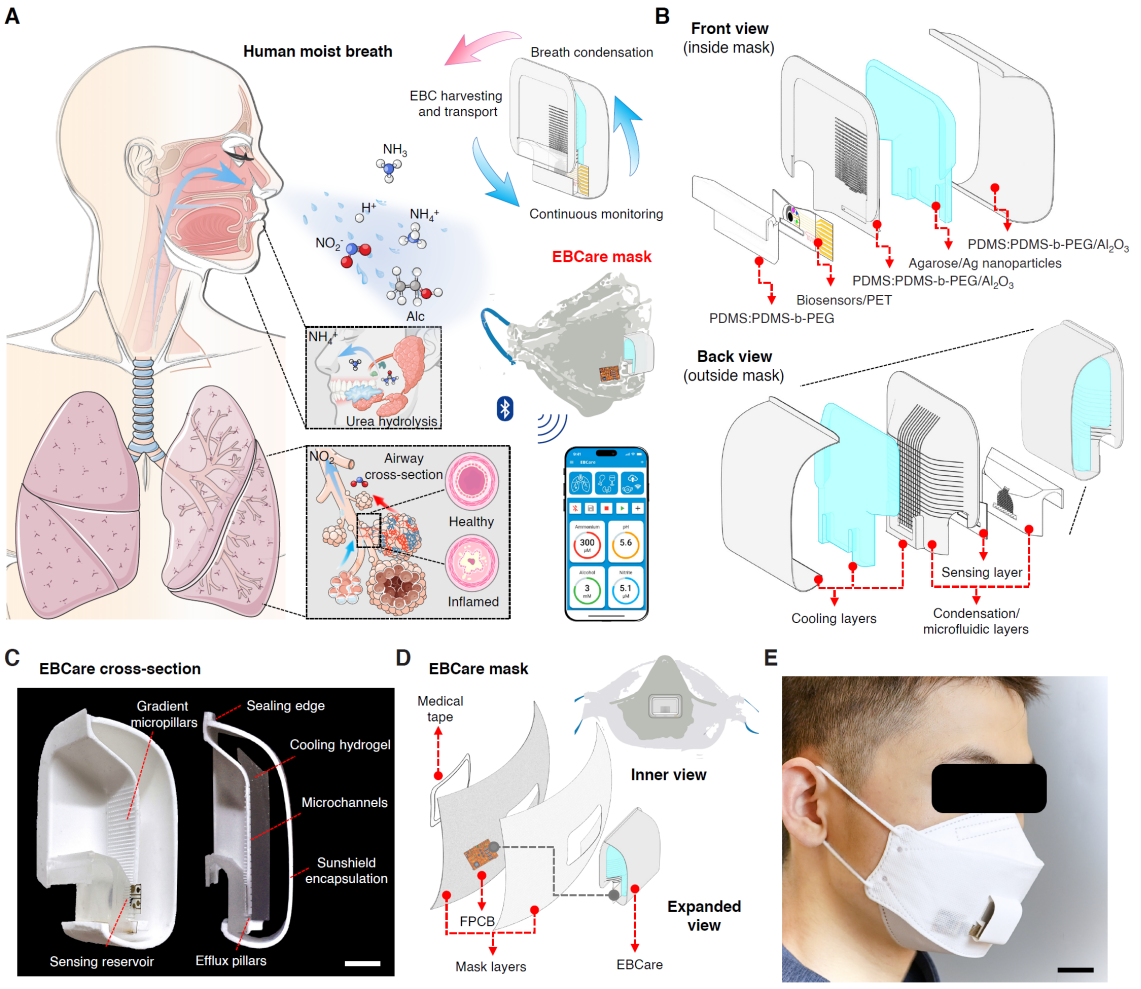

Figure 2-1. A smart EBCare (Exhaled Breath Condensate Analysis and Respiratory Evaluation) mask for efficient harvesting and continuous analysis of exhaled breath condensate (EBC). (**A**) EBCare is capable of exhaled breath condensation, EBC harvesting and transport, and continuous analysis of biomarkers from the human respiratory tract. Alc, alcohol. (**B** and **C**) Exploded-view schematic illustration (B) and cross-sectional optical images (C) of the main components of an EBCare device. Scale bar, 4 mm. PDMS, Polydimethylsiloxane; PEG, Polyethylene Glycol; PET, Polyethylene Terephthalate. (**D**) Schematic showing the expanded and inner view of the smart mask integrated with an EBCare device. FPCB, Flexible printed circuit board. (**E**) Photograph of a fully-integrated wireless smart mask worn by a participant. Scale bar, 3 cm.

2.1 The tandem cooling strategy for exhaled breath condensation

EBC harvesting plays an underpinning role in achieving real-time and continuous EBC biomarkers analysis with high temporal resolution. To efficiently cool down the condensing surface temperature to the dew point of the exhaled breath in diverse real-life indoor and outdoor scenarios, EBCare employs a tandem passive cooling strategy combining hydrogel evaporation and radiative cooling (**Fig. 2-2A** and **B**). The main structural framework of EBCare utilizes a ceramic alumina-polymer hybrid metamaterial with high thermal conductivity and ideal radiative cooling properties (**Fig. 2-2C**), comprising micrometer-sized Al_2O_3 spheres distributed evenly in a polymeric matrix containing polydimethylsiloxane (PDMS) and copolymer PDMS-block-polyethylene glycol (PDMS-b-PEG) (**Figs. A-4** and **A-5**) [30, 31].

During operation in ambient conditions, the natural evaporation of water from the agarose hydrogel absorbs surrounding heat, substantially reducing the temperature of the hydrogel [32]. The addition of Ag nanoparticles into the hydrogel introduced high antibiotic effect and enhanced EBCare's biocompatibility during long-term on-body use (**Fig. A-6**). Simulating the heat from breath with a heating source (**Fig. A-7A**) demonstrates that hydrogel evaporation effectively reduces the surface temperature by 4–14ºC under varied relative humidity (RH) and ambient temperature (**Fig. 2-2D**). In a standard indoor environment (23 ºC and 50% RH), the temperature of the heating source is controlled to be similar to the human breath temperature, and hydrogel evaporation induces a temperature drop of approximately 8 ºC, well below the dew point of the exhaled breath (~5 ºC below breath temperature under 75% RH) (**Fig. 2-2D**). However, without continuous liquid replenishment, the evaporative cooling function of the hydrogel will diminish substantially after 2–3 hours (**Fig. A-7B** and **Fig. A-8A**). Introducing a condensate circulation system that transports the continuously harvested EBC to the hydrogel ensures sustainable and stable evaporative cooling for at least 7 hours (**Fig. A-7C**, **D** and **Fig. A-8**).

On sunny days with strong solar radiation, the potential elevation of EBCare temperature due to hydrogel sunlight absorption could compromise breath condensation during outdoor

wearing [33]. To address this issue, a tandem radiative cooling function is integrated into the device design using metamaterial PDMS:PDMS-b-PEG/Al_2O_3 as the main EBCare framework and sunshield layer. Owing to the Mie scattering of spherical alumina microparticles under solar spectrum and the strong emission properties of polymeric matrix in the mid-infrared (MIR) region, the hybrid polymeric metamaterial achieves ~95% solar reflectivity and ~95% MIR thermal emissivity (**Fig. 2-2C** and **Fig. A-9**). Such optical properties effectively reduce the solar radiation absorption and radiate heat through MIR range in atmospheric window to the outer space, ensuring the high efficiency of the condensation process even under strong sunlight exposure in outdoor environments.

EBCare's tandem cooling effects were evaluated in both indoor and outdoor environments, day and night, and were compared to the normal fabric mask material without cooling function and materials with only one type of cooling method (standalone exposed hydrogel and PDMS:PDMS-b-PEG/Al_2O_3 framework) (**Fig. 2-2E** and **Fig. A-10**). The EBCare device demonstrated temperature approximately 7°C lower than radiative cooling material alone and ~10ºC lower than non-radiative cooling mask material throughout the indoor and outdoor tests at night. The cooling effect was more substantial under 1 sun (~1 kW m^{-2}) radiation, with temperature of ~5ºC lower than the exposed hydrogel, and ~15ºC and ~20ºC below those of the radiative cooling layer and non-radiative cooling mask layer, respectively (**Fig. A-11**). The cooling system design of EBCare was further validated by comparing EBC collection results of these materials from healthy participants under daily indoor and outdoor environments (**Fig. 2-2F**, **Fig. A-12**, and **Table A-3**). EBCare's collection rate is five times greater than that without cooling under indoor conditions and twice as great as exposed hydrogel cooling alone under outdoor conditions. Even under 1 sun flux, the device still captures EBC at a high rate of around 4 μL min^{-1}, indicating highly efficient, continuous, and long-term EBC condensation through the tandem passive cooling strategy (**Fig. 2-2F** and **G**).

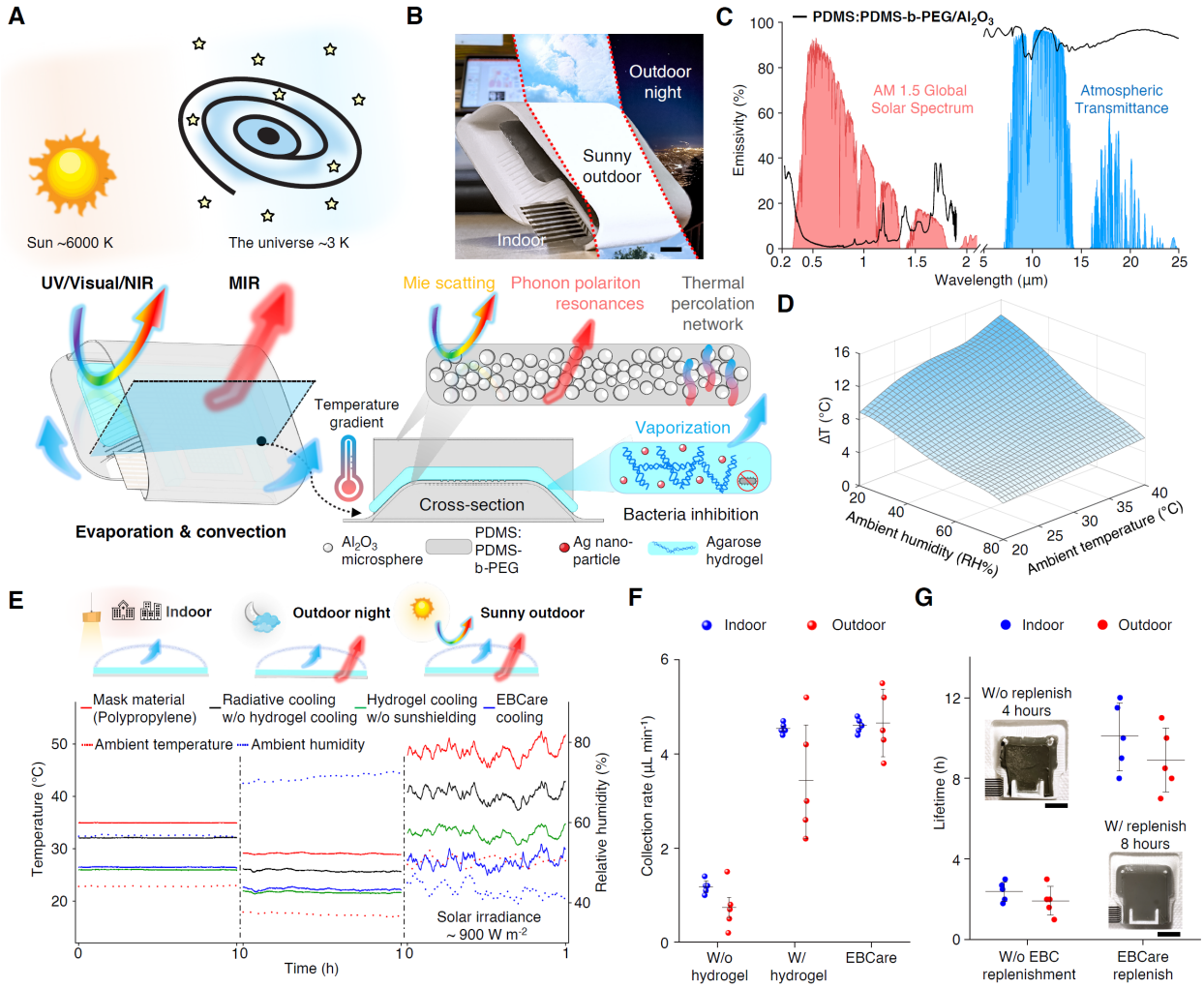

Figure 2-2. Characterization of EBCare's tandem cooling design for breath condensation. (**A**) Schematic of an EBCare device with simultaneous indoor and outdoor cooling capabilities for efficient breath condensation. UV, Ultraviolet; NIR, Near infrared; MIR, Mid infrared. (**B**) Photographs of an EBCare device in indoor, under sunlight, and outdoor night settings. Scale bar, 5 mm. (**C**) Spectral emissivity of a polymeric metamaterial film (0.5 mm-thick). Red and blue colors represent AM 1.5 solar spectrum and atmospheric window, respectively. (**D**) Cooling capacity of the hydrogel under varied ambient relative humidity and temperature. ΔT, surface temperature drops in the presence of hydrogel. (**E**) Surface temperature of different cooling strategies under indoor and outdoor (at night, under sunlight) environments. (**F**) EBC harvesting performance of different cooling strategies from

a healthy participant. (**G**) Hydrogel lifetime for the EBCare device with and without EBC refreshing. Inserted insets show the hydration state of hydrogel on EBCare with and without EBC refreshing. Scale bars, 1cm. All error bars in the figure represent standard deviations of the mean.

2.2 Bioinspired microfluidics for EBC sampling, transport, and refreshing

The continuous respiratory monitoring capability of the EBCare mask system hinges on the self-directed flow of EBC within an integrated bioinspired microfluidic system. The natural conveyance of water and chemicals in plants primarily relies on the capillary phenomenon (**Fig. A-13**). In plants, water transpires from the stomata of leaves, transforming into water vapor. This process induces a reduction of water content inside the leaves, creating negative pressure inside the plant's diminutive hydrophilic xylem vessels. Consequently, water is drawn upwards from the ground through the capillary forces to meet the plant's water needs [34]. Inspired by this biological process, EBCare's microfluidic module incorporates micropillars with structural gradients, hydrophilic microfluidic channels, and evaporative cooling hydrogels, serving as the graded capillary pumps for gravity-independent EBC sampling, transport, and refreshing (**Fig. 2-3A**).

Similar to xylem vessels, the hydrophilic interface of the EBCare device's inner surface is crucial for enabling the automatic circulation of harvested EBC through the microfluidics. In our study, increasing the doping ratio of the copolymer PDMS-b-PEG to 1% in EBCare's main framework material (PDMS:PDMS-b-PEG/Al_2O_3) substantially enhances hydrophilicity, achieving a low contact angle of 15.5° due to an increased C-O bond surface distribution (**Fig. 2-3B**, **Figs. A-14** and **A-15**) [35]. Unlike plasma treated pristine PDMS, which can lose its hydrophilicity within hours, the hybrid polymer PDMS:PDMS-b-PEG/Al_2O_3 was able to maintain high hydrophilicity over a period of one month (**Fig. A-16)**. This hydrophilic nature, in contrast to hydrophobic surfaces, offers advantages in terms of EBC nucleation, cohesion, and collection (**Fig. A-17**) [36]. Importantly, such hybrid material also exhibited excellent biological anti-adhesive and non-fouling properties, making it ideal for EBC sampling and subsequent in situ bioanalysis with high accuracy (**Fig. A-18**) [37].

The spontaneous and highly efficient directional transport of EBC to the sensing reservoir, following EBC capture at the hydrophilic inner surface of EBCare device, was facilitated by the graded capillary forces resulting from an array of micropillars with both height and density gradients (**Fig. 2-3C**,**D** and **Figs. A-19–A-21**). The stabilized EBC continuously flows through the sensing reservoir where it is analyzed by the built-in electrochemical sensors. Subsequently, driven by strong capillary forces from hydrogel covered microchannels on EBCare's outer surface, EBC is automatically transferred to the device's outer surface through efflux columns between the inner and outer interfaces and transports effectively against gravity via microfluidic channels (**Fig. 2-3E**). EBC is then absorbed by the hydrogel along with the hydrogel evaporation, providing a continuous water source for the hydrogel evaporative cooling.

The in vitro assessment of the fully assembled microfluidic system demonstrated efficient liquid harvesting, transport, effluxion, and evaporation, paving the way for sustainable wearable EBC analysis (**Figs. A-22** and **A-23**). By incorporating an impedimetric sensor into the sensing reservoir, we evaluated the EBC sampling capabilities of the EBCare in healthy participants, considering different inner surface materials and structures (**Fig. 2-3F**,**G**). The results revealed that the device made of pristine PDMS was not capable of sampling EBC into the sensing reservoir under both upright and supine conditions due to the hydrophobic surface. The device with planar hydrophilic PDMS:PDMS-b-PEG/Al_2O_3 was only able to access EBC under upright conditions, where gravity served as the driving force. In contrast, the EBCare device, constructed from hydrophilic PDMS:PDMS-b-PEG/Al_2O_3 with graded microstructures, demonstrated the ability to harvest and transport EBC into the sensing reservoir within 5 minutes even in supine postures. Stable and continuous wearable EBC analysis is possible under various real-life conditions, including gravity-defying supine positions, where graded capillary forces acted as the primary driving force (**Fig. A-24**). Based on the optimized design, EBCare's startup time for in situ EBC analysis is estimated at only 3 minutes when in an upright posture (**Fig. A-25**). Our tests further indicated that the EBCare device can efficiently harvest EBC from human participants at high rates of ~5 μL min^{-1} (**Fig. A-26**). This rate is sufficient for high temporal resolution EBC analysis, given the small

volume of the sensing reservoir (~5 μL) (**Fig. A-27**). Additionally, EBCare can be easily integrated into various types of face masks for efficient EBC sampling (**Fig. A-26**) owing to its high mechanical flexibility and stretchability (**Fig. A-28**). It should be noted that placing EBCare above the upper lip when integrated with a face mask effectively mitigates saliva contamination in EBC sampling, as confirmed by saliva amylase tests on collected EBCs (**Fig. A-29**). In cases of transient coughing and long-term coughing, saliva contamination effects on EBC analyte concentration can be eliminated within a few minutes through microfluidic refreshing, as demonstrated in simulations and on-body test results (**Fig. A-30**).

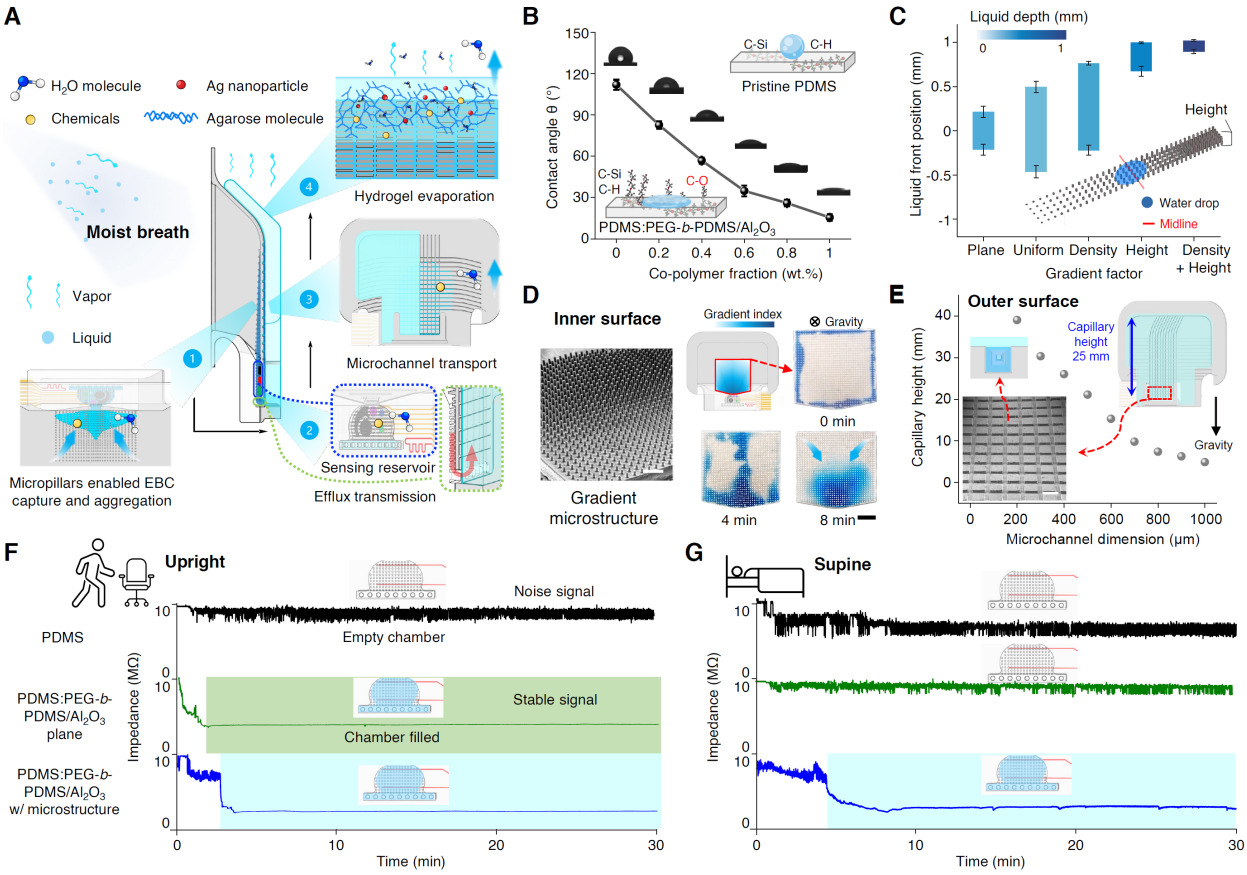

Figure 2-3. Characterization of the microfluidic design of the EBCare device for EBC sampling, transport, and refreshing. (**A**) Schematic of the microfluidic design of the EBCare device for EBC sampling, transport, and refreshing. (**B**) Contact angle of PDMS:PDMS-b-PEG/Al_2O_3 with varied mass fractions of the PDMS-b-PEG copolymer. (**C**)

Comparison of the unidirectional liquid transport capacity of the prewet micropillar array designs with varied gradient factors (density and height). (**D**) SEM image (left) of the micropillar structure at the inner surface of EBCare, and schematic and top-down-view snapshots (right) of liquid transport on the inner surface of EBCare. Gravity perpendicular to surface and inward. Scale bars, 1 mm (left) and 3 mm (right). (**E**) Height of capillary water transport for hydrogel refreshing on the outer surface of EBCare. Insets show microchannel cross-sectional schematic (left top), SEM image (left bottom) and capillary pumping schematic (right top) of the outer surface structure. Scale bar, 1 mm. (**F** and **G**) Impedance between a pair of electrodes in the sensing reservoir obtained using EBCare devices with varied inner surface properties (hydrophilicity, w/ or w/o microstructures) for participants under upright (F) and supine (G) conditions for verifying the presence of EBC in the sensing chamber. All error bars in the figure represent standard deviations of the mean.

2.3 Wireless electrochemical biosensor array for multiplexed EBC analysis

To demonstrate the wearable applications of EBCare, we integrated an electrochemical sensor array into the smart mask for simultaneous and multiplexed in situ EBC analysis. The mechanically flexible and disposable sensor array included amperometric nitrite (NO_2^-) and alcohol sensors, potentiometric ion-selective pH and NH_4^+ sensors, and a resistive temperature sensor (**Fig. 2-4A**). The electrochemical sensor can be mass-produced at low cost via inkjet printing on a flexible substrate such as polyethylene terephthalate (PET). EBC is characterized as a highly diluted solution with low ionic strength with NH_4^+ dominating the EBC cation composition, reflecting its electrical conductivity (**Fig. A-31**) [38]. We have designed our sensors to optimize their performance for EBC analysis. This includes ensuring a linear range that accommodates physiological concentrations and maintaining stability in matrices with low ionic strength (**Figs. A-32**–**A-34**). The target analytes were selected owing to their clinical significance, with alcohol detection facilitated by alcohol oxidase modified Pt-decorated Au electrode, nitrite quantification based on selective oxidation under the applied redox potential (0.75 V) on the inkjet-printed carbon nanoparticle electrode (outperforming commercially available screen-printed and glassy carbon electrodes as

illustrated in **Fig. A-33**), and pH and NH_4^+ sensing based on pH-responsive polyaniline film and NH_4^+-selective membrane modified electrodes, respectively.

Electrochemical characterization of each EBC biosensor in standard solutions containing analyte with physiologically relevant concentrations revealed linear responses between the measured current signals and the target concentrations for alcohol and NO_2^- and between the measured voltage signals and the logarithmic target concentrations for pH and NH_4^+ sensors (**Fig. 2-4B** to **E** and **Fig. A-34**). All biosensors exhibited high selectivity in simulated EBC against potential interference analytes (**Fig. A-35**). While pH and NH_4^+ concentration in EBC provide clinically-relevant information, they can also act synergistically to calibrate the alcohol and nitrite sensors (**Fig. A-36**). Additionally, real-time temperature information from the integrated carbon-based resistive temperature sensor contributes to further sensor calibration during wearable device use (**Fig. A-37**). With these calibration mechanisms, the electrochemical NH_4^+ and NO_2^- sensors demonstrated high accuracy for human EBC analysis, validated against commercial assay kits (**Fig. 2-4F**).

To realize wireless multiplexed wearable EBC analysis, an FPCB was designed for multimodal electrochemical measurements (e.g., voltammetry, potentiometry, and impedimetry), signal processing, and wireless communication (**Fig. 2-4G**, **Figs. A-38** and **A-39**, **table A-4**). Real-time collected analyte information can be transmitted to a user interface via Bluetooth Low Energy (BLE) and displayed on a custom developed mobile app. As EBCare employs a multiplexed circuit for continuous monitoring, the sampling rate can be programmatically adjusted to any desired frequency below 100 Hz. Balancing the data processing load and the time-varying nature of the selected biomarkers, an analysis period of 3.6 seconds was chosen for on-body tests (**Fig. A-40**). EBCare features three operational modes to optimize power consumption: Running Mode, Low Power Mode, and Lower Power Intermittent Mode. These modes adjust the electrochemical measurement and data collection processes, enabling efficient, long-term continuous sensing (**table A-4** and **Fig. A-41**). The fully integrated EBCare accurately and simultaneously monitored dynamic responses of the integrated NO_2^-, alcohol, NH_4^+, pH, and temperature sensors; all biosensors

exhibited high stability during continuous microfluidic sensing and high selectivity to other interferent molecules, showcasing the great promise for in situ wearable EBC analysis (**Fig. 2-4H**). For the integrated EBCare system, the cost of the reusable FPCB is approximately $40, while the disposable sensor patch and microfluidic components each cost around $0.6 (**table A-5**).

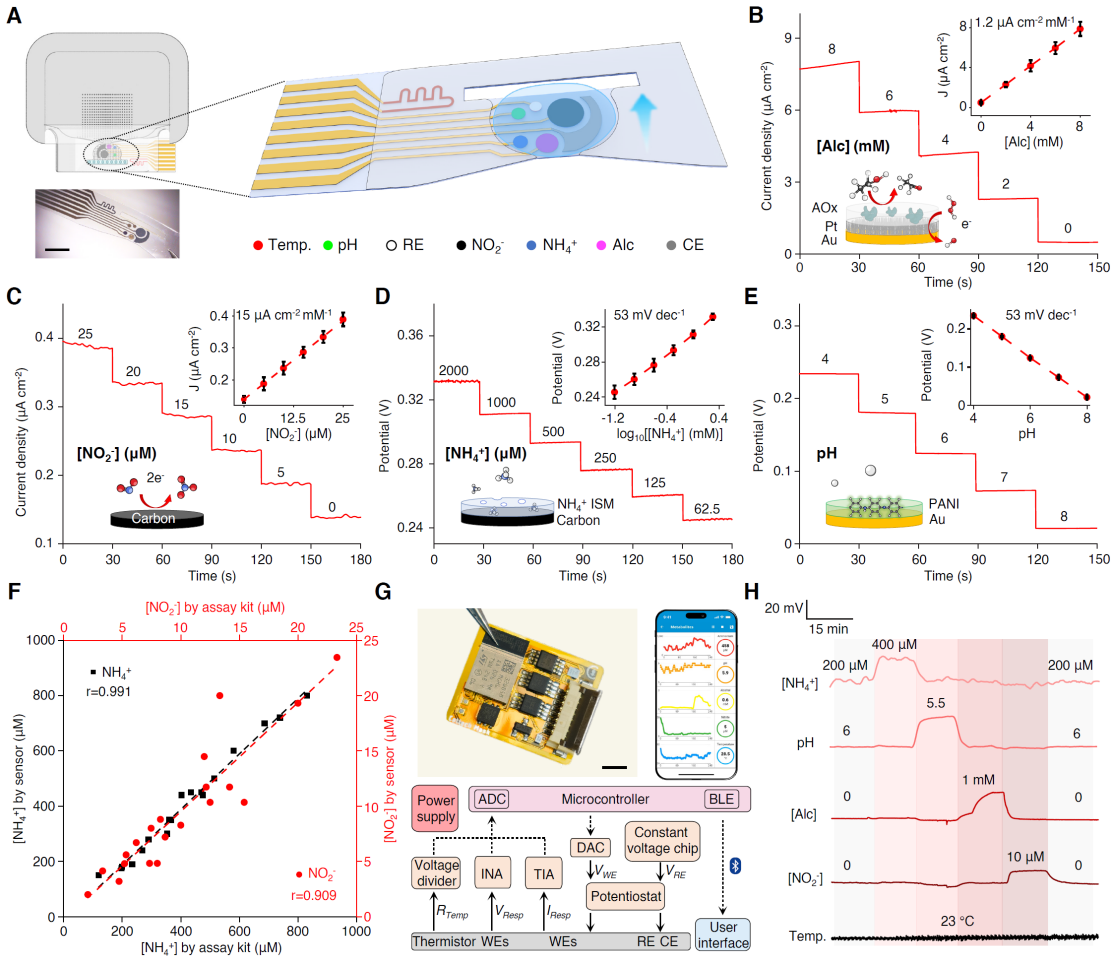

Figure 2-4. Design and characterization of the wireless electrochemical biosensor array for in situ multiplexed EBC analysis. (**A**) Schematic and optical image of an inkjet-printed electrochemical sensing array for simultaneous in situ multiplexed monitoring of EBC NH_4^+, pH, alcohol, NO_2^-, and temperature. RE, reference electrode; CE, counter electrode; Alc, alcohol. Inset, photo of a flexible inkjet-printed electrochemical sensor array. Scale bar, 5 mm. (**B** and **C**) Amperometric responses of an enzymatic alcohol sensor (**B**) and a NO_2^-

sensor (**C**) in artificial EBC (400 μM NH_4HCO_3) containing varied analyte concentrations. Insets: the corresponding calibration plots (right top) and schematic (left bottom) of the alcohol and NO_2^- sensors. J, current density. AOx, alcohol oxidase. (**D** and **E**) Open circuit potential responses of an ion-selective NH_4^+ sensor (**D**) and a polyaniline-based pH sensor (**E**) in standard analyte solutions. Insets: the corresponding calibration plots (right top) and schematic (left bottom) of the NH_4^+ and pH sensors. ISM, ion-selective membrane; PANI, polyaniline. (**F**) Validation of the NH_4^+ and NO_2^- sensors against commercial assay kits for analyzing collected EBC samples from participants (n=15 biological replicates from N=5 healthy participants). (**G**) Image and schematic diagram of the integrated electronic system and mobile app for wireless EBC analysis. ADC, analogue-to-digital converter; BLE, Bluetooth Low Energy; DAC, digital-to-analogue converter; INA, instrumentation amplifier; TIA, trans-impedance amplifier. Scale bar, 3 mm. (**H**) System-level multiplexed interference study of the electrochemical biosensor array in a microfluidic test. All error bars in the figure represent standard deviations of the mean.

2.4 Evaluation of EBCare in healthy and patient participants for personalized medicine

To evaluate EBCare's long-term usability for continuous EBC sampling and analysis in daily-life scenarios, we conducted studied a healthy individual over a time span of 14 hours involving activities such as exercise, dietary and alcohol intakes, office work, and napping (**Fig. 2-5A**). After breakfast, EBC NH_4^+ concentration slightly decreased initially and then increased, and rose more substantially after lunch and dinner, each of which involved a larger amount of protein intake. Associations between changes in EBC pH and NH_4^+ concentration was attributed to the NH_4HCO_3 buffer matrix in the EBC. Additionally, alcohol intake with meals led to rapid elevation of EBC alcohol concentration, consistent with the dynamics of alcohol metabolism. Throughout the day, EBC NO_2^- in the healthy individual remained relatively stable at low levels.

Multiple human studies were performed to demonstrate that the analyte information collected by EBCare from human participants holds potential for a broad spectrum of personalized

healthcare applications (**Fig. 2-5B**). For example, nasal EBC alcohol concentration analyzed using EBCare post consumption exhibited strong correlation with blood alcohol content (BAC) — the gold standard for monitoring alcohol metabolism or assessing drunk driving under the influence (DUI) (**Fig. 2-5C**). Comparing to the standard mouth-blow-based BAC tests, which provide discrete information and is susceptible to contamination from alcohol-containing salivary droplets in the oral cavity, EBCare represents a solution for continuous, accurate, and real-time alcohol metabolism monitoring [39].

Through a series of protein challenge studies in healthy individuals employing in situ real-time analysis with EBCare masks and in vitro analysis with collected human EBC samples, we identified elevated NH_4^+ concentration in EBC, alongside increased serum urea concentration (**Fig. 2-5D** and **Figs. A-42**–**A-44**). Controlled low protein and high protein diets in a healthy individual over a 2-week period resulted in similar dynamic patterns between EBC NH_4^+ and serum urea concentrations (**Fig. A-45**). A linear correlation between the EBC NH_4^+ and serum urea concentration was obtained with a correlation coefficient (r) of 0.846 (**Fig. 2-5E**). These findings suggest that the EBC NH_4^+ is derived from oral saliva urea degradation and has the potential to serve as a noninvasive alternative biomarker for serum urea in renal disease management and personalized protein metabolism monitoring [40, 41].

The clinical utility of the EBCare mask-enabled EBC analysis was evaluated in patients with respiratory diseases such as COPD, asthma, and following infection of COVID-19 (**Fig. 5F**, **Fig. A-46**, **tables A-6–8**). Given the commonality of airway inflammation in respiratory diseases, we first investigated the concentration of EBC NO_2^- using the EBCare mask in individuals categorized by airway inflammation type: healthy control (n = 31), smokers (n = 10), participants newly recovered from COVID (n = 12), patients with COPD (n = 9), and patients with asthma (n = 10); where NO_2^- is a representative marker of reactive nitrogen species [42]. Elevated EBC NO_2^- concentration was observed in groups with airway inflammation, particularly asthma groups ($p < 0.0001$), surpassing those in the healthy control group (**Fig. 2-5F** and **Fig. A-47**), and highlighting the potential for EBC NO_2^- in the

diagnosis, monitoring, and management of patients with respiratory airway inflammation [43, 44]. Our studies including physical experiments (**Fig. A-48**) and patient questionnaires (**table A-9** and **Fig. A-49**) also demonstrated the high breathability and comfort of the EBCare mask, even for patients experiencing breathing difficulties.

To further demonstrate the clinical significance of EBC NO_2^- for asthma and other respiratory disease management, we validated our sensors' results against a clinically well-recognized biomarker — fractional exhaled nitric oxide (FeNO), often referred to as the "inflammometer" [45]. FeNO has demonstrated promise in identifying type II inflammation in asthma and in the management of allergic asthma [46–48], serving as a crucial indicator of lung inflammation levels and the effectiveness of inhaled steroid treatment [47, 49, 50]. Our study revealed a robust correlation coefficient of 0.795 between EBC NO_2^- and FeNO across a cohort of 31 human subjects (**Fig. 2-5G**).

Multiplexed sensor data collected by the EBCare mask from individuals with varying health conditions revealed rich personalized health information at molecular levels (**Fig. 2-5H** to **L**, **Figs. A-50**–**A-52**). Beyond inflammatory conditions reflected by EBC NO_2^-, elevated EBC NH_4^+ in COPD patients potentially indicate a higher serum urea, and a lower EBC pH may be related with airway acidification in asthma patients [2].

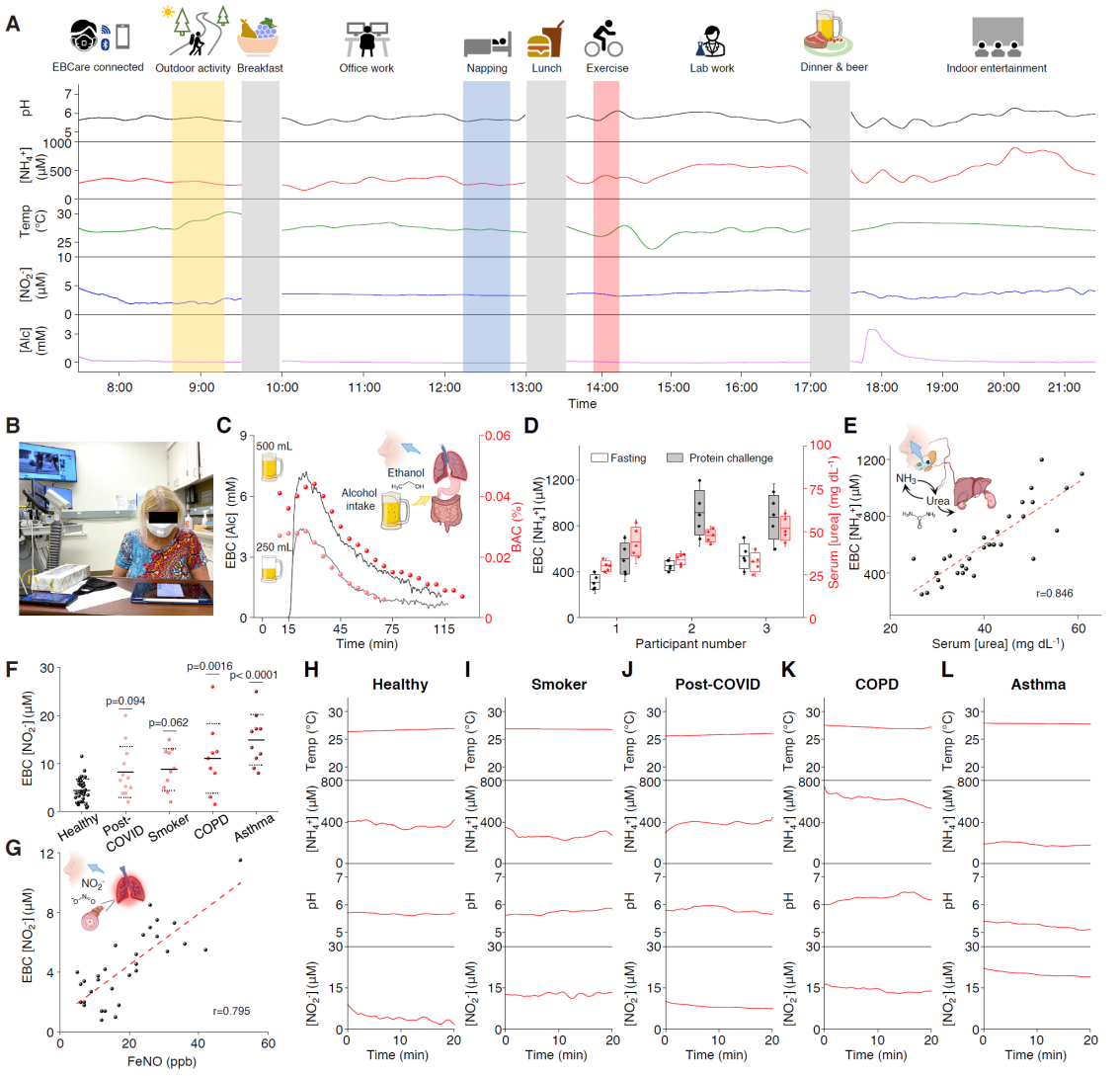

Figure 2-5. On-body evaluation of EBCare for EBC analysis in healthy and patient populations. (**A**) Full-day cross-activity in situ EBC analysis of a healthy participant with EBCare monitoring. (**B**) Photograph of a COPD patient wearing an EBCare mask during a clinical study. (**C**) Breath alcohol concentration monitored by EBCare mask from a healthy participant vs. blood alcohol concentration (BAC) breath test post consumption of alcohol with different doses. (**D**) Evaluation of EBCare during a protein challenge: EBC NH_4^+ and serum urea concentrations (n = 15 biological replicates from N=3 healthy participants) before and after consuming 120 g protein in a day. (**E**) The correlation between EBC NH_4^+ and serum urea concentration (n=35 biological replicates from N=5 healthy participants). (**F**)

EBC NO_2^- concentration in participants with or potential with airway inflammation. (n=72 biological replicates from N=31 healthy controls, N=12 individuals newly recovered from COVID-19, N=10 current smokers, N=9 patients with COPD, and N=10 patients with asthma). Statistical analysis of EBC NO_2^- concentration: one-way ANOVA and Tukey's post-hoc test. (**G**) The correlation between EBC NO_2^- and fractional exhaled nitric oxide (FeNO) (n=31 biological replicates from 31 independent participants). (**H** to **L**) On-body multiplexed EBC analysis with real-time sensor calibrations using the EBCare mask from a healthy participant (H), a current smoker (I), an individual newly recovered from COVID-19 (J), a patient with COPD (K), and asthma (L). All error bars in the figure represent standard deviations of the mean.

2.5 Conclusion

Unlike traditional time-consuming laboratory EBC tests or wearable biosensors analyzing sweat or saliva, EBCare enables continuous collection of intricate molecular information from exhaled breath with high selectivity and temporal resolution. Incorporated seamlessly into everyday face masks, EBCare utilizes a powerless tandem cooling strategy for stable and continuous exhaled breath condensation, a pre-programmed capillary force gradient design ensuring automatic sampling and refreshing of EBC, and a disposable multiplexed electrochemical biosensor array for in situ dynamic monitoring of exhaled breath biomarkers with high accuracy during daily activities. EBCare introduces a dynamic, user-friendly, and real-time detection platform that overcomes complex challenges like saliva contamination, ongoing monitoring, wearable tracking, extended analysis periods, nasal breath condensate collection, and cost-effective surveillance in the traditional clinical EBC field.

Our pilot human trials involving healthy individuals and patients with diagnosed COPD, asthma, or COVID-19 underscore the potential of EBC and EBCare for personalized assessment of metabolic and inflammatory conditions. Moreover, EBCare's adaptability allows for the monitoring of various clinically relevant molecules in the EBC through electrochemical analysis. The significance of EBCare lies in its role as a versatile, convenient,

efficient, real-time research platform and solution in various medical domains, providing a robust and effective tool for this kind of future advancing clinical and medical studies.

Bibliography of Chapter 2

1. C. C. Wang, K. A. Prather, J. Sznitman, J. L. Jimenez, S. S. Lakdawala, Z. Tufekci, L. C. Marr, Airborne transmission of respiratory viruses. *Science* **373**, eabd9149 (2021).

2. I. Horváth, J. Hunt, P. J. Barnes, Exhaled breath condensate: methodological recommendations and unresolved questions. *Eur. Respir. J.* **26**, 523–548 (2005).

3. W. Ibrahim, M. J. Wilde, R. L. Cordell, M. Richardson, D. Salman, R. C. Free, B. Zhao, A. Singapuri, B. Hargadon, E. A. Gaillard, Visualization of exhaled breath metabolites reveals distinct diagnostic signatures for acute cardiorespiratory breathlessness. *Sci. Transl. Med.* **14**, eabl5849 (2022).

4. R. A. Dweik, P. B. Boggs, S. C. Erzurum, C. G. Irvin, M. W. Leigh, J. O. Lundberg, A.-C. Olin, A. L. Plummer, D. R. Taylor, An official ATS clinical practice guideline: Interpretation of exhaled nitric oxide levels (FeNO) for clinical applications. *Am. J. Respir. Crit. Care Med.* **184**, 602–615 (2011).

5. P. J. Barnes, Inflammatory mechanisms in patients with chronic obstructive pulmonary disease. *J. Allergy Clin. Immunol.* **138**, 16–27 (2016).

6. N. H. L. Leung, D. K. W. Chu, E. Y. C. Shiu, K.-H. Chan, J. J. McDevitt, B. J. P. Hau, H.-L. Yen, Y. Li, D. K. M. Ip, J. S. M. Peiris, W.-H. Seto, G. M. Leung, D. K. Milton, B. J. Cowling, Respiratory virus shedding in exhaled breath and efficacy of face masks. *Nat. Med.* **26**, 676–680 (2020).

7. G. Peng, U. Tisch, O. Adams, M. Hakim, N. Shehada, Y. Y. Broza, S. Billan, R. Abdah-Bortnyak, A. Kuten, H. Haick, Diagnosing lung cancer in exhaled breath using gold nanoparticles. *Nat. Nanotechnol.* **4**, 669–673 (2009).

8. S. F. Mosquera-Restrepo, S. Zuberogoïtia, L. Gouxette, E. Layre, M. Gilleron, A. Stella, D. Rengel, O. Burlet-Schiltz, A. C. Caro, L. F. Garcia, C. Segura, C. A. Peláez Jaramillo, M.

Rojas, J. Nigou, A Mycobacterium tuberculosis fingerprint in human breath allows tuberculosis detection. *Nat. Commun.* **13**, 7751 (2022).

9. F. Röck, N. Barsan, U. Weimar, Electronic nose: Current status and future trends. *Chem. Rev.* **108**, 705–725 (2008).

10. U. Yaqoob, M. I. Younis, Chemical gas sensors: Recent developments, challenges, and the potential of machine learning—A review. *Sensors* **21**, 2877 (2021).

11. S. Y. Park, Y. Kim, T. Kim, T. H. Eom, S. Y. Kim, H. W. Jang, Chemoresistive materials for electronic nose: Progress, perspectives, and challenges. *InfoMat* **1**, 289–316 (2019).

12. J. Hunt, Exhaled breath condensate: An evolving tool for noninvasive evaluation of lung disease. *J. Allergy Clin. Immunol.* **110**, 28–34 (2002).

13.
E. M. Konstantinidi, A. S. Lappas, A. S. Tzortzi, P. K. Behrakis, Exhaled breath condensate: Technical and diagnostic aspects. *Sci. World J. 2015*, e435160 (2015).

14. M. Khorshid, S. Bakhshi Sichani, D. L. Barbosa Estrada, W. Neefs, A. Clement, G. Pohlmann, R. Epaud, S. Lanone, P. Wagner, An efficient low-cost device for sampling exhaled breath condensate EBC. *Adv. Sens. Res.* 2400020.

15. X. Chen, X. Hu, X. Zhang, H. Huang, H. Meng, J. Yang, C. Tao, W. Zhang, X. Li, K. Zhang, Breath analysis: Harnessing its potential for non-volatile drug caffeine monitoring in human body. *Microchem. J.* **198**, 110130 (2024).

16. P. Kubáň, F. Foret, Exhaled breath condensate: Determination of non-volatile compounds and their potential for clinical diagnosis and monitoring. A review. *Anal. Chim. Acta* **805**, 1–18 (2013).

17. P. Montuschi, Exhaled breath condensate analysis in patients with COPD. *Clin. Chim. Acta* **356**, 22–34 (2005).

18. N. Hashemzadeh, E. Rahimpour, A. Jouyban, Applications of exhaled breath condensate analysis for drug monitoring and bioequivalence study of inhaled drugs. *J. Pharm. Pharm. Sci.* **25**, 391–401 (2023).

19. W. Gao, S. Emaminejad, H. Y. Y. Nyein, S. Challa, K. Chen, A. Peck, H. M. Fahad, H. Ota, H. Shiraki, D. Kiriya, D.-H. Lien, G. A. Brooks, R. W. Davis, A. Javey, Fully integrated wearable sensor arrays for multiplexed in situ perspiration analysis. *Nature* **529**, 509–514 (2016).

20. H. C. Ates, P. Q. Nguyen, L. Gonzalez-Macia, E. Morales-Narváez, F. Güder, J. J. Collins, C. Dincer, End-to-end design of wearable sensors. *Nat. Rev. Mater.* **7**, 887–907 (2022).

21. J. Kim, A. S. Campbell, B. E.-F. de Ávila, J. Wang, Wearable biosensors for healthcare monitoring. *Nat. Biotechnol.* **37**, 389–406 (2019).

22. H. C. Ates, C. Dincer, Wearable breath analysis. *Nat. Rev. Bioeng.* **1**, 80–82 (2023).

23. A. Yang, L. Cai, R. Zhang, J. Wang, P.-C. Hsu, H. Wang, G. Zhou, J. Xu, Y. Cui, Thermal management in nanofiber-based face mask. *Nano Lett.* 17, 3506–3510 (2017).

24. S. K. Pal, D. Y. Choi, G. Kim, Radiative cooling face mask. *ACS Appl. Polym. Mater.* **5**, 5888–5895 (2023).

25. X. Liu, B. Hu, Mask device as a new wearable sampler for breath analysis: what can we expect in the future? *Anal. Bioanal. Chem.* **415**, 3759–3768 (2023).

26. D. Maier, E. Laubender, A. Basavanna, S. Schumann, F. Güder, G. A. Urban, C. Dincer, Toward continuous monitoring of breath biochemistry: A paper-based wearable sensor for real-time hydrogen peroxide measurement in simulated breath. *ACS Sens.* **4**, 2945–2951 (2019).

27. P. Q. Nguyen, L. R. Soenksen, N. M. Donghia, N. M. Angenent-Mari, H. de Puig, A. Huang, R. Lee, S. Slomovic, T. Galbersanini, G. Lansberry, H. M. Sallum, E. M. Zhao, J. B. Niemi, J. J. Collins, Wearable materials with embedded synthetic biology sensors for biomolecule detection. *Nat. Biotechnol.* **39**, 1366–1374 (2021).

28. C. M. Williams, M. Abdulwhhab, S. S. Birring, E. De Kock, N. J. Garton, E. Townsend, M. Pareek, A. Al-Taie, J. Pan, R. Ganatra, A. C. Stoltz, P. Haldar, M. R. Barer, Exhaled Mycobacterium tuberculosis output and detection of subclinical disease by face-mask sampling: prospective observational studies. *Lancet Infect. Dis.* **20**, 607–617 (2020).

29. H. Li, H. Gong, T. H. Wong, J. Zhou, Y. Wang, L. Lin, Y. Dou, H. Jia, X. Huang, Z. Gao, R. Shi, Y. Huang, Z. Chen, W. Park, J. Y. Li, H. Chu, S. Jia, H. Wu, M. Wu, Y. Liu, D. Li, J. Li, G. Xu, T. Chang, B. Zhang, Y. Gao, J. Su, H. Bai, J. Hu, C. K. Yiu, C. Xu, W. Hu, J. Huang, L. Chang, X. Yu, Wireless, battery-free, multifunctional integrated bioelectronics for respiratory pathogens monitoring and severity evaluation. *Nat. Commun.* **14**, 7539 (2023).

30. Y. Zhai, Y. Ma, S. N. David, D. Zhao, R. Lou, G. Tan, R. Yang, X. Yin, Scalable-manufactured randomized glass-polymer hybrid metamaterial for daytime radiative cooling. *Science* **355**, 1062–1066 (2017).

31. H. Zhang, K. C. S. Ly, X. Liu, Z. Chen, M. Yan, Z. Wu, X. Wang, Y. Zheng, H. Zhou, T. Fan, Biologically inspired flexible photonic films for efficient passive radiative cooling. *Proc. Natl. Acad. Sci.* **117**, 14657–14666 (2020).

32. M. Park, J.-Y. Yoo, T. Yang, Y. H. Jung, A. Vázquez-Guardado, S. Li, J.-H. Kim, J. Shin, W.-Y. Maeng, G. Lee, S. Yoo, H. Luan, J.-T. Kim, H.-S. Shin, M. T. Flavin, H.-J. Yoon, N. Miljkovic, Y. Huang, W. P. King, J. A. Rogers, Skin-integrated systems for power efficient, programmable thermal sensations across large body areas. *Proc. Natl. Acad. Sci.* **120**, e2217828120 (2023).

33. J. Li, X. Wang, D. Liang, N. Xu, B. Zhu, W. Li, P. Yao, Y. Jiang, X. Min, Z. Huang, S. Zhu, S. Fan, J. Zhu, A tandem radiative/evaporative cooler for weather-insensitive and high-performance daytime passive cooling. *Sci. Adv.* **8**, eabq0411 (2022).

34. N. A. Dudukovic, E. J. Fong, H. B. Gemeda, J. R. DeOtte, M. R. Cerón, B. D. Moran, J. T. Davis, S. E. Baker, E. B. Duoss, Cellular fluidics. *Nature* **595**, 58–65 (2021).

35. M. Yao, J. Fang, Hydrophilic PEO-PDMS for microfluidic applications. *J. Micromech. Microeng.* **22**, 025012 (2012).

36. Y. Wang, W. Zhao, M. Han, J. Xu, K. C. Tam, Biomimetic surface engineering for sustainable water harvesting systems. *Nat. Water* **1**, 587–601 (2023).

37. P. P. Rosias, C. M. Robroeks, H. J. Niemarkt, A. D. Kester, J. H. Vernooy, J. Suykerbuyk, J. Teunissen, J. Heynens, H. J. Hendriks, Q. Jobsis, E. Dompeling, Breath condenser coatings affect measurement of biomarkers in exhaled breath condensate. *Eur. Respir. J.* **28**, 1036–1041 (2006).

38. R. M. Effros, R. Casaburi, J. Su, M. Dunning, J. Torday, J. Biller, R. Shaker, The effects of volatile salivary acids and bases on exhaled breath condensate pH. *Am. J. Respir. Crit. Care Med.* **173**, 386–392 (2006).

39. F. Tehrani, H. Teymourian, B. Wuerstle, J. Kavner, R. Patel, A. Furmidge, R. Aghavali, H. Hosseini-Toudeshki, C. Brown, F. Zhang, K. Mahato, Z. Li, A. Barfidokht, L. Yin, P. Warren, N. Huang, Z. Patel, P. P. Mercier, J. Wang, An integrated wearable microneedle array for the continuous monitoring of multiple biomarkers in interstitial fluid. *Nat. Biomed. Eng.* **6**, 1214–1224 (2022).

40. L. R. Narasimhan, W. Goodman, C. K. N. Patel, Correlation of breath ammonia with blood urea nitrogen and creatinine during hemodialysis. *Proc. Natl. Acad. Sci.* **98**, 4617–4621 (2001).

41. W. Chen, M. Metsälä, O. Vaittinen, L. Halonen, The origin of mouth-exhaled ammonia. *J. Breath Res.* **8**, 036003 (2014).

42. J. O. Lundberg, E. Weitzberg, M. T. Gladwin, The nitrate–nitrite–nitric oxide pathway in physiology and therapeutics. *Nat. Rev. Drug Discov.* **7**, 156–167 (2008).

43. W. Formanek, D. Inci, R. P. Lauener, J. H. Wildhaber, U. Frey, G. L. Hall, Elevated nitrite in breath condensates of children with respiratory disease. *Eur. Respir. J.* **19**, 487–491 (2002).

44. V. Rihák, P. Zatloukal, J. Chládková, A. Zimulová, Z. Havlínová, J. Chládek, Nitrite in exhaled breath condensate as a marker of nitrossative stress in the airways of patients with asthma, COPD, and idiopathic pulmonary fibrosis. *J. Clin. Lab. Anal.* **24**, 317–322 (2010).

45. M. W. H. Pijnenburg, J. C. De Jongste, Exhaled nitric oxide in childhood asthma: a review. *Clin. Exp. Allergy* **38**, 246–259 (2008).

46. S. Turner, Exhaled nitric oxide in the diagnosis and management of asthma. *Curr. Opin. Allergy Clin. Immunol.* **8**, 70–76 (2008).

47. S. Karrasch, K. Linde, G. Rücker, H. Sommer, M. Karsch-Völk, J. Kleijnen, R. A. Jörres, A. Schneider, Accuracy of FENO for diagnosing asthma: a systematic review. *Thorax* **72**, 109–116 (2017).

48. N. Murugesan, D. Saxena, A. Dileep, M. Adrish, N. A. Hanania, Update on the role of feno in asthma management. *Diagnostics* **13**, 1428 (2023).

49. FeNO Tests to Monitor FeNO Levels. https://aafa.org/asthma/asthma-diagnosis/lung-function-tests-diagnose-asthma/feno-tests-to-monitor-feno-levels.

50. What Is A FeNO Test? https://www.aaaai.org/tools-for-the-public/conditions-library/asthma/what-is-a-feno-test.

51. X. Yin, R. Yang, G. Tan, S. Fan, Terrestrial radiative cooling: Using the cold universe as a renewable and sustainable energy source. *Science* **370**, 786–791 (2020).

52. J. Kou, Z. Jurado, Z. Chen, S. Fan, A. J. Minnich, Daytime radiative cooling using near-black infrared emitters. *ACS Photonics* **4**, 626–630 (2017).

53. S. Hong, Y. Gu, J. K. Seo, J. Wang, P. Liu, Y. S. Meng, S. Xu, R. Chen, Wearable thermoelectrics for personalized thermoregulation. *Sci. Adv.* **5**, eaaw0536 (2019).

54. Y. Song, R. Y. Tay, J. Li, C. Xu, J. Min, E. Shirzaei Sani, G. Kim, W. Heng, I. Kim, W. Gao, 3D-printed epifluidic electronic skin for machine learning–powered multimodal health surveillance. *Sci. Adv.* **9**, eadi6492 (2023).

55. H. U. Chung, A. Y. Rwei, A. Hourlier-Fargette, S. Xu, K. Lee, E. C. Dunne, Z. Xie, C. Liu, A. Carlini, D. H. Kim, D. Ryu, E. Kulikova, J. Cao, I. C. Odland, K. B. Fields, B. Hopkins, A. Banks, C. Ogle, D. Grande, J. B. Park, J. Kim, M. Irie, H. Jang, J. Lee, Y. Park, J. Kim, H. H. Jo, H. Hahm, R. Avila, Y. Xu, M. Namkoong, J. W. Kwak, E. Suen, M. A. Paulus, R. J. Kim, B. V. Parsons, K. A. Human, S. S. Kim, M. Patel, W. Reuther, H. S. Kim, S. H. Lee, J. D. Leedle, Y. Yun, S. Rigali, T. Son, I. Jung, H. Arafa, V. R. Soundararajan, A. Ollech, A. Shukla, A. Bradley, M. Schau, C. M. Rand, L. E. Marsillio, Z. L. Harris, Y. Huang, A. Hamvas, A. S. Paller, D. E. Weese-Mayer, J. Y. Lee, J. A. Rogers, Skin-interfaced biosensors for advanced wireless physiological monitoring in neonatal and pediatric intensive-care units. *Nat. Med.* **26**, 418–429 (2020).

56. E. Shirzaei Sani, C. Xu, C. Wang, Y. Song, J. Min, J. Tu, S. A. Solomon, J. Li, J. L. Banks, D. G. Armstrong, W. Gao, A stretchable wireless wearable bioelectronic system for multiplexed monitoring and combination treatment of infected chronic wounds. *Sci. Adv.* **9**, eadf7388 (2023).

57. A. Gökaltun, Y. B. Kang, M. L. Yarmush, O. B. Usta, A. Asatekin, Simple surface modification of poly(dimethylsiloxane) via surface segregating smart polymers for biomicrofluidics. *Sci. Rep.* **9**, 7377 (2019).

58. L. H. Kwong, R. Wilson, S. Kumar, Y. S. Crider, Y. R. Sanchez, D. Rempel, A. Pillarisetti, Review of the breathability and filtration efficiency of common household materials for face masks. *ACS Nano* **15**, 5904–5924 (2021).

59. R. S. Hale, R. Ranjan, C. H. Hidrovo, Capillary flow through rectangular micropillar arrays. *Int. J. Heat Mass Transf.* **75**, 710–717 (2014).

60. J. Vaughan, L. Ngamtrakulpanit, T. N. Pajewski, R. Turner, T.-A. Nguyen, A. Smith, P. Urban, S. Hom, B. Gaston, J. Hunt, Exhaled breath condensate pH is a robust and reproducible assay of airway acidity. *Eur. Respir. J.* **22**, 889–894 (2003).

61. J. Hunt, Y. Yu, J. Burns, B. Gaston, L. Ngamtrakulpanit, D. Bunyan, B. K. Walsh, A. Smith, S. Hom, Identification of acid reflux cough using serial assays of exhaled breath condensate pH. *Cough* **2**, 3 (2006).

62. G. E. Carpagnano, S. A. Kharitonov, O. Resta, M. P. Foschino-Barbaro, E. Gramiccioni, P. J. Barnes, 8-Isoprostane, a marker of oxidative stress, is increased in exhaled breath condensate of patients with obstructive sleep apnea after night and is reduced by continuous positive airway pressure therapy. *Chest* **124**, 1386–1392 (2003).

63. G. E. Carpagnano, S. A. Kharitonov, O. Resta, M. P. Foschino-Barbaro, E. Gramiccioni, P. J. Barnes, Increased 8-isoprostane and interleukin-6 in breath condensate of obstructive sleep apnea patients. *Chest* **122**, 1162–1167 (2002).

64. P. Montuschi, S. A. Kharitonov, G. Ciabattoni, P. J. Barnes, Exhaled leukotrienes and prostaglandins in COPD. *Thorax* **58**, 585–588 (2003).

65. C. Cruickshank-Quinn, M. Armstrong, R. Powell, J. Gomez, M. Elie, N. Reisdorph, Determining the presence of asthma-related molecules and salivary contamination in exhaled breath condensate. *Respir. Res.* **18**, 57 (2017).

66. S. De, Q. Khan, D. Sahu, Do we require de-aeration of exhaled breath condensate samples for measuring pH. *Eur. Respir. J.* **56** (2020).

67. P. V. Romero, B. Rodríguez, S. Martínez, R. Cañizares, D. Sepúlveda, F. Manresa, Analysis of oxidative stress in exhaled breath condensate from patients with severe pulmonary infections. *Arch. Bronconeumol. Engl. Ed.* **42**, 113–119 (2006).

68. S. Tate, G. MacGregor, M. Davis, J. A. Innes, A. P. Greening, Airways in cystic fibrosis are acidified: detection by exhaled breath condensate. *Thorax* **57**, 926–929 (2002).

69. J. Daniels, S. Wadekar, K. DeCubellis, G. W. Jackson, A. S. Chiu, Q. Pagneux, H. Saada, I. Engelmann, J. Ogiez, D. Loze-Warot, R. Boukherroub, S. Szunerits, A mask-based diagnostic platform for point-of-care screening of Covid-19. *Biosens. Bioelectron.* **192**, 113486 (2021).

70. Y.-C. Chen, D. O'Hare, Exhaled breath condensate based breath analyser – a disposable hydrogen peroxide sensor and smart analyser. *Analyst* **145**, 3549–3556 (2020).

71. S. Zhang, Y.-C. Chen, A. Riezk, D. Ming, L. Tsvik, L. Sützl, A. Holmes, D. O'Hare, Rapid measurement of lactate in the exhaled breath condensate: biosensor optimization and in-human proof of concept. *ACS Sens.* **7**, 3809–3816 (2022).

72. X. Li, R. Sun, J. Pan, Z. Shi, Z. An, C. Dai, J. Lv, G. Liu, H. Liang, J. Liu, Y. Lu, F. Zhang, Q. Liu, Rapid and on-site wireless immunoassay of respiratory virus aerosols via hydrogel-modulated resonators. *Nat. Commun.* **15**, 4035 (2024).

Appendix A

SUPPLEMENTARY INFORMATION FOR CHAPTER 2

Materials from this chapter appear in Heng, W.; Yin, S.; Min, J.; Wang, C.; Han, H.; Sani, E. S.; Li, J.; Song, Y.; Rossiter, H. B.; Gao, W. A smart mask for exhaled breath condensate harvesting and analysis. Science 385, 954–961 (2024). https://doi.org/10.1126/science.adn6471.

Materials and Methods

Materials

Chloroplatinic acid hydrate, silver nitrate, and iron (III) chloride were purchased from Alfa Aesar. Dimethylformamide (DMF), polyurethane (PU), and potassium chloride were purchased from Fisher Scientific. Sodium thiosulfate pentahydrate, sodium bisulfite, bovine serum albumin (BSA), fluorescein isothiocyanate conjugate (FITC) albumin, aniline, polyvinyl butyral resin BUTVAR B-98 (PVB), polyvinyl chloride (PVC), agarose, formic acid, lactic acid, dextrose (d-glucose) anhydrous, tetrahydrofuran (THF), isopropanol, hydrochloric acid, ethanol, ammonium ionophore I, bis(2-ethylehexyl) sebacate (DOS), ammonium bicarbonate, and sodium nitrite were purchased from Sigma-Aldrich. The polystyrene-block-poly (ethylene butylene)-block-polystyrene (SEBS) (Tuftec™ H1221) was provided by the Asahi Kasei Corporation. Carbon ink (5 wt.%) was purchased from NovaCentrix. Gold ink (10 wt.%) was purchased from C-INK Co. Ltd. SU-8 was purchased from Kayaku Advanced Materials. Polydimethylsiloxane (PDMS) Sylmar 184 and MG-2401 silicone adhesive were purchased from Dow Inc. Silver nanoparticles were purchased from SkySpring Nanomaterials, Inc. Alumina microspheres were purchased from Meiqi Industry Ltd. Polyethylene Terephthalate (PET) was purchased from McMaster-Carr. Polydimethylsiloxane-block-Polyethylene Glycol (PDMS-b-PEG) copolymer was purchased from SPECIFIC POLYMERS Inc. Medical tapes were purchased from Adhesives Research. Glassy carbon electrodes were purchased from CH Instruments. Screen-printed carbon electrodes were purchased from Metrohm. EnzyChrom™ Ammonia/Ammonium assay kit, EnzyChrom™ α-Amylase assay kit and QuantiChrom™ urea assay kit were purchased from BioAssay Systems. Nitrite colorimetric assay kit was purchased from Elabscience Biotechnology Inc. UV sensitive 3D printing resin was purchased from Anycubic.

Methods

Fabrication of the EBCare mask

The fabrication process is shown in **Fig. A-2.** The mold-based method was employed to prepare the condensation layer, microfluidic layer, and sunshield layer of EBCare. Three-dimensional (3D) models were designed using Fusion 360, Autodesk. Subsequently, molds were printed by a Stereolithography (SLA) 3D printer (Mars 3 Pro, Elegoo Inc.). The obtained molds were cleaned with isopropyl alcohol (IPA) and then exposed to a 50 W, 360 nm UV lamp for 8 hours, followed by baking in an oven at 100°C for 24 hours to allow curing of the hybrid polymers within the molds. For parts with fine micropillar structures, the reverse molding process was repeated twice (in the first step, PDMS molds with reverse holes were obtained). The PDMS (10:1 mass ratio of prepolymer to crosslinker), PDMS-b-PEG copolymer, and Al_2O_3 microspheres were mixed in a 50:1:50 mass ratio (Al_2O_3 mass ratio can be optionally decreased for easier curing) to create the liquid hybrid polymeric metamaterial (PDMS:PDMS-b-PEG/Al_2O_3). The resulting mixture was then poured into molds, whose surfaces were pre-treated with a release agent (Ease Release 200, Mann Release Technologies) to facilitate the subsequent removal of the cured samples. Vacuum was then applied to extract the gas inside. These parts were then cured in an oven at 130°C for 3 hours before being demolded.

The process for preparing the cooling hydrogel was as follows: Initially, agarose and Ag nanoparticles were added to deionized (DI) water in proportions of 1 wt.% and 0.4 wt.%, respectively. The mixture was then stirred on a 220°C hot plate until it became homogeneous. To ensure uniform dispersion, the solution underwent a 5-minute ultrasonic bath. Subsequently, the solution was poured into 3D-printed molds and went through room temperature gelation. Finally, the hydrogel was taken out and stored in DI water.

The biosensor layer (the detailed fabrication steps are shown in the Biosensor preparation (ii) Biosensor Preparation section), the condensation layer, the microfluidic layer, and the sunshield layer were integrated together using silicone adhesive. Subsequently, cooling hydrogel was incorporated to complete the assembly of the EBCare device.

In the EBCare mask assembly procedure, a mounting hole was precisely cut into the mask (Respirator 9205+, 3M) using a laser cutter (Universal Laser System). The flexible printed

circuit board (FPCB) and battery (LIR 640) were then installed within the interlayers of the mask. Using laser-cut medical tape, the edges of EBCare were sealed to the mounting hole in the mask, followed by connecting the FPCB with the biosensor interface.

Cooling strategy and characterization

(i) Optical and compositional characterization

The ultraviolet -visible (UV-vis) reflectance (0.25–1.8 μm) of the materials was measured using a spectrophotometer (Cary 5000, Agilent) with an integrating sphere. For assessment of emissivity (1-reflectivity) in the wavelength range of 5–25 μm, a Fourier transform infrared spectrometer (FTIR; iS50, Thermo-Nicolet) equipped with a diffuse reflectance accessory was employed (**Fig. 2-2C** and **Fig. A-9**) [51, 52]. A scanning electron microscope (ZEISS 1550VP Field Emission SEM - Oxford EDS) was used to characterize the morphology and structure of the polymeric metamaterial, while elemental maps were obtained by energy dispersive spectroscopy (EDS) (**Fig. A-4**).

(ii) Thermal conductivity characterization

The experimental setup for measuring thermal conductivity is shown in **Fig. A-5A**. A Polyimide (PI) flexible thermocouple (FTC Thin-Film, FluxTeq) was employed for measuring the temperature on the heating side, while a dual temperature and heat flux sensor (PHFS-01, FluxTeq) was utilized for measuring the temperature and heat flux on the sink side. The hydrogel was used to ensure a stable thermal interface. In the experiment, heating flux (Q) and the temperature difference on the material surface was measured ($\Delta T = T_h - T_c$, where T_h was the hot side temperature and T_c was the cold side temperature) to quantify the thermal conductivity of the hybrid polymer [53]. The thermal conductivity (k_p) was then calculated using:

$$k_p = \frac{H}{A}\frac{Q}{\Delta T} \quad (1)$$

where A was the sample surface area. H was the sample thickness. The result is plotted in **Fig. A-5B**.

(iii) Cooling performance experimental setup

To assess the performance of different cooling strategies under various environments, a cooling temperature measurement setup was established (**Fig. A-11A**). The platform included places for sample loading, a thermocouple for surface temperature measuring, a heat-conductive copper plate for uniform thermal conduction, and a Kapton heater to provide a 280-mW heating (simulating the heat exchange power between human breath and the EBCare device, as detailed in **Theoretical analysis in the EBCare - Thermal analysis** section in Supplementary Text). The 280-mW heating was applied to all thermal-related evaluations as the simulated breath heat exchange to the device in the project. These layers were sequentially mounted on polystyrene insulation foam covered with aluminum foil, to minimize conduction and radiative heat exchange between the platform and surroundings. During experiments, the thermocouple and heater were logged and controlled in real time by a data acquisition system (DAQ, COMPAQ DAQ, FluxTeq) and an external power supply (2231A-30-3, KEITHLEY), respectively.

(iv) Hydrogel cooling characterization

To establish the hydrogel cooling test platform, based on the temperature measuring setup described in (iii) Cooling performance experimental setup section, a hydrogel cooling module was placed in sample loading area. consisting of a hydrogel (2-mm thickness, ~5 cm^2 surface area) situated on a metamaterial layer (EBCare framework, measuring 2.5 cm by 3 cm, with a thickness of 0.5 mm) featuring microfluidic channels (**Fig. A-7A**).

Cooling performance and evaporation rates of hydrogels in various environments were tested in a digitally controlled temperature and humidity chamber (SM-16C, Thermotron) (**Fig. 2-2D** and **Fig. A-7B**). The temperature difference (ΔT) representing cooling performance was

defined as surface temperature without hydrogel (control group) minus the surface temperature with hydrogel. The mass of the hydrogel was measured periodically (at 20-minute intervals). And the evaporation rate was obtained by mass difference divided by the surface area of hydrogel.

To validate the effectiveness of exhaled breath condensate (EBC) replenishment on sustained hydrogel cooling (**Fig. A-8**), a simulated EBC (sEBC, 400 μM NH_4HCO_3) replenishment was added to the microfluidic channels under the hydrogel at a rate of 5 μL min^{-1} via a syringe pump (AL-6000, WPI). Control groups were established, including a group without hydrogel and a group with hydrogel but without sEBC replenishment. Surface temperatures were recorded by the thermocouples to illustrate the continuous cooling performance.

In the hydrogel absorption experiment (**Fig. A-7C**), a piece of hydrogel with 50% of its saturation mass was put on the module to demonstrate that the absorption was faster than evaporation under enough sEBC replenishment. Thus, the sEBC replenishment rate was set at 10 μL min^{-1}. The mass of the hydrogel over the next 15 hours was recorded.

In the context of interfacial heat conduction (**Fig. A-7**), the absence of sEBC supplementation indicated that the heat transfer mediator at the framework-hydrogel interface included some air gaps. In contrast, the EBC replenishment function designed in EBCare promoted the presence of EBC as a liquid thermal mediator in this space. To replicate the heat conduction conditions of the EBCare system, the microchannels in the metamaterial layer were filled with sEBC liquid. The control group, in contrast, consisted of a plain surface without any liquid. Subsequently, pieces of semi-dry hydrogels (50% of their saturation mass) were placed on these modules, and surface temperatures were recorded after achieving thermal stability.

(v) Tandem cooling strategies evaluation

In the direct temperature evaluations of different cooling strategies under indoor and outdoor conditions (**Fig. 2-2E** and **Fig. A-11C**), the EBCare group had a three tandem cooling layers

(radiative cooling framework, hydrogel layer, sunshield layer) and was fixed to the position of the sample loading place in the experimental setup (**Fig. A-11A**). For comparison, thermal measurements were also performed for three other cooling setups: a.) metamaterial-based framework + N95 mask layers (polypropylene) representing w/o radiative & hydrogel cooling; b.) metamaterial-based framework representing radiative cooling & w/o hydrogel cooling; c. metamaterial-based framework & hydrogel layer representing hydrogel cooling & w/o sunshielding. The indoor environment was at ambient temperature of ~23°C, relative humidity of ~50% and wind speed of ~0.5 m s^{-1}. While in outdoor settings, ambient temperature and humidity were monitored by a temperature and humidity logger (GSP-8, Elitech), and wind speed was monitored by an anemometer (405i, Testo) in real time and multiple directions. Solar power was recorded from the Caltech TCCON weather station (http://tccon-weather.caltech.edu/index.php). These experiments were conducted on roofs in the Caltech campus, Pasadena, CA. 34.15° N 118.14° W at different weather condations, times of the day (**Fig. A-11B**, and **table A-3**).

(vi) On-body evaluation of cooling strategies

For the evaluation of the cooling performance of EBCare in indoor environments using infrared imaging, a healthy participant was instructed to wear no mask, as well as to wear different masks (N95, EBCare framework on N95, and EBCare on N95) in chronological order. It's worth mentioning that the sunshield layer was not added to the EBCare device to better display the cooling surface temperature. An infrared thermal camera (T540, FLIR) was used to capture the infrared images and videos (**Fig. A-10A** to **D**).

In the experiments investigating EBC collection rates under different cooling strategies, surface properties, participants, and mask types (**Fig. 2-2F**, **Figs. A-17** and **A-26**), the efflux hole in EBCare was blocked by PDMS for EBC collection purpose. Participants were informed to performed nasal breathing in an upright posture under various specified surroundings. At 20-minute intervals during the experiments, the accumulated EBC fluid in the EBCare device was aspirated using a pipette for volume measurements. Note that all experiments were completed by the same healthy participant except for the collection rate

study experiments for different participants (**Fig. A-26**). **Table A-3** shows ambient information (temperatures of 16–33°C, relative humidity of 30–85%, and solar irradiance ranging from 0 to 800 W/m²) and EBC harvesting rates for outdoor tests of the EBCare group. EBC was collected for 20 minutes under different external environmental conditions, and subsequently, EBC was collected over the following 20 minutes in an indoor environment (23°C and 50% RH). The NH_4^+ and NO_2^- concentrations in the EBC samples from both settings were analyzed, and the results are depicted in **Fig. A-12.**

To assess the functionality of the EBC replenishing structure on-body for sustained condensation (**Fig. A-8A**) and hydrogel lifetime extension (**Fig. A-8B** and **Fig. 2-2G**), a healthy participant was required to wear an EBCare mask, while the control group was the same individual wearing a mask with the EBC refreshing structure blocked. Throughout the tests, these masks were weighed at 20-minute intervals to measure the change in hydrogel mass (accumulated EBC in the control group was aspirated). Notably, 1.) 50% of the saturation mass of the hydrogel was considered as the hydrogel failure criterion. 2.) In three of the five EBCare hydrogel lifetime experiments, the mass of the EBCare hydrogel remained above 50% at the end of a single day. Therefore, the hydrogel lifespan of the EBCare hydrogel in these three days was defined as the full length of the experiment. 3.) During mealtimes, a corresponding volume (5 μL min^{-1} times duration) of DI water was added to the EBCare device to make up for missing EBC replenishment. 4.) The experimental conditions in **Fig. A-8B** were indoor environments, and those in **Fig. 2-2G** involved indoor and outdoor environments.

Microfluidics design and characterization

(i) Materials characterization

X-ray photoelectron spectroscopy (XPS) characterizations were carried out on a high-resolution Kratos AXIS 165 X-ray photoelectron spectrometer (**Fig. A-14**). A scanning electron microscope (Sirion XL-30 SEM, Phillips) and a digital optical microscope (AD246-

M, Andonstar) were used to characterize the microstructures of EBCare (**Fig. 2-3D**, **E** and **Fig. A-3C** to **E**).

(ii) Water contact angle

The contact angles on surfaces of different materials were measured using a goniometer (Ramey-Hart) (**Fig. A-15**). In the hydrophilicity stability experiment (**Fig. A-16**), the control group PDMS sample underwent a 10-minute treatment with O_2 plasma (20-30 cm^3 min^{-1} O_2, 100 W, 150 to 200 mTorr, PE-25, Plasma Etch). Additionally, a 20-minute breathing experiment was conducted, where material samples were placed in a mask, and the participant breathed for 20 minutes. Following this, the samples were allowed to dry at room temperature before measurement. All materials were stored in Petri dishes at indoor environment for subsequent measurements.

(iii) Unidirectional liquid transport

To investigate the effect of different gradient factors on the unidirectional liquid transfer function (**Fig. 2-3C**, **Fig. A-19**), five gradient structures based on hydrophilic hybrid polymer (PDMS:PDMS-b-PEG/Al_2O_3) were designed for comparative testing: planar, uniform, height gradient, density gradient, and height + density gradient micropillars. Subsequently, experiments involving both dry and prewet interfaces were conducted. For the dry interface, 7 μL of water was dropped in the start line (middle of micropillar array). After 5 minutes, the liquid position was recorded. The prewet interface initially underwent static immersion in the water. Thereafter, the floating water on the surface was absorbed by paper tissue, and 1 μL of water was subsequently dropped in the start line. After 2 seconds, the liquid position was recorded. The cross-sections (**Fig. A-19D** and **F**) for this experiment were taken with the high-speed goniometer camera. As for the parameters of these arrays, each array had a total of 5 columns and about 40 rows of micropillars, whose diameters of the micropillars were all 200 μm. In the case of the uniform micropillars, the height was 500 μm, and they were spaced 400 μm apart. In the height-gradient arrays, the tallest pillars measured 1000 μm, the lowest pillars were 0 μm, and their height was arranged isometrically with a spacing

of 400 μm. The height of the micropillars in the graded-density array was 500 μm, with the densest pillars had a spacing of 200 μm, which increased by 10 μm for every other pillar until reaching a spacing of 550 μm. The morphology of the height + density-gradient arrays was a superimposition of the aforementioned height and density factors.

(iv) Microfluidic design in EBCare

The design of the EBCare microstructure can be divided into three parts (inner, reservoir, and outer structures in **Fig. A-20**). The overall design principle was that the capillary pressure of EBC liquid in these microstructures should be reservoir > outer surface > inner surface. Inner surface had a graded micropillars array for gravity-independent self-aggerating of EBC liquid to biosensing reservoir. In the first part, the microstructure of EBCare's inner surface was a micropillar array with a height + density composite gradient. The diameter of micropillars was the minimum feature size of the 3D printer, i.e., 200 μm. The graded density distribution of the micropillars was achieved using a two-dimensional (2D) circular array designed with AutoCAD. The density was the highest at the origin point in **Fig. A-20A** (a 200 μm spacing of the micropillars and a density of 625 pillars cm^{-2}). Subsequently, the spacing of the pillars increased by 20 μm per pillar along the x- and y-axis until reaching the edge of the internal interface (1.5 cm × 1.8 cm), thus the density of the micropillars decreased progressively. After importing the 2D array into Fusion 360, it was extruded to form a 3D micropillar array with a height of 800 μm. To create the height gradient, three planes (A, A', and B) were generated by positioning at 200 μm along the z-axis on the sides (left, right, and top) and 800 μm at the origin, respectively (**Fig. A-20D**). The 3D pillars above these planes were then deleted. Through these operations, an array of EBCare micropillars with both height and density gradients was formed on the inner surface. The second part was the micropillar and efflux structure inside the biosensing reservoir. The pillars' density inside was the highest (625 pillars cm^{-2}), with a height of 500 μm. The distance from the bottom biosensor to the top of the pillars was 200 μm. The efflux pillars for internal and external flow connection had the same spacing of 200 μm from the pillars inside the chamber. The height of these efflux pillars was designed to contact with the hydrogel. The third section

consisted of external microchannels with a spacing of 800 μm. The cross-sections of these channels were open squares with sides measuring 200 μm, and a piece of cooling hydrogel were attached at the top of these channels (**Fig. 2-3E** and **Fig. A-20C**).

In the condensation experiment for EBCare inner surface structural design (**Fig. 2-3D**, **Fig. A-21B**), Blue ink was drop casted along the edges of EBCare inner surface and left to dry, allowing for the visualization of the condensed liquid. Subsequently, EBCare inner surface and a plane surface (control group) were positioned on a Peltier cooling device (CP-031, TE Technologies) equipped with a feedback temperature control circuit to maintain the surface temperature at 27°C. The assembly was then placed inside a constant temperature and humidity chamber with a relative humidity of 90% and a temperature of 37°C inside. The distribution of liquid condensation and transport on these surfaces were recorded for 10 minutes.

(v) Capillary height

To replicate the microstructure of the outside of EBCare, a thin sheet of EBCare framework material with microchannels was used in capillary height experiment. The back flat side of this sheet was adhered to a glass sheet (to act as a support) and the surface with microchannels was laminated to a cooling agarose hydrogel. Followed by this, the bottom of assembly was immersed in a sink containing blue inked water until the microfluidic channels were in contact with the liquid surface. When the liquid level in microchannels reached a steady state, the capillary height (h) was recorded (**Fig. 2-3E**).

(vi) In vitro flow test

The EBCare device and the longitudinal half of EBCare (for better observing the flow of liquid inside EBCare) were placed in the direction parallel and perpendicular to gravity, respectively. Simultaneously, the sunshield layer was removed and a transparent hydrogel without Ag nanoparticles served as the cooling hydrogel. These steps were taken to enhance

the visibility of sEBC flow. Then, blue ink was dropped on the inner surface of EBCare as the sEBC, and the flow of sEBC was observed. The results are displayed in **Figs. A-22**.

(vii) On-body evaluation of microfluidics

Regarding the on-body test to validate the performance of EBCare microfluidics using electrical impedance method (**Fig. 2-3F** and **G**), a pair of gold electrodes with 3 mm spacing were installed into the sensing reservoir of the EBCare device (control groups: one made of PDMS, and the other without microstructures inside). These electrodes were connected to the temperature sensing ports on the EBCare's FPCB, which contained a voltage divide module for real-time measurement of direct current (DC) impedance between two ports. This DC impedance reflected the presence or absence of a stable and sufficient volume of EBC fluid in the reservoir to assess the EBC harvesting ability. Subsequently, a healthy participant was instructed to wear the impedance measuring mask and required to sit or lie down with upright and supine postures, and in each case, the EBC flow in EBCare was either parallel or perpendicular to gravity. Impedance was continuously recorded for half an hour. The duration from the commencement of the experiment until the attainment of a stable impedance signal was recorded multiple times for the EBCare group to obtain the startup time of EBCare (**Fig. A-25**). In the experimental assessment of potential saliva contamination and microfluidics refreshing, a post-covid participant was instructed to engage in two distinct coughing activities. The first, classified as a transient cough, required the subject to cough for a duration of 10 seconds. The second activity involved a more prolonged exposure, where subjects were asked to cough continuously for 1 minute, interspersed with deep breaths, to simulate a scenario of potential saliva contamination. The results of these trials were recorded by biosensors (**Fig. A-30**).

In visual observation of EBC flowing in the EBCare system while on-body tests (**Fig. A-24**), blue ink was applied along the top part of the inner surface of the EBCare device and then left to dry. Simultaneously, the sunshield layer was removed and a transparent hydrogel without Ag nanoparticles served as the cooling hydrogel. These steps were taken to enhance the visibility of EBC. Subsequently, the participant was instructed to wear the EBCare mask

and sit upright or lie down supine as aforementioned. The liquid distribution on the backside of EBCare was observed and recorded over the next hour.

Biosensor preparation and characterization

(i) Inkjet-printed electrodes preparation

The fabrication procedures of the inkjet-printed sensor patch are illustrated in **Fig. A-2**. Initially, the PET substrate was washed with IPA and then dried with compressed air flow. The multimodal sensor patch was fabricated via a serial printing of gold (reference, counter electrodes, pH, and alcohol sensors), carbon (NH_4^+, NO_2^-, and temperature sensors) and SU-8 (encapsulation) layers using an inkjet printer (DMP-2850, Fujifilm). The printer plate temperature was set to 40°C when printing gold layer, to ensure the rapid ink solvent vaporization during printing. Subsequently, the printed electrodes array was placed in an oven at a temperature of 120°C for 2-hour sintering of the biosensors pattern. Finally, the separation of sensors and efflux holes were patterned using a laser cutter.

(ii) Biosensors preparation

The Ag/AgCl reference electrode was fabricated by electrodeposition of Ag on the Au electrode in a solution containing silver nitrate, sodium thiosulfate and sodium bisulfite (250 mM, 750 mM, and 500 mM, respectively). Electrodeposition was carried out using a multi-current step protocol (30 s at −1 μA, 30 s at −5 μA, 30 s at −10 μA, 30 s at −50 μA, 30 s at −0.1 mA, and 30 s at −0.2 mA), followed by drop-casting a 10 μL aliquot of 0.1 M iron (III) chloride for 1 minute for chlorination. To prepare the reference electrode membrane, a reference solution was prepared by dissolving 79.1 mg PVB and 50 mg of fine NaCl particles into 1 ml methanol. Subsequently, 1.5 μL PVB reference cocktail with fine NaCl particles inside was drop casted on the 1 mm diameter Ag/AgCl surface, followed by drop-casting of 0.5 μL of PDMS as an encapsulation. In the end, the electrode was left to cure at 40°C overnight. Optional punching of small holes on the PDMS layer for faster hydration of the reference electrode. To investigate the performance of reference electrodes in EBC, a

commonly used solid-state reference electrode was also prepared following a previously reported approach [19].

The pH sensing electrode was prepared by electrodeposition of polyaniline (PANI) pH sensing membrane on the inkjet-printed Au electrode by cyclic voltammetry between −0.2 V and 1.0 V at a scan rate of 50 mV s^{-1} for 20 cycles.

In the preparation of the NH_4^+ sensor, the NH_4^+ selective cocktail solution was prepared by dissolving 1 mg of Ammonium ionophore I, 30 mg of PVC, 30 mg of SEBS, and 65 mg of DOS in 2 mL of THF by sonication bath. Subsequently, 0.8 µL of the NH_4^+ selective cocktail was drop-cast onto a 1 mm diameter carbon electrode to achieve complete coverage. The coated electrode was then left to dry overnight.

For alcohol sensor fabrication, a transducer layer of Pt nanoparticles (PtNPs) on the Au electrode was firstly electrodeposited by applying a constant voltage of -0.1 V in an aqueous solution containing 5 mM H_2PtCl_6 and 1.5 mM formic acid for 30 seconds. Subsequently, an Alcohol Oxidase (AOx) cocktail was prepared as follows: 1 wt.% chitosan was dissolved in 0.1 M acetic acid, and 10 mg mL^{-1} of Bovine Serum Albumin (BSA) was dissolved in Phosphate-Buffered Saline (PBS). The chitosan and BSA solution were mixed thoroughly with AOx at a volume ratio of 1:1:8. Thereafter, 0.5 µL AOx cocktail was drop-casted onto the electrode surface and dried overnight to form an enzymatic layer. Finally, an encapsulation membrane was further drop-casted by applying 0.5 µL polymeric solution, which was THF solution containing 2 wt.% DMF and 3 wt.% PU [54].

(iii) Sensor characterizations

An electrochemical workstation (CHI 660E, CH Instruments, USA) was employed for electrodepositing, characterization (sensitivity, selectivity, stability, saturation, and calibration), and in vitro tests of biosensors (**Fig. 2-4B** to **F**, **Figs. A-32** to **A-37**). The potential of the reference electrode was measured against a commercial Ag/AgCl electrode in the collected EBC. All amperometric sensor characterizations were conducted in solutions

of sEBC buffer containing target analytes. The sEBC buffer solution comprised a 400 μM NH_4HCO_3 solution with a pH of 6, which was precisely adjusted using HCl/NaOH. A constant voltage of 0.75V and 0.4 V was applied between the working electrodes and the reference electrode for detection of NO_2^- and alcohol, respectively. The pH sensor calibration and selectivity tests were performed in McIlvaine buffer solutions. The NH_4^+ sensor calibration and selectivity tests were performed in NH_4HCO_3 solution with different concentrations. Temperature influence and thermistor characterization were carried out on a ceramic hot plate (Cimarec+, Thermo Fisher).

In the experiment to determine the required solution volume for electrochemical sensor operation, simulated EBC solution was dispensed onto the surface of standalone sensors and sensors integrated within microfluidic channels. The solution was added in 1 μL increments, and the dispensed volume was recorded until all multiplexed sensors achieved a stable signal response, as shown in **Fig. A-27**. Considering the lower surface tension of EBC samples, it is anticipated that a smaller volume would likely suffice under actual operating conditions.

Electronic system design and characterization

The EBCare circuit can be broadly categorized into three functional parts: power and sensor ports, data processing and wireless communication, and electrochemical instrumentation (**Figs. A-38**, **A-39** and **table A-4**). To power the circuit, a LIR 640 lithium polymer coin battery (3.7 V) was electrically connected to the PCB board via magnets (*55*). The battery voltage was regulated to a stable 3.3 V through a voltage regulator (LD39050PU33R). The analog power supply part was managed by a load switch (TPS22916). Data processing and wireless communication were executed by a compact wireless module (STM32WB5MMG, STMicroelectronics) featuring an integrated Microcontroller Unit (MCU) and Bluetooth Low Energy (BLE) radio. The module was programmed using the ST-link/v2 in-circuit debugger. The reference potential of the reference electrode was upheld by a constant voltage chip (ISL60002BIH310Z-TK). For open-circuit potential (OCPT) measurements, the voltage between the working and reference electrodes was amplified through Instrumentation Amplifiers (INA, INA333) and then read by the MCU's Analog-to-Digital

Converter (ADC) peripheral. In amperometric scans, the MCU controlled the DAC8552 digital-to-analog (DAC) converters through the Serial Peripheral Interface (SPI) protocol, outputting a constant working potential for the working electrodes. The current through the working electrodes was amplified by the trans-impedance amplifier (TIA) module and converted to a voltage, which was then read by the MCU's ADC peripheral. The MCU could also measure the resistance of the temperature sensor using a voltage divider circuit and the built-in ADC. The acquired multimodal data was wirelessly transmitted via BLE to the user's mobile device and further calibrated and analyzed by custom-developed software. Since the output of the electronic system was a series of potentials, the wirelessly acquired raw signals are plotted in mV in **Fig. 2-4H**. The sampling frequency can be programmed according to the requirements of application scenarios (see **Fig. A-40**). The coin battery can be charged through USB charger (Micro LiPo charger_V2, Adafruit) with customed magnets ports. The electrical connection between the battery and circuitry with magnets was obtained by applying conductive silver adhesive. In order to obtain a stable mechanical connection, UV resin was further applied and cured.

In the power consumption experiments, the power supply current was recorded using a Power Profiler (Power Profiler Kit II, Nordic) at 1 ms sampling rate. Three power supply strategies were implemented and evaluated: 1) Running mode: Functional module (electrochemical frontend) and the MCU were continuously running. 2) Low power mode: Functional modules were running, with the MCU running only during BLE/ADC events and idling otherwise. **Fig. A-41** illustrates the power consumption profile in this mode over a 1.5 second BLE connection interval and 1 second reading interval. 3) Low power intermittent mode, where during the active intervals the system operated as in low power mode, while during the idle intervals the MCU slept, analog switch was turned off, and electrochemical modules were shut down until the sleep timer expired. **Fig. A-41** depicts an example of this mode's power consumption profile over a 2-minute interval. The battery life was calculated through average current and experimentally verified for each mode.

<u>Evaluations of the EBCare mask</u>

For on-body evaluations of the smart mask, the FPCB of EBCare conducted multiplexed measurements of NH_4^+, pH, NO_2^-, alcohol, and temperature at intervals of 3.6 seconds. Simultaneously, the acquired data was wirelessly transmitted to the phone via BLE, enabling continuous real-time monitoring.

During in vitro testing of the EBCare mask, the microfluidic structure for effluxion within EBCare was intentionally obstructed to facilitate a collection function. The EBC liquid that accumulated were extracted from the EBCare device at set intervals as in vitro EBC samples (the initial samples were discarded to obtain stable condensed EBC samples). All in vitro analysts in EBC samples were promptly measured by using electrochemical biosensors within one hour or, if not, stored in a refrigerator at 4°C and measured within one day. Admittance measurement involved using a pair of gold electrodes with a spacing of 3 mm in the impedance-time mode of CHI to measure the admittance of the collected EBC (**Fig. A-31**).

Throughout the entire (in situ or in vitro) EBC related experiments, except for essential matters, participants were instructed to exclusively breathed through their noses, and the upper lip was placed close to the lower edge of the device to prevent potential saliva contamination (see **Fig. A-29A**).

For the collection of serum samples, 100 μL fresh blood was acquired using the finger-prick method. After the standard coagulation procedures, serum was isolated through centrifugation at 1500 relative centrifugal force (rcf) for a duration of 15 minutes. All serum samples for urea concentrations were tested within 3 hours after sampling. The measurements of serum urea were performed using a urea assay kit (QuantiChrom, bioassay).

(i) Participant recruitment

The validation and evaluation of the smart mask were conducted in accordance with ethical regulations under approved protocols (IR22-1278 and IR19-0892) by the institutional review board at the California Institute of Technology. Participants, aged 18 years and above, were

recruited from the California Institute of Technology campus and neighboring communities through advertising as healthy, smokers, and post-COVID-19 groups. All participants provided written informed consent prior to study participation. Smokers were recruited on the condition of >5 cigarettes-day. Participants for the evaluation of the clinical airway inflammation monitoring, including COPD and asthma, monitoring were recruited at The Lundquist Institute/Harbor–University of California, Los Angeles (UCLA) Medical Center with the protocol approved by the IRB at the Lundquist Institute (number 32051-01). The detailed information of participants is recorded in **tables A-6** to **A-8**.

(ii) Salivary amylase activity

To detect salivary amylase activity in EBC samples, five participants were enlisted to perform nasal and oral breathing tests. Each participant donned the EBCare mask, positioning it such that the upper lip was below the bottom edge of the device. They were then instructed to breathe first through their nose for 15 minutes, and then through their mouth for 15 minutes. EBC samples were collected immediately following each breathing session. For comparison, saliva from a healthy participant was collected as a reference standard and was diluted to various concentrations. All samples underwent analysis using the EnzyChrom™ α-Amylase Assay Kit, with results presented in **Fig. A-29**.

(iii) Daily activities

In the full-day EBCare evaluation study (**Fig. 2-5A**), participants engaged in various activities spanning from 7:30 a.m. to 9:30 p.m. Throughout the day, except for three thirty-minute eating periods, the individual wore the EBCare mask. The experiment started at 7:30 a.m. After wearing the EBCare mask and connecting it to the smartphone app, the individual engaged in outdoor activities (temperature ~28°C, humidity ~30%RH) for around 1 hour under solar radiation (~600 W m^{-2}). At 9:30 a.m., the individual consumed a light breakfast with 10 grams of protein. Subsequent seated office work and a one-hour-long lying-down nap provided the individual with a work-rest balance. At 1 p.m., the individual consumed a lunch containing 60 grams of protein. Indoor cycling was performed after lunch within half

an hour to promote metabolism. Between 2:30 p.m. and 5:30 p.m., the individual was involved in laboratory work and had a relatively low activity level. At 5:30 p.m., the individual consumed a dinner consisting of 50 grams of protein and 330 mL of beer (5% Alc./Vol.), providing energy and relaxation for the last part of the day. From 5:30 p.m. to 9:30 p.m., the individual engaged in indoor entertainment. Throughout the experiment of the day, the system consistently kept recording and sending data in real-time.

(iv) Alcohol intake

In alcohol intake study, a healthy participant engaged in two alcohol intake experiments (independently involving 250 mL and 500 mL beer, 5% Alc./Vol.). In the first segment, a blow test (5-minute interval) was conducted with a commercial breath alcohol (BAC) analyzer (S80, BACtrack). This analysis began 10 minutes after the consumption of the beer and continued until the exhaled alcohol concentration fell below the lowest detection limit of the commercial analyzer. In the second segment, 15 minutes after consuming the same volume of alcohol drink, the participant wore an EBCare mask for a 100-minute EBC alcohol concentration monitoring (**Fig. 2-5C**).

(v) Protein challenge

The EBCare device was evaluated on a healthy person for in situ multiplexed physiological monitoring through a protein challenge (**Fig. A-42**). The experimental protocol included an overnight fasting, after which the individual ingested both food and a protein drink, totaling 60 grams of protein. Followed by the intake, the individual wore an EBCare mask for a continuous 4-hour period, enabling wireless multimodal monitoring. To serve as a control, the same individual consumed water after a fasting period and underwent identical monitoring procedures.

The changes in EBC NH_4^+ concentrations and its relation to serum urea concentrations were accessed through protein challenges in healthy individuals. After an overnight fasting, participants in the experiment consumed a cumulative total of 120 grams of protein

distributed across two or three meals one day. In contrast, the control group continuously maintained a fasting state for another four more hours for the test. EBC samples were collected at 20-minute intervals over the course of three days, and serums were sampled at 1-hour intervals on one of the experiment days. The results are presented in **Fig. A-43** and **A-44**. Consistent with protein challenge procedure mentioned above, EBC NH_4^+ and serum urea levels of several participants were recorded both in the fasting state and three hours after the last protein intake. The results are shown in **Fig. 2-5D** and **2-5E**. During a two-week protein challenge assessment (**Fig. A-45**), a participant consumed 120 grams of protein per day during a high protein intake period and subsequently transitioned to a low protein intake period of 40 grams of protein per day. Throughout these two periods, EBC and serum samples were collected and recorded every morning in a fasting state.

(vi) Clinical airway inflammation

Participants were instructed to arrive at the indoor laboratory site (23°C and 50% RH) in an overnight fasting state (partially shown in **Fig. A-46**). The experiment comprised two distinct parts. In the first segment, one hour multiplexed real-time monitoring of EBC was conducted by wearing EBCare masks. Patients were requested to breathe only through their nose while in a sitting position. Valid data was recorded for 20 minutes after signal stabilization (**Fig. 2-5H** to **2-5L** and **Figs. A-50** to **A-52**). The second segment involved a 1-hour collection of EBC, followed by in vitro analysis. The analysts of EBC were detected using electrochemical sensors and assay kit (E-BC-K035-M, Elabscience), simultaneously, serving as a reference for validating the results obtained from on-body experiments. All participants' related information is recorded in **Fig. 2-5F**, **Fig. A-47** and **tables A-6** and **A-7**. At the end of the experiment, the participants were asked to complete a questionnaire regarding their experience with using the EBCare mask. The results were recorded and summarized in the **table A-9** and **Fig. A-49**.

(vii) Exhaled nitric oxide testing

Participants recruitment occurred within the Caltech community. Prior to testing, participants were required to fast overnight. Initial assessment involved measurement of fractional exhaled nitric oxide (FeNO) levels through commercial FeNO tester, VERO (NIOX, Circassia). Participants then underwent the EBCare smart mask evaluation, wherein nasal breathing was mandated, and oral airflow was precluded via application of medical-grade adhesive tape across the oral cavity. The correlation result is shown in **Fig. 2-5G**.

Cooling hydrogel's antimicrobial evaluation

Methicillin-resistant S. aureus American Type Culture Collection (ATCC) BAA-2313 and MDR E. coli (ATCC BAA-2452) were employed for antimicrobial tests. A 100 μL bacteria solution (106 CFU mL^{-1}) was evenly dispersed in each agar plate. Then, sterilized cooling hydrogel disks (1 mm in diameter), loaded with different Ag nanoparticles fractions, were positioned into 2-mm holes created in the agar plates. The zone of inhibition was measured after an 18-hour incubation period (**Fig. A-6**) [56].

EBCare inner surface non-adhesion testing

An ultrasonic nebulizer was loaded with a 37°C adhesion test solution (0.1 mg mL^{-1} FITC-albumin in 22 mL of PBS). Condensing interfaces (5 mm discs) of various materials were affixed to a 27°C Peltier cooling surface, ensuring direct contact with moisture generated from the nebulizer. After a 20-minute exposure, the liquid on surfaces was collected and the albumin concentration was determined using ultraviolet–visible spectroscopy (UV-vis) (NanoDrop, Thermo Scientific). Following the liquid collection, the surfaces underwent three successive rinses with 50 μL PBS each time. Subsequently, the sample discs were imaged using a confocal laser scanning microscope (LSM 800, ZEISS) [35,57]. All results are shown in **Fig. A-18**.

Mechanical characterization

The mechanical properties of PDMS:PDMS-b-PEG/Al_2O_3 composites, with varying PDMS-b-PEG copolymer and Al_2O_3 mass fractions, were assessed through tensile tests utilizing a

force gauge (M5-50, Mark-10). Dog-bone-shaped samples (width, 5 mm; length, 50 mm; thickness, 2 mm) were fabricated using molds and cured in an oven at 130°C for 3 hours before demolding for material mechanical characterization. For testing the mechanical properties of the device, the framework (condensation layer) of EBCare was prepared. Subsequently, these samples were subjected to tensile tests, being suspended between two parallel jaw grips (G1101, Mark-10) at the edges. The displacement was controlled at a loading rate of 10 mm min^{-1}, and the samples were stretched until failure. The resulting data is presented in **Fig. A-28**.

Breathability characterization

A differential pressure measurement setup was designed as depicted in **Fig. A-48A.** An air supply system with a regulating valve was employed to maintain a constant airflow rate. The airflow velocity was set to 9.4 cm/s through the mask specimen, conforming to the face velocity stipulated by the NIOSH-42 CFR84 standard (*58*). Circular mask specimens of 4 cm diameter with varying tape coverage ratios (mimicking EBCare mask structure) were tightly sealed inside an air chamber for air passage, ensuring an airtight seal to prevent leakage. A differential manometer connected across the inlet and outlet of the air chamber facilitated the measurement of pressure drop across the mask specimen. An optional airflow meter could be incorporated at the terminus of the setup to enable leakage verification. To simulate both exhalation and inhalation scenarios, the airflow direction was reversed, and the corresponding pressure differentials were recorded as shown in the **Fig. A-48B** and **A-48C**.

Finite Element Analysis (FEA)

The simulations of the temperature distribution (**Fig. A-10E**) and unidirectional liquid transport process in the EBCare device (**Fig. A-21**) were conducted using the commercial software COMSOL Multiphysics through FEA.

(i) Thermal simulation

The solid heat transfer process was described by Fourier's law and conservation of energy.

$$\rho c_p \frac{\partial T}{\partial t} - \nabla \cdot (k \nabla T) = Q \tag{2.1}$$

where ρ, c_p, k, T, t, and Q denote the density of materials, heat capacity of materials at constant pressure, thermal conductivity of materials, temperature, time, and heat source respectively. The heat capacity, thermal conductivity, and density of hybrid polymer (PDMS:PDMS-b-PEG/Al_2O_3) and hydrogel were 1.1 J g^{-1} °C^{-1}, 0.8 W m^{-1} K^{-1}, 2.4 g cm^{-3} and 4.18 J g^{-1} °C^{-1}, 0.6 W m^{-1} K^{-1}, 1 g cm^{-3}, respectively. At steady state, where $\frac{\partial T}{\partial t} = 0$, the absence of an internal heat source resulted in $Q = 0$. The ambient temperature was set to be 24°C and the hydrogel cooling power was 500 W m^{-2}.

The gas heat transfer process was described by heat equation.

$$\rho c_p \left(\frac{\partial T}{\partial t} + \boldsymbol{v} \cdot \nabla T \right) - (k \nabla T) = Q \tag{2.2}$$

and Navier-Stokes equation

$$\rho \left(\frac{\partial \boldsymbol{v}}{\partial t} + (\boldsymbol{v} \cdot \nabla) \boldsymbol{v} \right) = -\nabla p + \mu \nabla^2 \boldsymbol{v} \tag{2.3}$$

$$\rho \nabla \cdot \boldsymbol{v} = 0$$

where v, p and μ were the velocity, pressure, and viscosity of breath, respectively. The initial velocity and temperature of breath were set to be 0.5 m s^{-1} and 34°C, respectively. At steady state, where $\frac{\partial T}{\partial t} = 0$, $\frac{\partial \boldsymbol{v}}{\partial t} = 0$, the absence of an internal heat source resulted in $Q = 0$.

(ii) Microfluidic simulation

The unidirectional liquid transport process was described by Navier-Stokes equation for incompressible flow:

$$\rho\left(\frac{\partial v}{\partial t} + (\boldsymbol{v}\cdot\nabla)\boldsymbol{v}\right) = -\nabla p + \mu\nabla^2\boldsymbol{v} \quad (3.1)$$

$$\nabla\cdot\boldsymbol{v} = 0$$

and phase field equation:

$$\frac{\partial\phi}{\partial t} + \boldsymbol{v}\cdot\nabla\phi = \nabla\frac{\gamma\lambda}{\varepsilon^2}\nabla\Psi \quad (3.2)$$

$$\Psi = -\nabla\cdot\varepsilon^2\nabla\phi + (\phi^2 - 1)\phi \quad (3.3)$$

$$\lambda = \frac{3\varepsilon\sigma}{2\sqrt{2}}$$

$$\gamma = \chi\varepsilon^2$$

Where ϕ, ε, σ, and χ were phase field parameter, capillary width, surface tension coefficient, and mobility tuning parameter. Here, ε was settled as 0.05 mm; σ was set as 72.8 mN m^{-1}, and χ as mobility tuning parameter was set as 1 m s kg^{-1}. The boundary condition was set as wetting surface and contact angle was set to be Pi/12.

For the microfluidic refreshing (see **Fig. A-30A**), the refreshing process was described by Navier-Stokes equation (equation 3.1). The initial fluidic velocity was set to be 5 mm min^{-1} and the non-slippery condition was applied to the boundary. The diffusion process was described by:

$$\frac{\partial c}{\partial t} + v\cdot\nabla c = D\nabla^2 c \quad (3.4)$$

where c and D denote the concentration and diffusion coefficient, respectively. The diffusion coefficient of ions (NH_4^+ and NO_2^-) is ~1.9 x 10^{-9} m^{-2} s^{-1}.

Supplementary Text. Theoretical analysis in the EBCare

Thermal analysis

The heat transfer between EBCare's inner surface and gas is calculated according to the Newton's law of cooling.

$$Q = h\,A\,\Delta T \tag{4}$$

where Q is the heat transfer power, h is the heat transfer coefficient (air weak forced convection), here set to 100 W m^{-2} K^{-1}; A is the heat transfer surface area (EBCare inner surface area, ~4 cm^2);ΔT was temperature difference between solid surface (EBCare inner surface) and gas. According to our measurements and previous research [47], the temperature of EBCare inner surface is measured on-body to be 27.5°C, and the temperature of the exhaled breath is about 34.5°C, so the temperature difference is ~7°C.

$$Q = 100\,W\,m^{-2}K^{-1} \times 4\,cm^2 \times 7\,K = 0.28\,W = 280\,mW$$

The heat comes from exhalation and originates from two physical processes: the heat Q_1 released due to the temperature drop in exhale breath and the latent heat Q_2 generated by the condensation of high-humidity expiration:

$$Q = Q_1 + Q_2 \tag{5.1}$$

$$Q_1 = m_{1u}\,c\,\Delta T \tag{5.2}$$

$$Q_2 = m_{2u}\,L \tag{5.3}$$

Here, m_{1u} is the mass of moist breath renewal rate in the EBCare device (~10 ml s^{-1}; 11.2 mg s^{-1}), c is the specific heat capacity of the moist breath (~1500 J kg^{-1} K^{-1}), and ΔT is the average of temperature drop of expiration (average set 2°C). Thus, Q_1 ~35 mW.

Because,

$$Q_2 = Q - Q_1 = 245\ mW$$

$$m_{2u} = \frac{Q_2}{L} \approx 0.11 uL\ s^{-1} \sim 6.5\ uL\ min^{-1}$$

m_{2u} is the breath condensation rate, and L is the latent heat of water vapor (2260 J g^{-1} °C^{-1}). Considering the estimation errors from Q, Q_2, the influence of the interface on the condensate capture efficiency, and the small droplets in the breath, the value of m_{2u} is basically consistent with our experimental results, which is ~5 μL min^{-1}.

From the heat dissipation (the EBCare tandem cooling) perspective, the heat conducted from breath gas to the EBCare device was dissipated by hydrogel cooling and radiative cooling.

In indoor settings, the radiative cooling is mostly restricted, where hydrogel cooling is the dominant cooling method. Under an ambient temperature of ~23°C, a relative humidity of ~50%, and a constant wind speed of ~0.5 m s^{-1}, the spontaneous unit area evaporation rate of cooling hydrogel on the EBCare was m_{evapor}~0.8 kg m^{-2} h^{-1}, and the surface area of the hydrogel A_h was ~4 cm^2. Thus, the unit area cooling power carried away by water evaporation is:

$$Q_{ch\ unit} = m_{evapor} L \tag{6.1}$$

$$Q_{ch\ unit} \approx 500\ W\ m^{-2}$$

For the EBCare device:

$$Q_{ch} = Q_{ch\ unit}\ A_h \tag{6.2}$$

$$Q_{ch} = 200\ mW$$

Considering the subordinate air heat convection, and infrared heat radiation, the cooling heat was basically aligned with the heat transfer energy Q.

In outdoor environments, according to most radiative cooling reports [26, 48], the radiative cooling materials cooling power $Q_{cr\,unit} \approx 100\ W\ m^{-2}$ thus enhanced the EBCare cooling performance. For radiative cooling power:

$$Q_{cr} = Q_{cr\,unit}\, A_r \tag{6.3}$$

$$Q_{cr} \approx 90\ mW$$

A_r is the radiative cooling surface area of the EBCare device ~9 cm^2.

Sunlight with strong solar radiation $Q_s \approx 1000\ \mathrm{W}\ m^{-2}$ can easily eliminate the cooling effect of both the exposed hydrogel cooling and MIR radiation. Thus, the sunshield layer (reflectance higher than 90%) was added to encapsulate the EBCare device.

Microfluidics analysis

For capillary force on micropillar array of hydrophilic EBCare inner surfaces, the density and height combined factors are defined as the gradient's indexes. To simplify theoretical analysis of the gradient array, the introduction of a four-pillar square array is used for the analysis.

For the dimensionless porosity coefficient is:

$$\epsilon = 1 - \frac{\pi}{4}\left(\frac{d}{D}\right)^2 \tag{7.1}$$

where d is the diameter of the pillar, and D is the distance between two pillars.

Thus, according to equations in previous research about capillary pressure in rectangular micropillar array [59].

$$P_{capillary} = (26.84\epsilon - 58.52\epsilon^{0.5} + 31.82)\, cos\theta \tag{7.2}$$

θ represents the contact angle of the surface.

According to (7.2), the capillary pressure $P_{capillary}$ decreases monotonically with ϵ and thus increases monotonically with $\frac{d}{D}$, which means higher density leads to a higher capillary pressure in liquids among pillars.

Because the pillars array volume can be calculated through:

$$V = \left(D^2 - \frac{\pi d^2}{4}\right) h \tag{7.3}$$

Thus, higher pillars provide a larger space for unidirectional EBC transport.

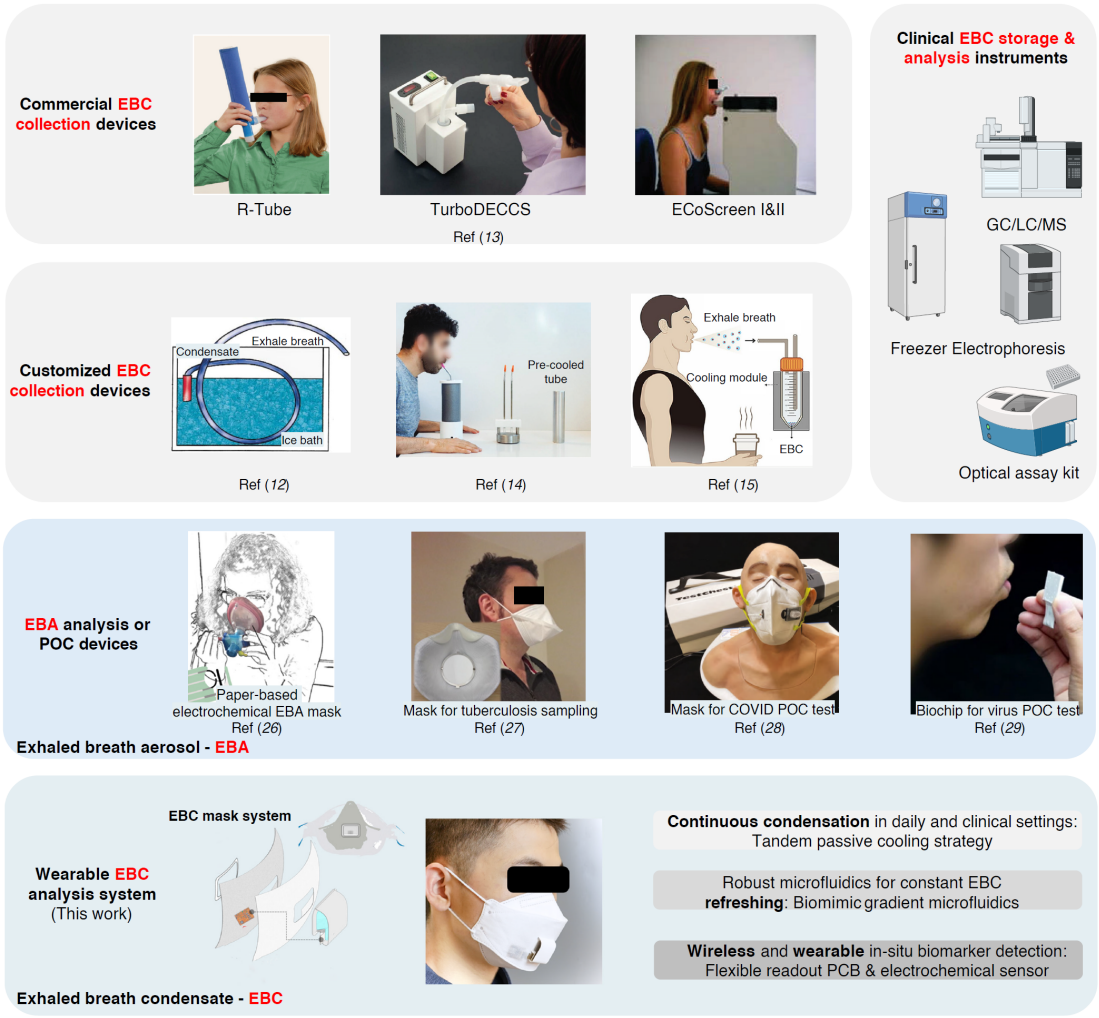

Figure A-1. Recent advances in the field of non-volatile breath analysis Images adapted with permission from [12-15, 26-29].

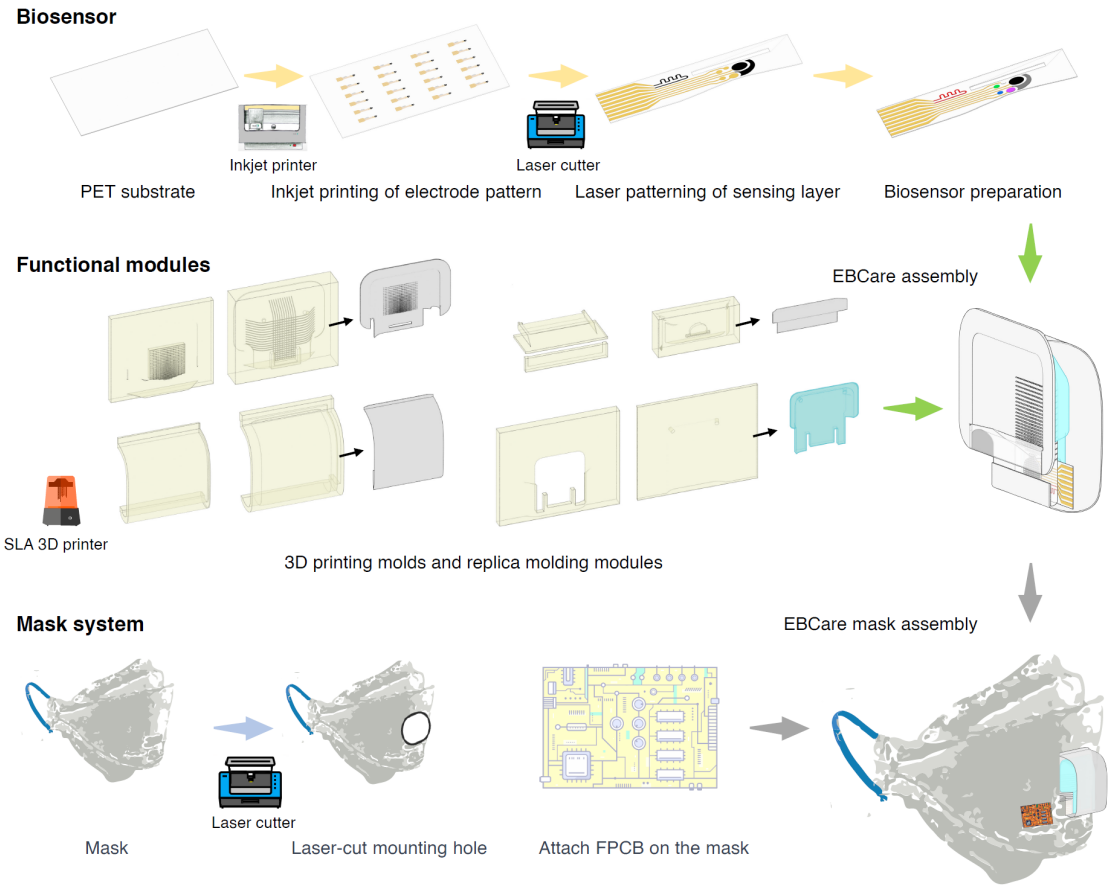

Figure A-2. Step-by-step fabrication process of the EBCare mask. PET, Polyethylene terephthalate; SLA, Stereolithography apparatus; FPCB, Flexible printed circuit board.

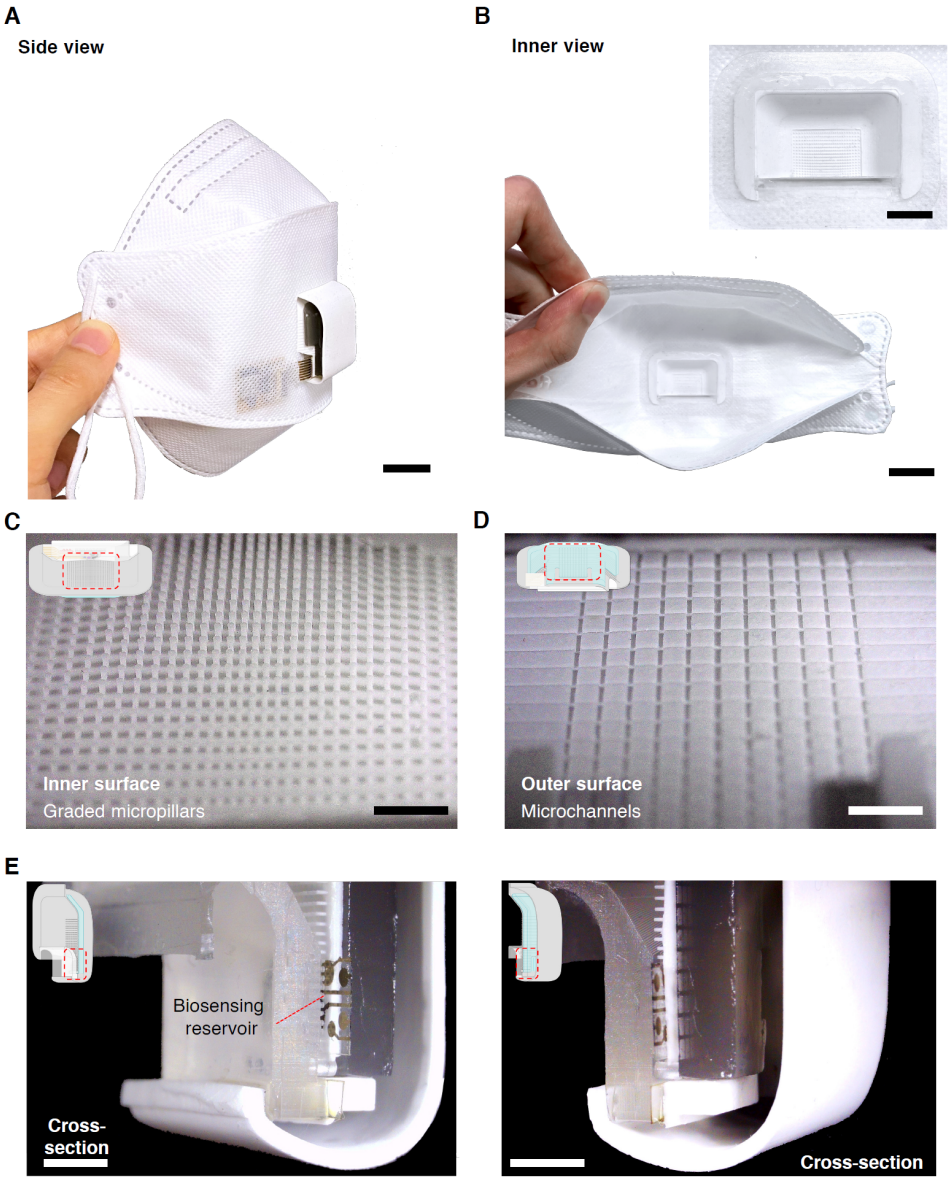

Figure A-3. Optical images of the EBCare mask and micro-engineered EBCare surface structures. (**A** and **B**) Optical images showing the side view (A) and inner view (B) of the EBCare mask. Scale bars, 2 cm; inset scale bar, 1 cm. (**C** to **E**) Zoomed-in view of the EBCare inner surface graded micropillars (C), outer surface microchannels (D) and biosensing reservoir (E) of the EBCare device. Scale bars for (C) and (D), 300μm; Scale bars for (E), 2 mm.

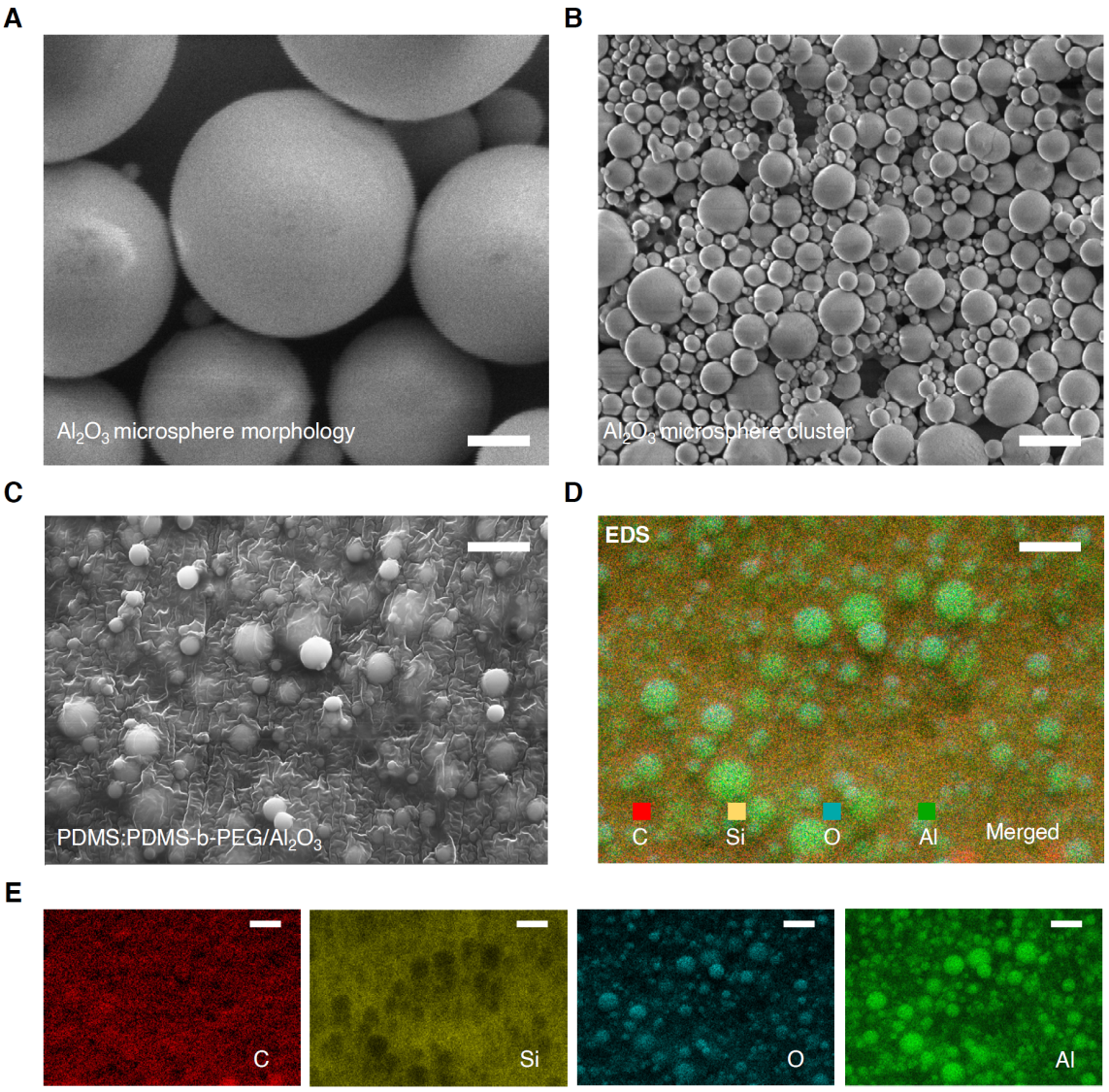

Figure A-4. Scanning electron microscopy (SEM) characterization of EBCare's framework material PDMS:PDMS-b-PEG/Al_2O_3. (**A** and **B**) SEM image of the Al_2O_3 microspheres. Scale bars, 500 nm and 5 µm for (A) and (B), respectively. (**C**) SEM image of the PDMS:PDMS-b-PEG/Al_2O_3 polymer composite. (**D** and **E**) Energy dispersive X-ray spectroscopy (EDS) of the hybrid polymer showing merged (D) and separate (E) elemental distribution. Scale bars for (C to E), 5 µm.

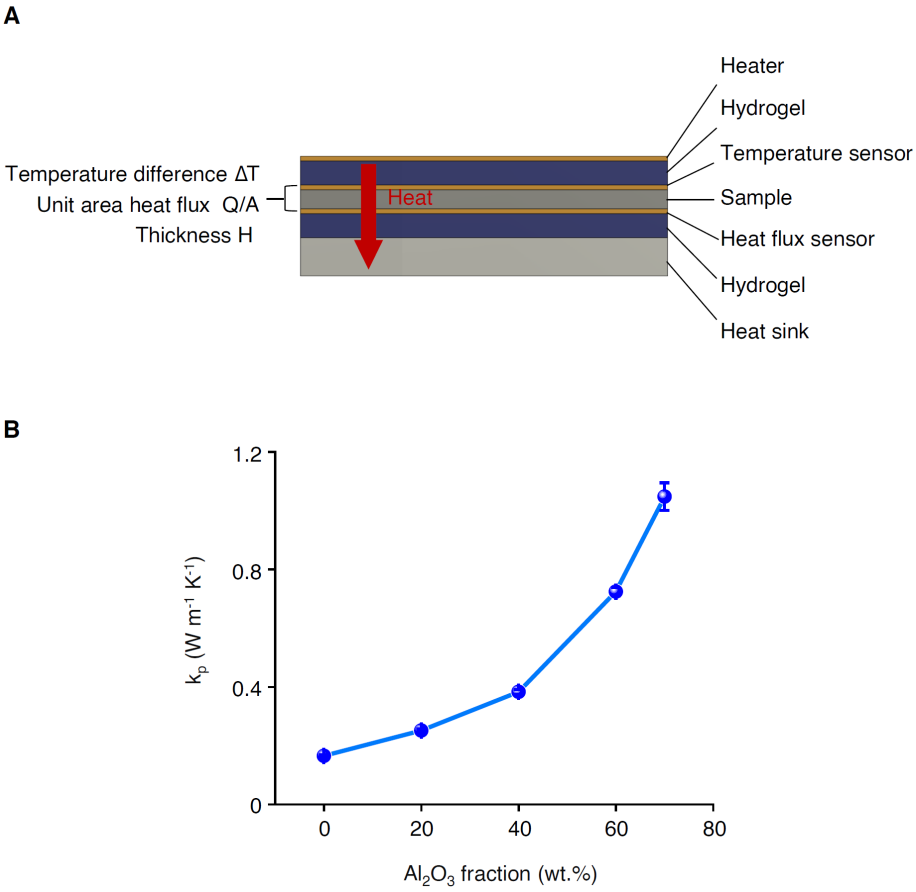

Figure A-5. Thermal conductivity measurement of a polymeric metamaterial film. (**A**) Experimental setup for thermal conductivity measurement. $k_p = \frac{Q\,H}{A\,\Delta T}$, where Q is the heat flux passing through the sample, H is the length of heat conduction (sample thickness), A is the cross-sectional area of conduction (sample surface area), and ΔT is the temperature difference between two sides. (**B**) The dependence of thermal conductivity (k_p) of the PDMS:PDMS-b-PEG/Al_2O_3 hybrid polymer on mass fraction of the Al_2O_3 microspheres.

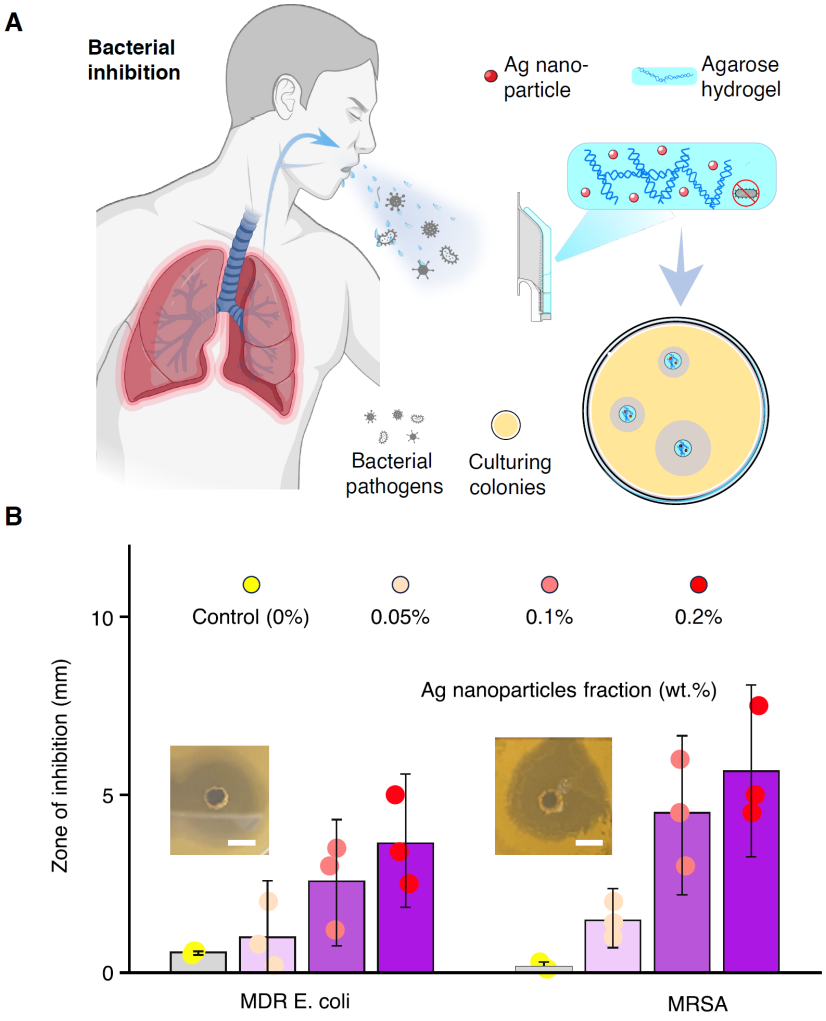

Figure A-6. Antibacterial performance of the cooling hydrogel. (**A**) Schematic illustration of the inhibitory effect of Ag nanoparticles (AgNPs)/agarose cooling hydrogel on respiratory bacterial pathogens. (**B**) Bacterial zone inhibition of the multidrug-resistant *E.coli* (MDR *E. coli*) and gram-positive methicillin-resistant *S. aureus* (MRSA) conditioned on AgNPs/agarose hydrogel for 18 hours. Insets, images of the zone of MDR *E. coli* and MRSA inhibition. Scale bars, 2 mm. All data are presented as mean values ± S.D. from 3 tests.

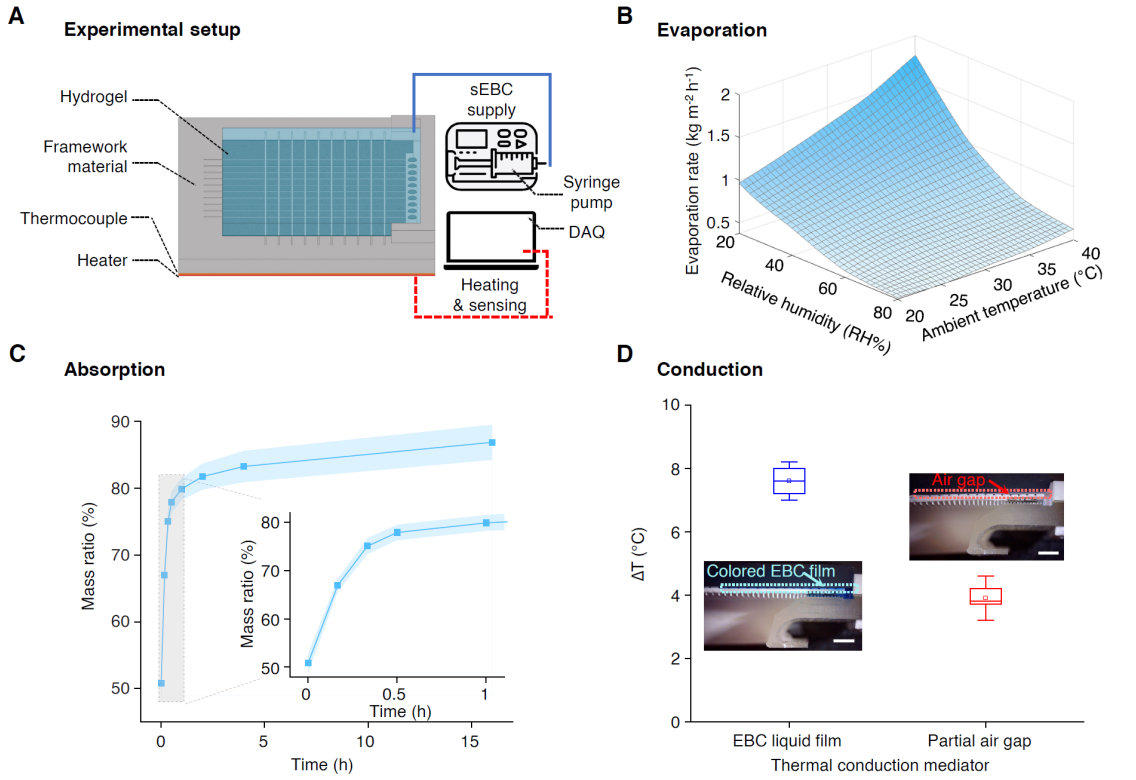

Figure A-7. Experimental setup and characterization for hydrogel cooling. (**A**) The real-time temperature measurement setup of hydrogel cooling. sEBC, simulated EBC (400 μM NH_4HCO_3); DAQ, data acquisition. (**B**) The evaporation rate of a cooling hydrogel under various ambient temperature and humidity conditions at a constant wind speed of 0.5 m s^{-1}. (**C**) Absorption rate of an initial 50% mass (compared to a saturation hydrogel) hydrogel under simulated human respiratory power heating with sEBC replenishment on bottom side. (**D**) The cooling performance (ΔT, temperature drop) of EBCare devices with and without renewed thermal conduction of liquid film between the radiatively cooling layer and the hydrogel cooling layer. Insets are optical images illustrating thermal conductive medium between the two layers. The experiments in (C and D) were conducted under an ambient temperature of ~23°C, a relative humidity of ~50% and a wind speed of ~0.5 m s^{-1}. Scale bars, 2 mm. All data are presented as mean values ± S.D. from 3 samples.

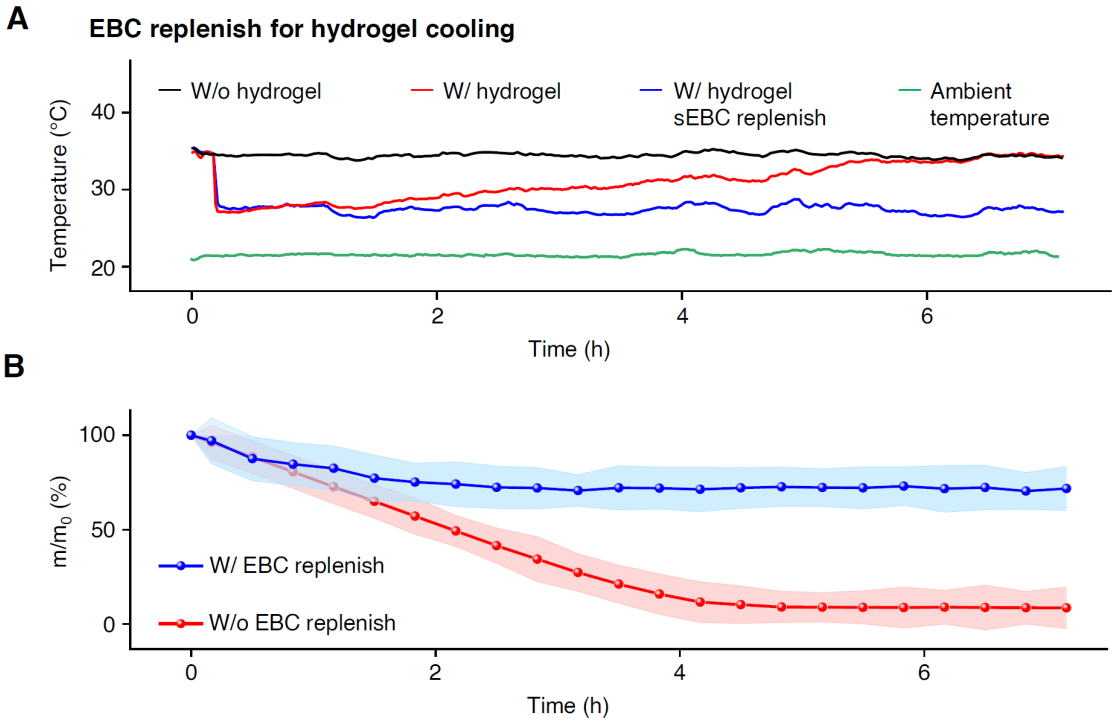

Figure A-8. EBC replenishment for hydrogel continuous cooling and lifetime extension. (**A**) Influence of the cooling hydrogel on the temperature of simulate respiratory heat surfaces (to mimic the condensation layer temperature). w/, with; w/o, without. (**B**) The relative mass changes of the hydrogel over time with and without EBC refreshing structure during on body tests. m and m_0 represent the hydrogel mass during the test and at the initial time, respectively.

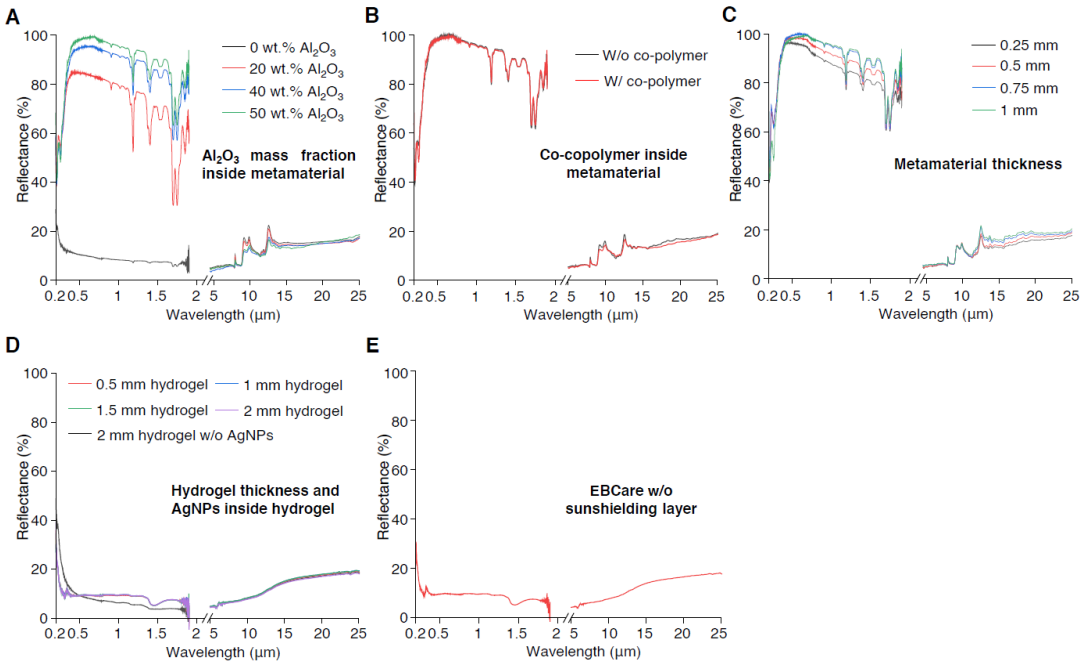

Figure A-9. Optical properties of radiative cooling hybrid polymeric metamaterial and cooling hydrogel. (**A**) Spectral reflectance of 1 mm-thick radiative cooling metamaterial with different Al_2O_3 microsphere mass contents. (**B**) Spectral reflectance of metamaterial films with and without PDMS-b-PEG copolymer inside. (**C**) Spectral reflectance of different thickness metamaterial films with 50 wt.% Al_2O_3 microspheres inside. (**D**) Spectral reflectance of different thickness of hydrogel and influence of AgNPs inside. (**E**) Spectral reflectance of EBCare device without sunshield layer.

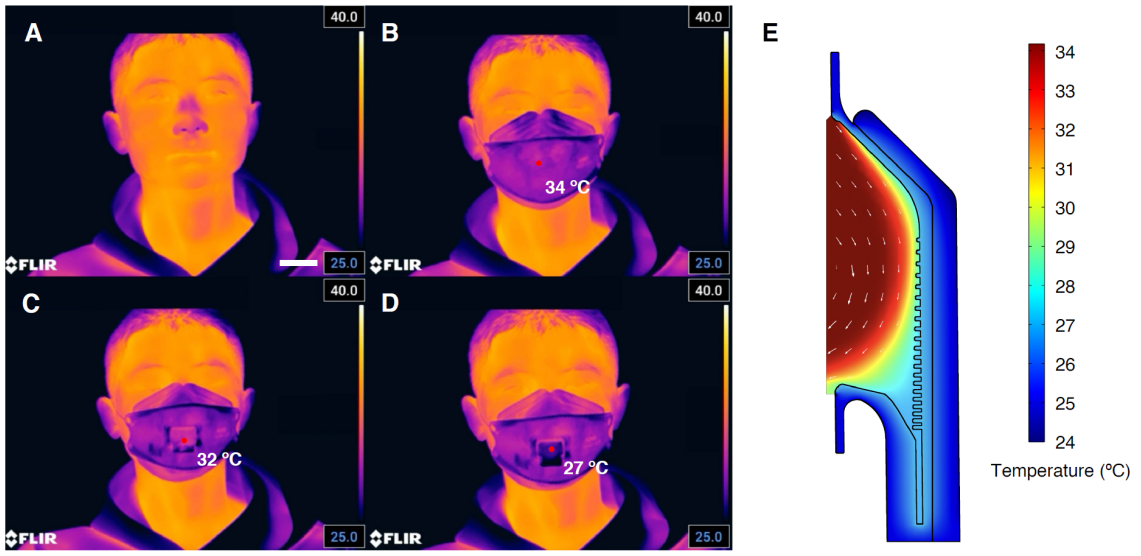

Figure A-10. Infrared images and numerically simulated temperature color mapping of a participant in an indoor environment with different mask status. (**A**) The participant without mask. (**B**) The participant wearing an N95 mask. (**C**) The participant wearing an N95 mask with the radiative cooling framework of the EBCare device. (**D**) The participant wearing an N95 mask with both radiative and hydrogel cooling layers of the EBCare device. The experiment was conducted under an ambient temperature of ~23°C, a relative humidity of ~50%, and a constant wind speed of ~0.5 m s^{-1}. Scale bar, 4 cm. (**E**) Numerically simulated temperature color mapping of an EBCare device during expiration (the simulation model has streamlined the structure of the EBCare for enhancing numerical computational efficiency).

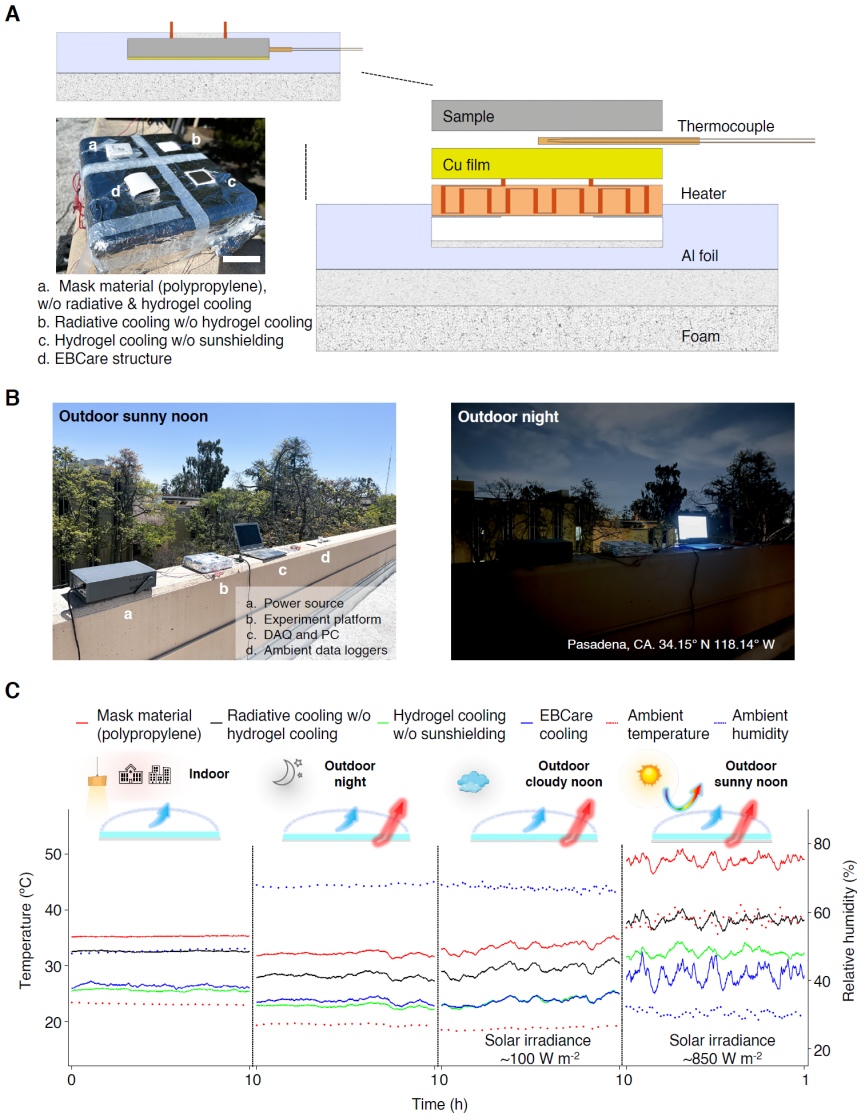

Figure A-11. Direct thermal analysis to evaluate the performance of cooling strategies. (**A**) Schematic of the thermal measurement system used to characterize the performance of cooling strategies. Inset, photo of the experimental setup in the test. Scale bar, 3 cm. (**B**) Photo of the thermal measurement system used to characterize cooling strategies performance under intense sunlight outdoor and outdoor night conditions. DAQ, data acquisition; PC, personal computer. (**C**) Surface temperature of different cooling designs under indoor and outdoor (at night, cloudy, and under sunlight) environments.

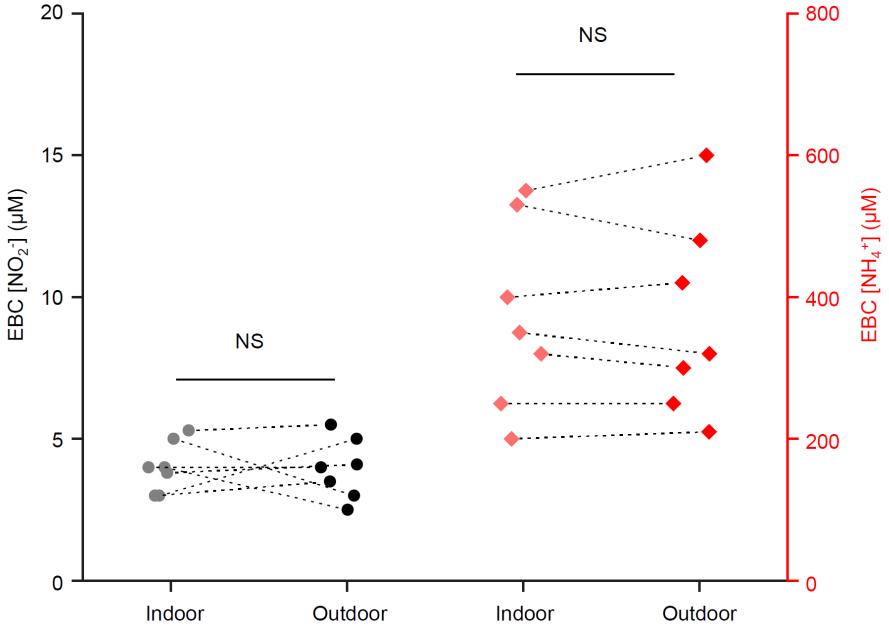

Figure A-12. Concentrations of EBC analytes from two healthy participants across varied environmental conditions (n=7 biological replicates from N=3 healthy participants). Indoor conditions: temperature 23°C, humidity 50%; Outdoor conditions: temperature range 5–30°C; humidity 30–80% RH. NS, not significant, p>0.05, One-way ANOVA and Tukey's post-hoc test.

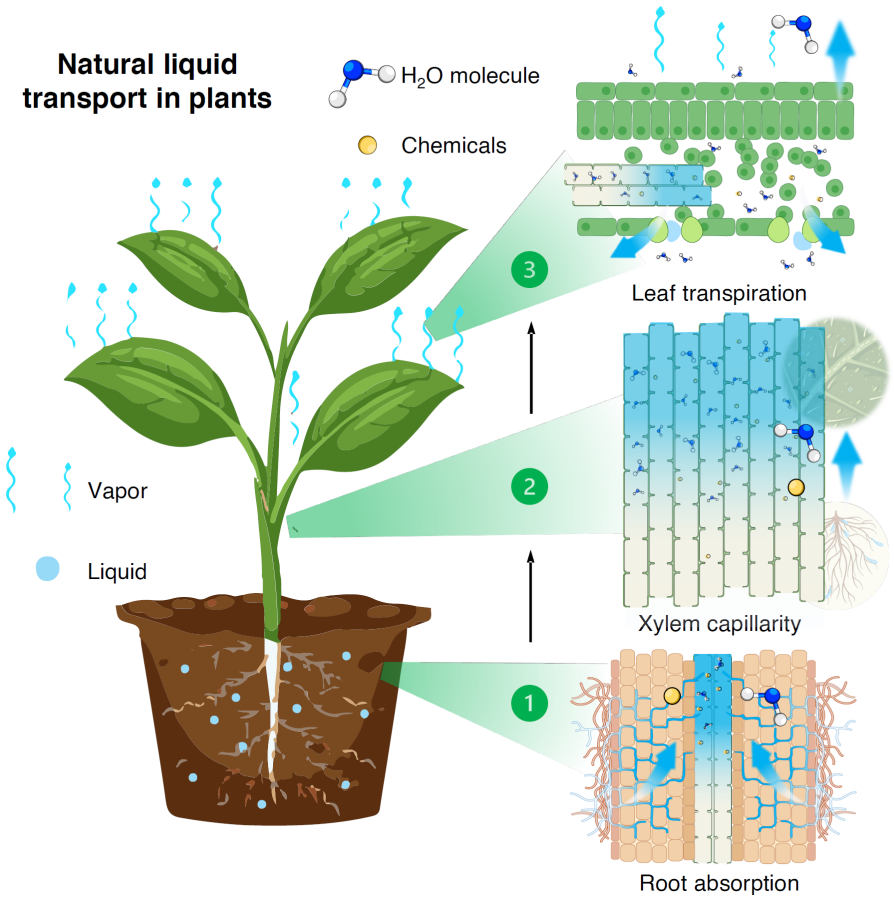

Figure A-13. Natural transport of water and chemical substances in plants due to the capillary effect.

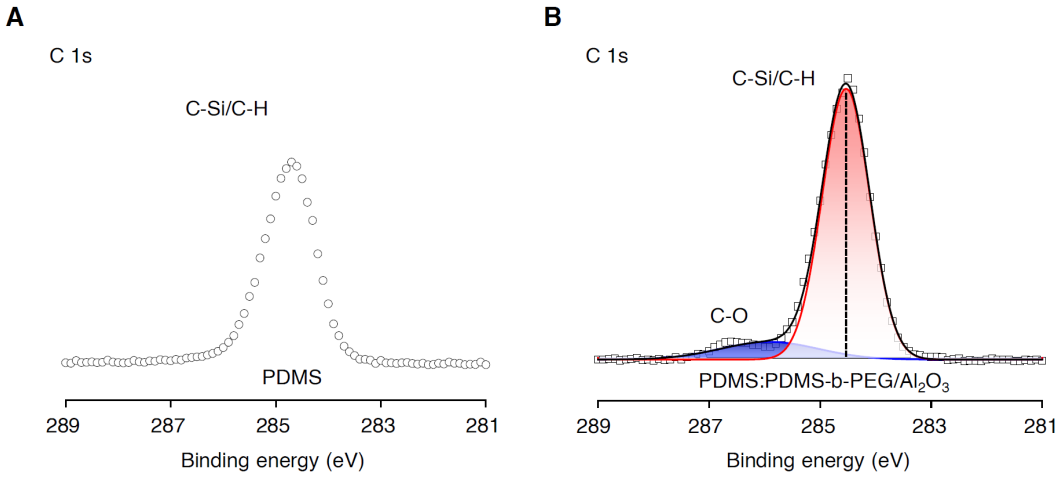

Figure A-14. C 1*s* X-ray photoelectron spectroscopy (XPS) characterization of hydrophilic hybrid polymer surfaces. (**A**) The XPS characterization of pristine PDMS which has C-H and C-Si bonds. (**B**) The XPS characterization of hybrid polymer PDMS:PDMS-b-PEG/Al_2O_3 which has C-H and C-Si bonds, as well as additional C-O bonds.

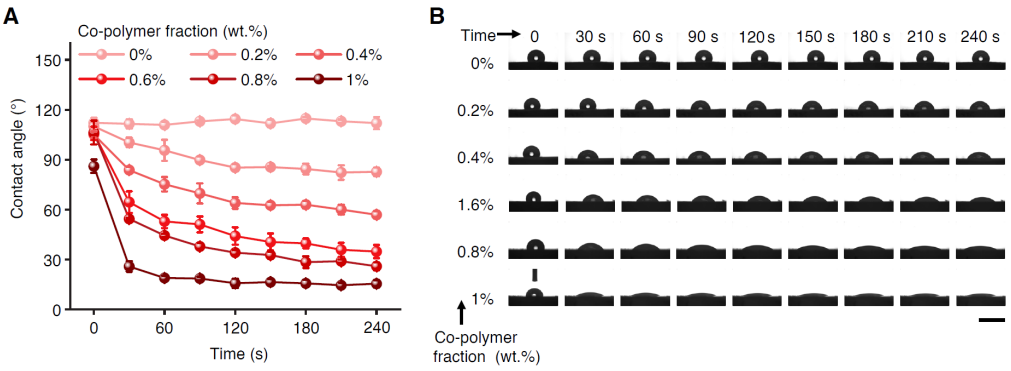

Figure A-15. Hydrophilicity characterization of hybrid polymer surfaces. (**A**) Contact angle change with time in wetting behavior of water on the surface of hybrid polymer with varied PDMS-b-PEG copolymer contents inside. (**B**) Snapshots of the wetting behavior of the hybrid polymer. Scale bar, 2 mm. All data are presented as mean values ± S.D.

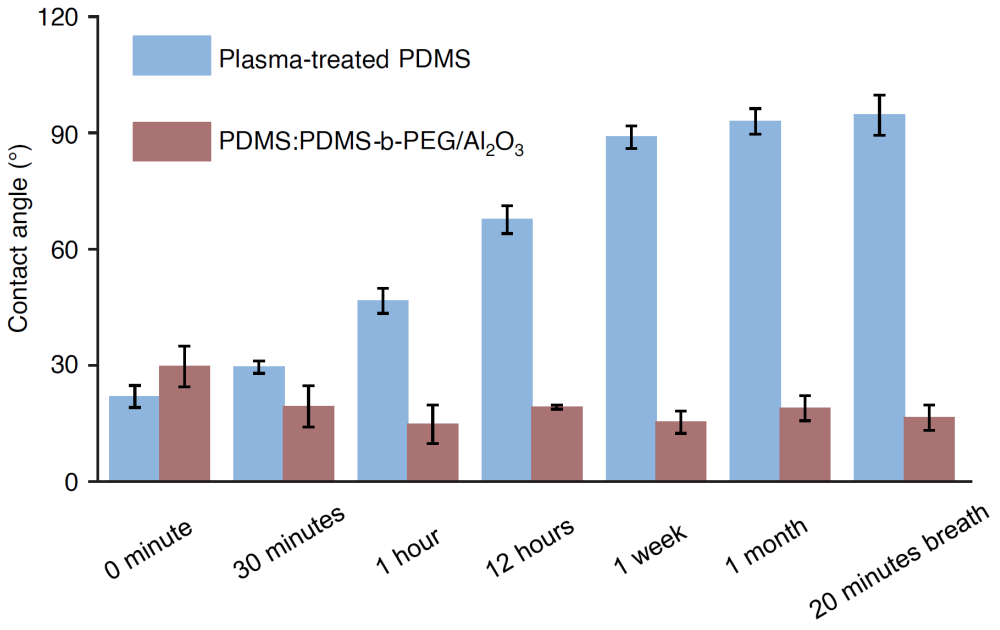

Figure A-16. Stability of surface hydrophilicity of the hybrid polymer PDMS:PDMS-b-PEG/Al_2O_3 and plasma-treated PDMS. All data are presented as mean values ± S.D. from 3 samples.

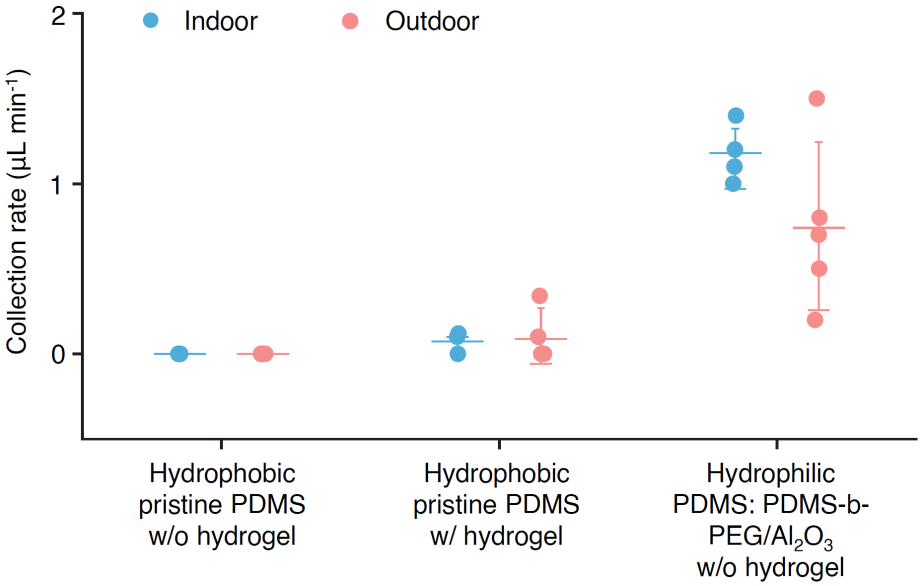

Figure A-17. EBC harvesting performance of different surface hydrophilicity. All data are presented as mean values ± S.D. from 5 tests.

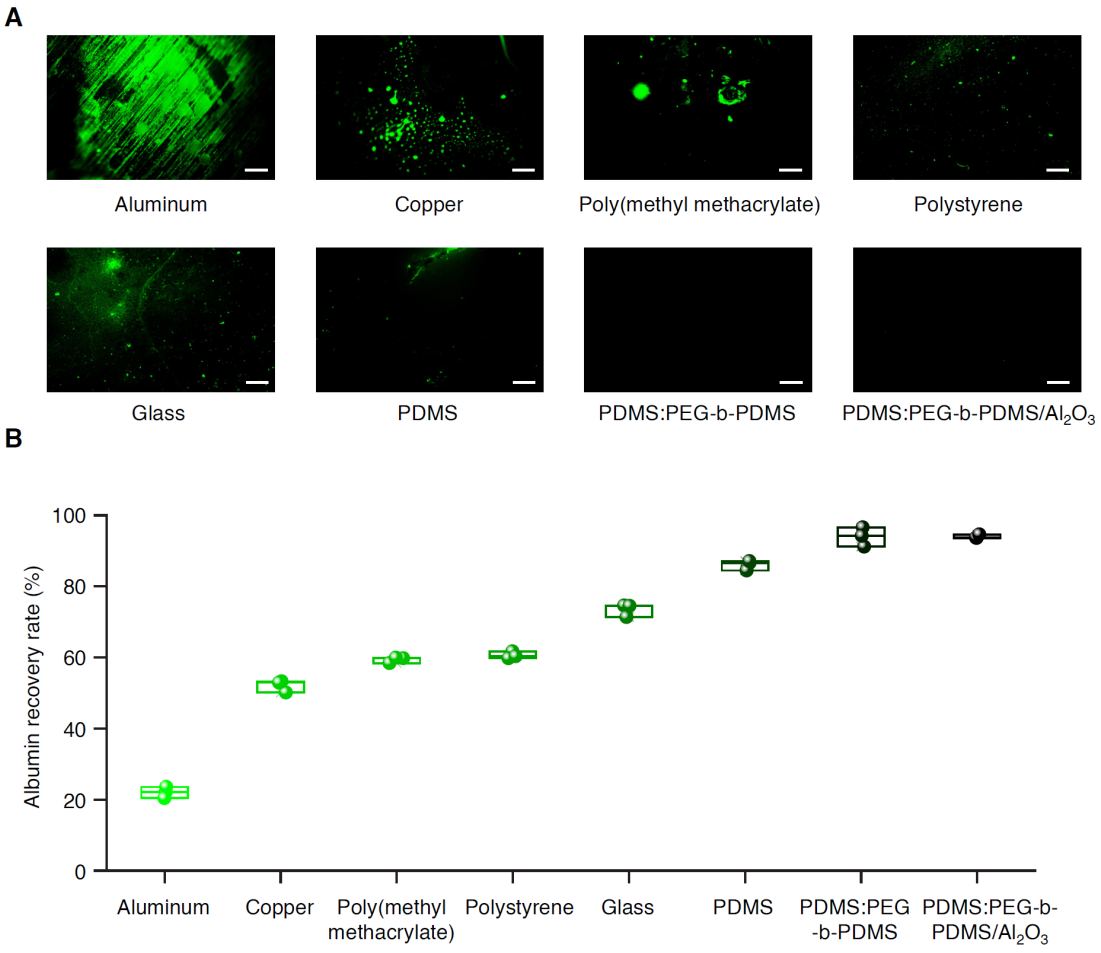

Figure A-18. Characterization of the biological anti-adhesive properties of the hybrid polymer. (**A**) Adhesion image of fluorescently labeled albumin on different condenser coatings. Scale bars, 100 μm. (**B**) In vitro albumin condensate recovery percentages (1 - adhesion percentages) of labeled albumin on different condenser coatings. All data are presented as mean values ± S.D. from 3 tests.

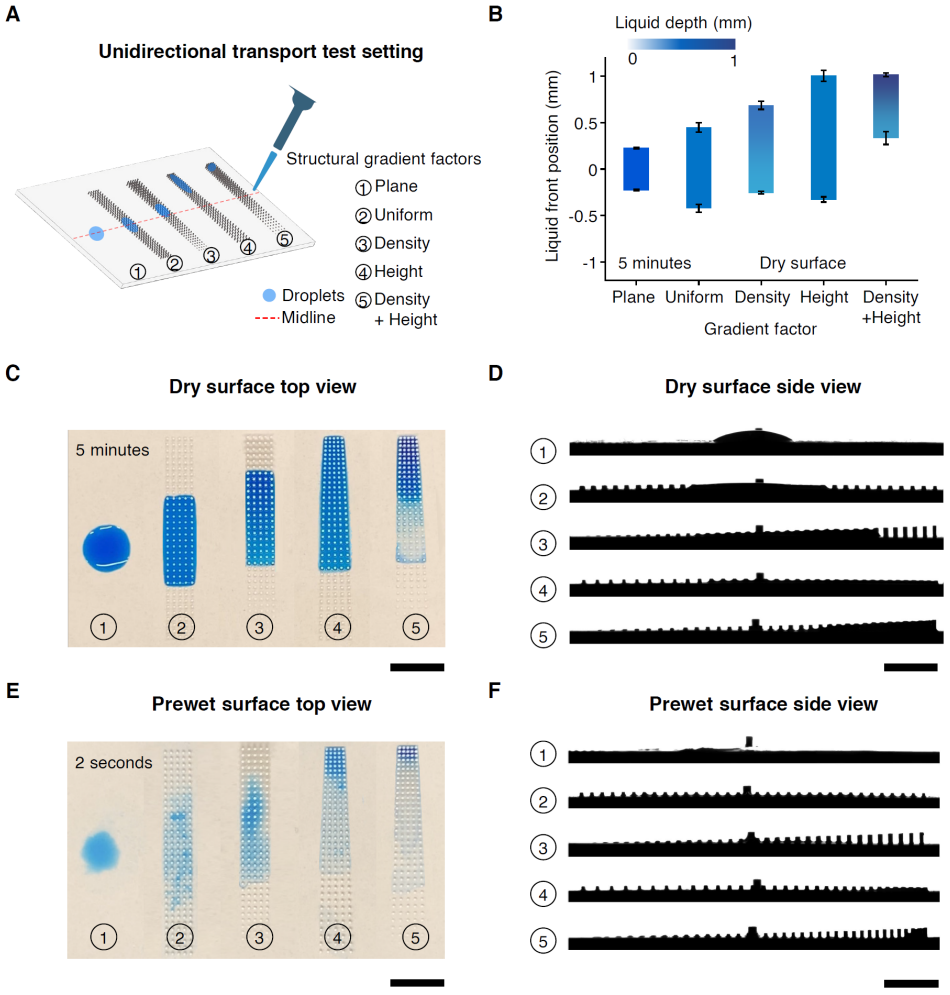

Figure A-19. Unidirectional liquid transport facilitated by the micropillars with height and density gradients. (**A**) Experimental setup of the unidirectional liquid transport test of the micropillar array designs with varied gradient factors (density and height). (**B**) Comparison of the unidirectional liquid transport capacity of the dry micropillar arrays with varied gradient factors. (**C** and **D**) Top view (C) and side view (D) optical images of the liquid distribution on the dry surfaces after dropping 7 μL colored water to the midline for 5 minutes. Scale bars, 4 mm. (**E** and **F**) Top view (E) and side view (F) optical images of the liquid distribution on the prewet micropillar arrays after dropping 1 μL colored water to the midline for 2 seconds. Scale bars, 4 mm. All data are presented as mean values ± S.D..

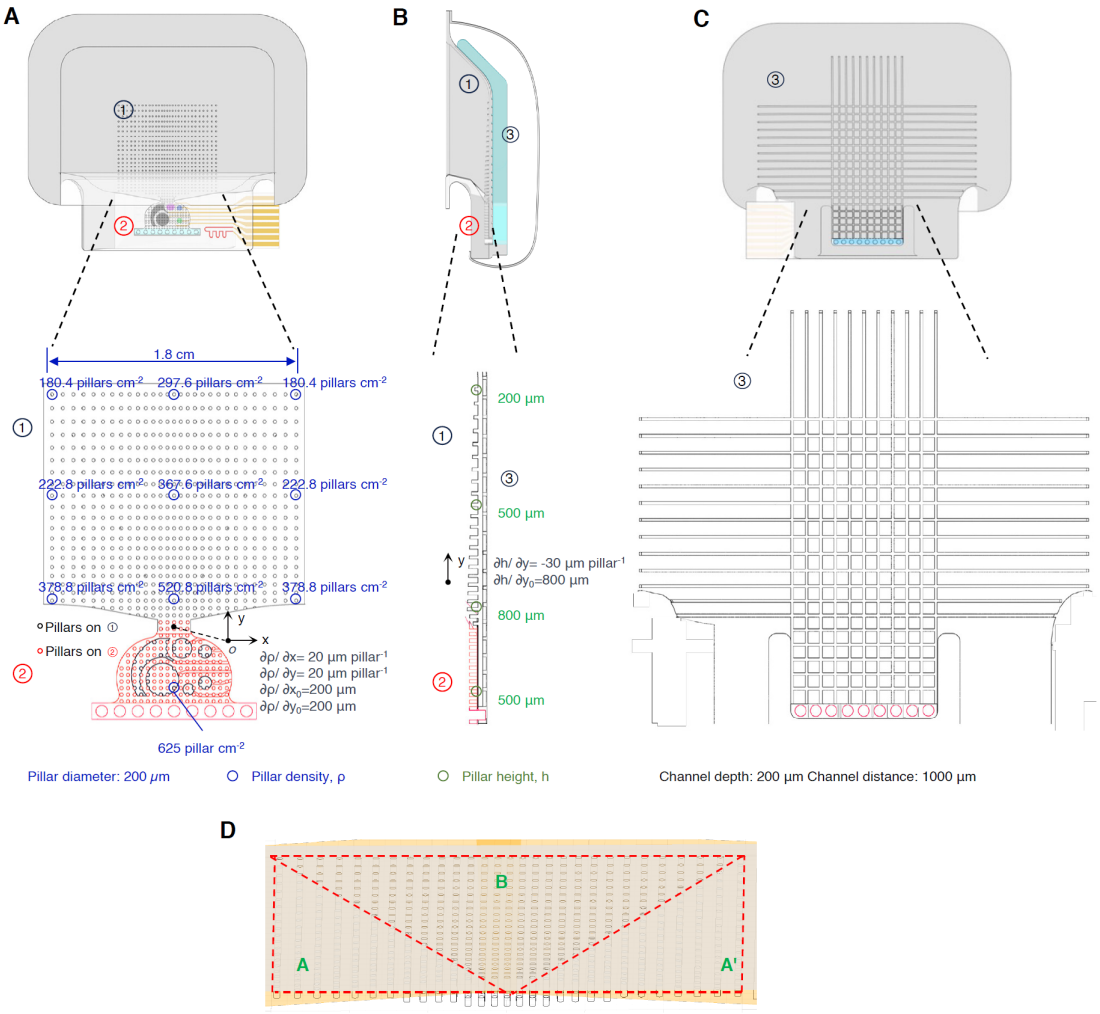

Figure A-20. Parameters of microstructures on the surfaces of the EBCare device. (**A** and **B**) Density gradient parameters of micropillars (A) and height gradient parameters of micropillars along the median axis (B) of the inner surface of EBCare. (**C**) The parameters of the microchannels on the EBCare outer surface. (**D**) Micropillars on inner surface of EBCare truncated by three planes to form a height gradient.

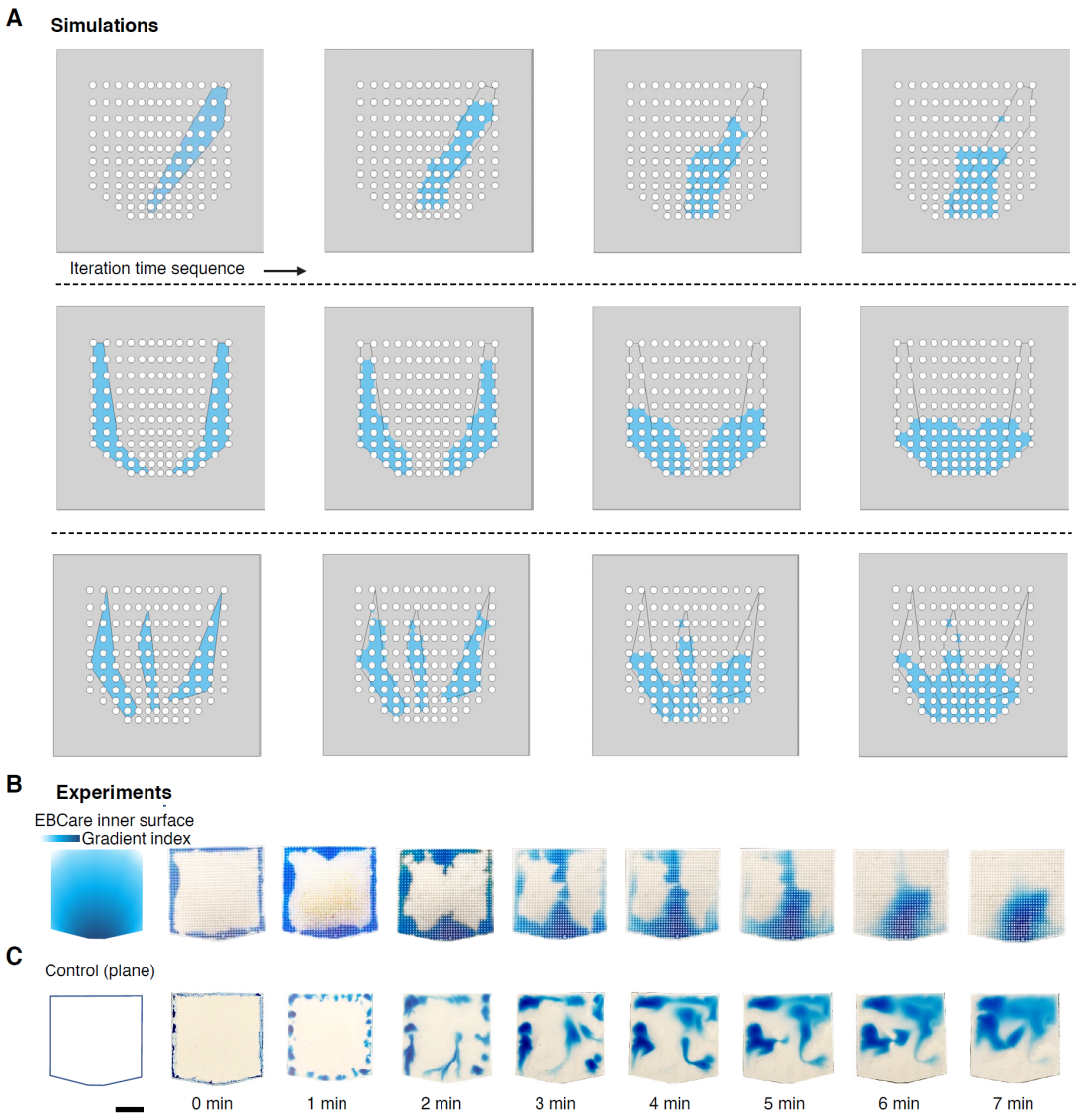

Figure A-21. Unidirectional liquid transport on the inner surface of the EBCare device. (**A**) Simulations of unidirectional liquid transport of randomly distributed liquids on the surface with gradient micropillars (the simulation model has streamlined the structure of the EBCare for enhancing numerical computational efficiency). (**B** and **C**) Snapshots of vapor condensation and liquid sampling process on the inner surface of EBCare (with micropillar arrays with both density and height gradient) (B) and on a control surface without any micropillar structures (C). Scale bar, 5 mm.

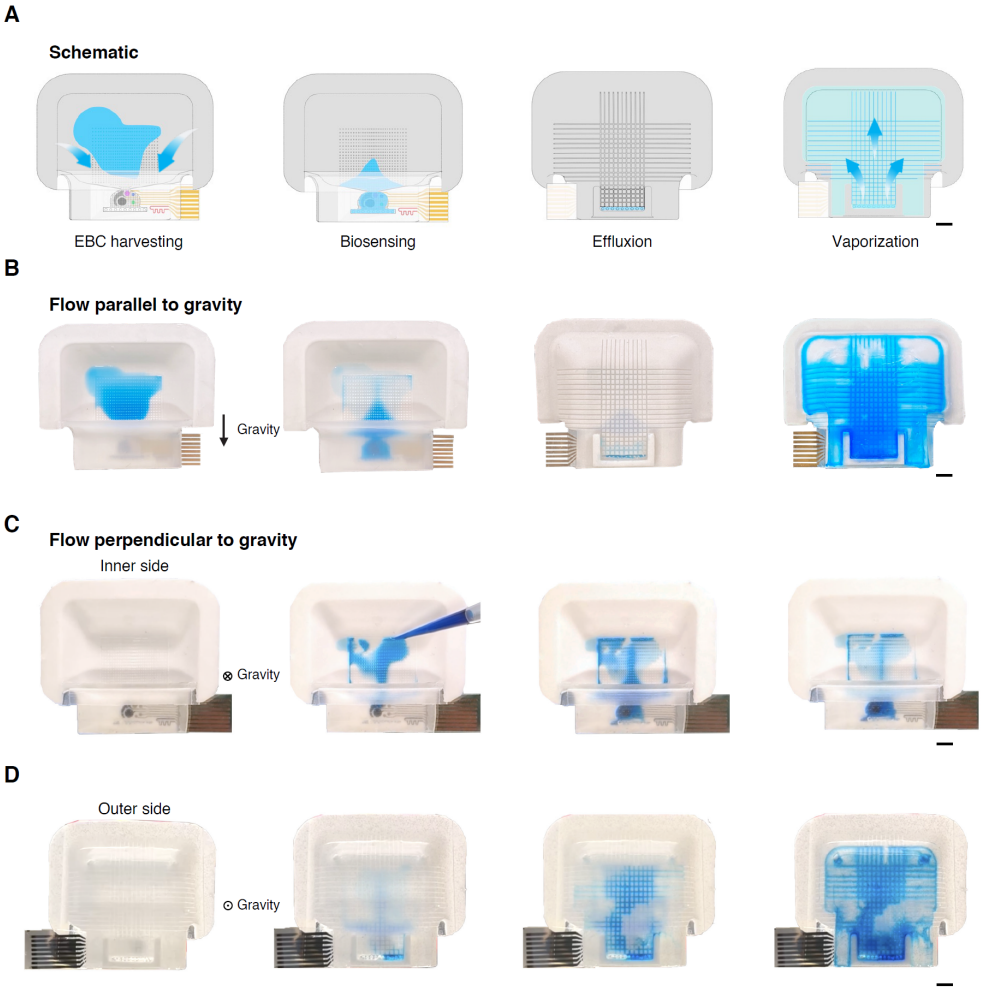

Figure A-22. Sequential optical photos of the automatic liquid automatic transport process in the EBCare device with gravity parallel and perpendicular to the EBC flow. (**A**) Sequential schematic illustrations and **(B)** snapshots of the EBCare's liquid harvesting and transport process including: the condensation of the moist breath into liquid EBC, the transport of EBC into the electrochemical sensing reservoir, the transfer of EBC to the outer surface, and the absorption of EBC by the hydrogel for evaporative cooling. Gravity is parallel to the EBC flow and downward. (**C** and **D**) Sequential optical (C) inner and (D) outer side images of EBCare's liquid harvesting and transport process. Gravity is perpendicular to the EBC flow (C) inward and (D) outward. All scale bars, 4 mm.

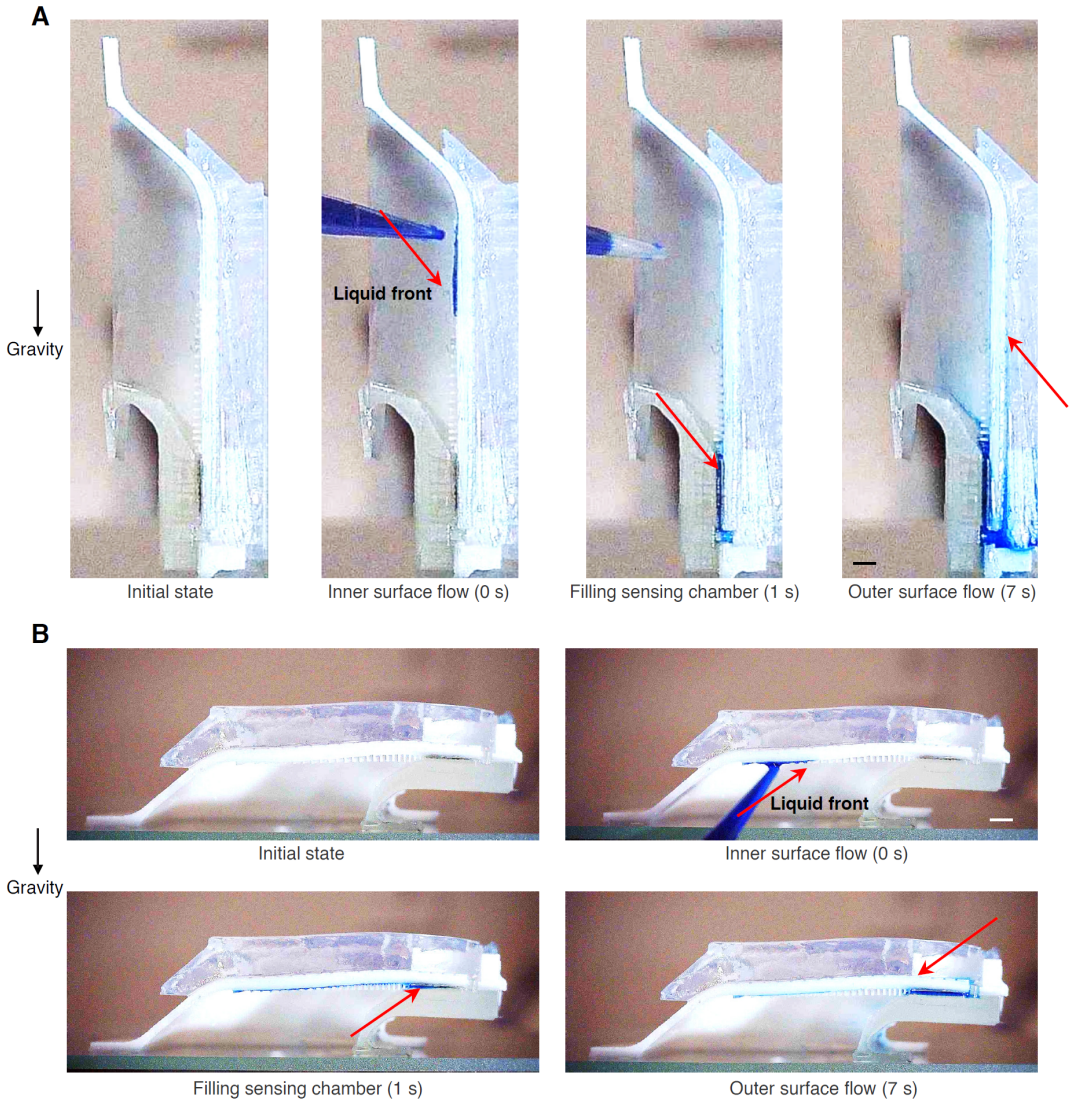

Figure A-23. Sequential cross-sectional optical photos of the automatic liquid transport process in the EBCare device. (**A**) Gravity parallel to the EBC flow. (**B**) Gravity perpendicular to the EBC flow. Scale bars, 1 mm.

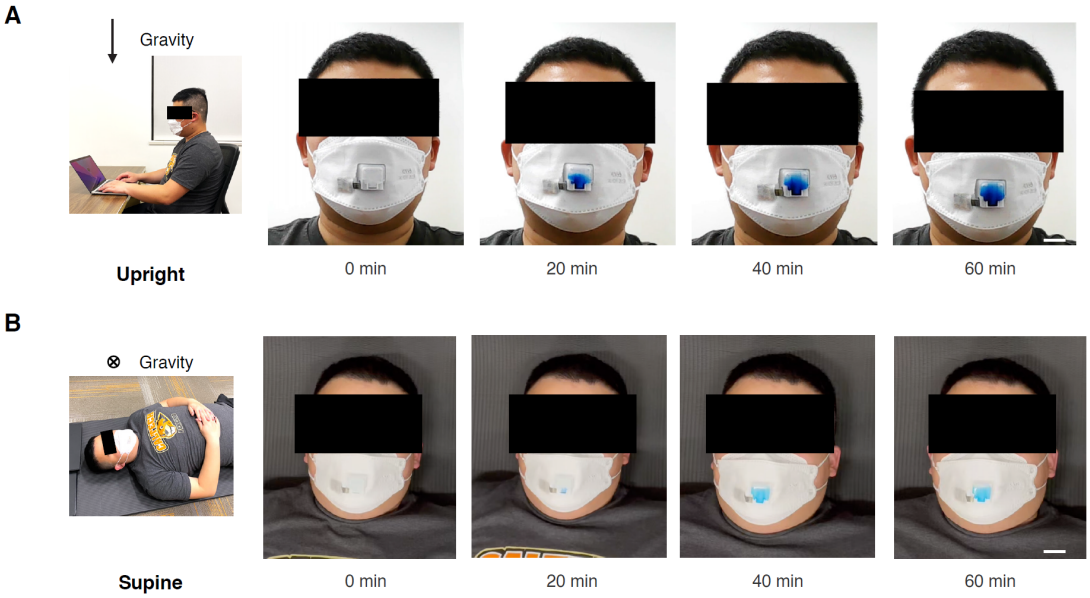

Figure A-24. Sequential optical photos of the on-body evaluation of EBCare's capability of the EBC sampling and transport. (**A**) Upright posture. (**B**) Supine posture. Scale bars, 3 cm.

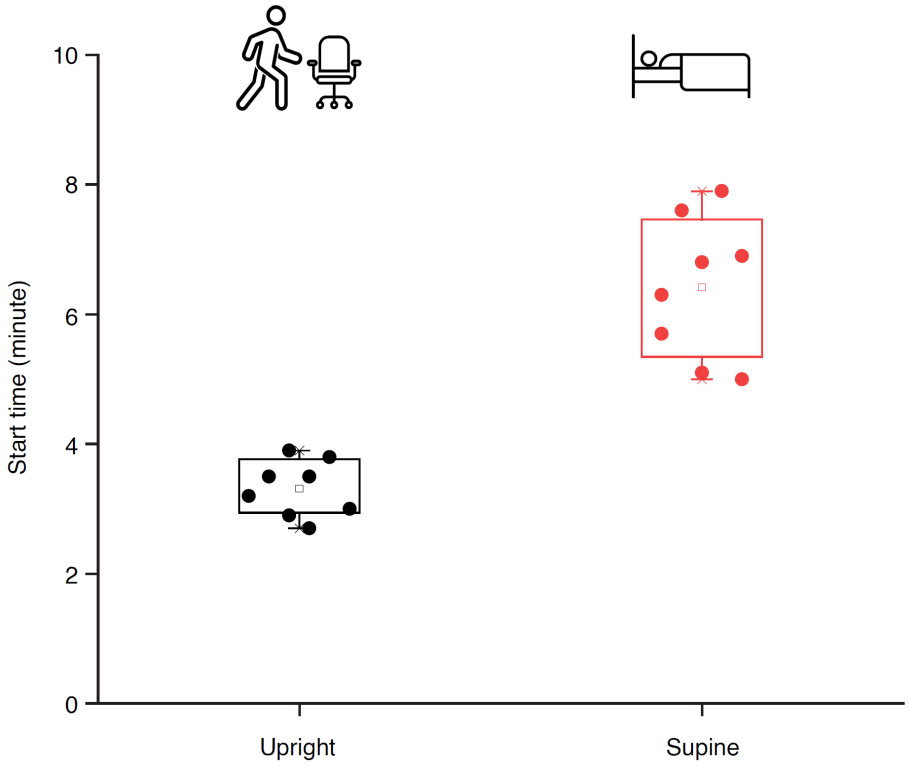

Figure A-25. Startup time for operating the smart EBCare mask. All data are presented as mean values ± S.D. from 8 measurements.

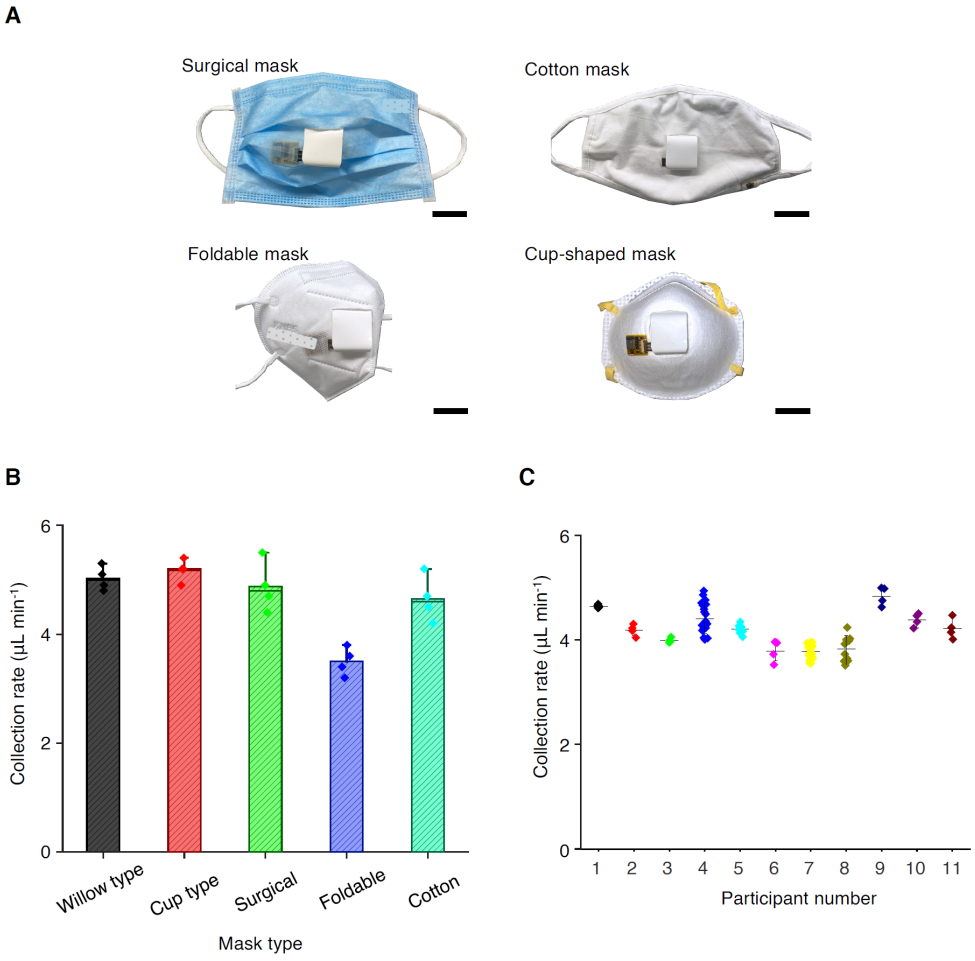

Figure A-26. EBCare device's applicability to different types of masks. (**A**) Photographs of different types of masks with integrated EBCare devices. Scale bars, 3 cm. (**B**) EBC collection rates for EBCare devices integrated on different types of masks. (**C**) Collection rate of the EBCare device from different participants. The experiments were conducted during the office work condition under an ambient temperature of ~23°C, a relative humidity of ~50%, and wind speed ~0.5 m s^{-1}. All data are presented as mean values ± S.D. from at least 3 measurements.

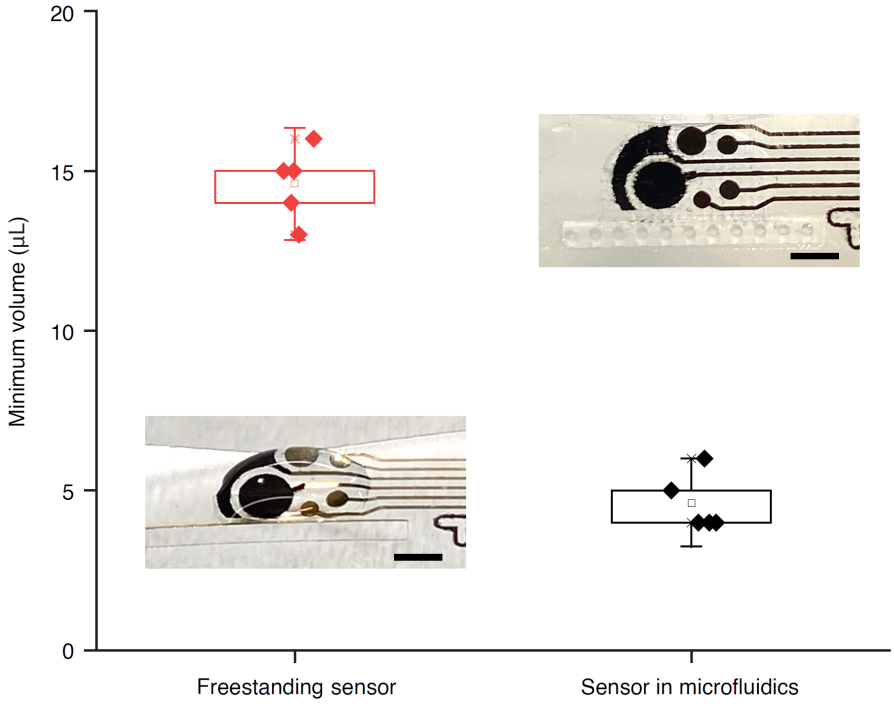

Figure A-27. Minimum volume for operating the multiplex electrochemical sensing array. All data are presented as mean values ± S.D. from 5 measurements.

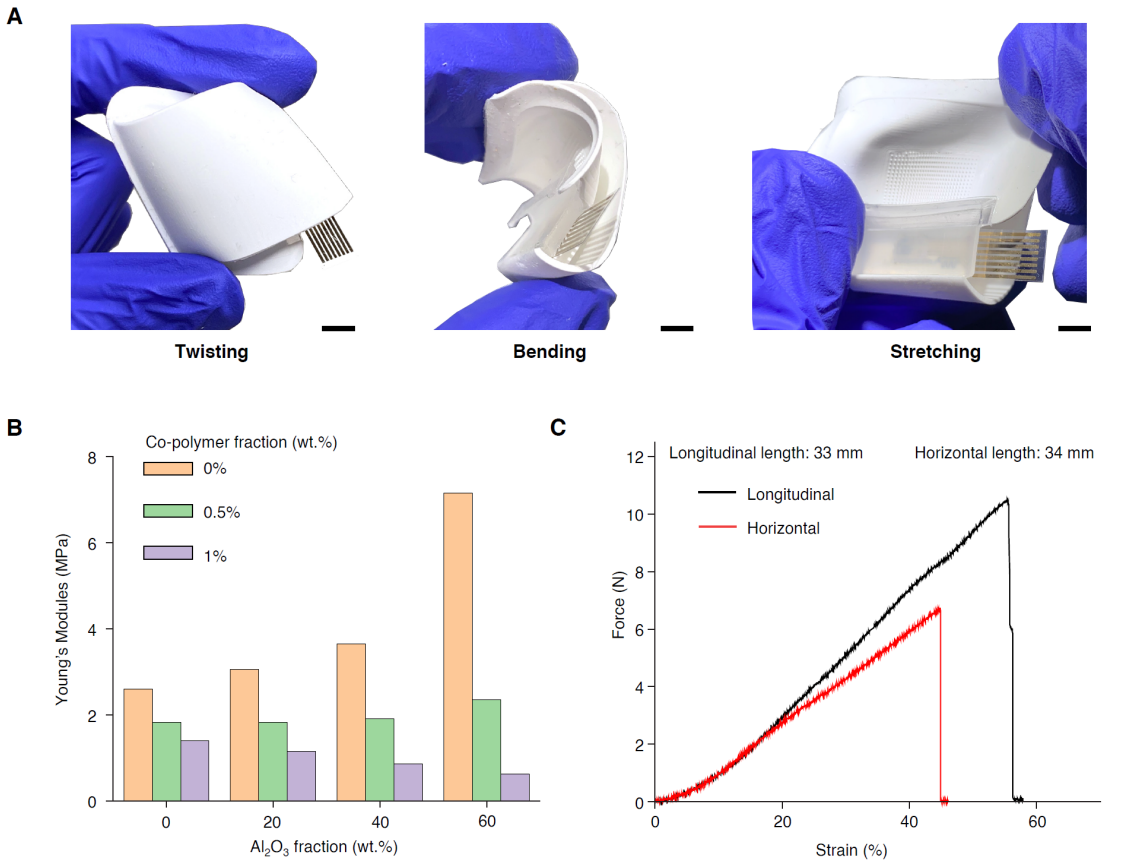

Figure A-28. Mechanical compliance of the EBCare. (**A**) Optical images showing the mechanical compliance of the EBCare during twisting, bending, and stretching. Scale bars, 5 mm. (**B**) Young's modulus of EBCare's framework material PDMS:PDMS-b-PEG/Al_2O_3 with varying copolymer and Al_2O_3 mass fraction. (**C**) Longitudinal and horizontal force-strain curve of EBCare framework.

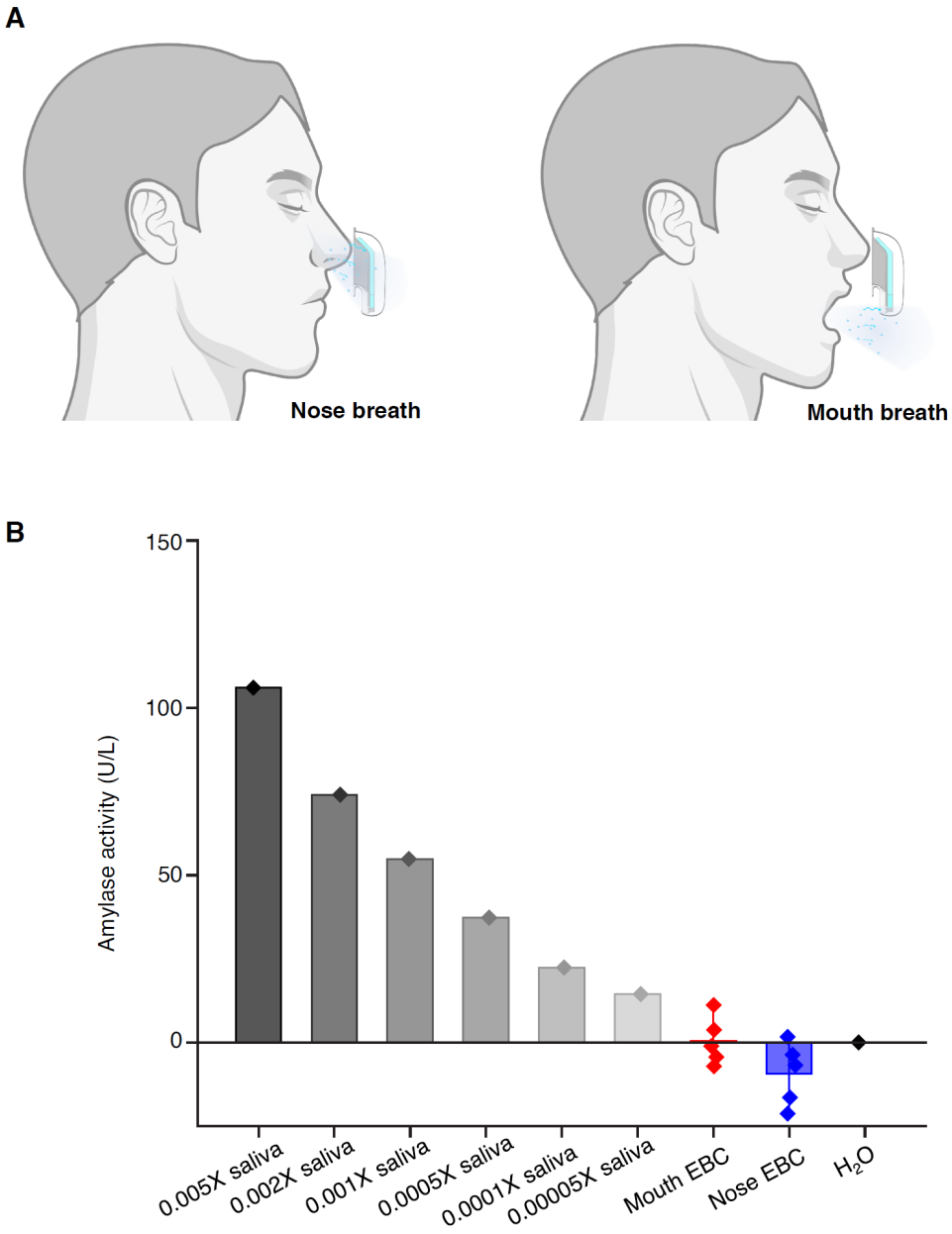

Figure A-29. EBCare adjustable positioning for nose EBC analysis. (**A**) Adjustable positioning of EBCare on masks for mitigating saliva contamination. (**B**) Saliva amylase signal strength in different diluted saliva and EBC samples.

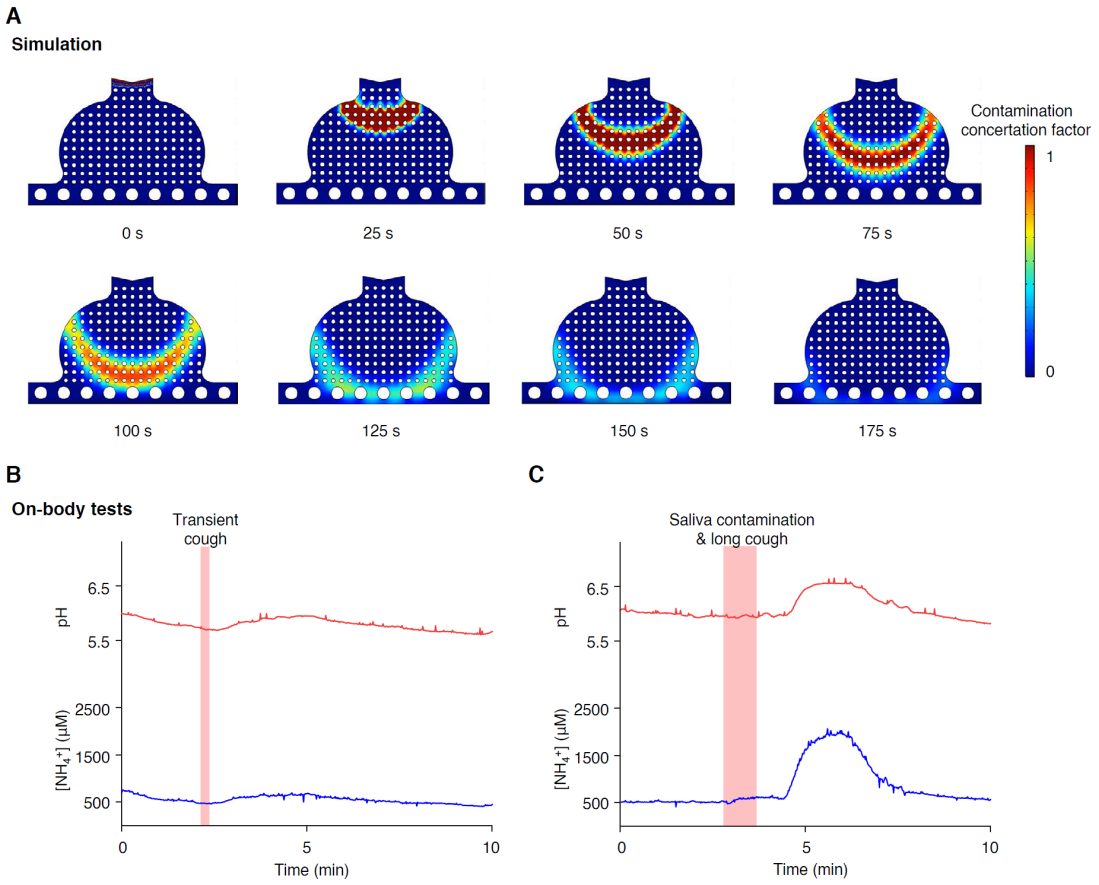

Figure A-30. Microfluidic refreshing for mitigating interference and contamination. (**A**) Simulation of renewal capability of EBCare microfluidics under potential saliva contamination. (**B** and **C**) On body tests of transient coughing (B) and saliva contamination induced by 1-min continuous coughing (C) on a participant recently recovered from COVID-19, utilizing the refreshing EBCare microfluidics.

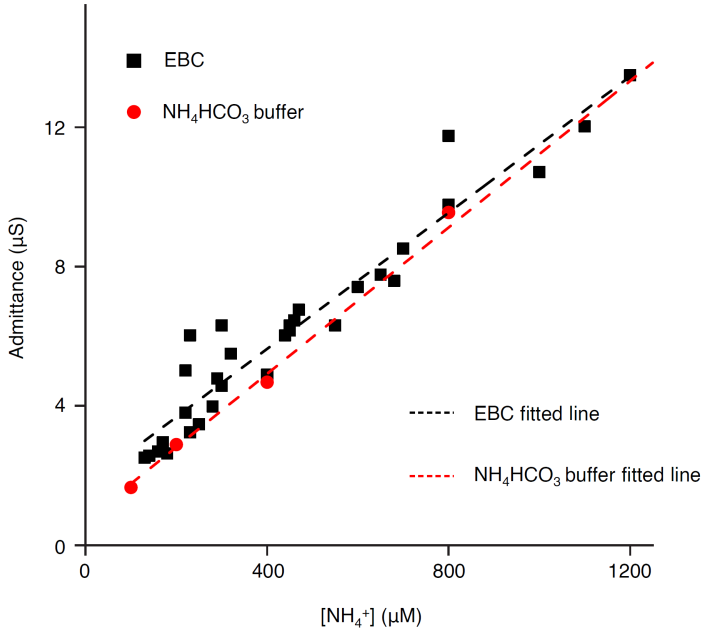

Figure A-31. The relationship between the admittance and NH_4^+ concentration in EBC samples collected from participants (n=31 biological replicates from N=7 independent healthy participants).

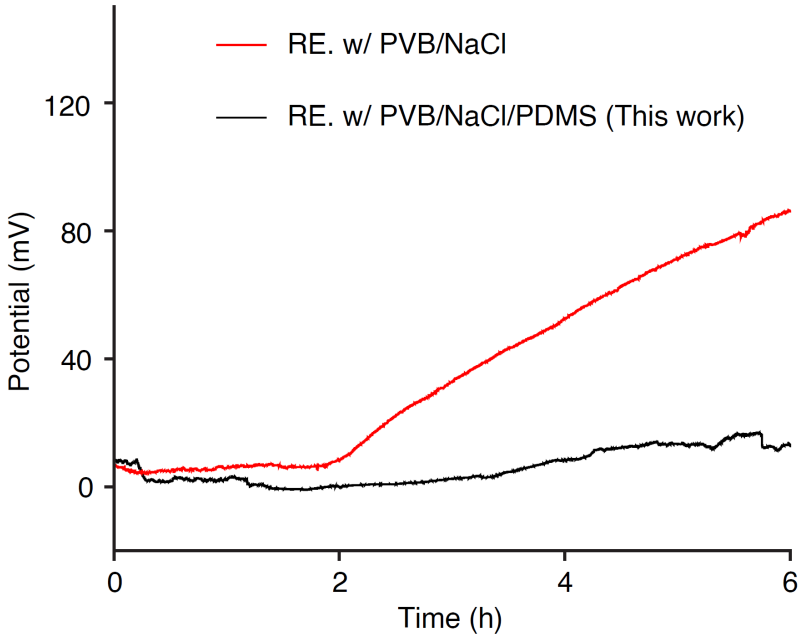

Figure A-32. Open circuit potential of different reference electrode structures in the sensing array when exposed to EBC (versus a commercial Ag/AgCl reference electrode). RE. reference electrode; PVB, polyvinyl butyral; PDMS, polydimethylsiloxane.

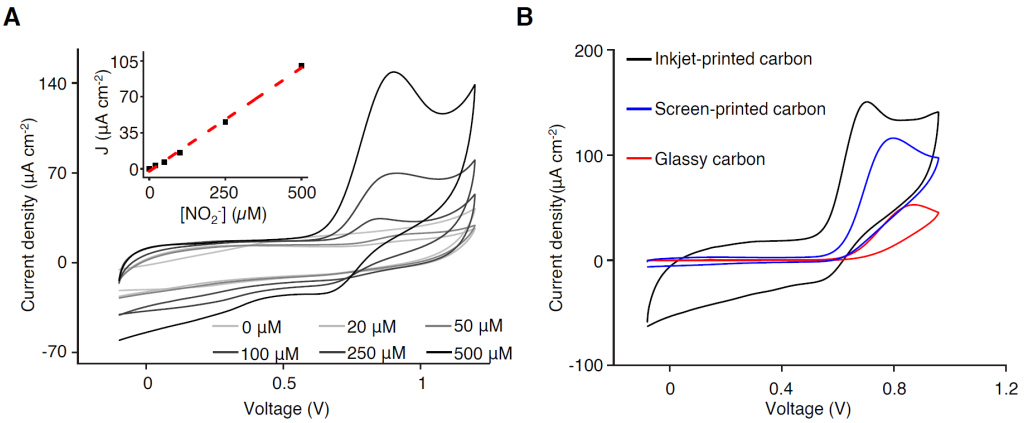

Figure A-33. Cyclic voltammetry of NO_2^- detection. (**A**) Cyclic Voltammetry and the corresponding calibration plots based on oxidation peak height using inkjet-printed carbon electrodes for NO_2^- detection. (**B**) Cyclic voltammetry of an inkjet-printed carbon electrode, a screen-printed carbon electrode, and a glassy carbon electrode in a 500 µM NO_2^- solution.

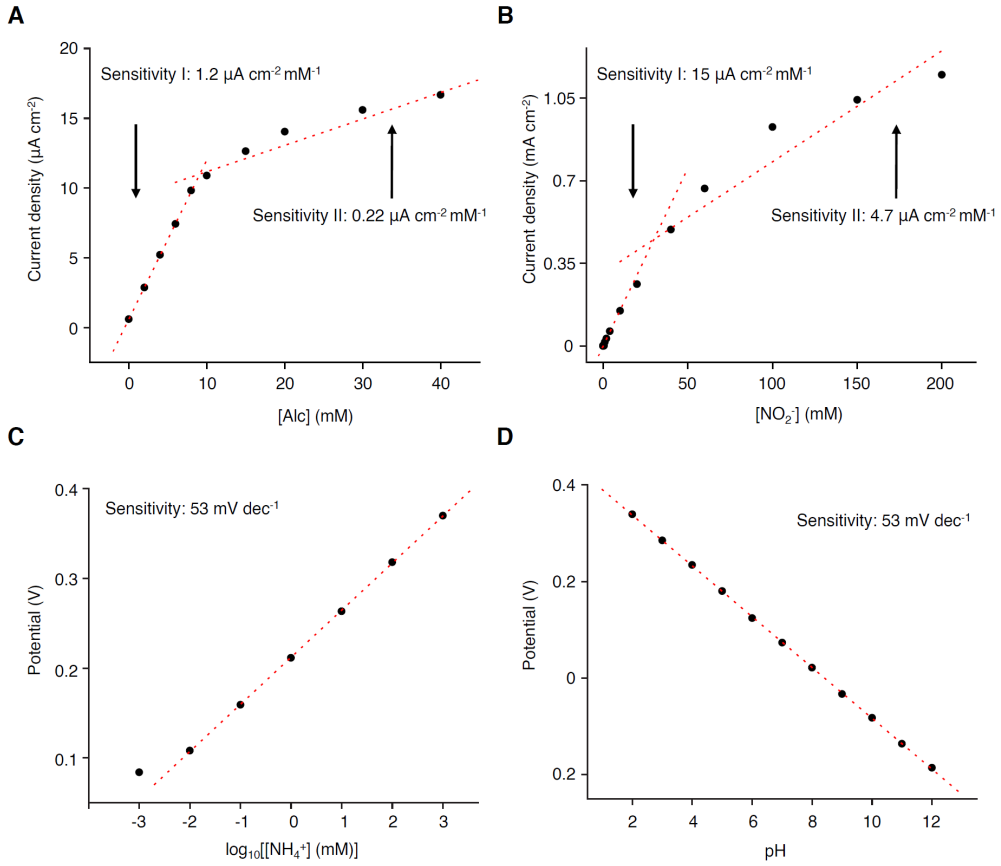

Figure A-34. The sensitivity and saturation characteristics of electrochemical sensors at different analyte concentrations. (**A**) Alcohol sensor. (**B**) NO_2^- sensor. (**C**) NH_4^+ sensor. (**D**) pH sensor.

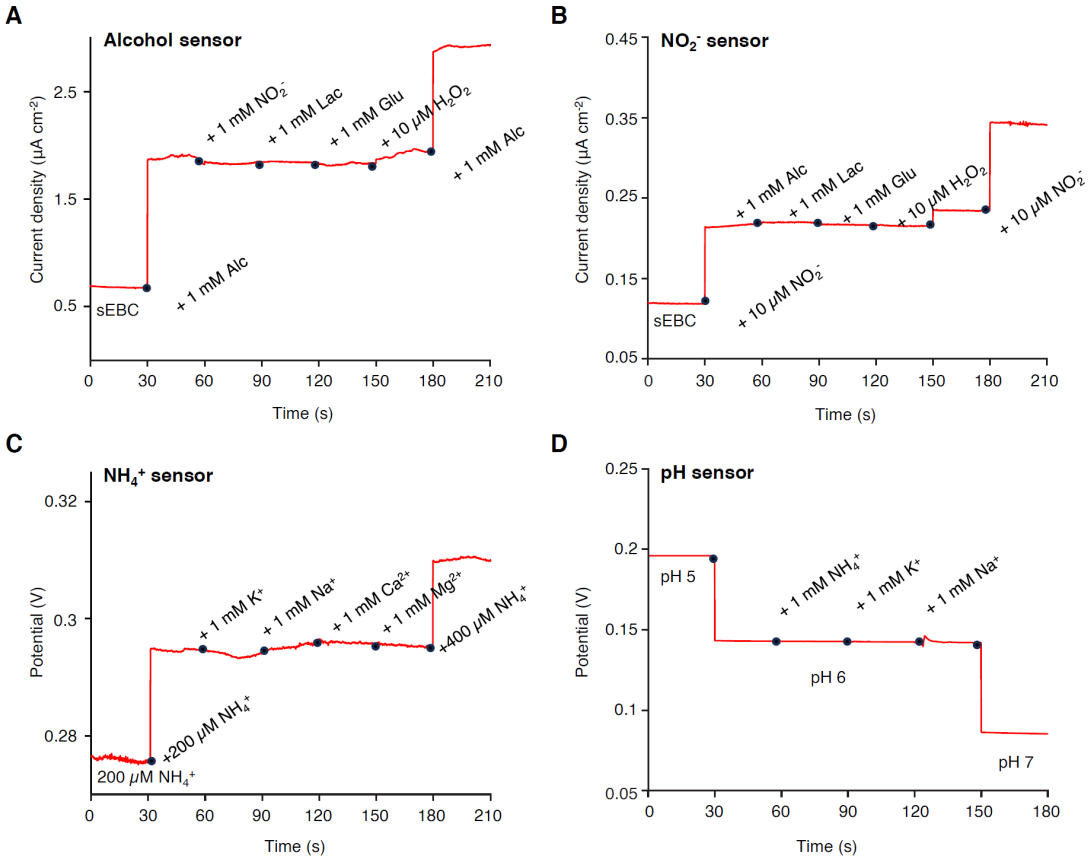

Figure A-35. Selectivity of the biosensors in sEBC. (**A** and **B**) Selectivity of the NO_2^- (A) and alcohol (B) sensors against other metabolites and electrolytes in sEBC. Alc, alcohol, Lac, lactate, Glu, glucose. (**C** and **D**) Selectivity of the NH_4^+ (C) and pH (D) sensors against other ions.

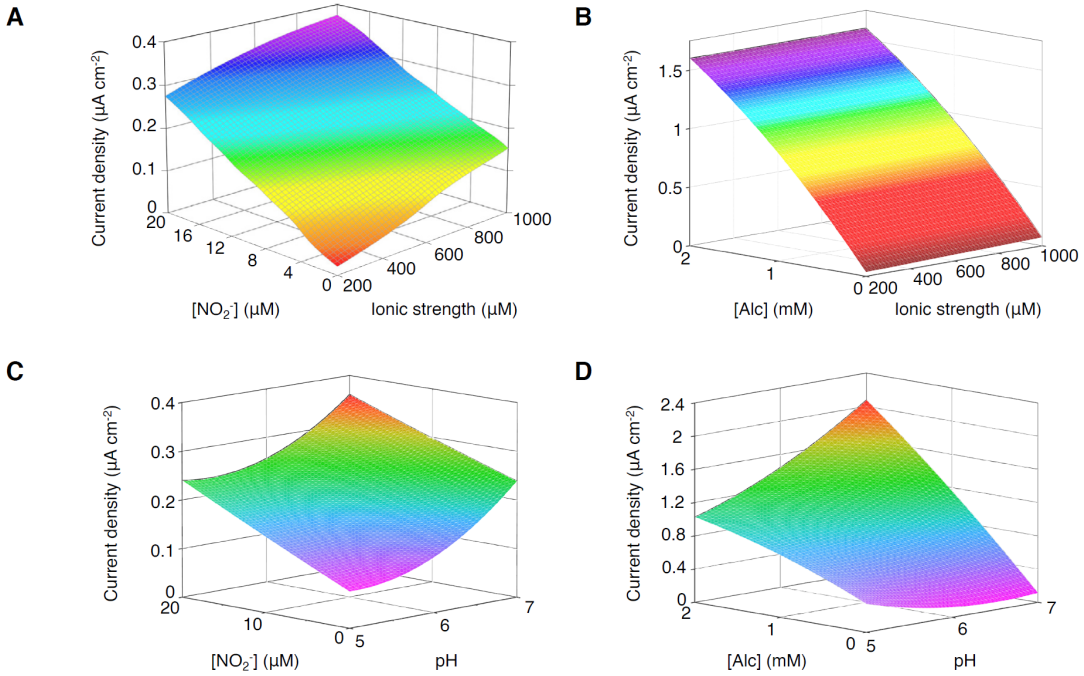

Figure A-36. The performance of biosensors under different pH and ionic strength conditions. (**A** and **B**) Color map showing the dependence of the NO_2^- (A) and alcohol (B) sensor response on ionic strength (labeled as NH_4HCO_3 concentration). (**C** and **D**) Color map showing the dependence of the amperometric NO_2^- (C) and alcohol (D) sensor responses on sEBC pH.

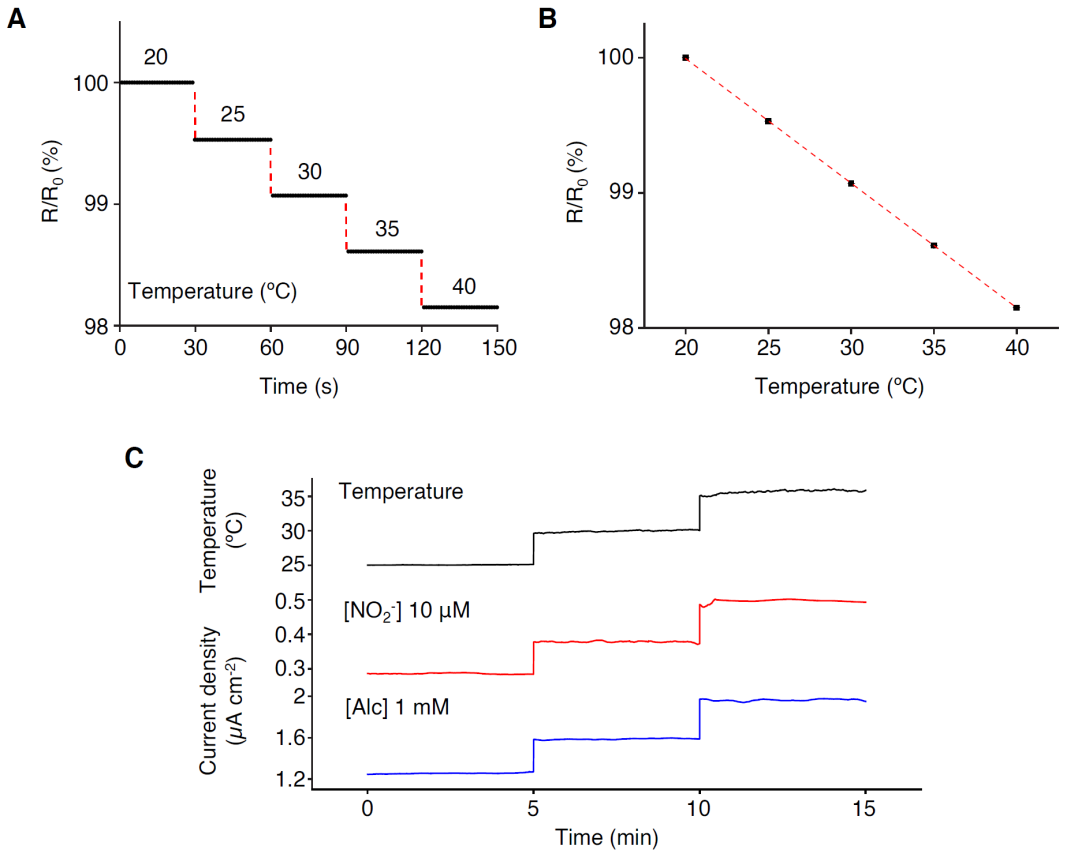

Figure A-37. Characterization of the inkjet-printed carbon-based resistive temperature sensor. (**A** and **B**) Dynamic response of the temperature sensor under physiologically relevant temperature (A) and the corresponding calibration plot between the relative resistance and temperature (B). (**C**) The current responses of amperometric NO_2^- and alcohol sensors in sEBC under varied temperature.

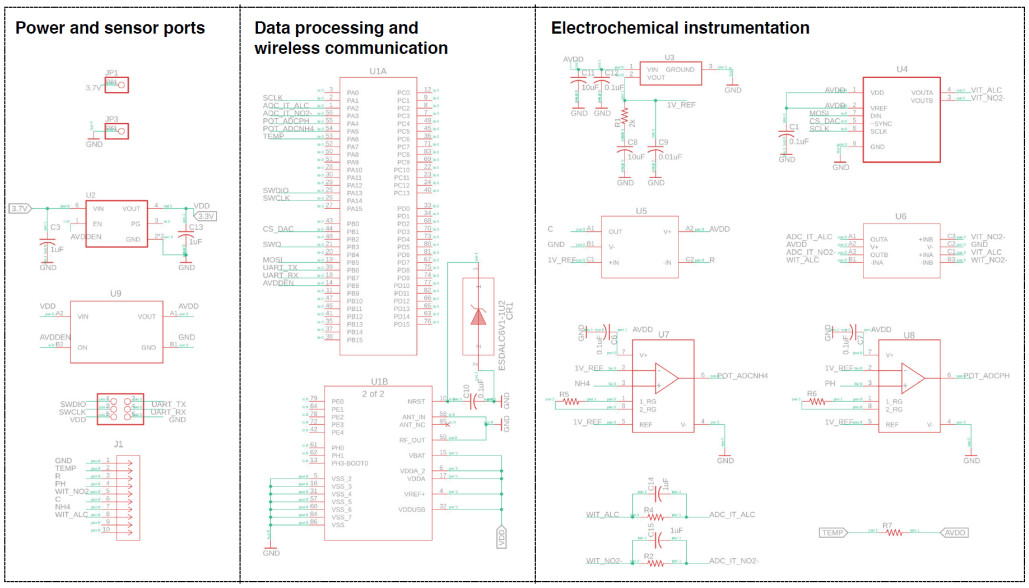

Figure A-38. Circuit schematic of EBCare's electronic system. The system contains 3 main blocks, including power management and sensor ports, electrochemical instrumentation, and data processing and wireless communication.

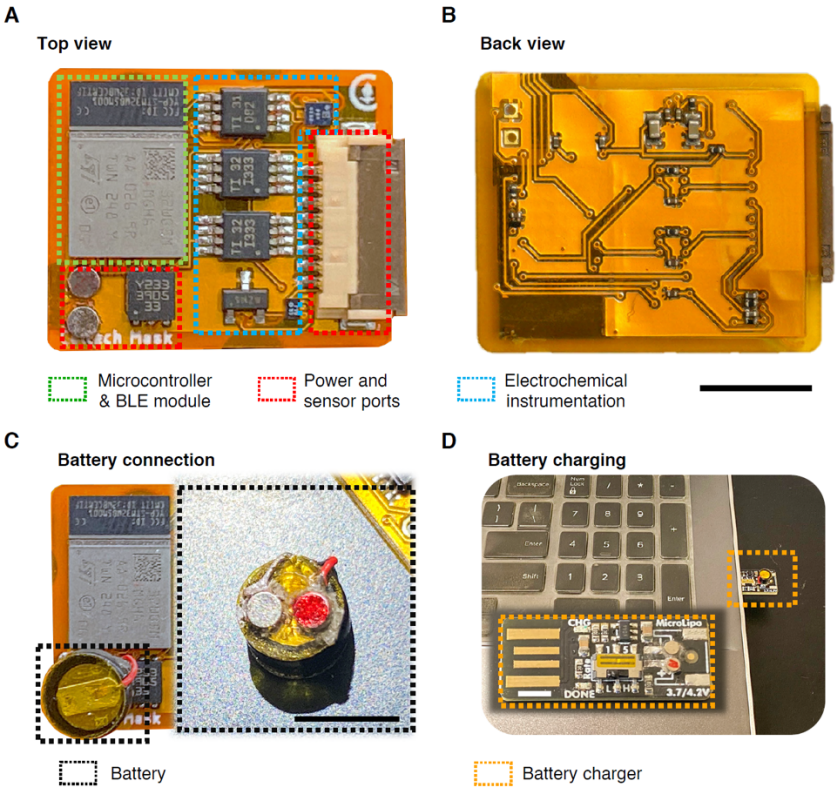

Figure A-39. The miniaturized FPCB of EBCare system. (**A** and **B**) top view (A) and back view (B). Scale bar, 5 mm. (**C** and **D**) Lithium polymer coin battery connection on FPCB (C) and battery charging on a USB charger (D). Scale bars, 5 mm.

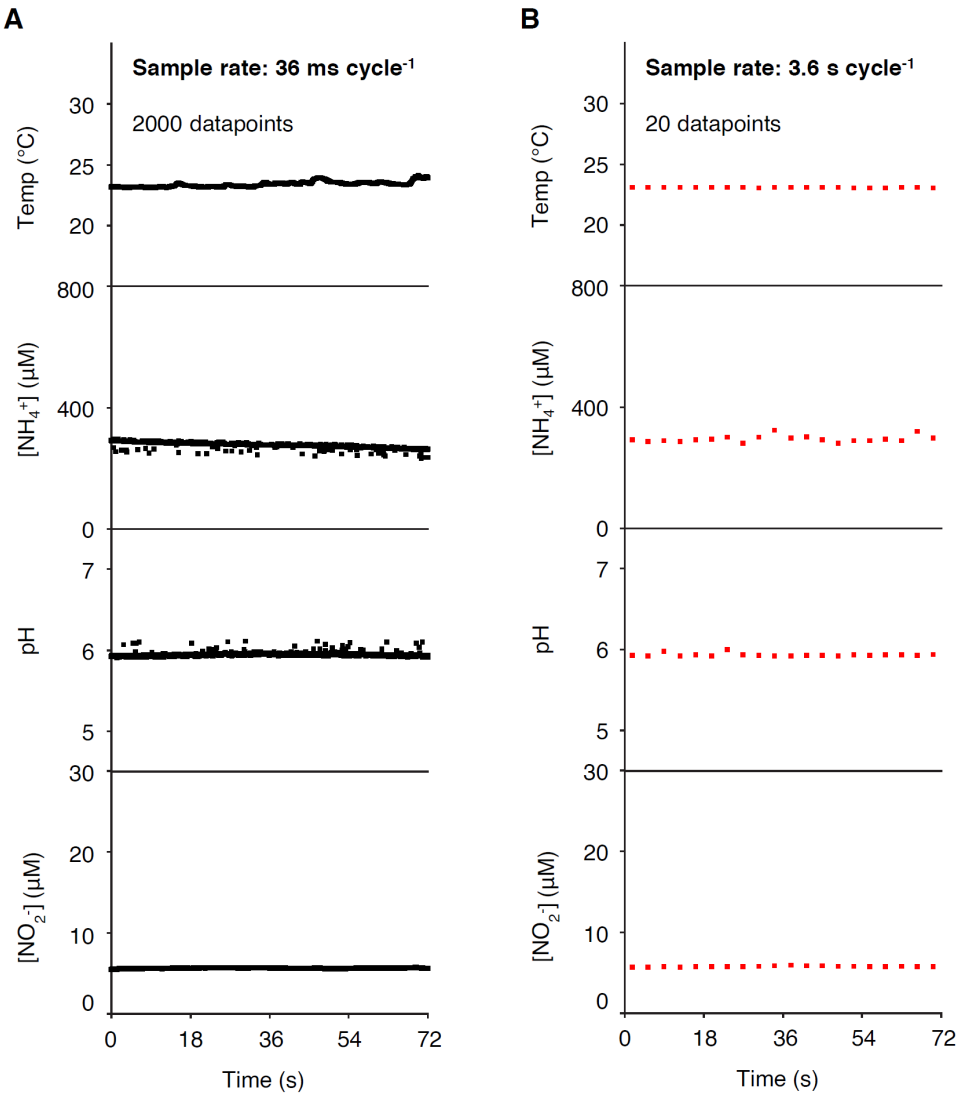

Figure A-40. Continuous signals acquired from the FPCB readout circuit at different sampling rates. (**A**) Each sampling cycle has a duration of 36 milliseconds, corresponding to a sampling frequency of approximately 100 Hz. (**B**) Each sampling cycle has a duration of 3.6 seconds, corresponding to a sampling frequency of approximately 1 Hz.

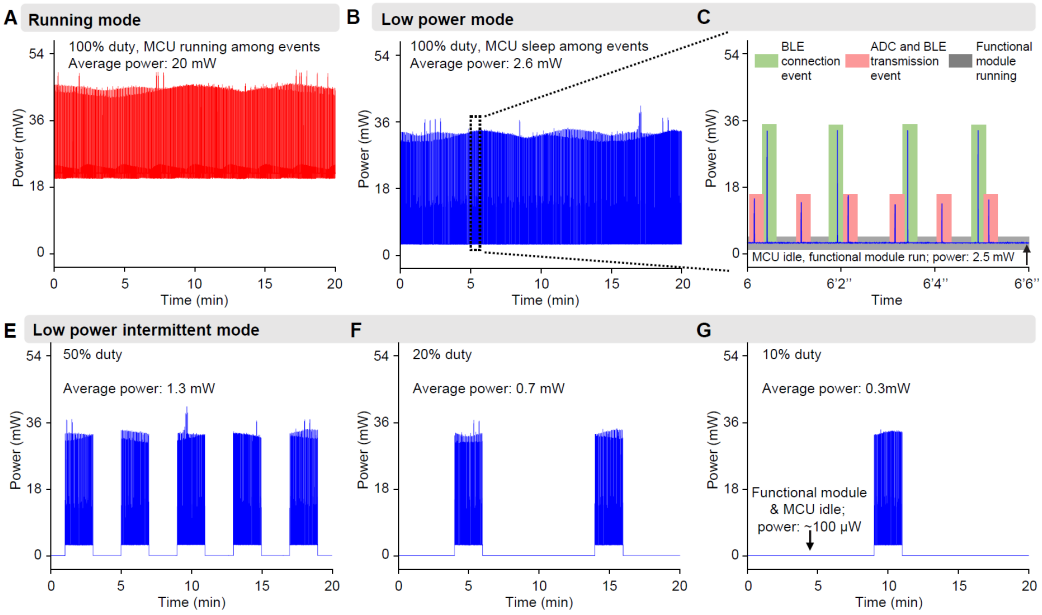

Figure A-41. Power profiling of EBCare's readout circuitry. (**A**) Running mode. (**B** and **C**) Overall and instantaneous power profiling of the low power mode. (**E** to **G**) Low power intermittent mode at different work duty cycles.

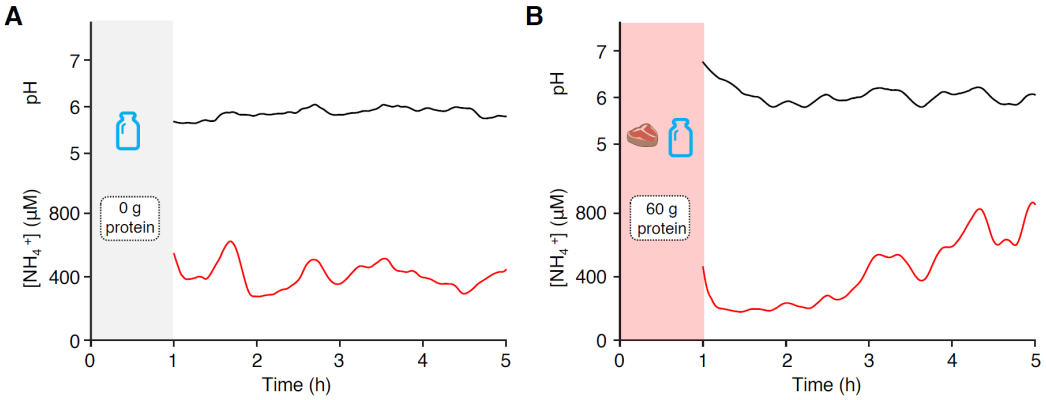

Figure A-42. Evaluation of the EBCare device for multiplexed physiological monitoring in situ through a protein challenge on a healthy participant. (**A**) Control fasting group. (**B**) Protein challenge group.

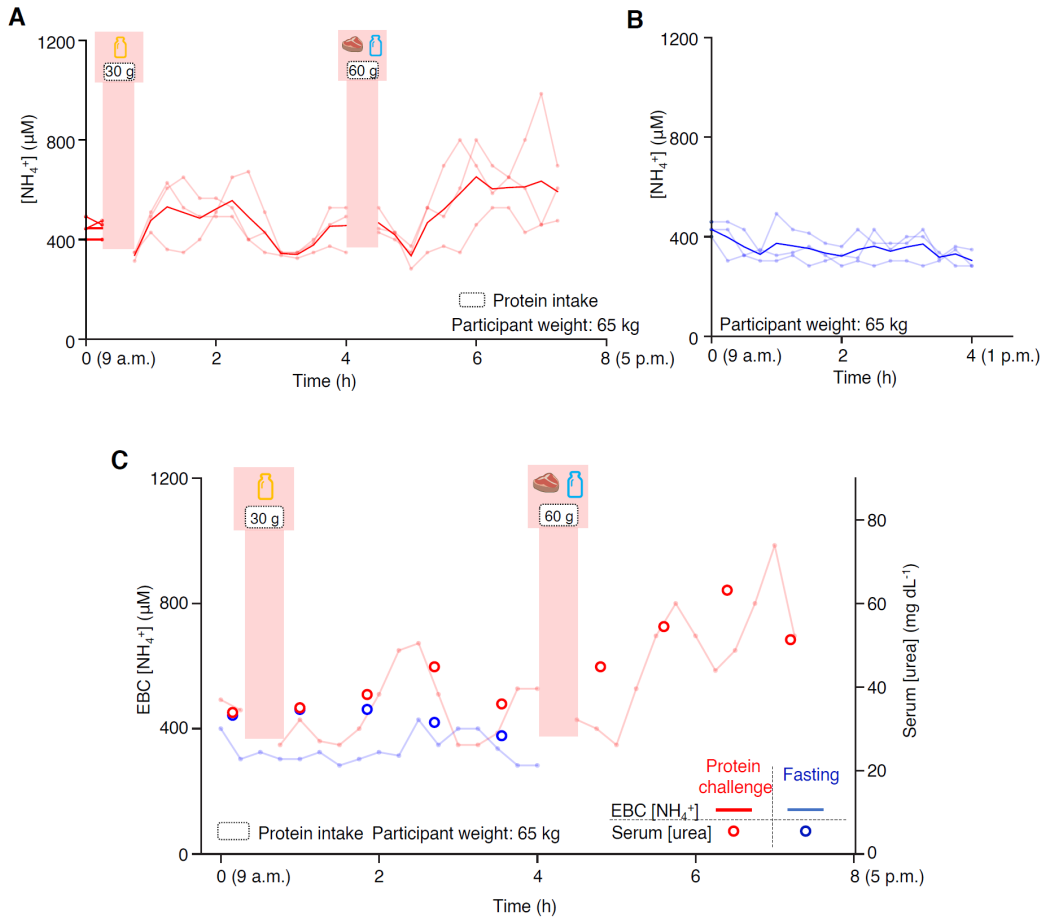

Figure A-43. In vitro dynamic EBC NH_4^+ monitoring through protein challenges on a healthy participant #1. (**A**) EBC NH_4^+ concentration increased in the participant during the protein challenges on 3 different days. (**B**) EBC NH_4^+ concentration monitored for 4 hours without dietary intake on 3 different days. (**C**) EBC NH_4^+ levels vs. serum urea concentration during fasting conditions and during a protein challenge. Hollow points indicate the serum urea concentration.

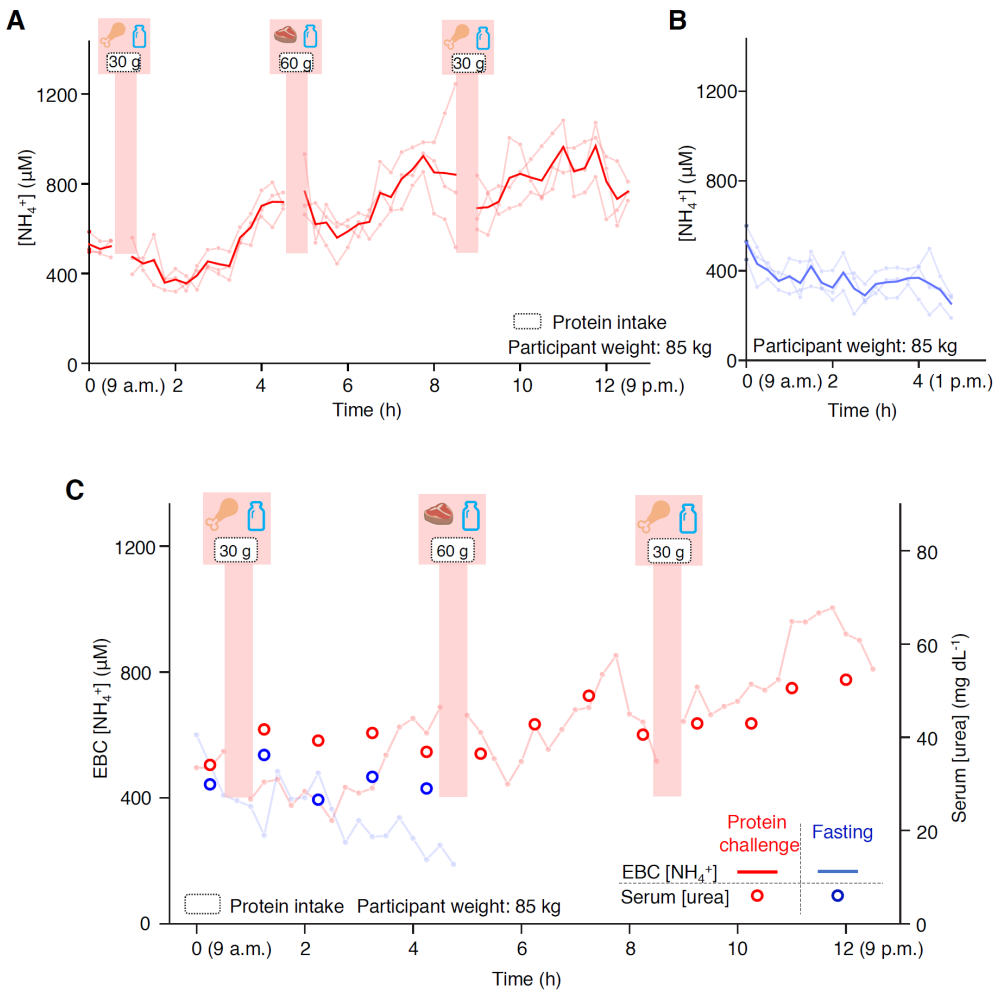

Figure A-44. In vitro dynamic EBC NH_4^+ monitoring through protein challenges in a healthy participant #2. (**A**) EBC NH_4^+ concentration increased in the participant during the protein challenges on 3 different days. (**B**) EBC NH_4^+ concentration monitored for 4 hours without dietary intake on 3 different days. (**C**) EBC NH_4^+ levels vs. serum urea concentration during fasting conditions and during a protein challenge. Hollow points indicate the serum urea concentration.

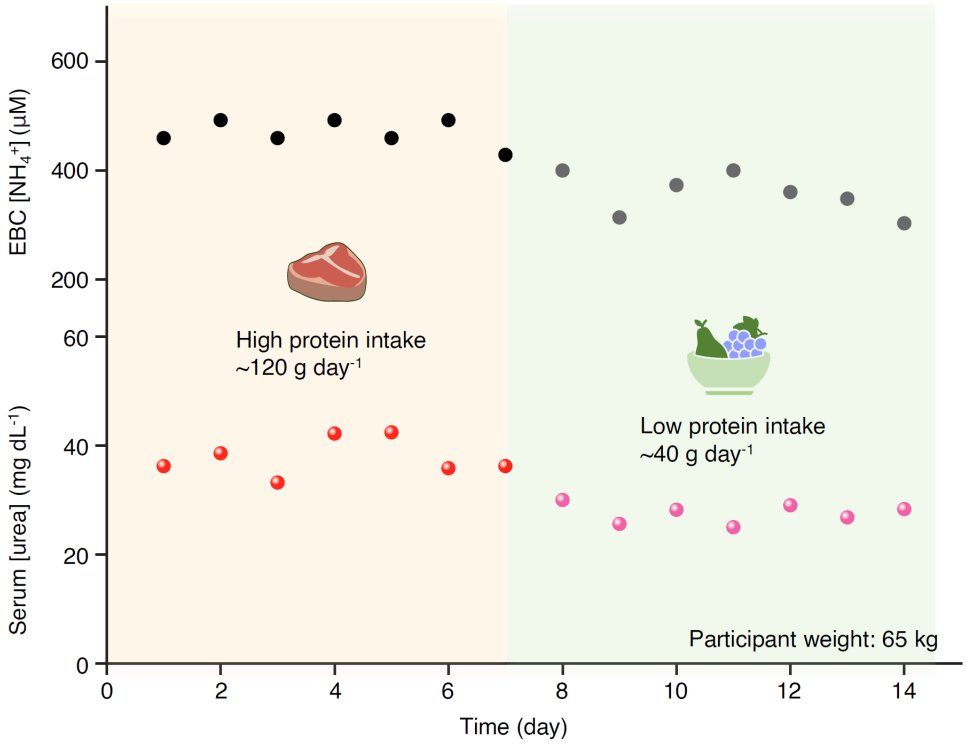

Figure A-45. In vitro dynamic morning EBC NH_4^+ and serum urea monitoring through controlled high-protein and low-protein dietary intakes over 2 weeks (measured every morning on fasting).

Figure A-46. Photographs of patients with COPD or asthma wearing EBCare masks in the clinical studies.

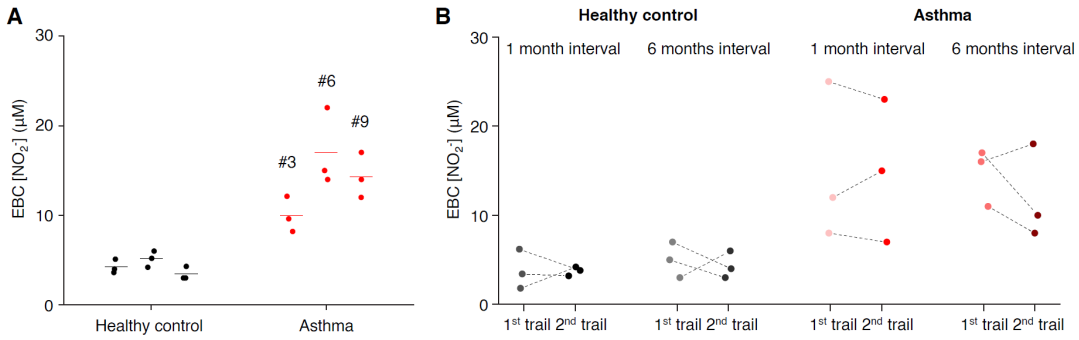

Figure A-47. Repeatability and longitude studies on variations in EBC NO_2^- levels among healthy participants and patients with asthma. (**A**) Repeatability within 1 hour. # means the asthma patient's sequential number (n=18 biological replicates from N=3 independent health participants and N=3 independent asthma patients). (**B**) Long-term follow-up of EBC NO_2^- concentrations. (n=24 biological replicates from N=3 follow-up healthy controls at 1-month intervals; N=3 follow-up healthy controls at 5-month intervals; N=3 asthmatics at 1-month intervals; N=3 asthmatics at 5-month intervals. All of participants are independent).

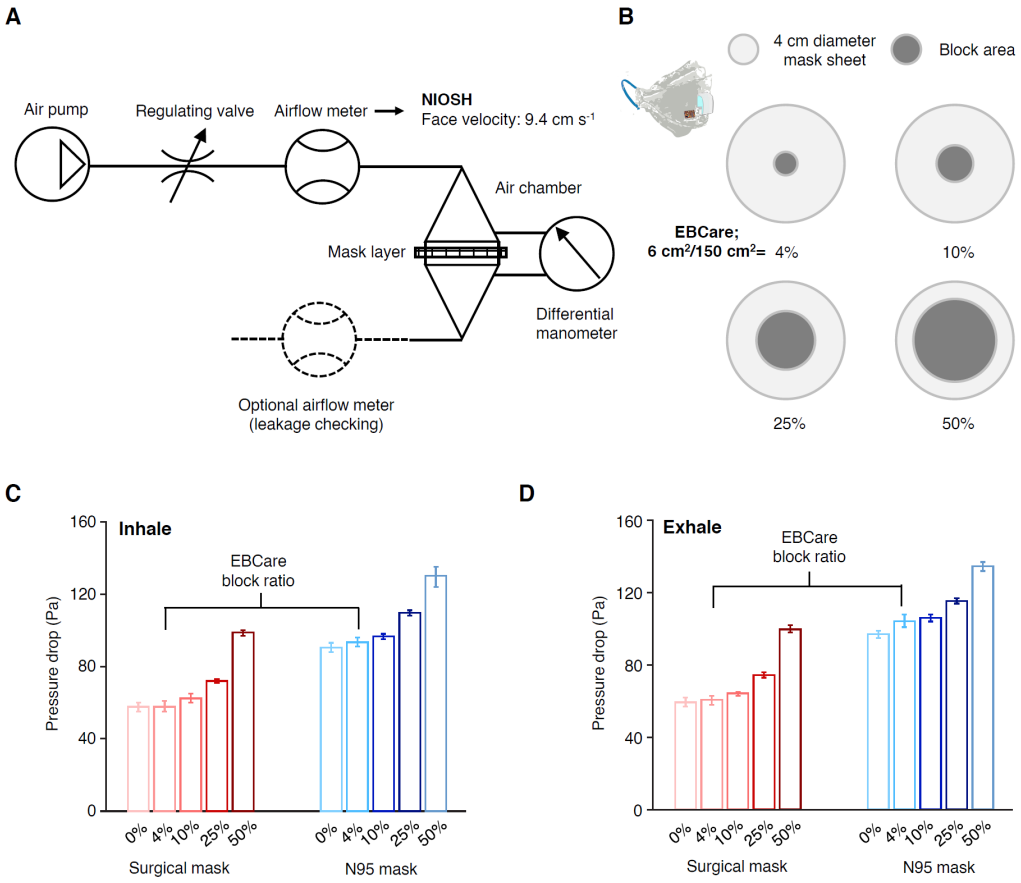

Figure A-48. Air pressure drop measurements for the breathability test of EBCare masks. (**A**) Experimental setup for pressure drops measurement. (**B**) The mask sheet and blockage area design for testing. (**C** and **D**) The pressure drops of mask samples under inhale and exhale air flowing direction. All data are presented as mean values ± S.D. from 3 measurements.

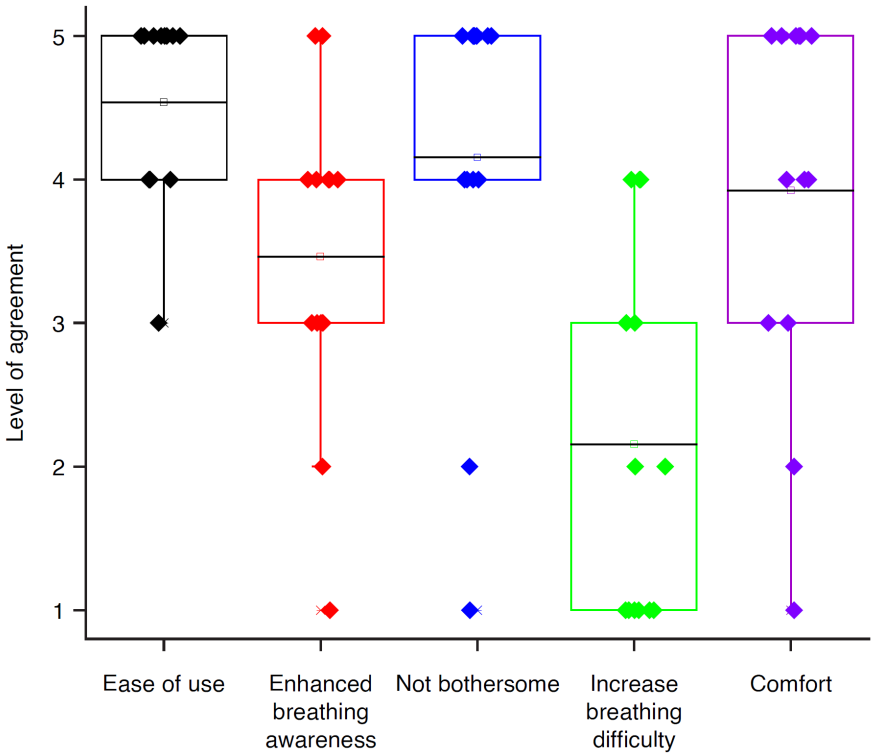

Figure A-49. The breathability questionnaire results (scale 1–5) from patients with COPD or asthma using the EBCare mask. The bottom whisker represents the minimum, the top whisker represents the maximum and the square in the box represents the mean from 15 questionnaires.

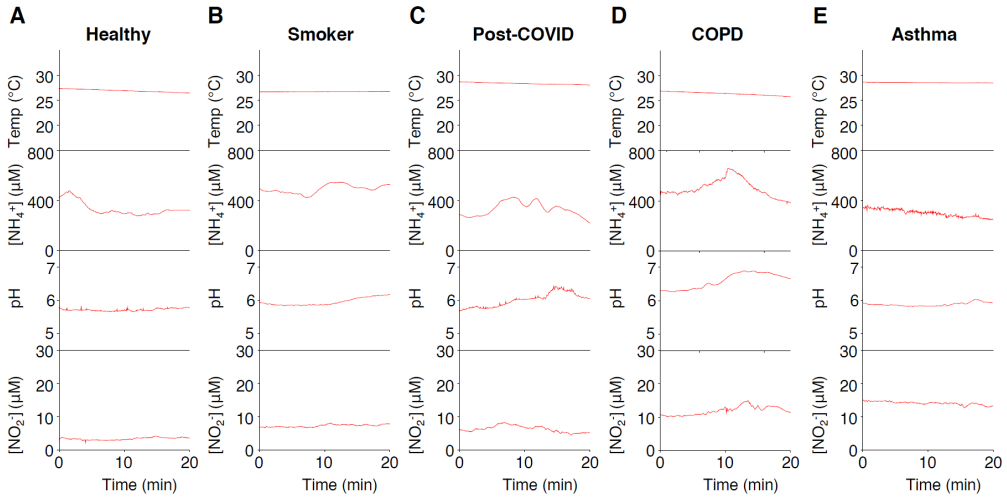

Figure A-50. On-body multiplexed EBC analysis with real-time sensor calibrations using the EBCare mask from (**A**) A healthy subject. (**B**) A current smoker. (**C**) A subject newly recovered from COVID-19. (**D**) A patient with COPD. (**E**) A patient with asthma.

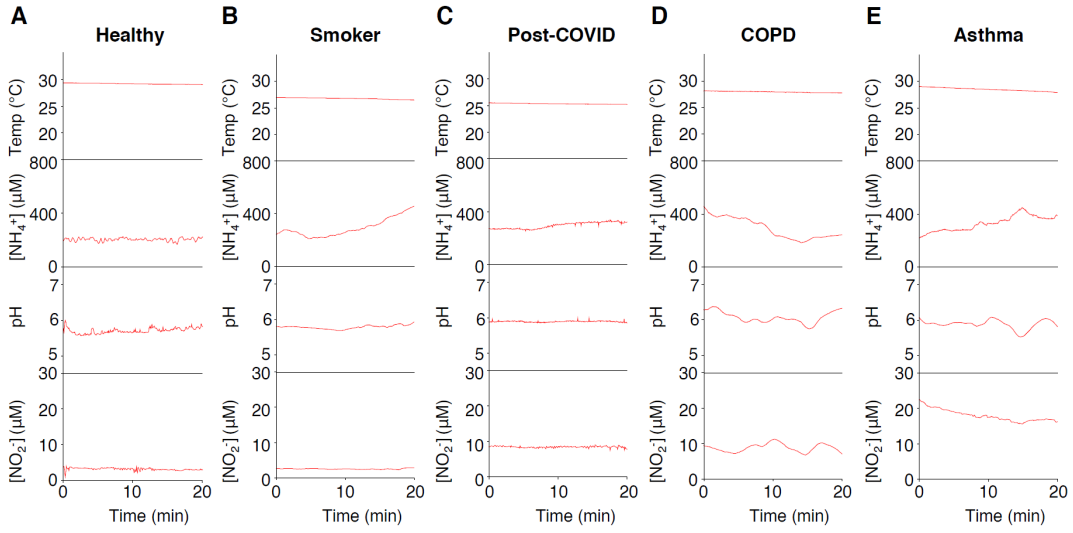

Figure A-51. On-body multiplexed EBC analysis with real-time sensor calibrations using the EBCare mask from (**A**) A healthy subject. (**B**) A current smoker. (**C**) A subject newly recovered from COVID-19. (**D**) A patient with COPD. (**E**) A patient with asthma.

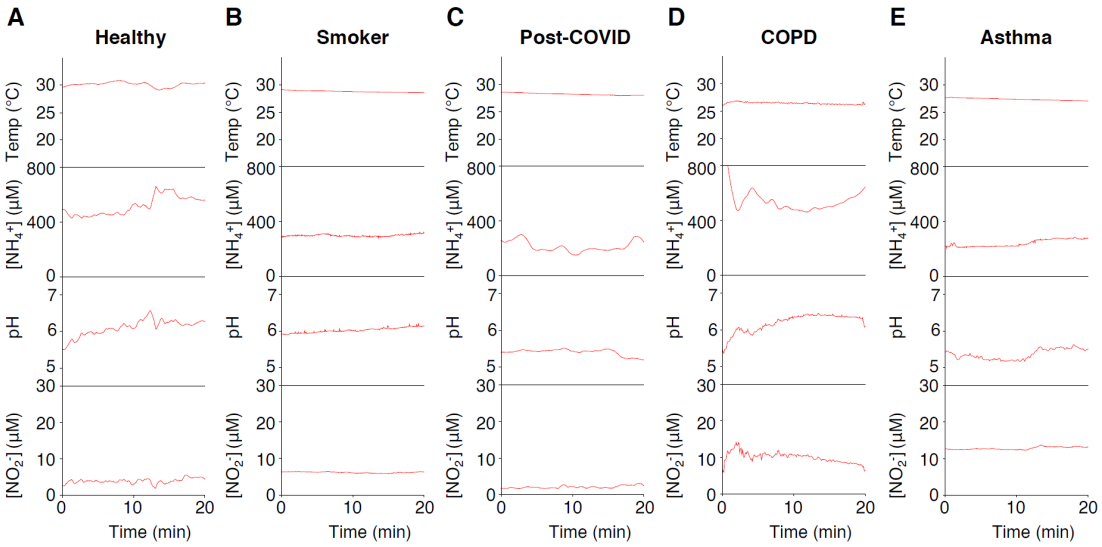

Figure A-52. On-body multiplexed EBC analysis with real-time sensor calibrations using the EBCare mask from (**A**) A healthy subject. (**B**) A current smoker. (**C**) A subject newly recovered from COVID-19. (**D**) A patient with COPD. (**E**) A patient with asthma.

Table A-1. Analysis of human breath of non-gaseous chemicals. *POC, point of care device; Multiple, various analysts including proteins, IL-6, H_2O_2, pH, NO_2^-, etc. Dimensions and lifespans estimated from references are marked ~.

Name	Commercial /Custom	Collection/ POC/Continuous	Size/mass	Analyst	Measurement	Wearable /Wireless	Source	Sample type	Cooling power /lifespan
R-tube *(8, 60, 61)*	Commercial	Collection	3.5*10*29 cm^3/0.44 kg	Multiple	In-vitro	-	Mouth/mechanical ventilation	EBC	Aluminum-Refrigerator/ ~10 minutes
EcoScreen I & II *(62-64)*	Commercial	Collection	30*40*50 cm^3 /20 kg	Multiple	In-vitro	-	Mouth/mechanical ventilation	EBC	Peltier/-
Turbo DECCS *(65,66)*	Commercial	Collection	16*19*28.5 cm^3 /3.9 kg	Multiple	In-vitro	-	Mouth	EBC	Peltier/-
ANACON *(67)*	Commercial	Collection	>45 cm/-	Multiple	In-vitro	-	Mouth/mechanical ventilation	EBC	Peltier/-
Cooling tube in ice-water *(68)*	Custom	Collection	~30 cm-1.5 m	Multiple	In-vitro	-	Mouth	EBC	Ice water/ ~30 minutes
Ice-mask *(69)*	Custom	POC	~10 cm/-	SARS-CoV-2	In-vitro	Wearable/-	Mouth	EBC	Mask-Refrigerator/ ~10 minutes
Handhold EBC testers *(70,71)*	Custom	POC	~10 cm/-	Lactate/H_2O_2	In-vitro	-	Mouth	EBC	Peltier/-
Paper-based breath analyzer *(26)*	Custom	Continuous	~5 cm/-	H_2O_2	Real-time	Wearable/-	Simulated breath	Moist breath in paper	No cooling
POC devices for pathogen test *(28, 29, 72)*	Custom	POC	~5 cm/-	Pathogens	Real-time qualitative analysis	Wearable & Wireless	Mouth	Breath vapor dissolved in water	No cooling
EBCare mask (this work)	**Custom**	**Continuous**	**1*3*3 cm^3/6 g**	**NO_2^-, NH_4^+,alcohol, pH, temperature**	**Real-time quantitative measurement**	**Wearable & Wireless**	**Nose/Mouth**	**EBC**	**Hydrogel and radiative tandem cooling/ > 8 hours**

Table A-2. Component mass of an EBCare device.

Component	Mass
Framework	4 g
Hydrogel	1.6 g
Flexible PCB	0.7 g
Battery	0.4 g
Sensors	40 mg
Total	**6.8 g**

Table A-3. EBC harvesting rate of the EBCare mask from a healthy participant across diverse environmental conditions.

Study ID	Time	Ambient temperature (°C)	Ambient humidity (%)	Solar irradiance (W m^{-2})	Wind speed (m s^{-1})	Collection rate (μL min^{-1})
1	12:00	33	30	800	0.5	3.8
2	17:00	27	45	500	2	5.2
3	14:00	32	20	850	1	4.3
4	9:00	23	85	100	1	4.5
5	20:00	16	30	0	0.8	5.5

Table A-4. List of discrete components, related power consumption and battery life used in the EBCare electronic system. * Low power mode.

Position	Component	Package	Function	Power consumption*
U1	STM32WB5MMGH6TR	86-LFLGA Module	MCU&BLE	~0.2 mA/ 0.6 mW
U2	LD39050PU33R	6-VDFN Exposed Pad	DC-DC	~0.02 mA/ 0.1 mW
U3	ISL60002BIH310Z-TK	SOT-23-3	LDO	-
U4	DAC8552IDGKT	8-VSSOP	DAC	~0.4 mA/ 1.3 mW
U5	AD8505ACBZ-REEL	5-WLCSP	AFE	~0.03 mA/ 0.1 mW
U6	AD8506ACBZ-REEL7	8-WLCSP	TIA	~0.02 mA/ 0.1 mW
U7, U8	INA333AIDGKR	8-VSSOP	INA	~0.06 mA×2/ 0.4 mW -
U9	TPS22916	WCSP (4)	Switch	
C1,C6,C7,C10,C12	GRM033R61A104ME15D	0201	-	-
C9	GRM033R61A103KA01D	0201	-	-
C3,C13,C14,C15	GRM033R61A105ME44D	0201	-	-
C8,C11	GRM155R60J106ME05J	0402	-	-
R1	ERJ-1GNF2001C	0201	-	-
R2	ERJ-1GNF1004C	0201	-	-
R7	ERJ-1GNF1003C	0201	-	~0.02 mA/ 0.1 mW
R5, R6	ERJ-1GNF2492C	0201	-	-
R4	ERJ-1GNJ205C	0201	-	-
CR1	ESDALC6V1-1U2	0201	-	-
Total				~0.8 mA/ 2.6 mW
7 mAh battery life	100% duty: ~8 hours	50% duty: ~16 hours	20% duty: ~40 hours	10% duty: ~80 hours

Table A-5. The cost analysis of the EBCare device.

Material	Single cost	Amount/Sensor	Cost/Sensor ($)
Inks (Au, Carbon, Su-8)	$ 30,2,10 ml^{-1}	~0.5 ml/100 pcs	0.21
PET substrate Sensor	$4 m^{-2}	20×12 cm^2	0.1
preparation	-	-	0.33
Sensor total	-	-	**~0.64**
PDMS	$0.175 g^{-1}	2 g	0.35
PDMS-b-PEG	$0.21 g^{-1}	40 mg	0.01
Al_2O_3 microsphere	$0.05 g^{-1}	2 g	0.1
Agarose	$2.3 g^{-1}	24 mg	0.06
Ag nanoparticles	$13 g^{-1}	6.4 mg	0.08
Framework total	-	-	**~0.6**
EBCare total	-	-	**~1.2**
Reuseable readout PCB			~40

Table A-6. Asthma patient information for the airway inflammation study. BMI, body mass index (kg m^{-2}).

Study ID	Sex	Age	BMI	Asthma severity	Smoking status	Number of exacerbation(s) in previous year	Exacerbation severity	1st EBC [NO_2^-] (μM)	2nd EBC [NO_2^-] (μM)
1	M	59	27.9	Moderate	Non-smoker	0	n/a	11.1	8.0 (after 5 months)
2	F	61	25.9	Severe	Non-smoker	1	Moderate	20.0	n/a
3	M	29	27.1	Moderate	Current smoker	0	n/a	17.2	10.0 (after 5 months)
4	F	36	37.0	Moderate	Non-smoker	0	n/a	16.7	n/a
5	F	60	37.2	Mild	Current smoker	0	n/a	13.3	n/a
6	M	72	25.9	Severe	Non-smoker	0	n/a	17.2	18.0 (after 5 months)
7	M	82	28.1	Severe	Former smoker	>2	Severe	9.0	n/a
8	M	69	24.9	Moderate	Non-smoker	0	n/a	8.0	7.0 (after 1 month)
9	M	63	30.7	Moderate	Non-smoker	0	n/a	12.0	15.0 (after 1 month)
10	F	58	26.3	Moderate	Current smoker	0	n/a	25.0	23.0 (after 1 month)

Table A-7. COPD patient information for the airway inflammation study. *GOLD classification: the Global Initiative for Chronic Obstructive Lung Disease severity status for COPD.

Study ID	Sex	Age	BMI	GOLD classification	Smoking status	Number of exacerbation(s) in previous year	Exacerbation severity	EBC [NO_2^-] (μM)
1	M	59	30.9	4	Former smoker	0	n/a	16.3
2	F	70	29.5	3	Current smoker	0	n/a	12.2
3	F	62	33.7	3	Current smoker	1	Severe	1.5
4	M	76	31.9	3	Former smoker	0	n/a	11.1
5	M	64	31.1	2	Former smoker	0	n/a	8.0
6	M	82	28.4	4	Former smoker	0	n/a	12.5
7	M	69	31.4	3	Current smoker	0	n/a	3.0
8	M	74	38.9	3	Former smoker	1	Moderate	7.5
9	M	69	27.2	3	Former smoker	1	Severe	26.0

Table A-8. Participant information for the post-COVID-19 infection study.

Study ID	Symptom	Sex	Days from recovery	EBC [NO_2^-] (μM)
1	Mild	M	3	3.8
2	Mild	F	5	5.2
3	Mild	M	5	12.1
4	Moderate	F	10	3.8
5	Moderate	F	5	10.0
6	Moderate	M	3	15.3
7	Moderate	M	7	20.0
8	Mild	F	30	5
9	Mild	F	15	6.5
10	Mild	M	8	7.6
11	Mild	F	25	2
12	Mild	M	20	7

Table A-9. Results of the breathability questionnaires (scale 1–5) completed by patients with COPD or asthma using the EBCare mask.

Study ID	Wearing the SmartMask was easy	Wearing the SmartMask made me more aware of my breathing	I was not bothered by wearing the SmartMask	Wearing the SmartMask increased my difficulty of breathing	The SmartMask was comfortable to wear
Asthma #1	4	4	4	3	4
Asthma #3	3	3	1	4	1
Asthma #5	5	3	5	4	4
Asthma #6	5	3	5	1	3
Asthma #7	5	2	5	1	5
Asthma #8	5	4	4	2	3
Asthma #9	5	5	5	1	5
Asthma #10	4	4	4	3	5
COPD #1	5	5	5	1	5
COPD #2	5	1	5	1	5
COPD #3	4	4	2	4	2
COPD #4	5	3	5	1	5
COPD #5	4	4	4	2	4

Bibliography of Appendix A

1. C. C. Wang, K. A. Prather, J. Sznitman, J. L. Jimenez, S. S. Lakdawala, Z. Tufekci, L. C. Marr, Airborne transmission of respiratory viruses. *Science* **373**, eabd9149 (2021).

2. I. Horváth, J. Hunt, P. J. Barnes, Exhaled breath condensate: methodological recommendations and unresolved questions. *Eur. Respir. J.* **26**, 523–548 (2005).

3. W. Ibrahim, M. J. Wilde, R. L. Cordell, M. Richardson, D. Salman, R. C. Free, B. Zhao, A. Singapuri, B. Hargadon, E. A. Gaillard, Visualization of exhaled breath metabolites reveals distinct diagnostic signatures for acute cardiorespiratory breathlessness. *Sci. Transl. Med.* **14**, eabl5849 (2022).

4. R. A. Dweik, P. B. Boggs, S. C. Erzurum, C. G. Irvin, M. W. Leigh, J. O. Lundberg, A.-C. Olin, A. L. Plummer, D. R. Taylor, An official ATS clinical practice guideline: Interpretation of exhaled nitric oxide levels (FeNO) for clinical applications. *Am. J. Respir. Crit. Care Med.* **184**, 602–615 (2011).

5. P. J. Barnes, Inflammatory mechanisms in patients with chronic obstructive pulmonary disease. *J. Allergy Clin. Immunol.* **138**, 16–27 (2016).

6. N. H. L. Leung, D. K. W. Chu, E. Y. C. Shiu, K.-H. Chan, J. J. McDevitt, B. J. P. Hau, H.-L. Yen, Y. Li, D. K. M. Ip, J. S. M. Peiris, W.-H. Seto, G. M. Leung, D. K. Milton, B. J. Cowling, Respiratory virus shedding in exhaled breath and efficacy of face masks. *Nat. Med.* **26**, 676–680 (2020).

7. G. Peng, U. Tisch, O. Adams, M. Hakim, N. Shehada, Y. Y. Broza, S. Billan, R. Abdah-Bortnyak, A. Kuten, H. Haick, Diagnosing lung cancer in exhaled breath using gold nanoparticles. *Nat. Nanotechnol.* **4**, 669–673 (2009).

8. S. F. Mosquera-Restrepo, S. Zuberogoïtia, L. Gouxette, E. Layre, M. Gilleron, A. Stella, D. Rengel, O. Burlet-Schiltz, A. C. Caro, L. F. Garcia, C. Segura, C. A. Peláez Jaramillo, M.

Rojas, J. Nigou, A Mycobacterium tuberculosis fingerprint in human breath allows tuberculosis detection. *Nat. Commun.* **13**, 7751 (2022).

9. F. Röck, N. Barsan, U. Weimar, Electronic nose: Current status and future trends. *Chem. Rev.* **108**, 705–725 (2008).

10. U. Yaqoob, M. I. Younis, Chemical gas sensors: Recent developments, challenges, and the potential of machine learning—A review. *Sensors* **21**, 2877 (2021).

11. S. Y. Park, Y. Kim, T. Kim, T. H. Eom, S. Y. Kim, H. W. Jang, Chemoresistive materials for electronic nose: Progress, perspectives, and challenges. *InfoMat* **1**, 289–316 (2019).

12. J. Hunt, Exhaled breath condensate: An evolving tool for noninvasive evaluation of lung disease. *J. Allergy Clin. Immunol.* **110**, 28–34 (2002).

13.
E. M. Konstantinidi, A. S. Lappas, A. S. Tzortzi, P. K. Behrakis, Exhaled breath condensate: Technical and diagnostic aspects. *Sci. World J. 2015*, e435160 (2015).

14. M. Khorshid, S. Bakhshi Sichani, D. L. Barbosa Estrada, W. Neefs, A. Clement, G. Pohlmann, R. Epaud, S. Lanone, P. Wagner, An efficient low-cost device for sampling exhaled breath condensate EBC. *Adv. Sens. Res.* 2400020.

15. X. Chen, X. Hu, X. Zhang, H. Huang, H. Meng, J. Yang, C. Tao, W. Zhang, X. Li, K. Zhang, Breath analysis: Harnessing its potential for non-volatile drug caffeine monitoring in human body. *Microchem. J.* **198**, 110130 (2024).

16. P. Kubáň, F. Foret, Exhaled breath condensate: Determination of non-volatile compounds and their potential for clinical diagnosis and monitoring. A review. *Anal. Chim. Acta* **805**, 1–18 (2013).

17. P. Montuschi, Exhaled breath condensate analysis in patients with COPD. *Clin. Chim. Acta* **356**, 22–34 (2005).

18. N. Hashemzadeh, E. Rahimpour, A. Jouyban, Applications of exhaled breath condensate analysis for drug monitoring and bioequivalence study of inhaled drugs. *J. Pharm. Pharm. Sci.* **25**, 391–401 (2023).

19. W. Gao, S. Emaminejad, H. Y. Y. Nyein, S. Challa, K. Chen, A. Peck, H. M. Fahad, H. Ota, H. Shiraki, D. Kiriya, D.-H. Lien, G. A. Brooks, R. W. Davis, A. Javey, Fully integrated wearable sensor arrays for multiplexed in situ perspiration analysis. *Nature* **529**, 509–514 (2016).

20. H. C. Ates, P. Q. Nguyen, L. Gonzalez-Macia, E. Morales-Narváez, F. Güder, J. J. Collins, C. Dincer, End-to-end design of wearable sensors. *Nat. Rev. Mater.* **7**, 887–907 (2022).

21. J. Kim, A. S. Campbell, B. E.-F. de Ávila, J. Wang, Wearable biosensors for healthcare monitoring. *Nat. Biotechnol.* **37**, 389–406 (2019).

22. H. C. Ates, C. Dincer, Wearable breath analysis. *Nat. Rev. Bioeng.* **1**, 80–82 (2023).

23. A. Yang, L. Cai, R. Zhang, J. Wang, P.-C. Hsu, H. Wang, G. Zhou, J. Xu, Y. Cui, Thermal management in nanofiber-based face mask. *Nano Lett.* 17, 3506–3510 (2017).

24. S. K. Pal, D. Y. Choi, G. Kim, Radiative cooling face mask. *ACS Appl. Polym. Mater.* **5**, 5888–5895 (2023).

25. X. Liu, B. Hu, Mask device as a new wearable sampler for breath analysis: what can we expect in the future? *Anal. Bioanal. Chem.* **415**, 3759–3768 (2023).

26. D. Maier, E. Laubender, A. Basavanna, S. Schumann, F. Güder, G. A. Urban, C. Dincer, Toward continuous monitoring of breath biochemistry: A paper-based wearable sensor for real-time hydrogen peroxide measurement in simulated breath. *ACS Sens.* **4**, 2945–2951 (2019).

27. P. Q. Nguyen, L. R. Soenksen, N. M. Donghia, N. M. Angenent-Mari, H. de Puig, A. Huang, R. Lee, S. Slomovic, T. Galbersanini, G. Lansberry, H. M. Sallum, E. M. Zhao, J. B. Niemi, J. J. Collins, Wearable materials with embedded synthetic biology sensors for biomolecule detection. *Nat. Biotechnol.* **39**, 1366–1374 (2021).

28. C. M. Williams, M. Abdulwhhab, S. S. Birring, E. De Kock, N. J. Garton, E. Townsend, M. Pareek, A. Al-Taie, J. Pan, R. Ganatra, A. C. Stoltz, P. Haldar, M. R. Barer, Exhaled Mycobacterium tuberculosis output and detection of subclinical disease by face-mask sampling: prospective observational studies. *Lancet Infect. Dis.* **20**, 607–617 (2020).

29. H. Li, H. Gong, T. H. Wong, J. Zhou, Y. Wang, L. Lin, Y. Dou, H. Jia, X. Huang, Z. Gao, R. Shi, Y. Huang, Z. Chen, W. Park, J. Y. Li, H. Chu, S. Jia, H. Wu, M. Wu, Y. Liu, D. Li, J. Li, G. Xu, T. Chang, B. Zhang, Y. Gao, J. Su, H. Bai, J. Hu, C. K. Yiu, C. Xu, W. Hu, J. Huang, L. Chang, X. Yu, Wireless, battery-free, multifunctional integrated bioelectronics for respiratory pathogens monitoring and severity evaluation. *Nat. Commun.* **14**, 7539 (2023).

30. Y. Zhai, Y. Ma, S. N. David, D. Zhao, R. Lou, G. Tan, R. Yang, X. Yin, Scalable-manufactured randomized glass-polymer hybrid metamaterial for daytime radiative cooling. *Science* **355**, 1062–1066 (2017).

31. H. Zhang, K. C. S. Ly, X. Liu, Z. Chen, M. Yan, Z. Wu, X. Wang, Y. Zheng, H. Zhou, T. Fan, Biologically inspired flexible photonic films for efficient passive radiative cooling. *Proc. Natl. Acad. Sci.* **117**, 14657–14666 (2020).

32. M. Park, J.-Y. Yoo, T. Yang, Y. H. Jung, A. Vázquez-Guardado, S. Li, J.-H. Kim, J. Shin, W.-Y. Maeng, G. Lee, S. Yoo, H. Luan, J.-T. Kim, H.-S. Shin, M. T. Flavin, H.-J. Yoon, N. Miljkovic, Y. Huang, W. P. King, J. A. Rogers, Skin-integrated systems for power efficient, programmable thermal sensations across large body areas. *Proc. Natl. Acad. Sci.* **120**, e2217828120 (2023).

33. J. Li, X. Wang, D. Liang, N. Xu, B. Zhu, W. Li, P. Yao, Y. Jiang, X. Min, Z. Huang, S. Zhu, S. Fan, J. Zhu, A tandem radiative/evaporative cooler for weather-insensitive and high-performance daytime passive cooling. *Sci. Adv.* **8**, eabq0411 (2022).

34. N. A. Dudukovic, E. J. Fong, H. B. Gemeda, J. R. DeOtte, M. R. Cerón, B. D. Moran, J. T. Davis, S. E. Baker, E. B. Duoss, Cellular fluidics. *Nature* **595**, 58–65 (2021).

35. M. Yao, J. Fang, Hydrophilic PEO-PDMS for microfluidic applications. *J. Micromech. Microeng.* **22**, 025012 (2012).

36. Y. Wang, W. Zhao, M. Han, J. Xu, K. C. Tam, Biomimetic surface engineering for sustainable water harvesting systems. *Nat. Water* **1**, 587–601 (2023).

37. P. P. Rosias, C. M. Robroeks, H. J. Niemarkt, A. D. Kester, J. H. Vernooy, J. Suykerbuyk, J. Teunissen, J. Heynens, H. J. Hendriks, Q. Jobsis, E. Dompeling, Breath condenser coatings affect measurement of biomarkers in exhaled breath condensate. *Eur. Respir. J.* **28**, 1036–1041 (2006).

38. R. M. Effros, R. Casaburi, J. Su, M. Dunning, J. Torday, J. Biller, R. Shaker, The effects of volatile salivary acids and bases on exhaled breath condensate pH. *Am. J. Respir. Crit. Care Med.* **173**, 386–392 (2006).

39. F. Tehrani, H. Teymourian, B. Wuerstle, J. Kavner, R. Patel, A. Furmidge, R. Aghavali, H. Hosseini-Toudeshki, C. Brown, F. Zhang, K. Mahato, Z. Li, A. Barfidokht, L. Yin, P. Warren, N. Huang, Z. Patel, P. P. Mercier, J. Wang, An integrated wearable microneedle array for the continuous monitoring of multiple biomarkers in interstitial fluid. *Nat. Biomed. Eng.* **6**, 1214–1224 (2022).

40. L. R. Narasimhan, W. Goodman, C. K. N. Patel, Correlation of breath ammonia with blood urea nitrogen and creatinine during hemodialysis. *Proc. Natl. Acad. Sci.* **98**, 4617–4621 (2001).

41. W. Chen, M. Metsälä, O. Vaittinen, L. Halonen, The origin of mouth-exhaled ammonia. *J. Breath Res.* **8**, 036003 (2014).

42. J. O. Lundberg, E. Weitzberg, M. T. Gladwin, The nitrate–nitrite–nitric oxide pathway in physiology and therapeutics. *Nat. Rev. Drug Discov.* **7**, 156–167 (2008).

43. W. Formanek, D. Inci, R. P. Lauener, J. H. Wildhaber, U. Frey, G. L. Hall, Elevated nitrite in breath condensates of children with respiratory disease. *Eur. Respir. J.* **19**, 487–491 (2002).

44. V. Rihák, P. Zatloukal, J. Chládková, A. Zimulová, Z. Havlínová, J. Chládek, Nitrite in exhaled breath condensate as a marker of nitrossative stress in the airways of patients with asthma, COPD, and idiopathic pulmonary fibrosis. *J. Clin. Lab. Anal.* **24**, 317–322 (2010).

45. M. W. H. Pijnenburg, J. C. De Jongste, Exhaled nitric oxide in childhood asthma: a review. *Clin. Exp. Allergy* **38**, 246–259 (2008).

46. S. Turner, Exhaled nitric oxide in the diagnosis and management of asthma. *Curr. Opin. Allergy Clin. Immunol.* **8**, 70–76 (2008).

47. S. Karrasch, K. Linde, G. Rücker, H. Sommer, M. Karsch-Völk, J. Kleijnen, R. A. Jörres, A. Schneider, Accuracy of FENO for diagnosing asthma: a systematic review. *Thorax* **72**, 109–116 (2017).

48. N. Murugesan, D. Saxena, A. Dileep, M. Adrish, N. A. Hanania, Update on the role of feno in asthma management. *Diagnostics* **13**, 1428 (2023).

49. FeNO Tests to Monitor FeNO Levels. https://aafa.org/asthma/asthma-diagnosis/lung-function-tests-diagnose-asthma/feno-tests-to-monitor-feno-levels.

50. What Is A FeNO Test? https://www.aaaai.org/tools-for-the-public/conditions-library/asthma/what-is-a-feno-test.

51. X. Yin, R. Yang, G. Tan, S. Fan, Terrestrial radiative cooling: Using the cold universe as a renewable and sustainable energy source. *Science* **370**, 786–791 (2020).

52. J. Kou, Z. Jurado, Z. Chen, S. Fan, A. J. Minnich, Daytime radiative cooling using near-black infrared emitters. *ACS Photonics* **4**, 626–630 (2017).

53. S. Hong, Y. Gu, J. K. Seo, J. Wang, P. Liu, Y. S. Meng, S. Xu, R. Chen, Wearable thermoelectrics for personalized thermoregulation. *Sci. Adv.* **5**, eaaw0536 (2019).

54. Y. Song, R. Y. Tay, J. Li, C. Xu, J. Min, E. Shirzaei Sani, G. Kim, W. Heng, I. Kim, W. Gao, 3D-printed epifluidic electronic skin for machine learning–powered multimodal health surveillance. *Sci. Adv.* **9**, eadi6492 (2023).

55. H. U. Chung, A. Y. Rwei, A. Hourlier-Fargette, S. Xu, K. Lee, E. C. Dunne, Z. Xie, C. Liu, A. Carlini, D. H. Kim, D. Ryu, E. Kulikova, J. Cao, I. C. Odland, K. B. Fields, B. Hopkins, A. Banks, C. Ogle, D. Grande, J. B. Park, J. Kim, M. Irie, H. Jang, J. Lee, Y. Park, J. Kim, H. H. Jo, H. Hahm, R. Avila, Y. Xu, M. Namkoong, J. W. Kwak, E. Suen, M. A. Paulus, R. J. Kim, B. V. Parsons, K. A. Human, S. S. Kim, M. Patel, W. Reuther, H. S. Kim, S. H. Lee, J. D. Leedle, Y. Yun, S. Rigali, T. Son, I. Jung, H. Arafa, V. R. Soundararajan, A. Ollech, A. Shukla, A. Bradley, M. Schau, C. M. Rand, L. E. Marsillio, Z. L. Harris, Y. Huang, A. Hamvas, A. S. Paller, D. E. Weese-Mayer, J. Y. Lee, J. A. Rogers, Skin-interfaced biosensors for advanced wireless physiological monitoring in neonatal and pediatric intensive-care units. *Nat. Med.* **26**, 418–429 (2020).

56. E. Shirzaei Sani, C. Xu, C. Wang, Y. Song, J. Min, J. Tu, S. A. Solomon, J. Li, J. L. Banks, D. G. Armstrong, W. Gao, A stretchable wireless wearable bioelectronic system for multiplexed monitoring and combination treatment of infected chronic wounds. *Sci. Adv.* **9**, eadf7388 (2023).

57. A. Gökaltun, Y. B. Kang, M. L. Yarmush, O. B. Usta, A. Asatekin, Simple surface modification of poly(dimethylsiloxane) via surface segregating smart polymers for biomicrofluidics. *Sci. Rep.* **9**, 7377 (2019).

58. L. H. Kwong, R. Wilson, S. Kumar, Y. S. Crider, Y. R. Sanchez, D. Rempel, A. Pillarisetti, Review of the breathability and filtration efficiency of common household materials for face masks. *ACS Nano* **15**, 5904–5924 (2021).

59. R. S. Hale, R. Ranjan, C. H. Hidrovo, Capillary flow through rectangular micropillar arrays. *Int. J. Heat Mass Transf.* **75**, 710–717 (2014).

60. J. Vaughan, L. Ngamtrakulpanit, T. N. Pajewski, R. Turner, T.-A. Nguyen, A. Smith, P. Urban, S. Hom, B. Gaston, J. Hunt, Exhaled breath condensate pH is a robust and reproducible assay of airway acidity. *Eur. Respir. J.* **22**, 889–894 (2003).

61. J. Hunt, Y. Yu, J. Burns, B. Gaston, L. Ngamtrakulpanit, D. Bunyan, B. K. Walsh, A. Smith, S. Hom, Identification of acid reflux cough using serial assays of exhaled breath condensate pH. *Cough* **2**, 3 (2006).

62. G. E. Carpagnano, S. A. Kharitonov, O. Resta, M. P. Foschino-Barbaro, E. Gramiccioni, P. J. Barnes, 8-Isoprostane, a marker of oxidative stress, is increased in exhaled breath condensate of patients with obstructive sleep apnea after night and is reduced by continuous positive airway pressure therapy. *Chest* **124**, 1386–1392 (2003).

63. G. E. Carpagnano, S. A. Kharitonov, O. Resta, M. P. Foschino-Barbaro, E. Gramiccioni, P. J. Barnes, Increased 8-isoprostane and interleukin-6 in breath condensate of obstructive sleep apnea patients. *Chest* **122**, 1162–1167 (2002).

64. P. Montuschi, S. A. Kharitonov, G. Ciabattoni, P. J. Barnes, Exhaled leukotrienes and prostaglandins in COPD. *Thorax* **58**, 585–588 (2003).

65. C. Cruickshank-Quinn, M. Armstrong, R. Powell, J. Gomez, M. Elie, N. Reisdorph, Determining the presence of asthma-related molecules and salivary contamination in exhaled breath condensate. *Respir. Res.* **18**, 57 (2017).

66. S. De, Q. Khan, D. Sahu, Do we require de-aeration of exhaled breath condensate samples for measuring pH. *Eur. Respir. J.* **56** (2020).

67. P. V. Romero, B. Rodríguez, S. Martínez, R. Cañizares, D. Sepúlveda, F. Manresa, Analysis of oxidative stress in exhaled breath condensate from patients with severe pulmonary infections. *Arch. Bronconeumol. Engl. Ed.* **42**, 113–119 (2006).

68. S. Tate, G. MacGregor, M. Davis, J. A. Innes, A. P. Greening, Airways in cystic fibrosis are acidified: detection by exhaled breath condensate. *Thorax* **57**, 926–929 (2002).

69. J. Daniels, S. Wadekar, K. DeCubellis, G. W. Jackson, A. S. Chiu, Q. Pagneux, H. Saada, I. Engelmann, J. Ogiez, D. Loze-Warot, R. Boukherroub, S. Szunerits, A mask-based diagnostic platform for point-of-care screening of Covid-19. *Biosens. Bioelectron.* **192**, 113486 (2021).

70. Y.-C. Chen, D. O'Hare, Exhaled breath condensate based breath analyser – a disposable hydrogen peroxide sensor and smart analyser. *Analyst* **145**, 3549–3556 (2020).

71. S. Zhang, Y.-C. Chen, A. Riezk, D. Ming, L. Tsvik, L. Sützl, A. Holmes, D. O'Hare, Rapid measurement of lactate in the exhaled breath condensate: biosensor optimization and in-human proof of concept. *ACS Sens.* **7**, 3809–3816 (2022).

72. X. Li, R. Sun, J. Pan, Z. Shi, Z. An, C. Dai, J. Lv, G. Liu, H. Liang, J. Liu, Y. Lu, F. Zhang, Q. Liu, Rapid and on-site wireless immunoassay of respiratory virus aerosols via hydrogel-modulated resonators. *Nat. Commun.* **15**, 4035 (2024).

Chapter 3

OUTLOOK AND CONCLUSION

Materials from this chapter appear in "Heng, W.; Yin, S.; Chen, Y.; Gao, W. Exhaled breath analysis: From laboratory test to wearable sensing. IEEE Reviews in Biomedical Engineering 1–25 (2024). https://doi.org/10.1109/RBME.2024.3481360."

3.1 Breathomics

As illustrated in **Fig. 3-1A** and **B**, the bioinformation contained in breath is remarkably complex and vast, requiring advanced data processing techniques for comprehensive analysis. While certain breath characteristics can be linked to specific health conditions, a single molecular marker may correspond to multiple physiological states, and conversely, a single state can be indicated by various molecular markers. This complexity is further compounded by individual variations in anatomical structure, leading to substantial differences in the physiological characteristics observed in breath. From a physical perspective, features such as individual breath patterns, breathing rhythms, along with temperature and humidity, are interrelated and collectively reflect the overall condition of the respiratory system [1,2]. Chemically, exhaled breath contains between 200 and 2000 different compounds, encompassing a wide range of metabolic pathways and physiological states [3], offering valuable insights into various processes, like glucose metabolism and lipid oxidation [4,5]. Additionally, the diversity and abundance of non-volatile components, such as various biomolecules [6,7] and proteins [8,9], further contribute to the complexity of breath analysis.

To effectively tackle the complexities of breath analysis, a comprehensive approach involving advanced data processing methods that can handle the high dimensionality and variability of breath data is essential. These methods are adept at identifying patterns and correlations among the diverse features found in breath samples. Supervised learning algorithms, like support vector machines [10] and random forests [11], are commonly used for classification tasks, helping to distinguish between different physiological or pathological states based on breath profiles. Unsupervised learning methods, such as principal component analysis (PCA) [12,13] and clustering [14] techniques, are useful for dimensionality reduction and the discovery of novel breath patterns (see **Fig. 3-1C**).

Additionally, deep learning approaches, particularly convolutional neural networks (CNNs) [15] and recurrent neural networks (RNNs) [16], can capture complex temporal dynamics and non-linear relationships within the data, making them ideal for analyzing breath waveform and rhythm. To ensure the robustness and accuracy of these models, rigorous validation and

cross-validation techniques are employed, alongside large, diverse datasets to train the algorithms effectively. Furthermore, as shown in **Fig. 3-1D**, integrating multi-omics data, including proteomics and metabolomics, with physical analysis of breath can enhance the understanding of underlying biological processes and improve diagnostic accuracy [17]. By leveraging these advanced data processing methods, researchers can develop more precise and individualized diagnostic tools, ultimately contributing to the advancement of precision medicine.

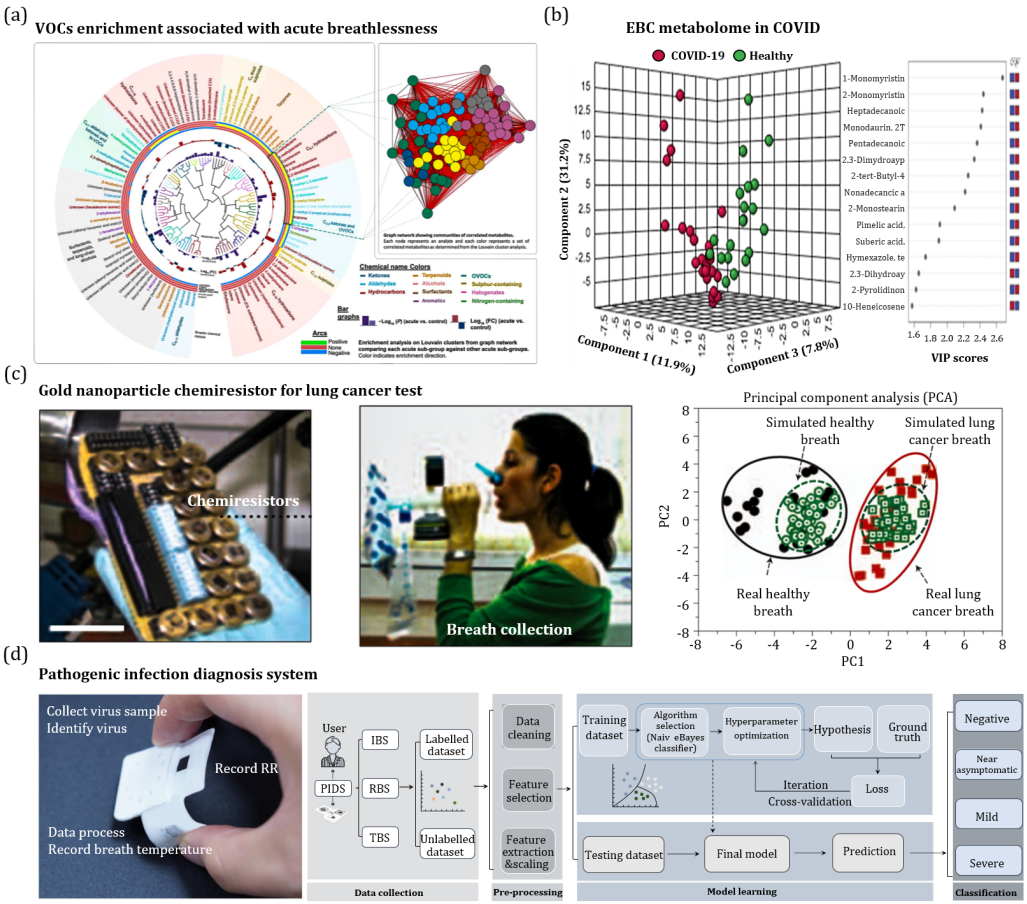

Figure 3-1 Breathomics and related data processing methodologies. (a). VOCs enrichment associated with acute breathlessness. 335 (b). EBC metabolome in COVID. 339 (c). Gold nanoparticle chemiresistor array for lung cancer test. 344 (d). A pathogen infection diagnostic system integrating physical and chemical sensing elements generates multimodal data for machine learning classification of COVID conditions. 257

3.2 Human machine interaction

Breathing, a fundamental and low-energy physiological process, has recently emerged as a focal point in the development of human-machine interaction (HMI) technologies. Traditional HMI methods typically depend on mechanical, acoustic, bioelectrical, or optical inputs [18,19]. While these established technologies offer reliable performance, they often entail significant motion consumption and visibility, which can constrain their practical applications and user comfort. In contrast, breathing input technology capitalizes on the natural patterns of nasal and oral breath, enhanced by the integration of accelerometers and advanced sensors, to provide a novel interaction mode characterized by minimal energy expenditure and inherent naturalness. By capturing variations in breath rate and pressure, this approach facilitates the implementation of continuous and discrete input patterns, thereby offering a more efficient and user-friendly solution for HMI applications [20,21].

Moreover, the use of machine learning algorithms to interpret non-vocalized breath patterns has the potential to revolutionize fields such as speech recognition and control systems [22]. By training models to recognize and respond to specific breathing patterns, this technology could enable new forms of interaction that are less reliant on traditional voice commands. The advantages of breathing input are underscored by its low visibility and its capacity to protect user privacy, coupled with its broad applicability across various user demographics and environmental contexts. This technology is particularly promising for users with physical disabilities and diverse settings where conventional input methods may be less effective or practical.

The potential applications of breathing input technology extend to smart hospital environments, where breathing input could provide intuitive control mechanisms that adapt to user needs with minimal physical effort [23]. Additionally, in virtual and augmented reality settings, breathing-based interactions could enhance immersion and user engagement by integrating a natural and seamless mode of control. As technological advancements continue to evolve, the integration of breathing input into HMI systems is expected to significantly enhance user experiences, making interactions more natural, efficient, and accessible [24,25].

3.3 Outlook and conclusion

In the wake of the five-year global COVID-19 pandemic, breath research has emerged as a critical focus across physiology, medicine, and engineering. Respiratory science, an ancient discipline, has been propelled forward in recent decades by advanced technologies such as CT and magnetic resonance imaging (MRI); sampling techniques including sputum, nasopharyngeal swabs, bronchoscopy, and exhaled breath analysis; along with MS and nucleic acid detection methods. The field of breath analysis still faces numerous pressing challenges and promising research frontiers. These include:

1) The clinical implementation and standardization of non-invasive breath analysis across diverse demographics to establish a robust diagnostic database.

2) The exploration of chemical information in breath to uncover novel biomarkers linked to physiological states necessitates the development of advanced analytical devices, requiring significant enhancements in selectivity and sensitivity to accurately detect and quantify diverse breath constituents at ultra-low concentrations.

3) Advanced data processing technologies, particularly machine learning, are transforming breath health analysis through large-scale omics data. This transformation encompasses raw data preprocessing, health status inference from biomarker distributions, and the establishment of comprehensive breathomics. This multifaceted approach integrates diverse data types, enabling personalized diagnostics and treatment strategies in pulmonary medicine.

4) The integration of emerging wearable technologies with real-time sampling and detection techniques promises to revolutionize precision and personalized medicine. Advancements in device miniaturization and wireless connectivity enable seamless, unobtrusive continuous respiratory monitoring in everyday settings. This breakthrough facilitates long-term monitoring across diverse physiological states, offering rich, individualized data on health trajectories and responses to various stimuli. Additionally, the development of cost-effective point-of-care solutions expands the applicability of these technologies, particularly in areas such as infectious disease management, making healthcare more accessible and responsive.

These directions hold the promise to provide more accurate data support for early diagnosis and tailored treatments, opening vast horizons for breath-related medical research and clinical applications. The future of breath analysis hinges on interdisciplinary collaboration. The synergistic application of engineering, material science, computer science, and biology are poised to catapult breath analysis and monitoring to unprecedented heights, ushering in a new era of breath health and personalized precision medicine.

Bibliography of Chapter 3

1. Li, H. *et al.* Wireless, battery-free, multifunctional integrated bioelectronics for respiratory pathogens monitoring and severity evaluation. *Nat Commun* **14**, 7539 (2023).
2. Yang, Y. *et al.* Artificial intelligence-enabled detection and assessment of Parkinson's disease using nocturnal breathing signals. *Nat Med* (2022) doi:10.1038/s41591-022-01932-x.
3. Ibrahim, W. *et al.* Visualization of exhaled breath metabolites reveals distinct diagnostic signatures for acute cardiorespiratory breathlessness. *Science translational medicine* **14**, eabl5849 (2022).
4. Smolinska, A. *et al.* Current breathomics—a review on data pre-processing techniques and machine learning in metabolomics breath analysis. *J. Breath Res.* **8**, 027105 (2014).
5. Nakhleh, M. K. *et al.* Diagnosis and Classification of 17 Diseases from 1404 Subjects via Pattern Analysis of Exhaled Molecules. *ACS Nano* **11**, 112–125 (2017).
6. Sinha, A. *et al.* Exhaled breath condensate metabolome clusters for endotype discovery in asthma. *J Transl Med* **15**, 262 (2017).
7. Barberis, E. *et al.* Metabolomics Diagnosis of COVID-19 from Exhaled Breath Condensate. *Metabolites* **11**, 847 (2021).
8. Kurova, V. S. *et al.* Proteomics of exhaled breath: methodological nuances and pitfalls. *Clinical Chemistry and Laboratory Medicine* **47**, 706–712 (2009).
9. Bloemen, K. *et al.* A new approach to study exhaled proteins as potential biomarkers for asthma. *Clinical & Experimental Allergy* **41**, 346–356 (2011).

10. Sakumura, Y. *et al.* Diagnosis by Volatile Organic Compounds in Exhaled Breath from Lung Cancer Patients Using Support Vector Machine Algorithm. *Sensors* **17**, 287 (2017).

11. Manzella, F., Pagliarini, G., Sciavicco, G. & Stan, I. E. The voice of COVID-19: Breath and cough recording classification with temporal decision trees and random forests. *Artificial Intelligence in Medicine* **137**, 102486 (2023).

12. Hakim, M. *et al.* Diagnosis of head-and-neck cancer from exhaled breath. *Br J Cancer* **104**, 1649–1655 (2011).

13. Peng, G. *et al.* Diagnosing lung cancer in exhaled breath using gold nanoparticles. *Nature Nanotech* **4**, 669–673 (2009).

14. Alkhalifah, Y. *et al.* VOCCluster: Untargeted Metabolomics Feature Clustering Approach for Clinical Breath Gas Chromatography/Mass Spectrometry Data. *Anal. Chem.* **92**, 2937–2945 (2020).

15. Lee, B. *et al.* Breath analysis system with convolutional neural network (CNN) for early detection of lung cancer. *Sensors and Actuators B: Chemical* **409**, 135578 (2024).

16. Hsu, F.-S. *et al.* Benchmarking of eight recurrent neural network variants for breath phase and adventitious sound detection on a self-developed open-access lung sound database—HF_Lung_V1. *PLoS One* **16**, e0254134 (2021).

17. Chen, X. *et al.* Breath analysis: Harnessing its potential for non-volatile drug caffeine monitoring in human body. *Microchemical Journal* **198**, 110130 (2024).

18. Heng, W., Solomon, S. & Gao, W. Flexible Electronics and Devices as Human–Machine Interfaces for Medical Robotics. *Advanced Materials* **34**, 2107902 (2022).

19. Pang, G. *et al.* CoboSkin: Soft Robot Skin With Variable Stiffness for Safer Human–Robot Collaboration. *IEEE Trans. Ind. Electron.* **68**, 3303–3314 (2021).

20. Pang, Y. *et al.* Self-Powered Multifunctional Human–Machine Interfaces for Respiratory Monitoring and Smart System Control. *Advanced Materials Interfaces* **9**, 2201202 (2022).

21. Xu, K. *et al.* Laser Direct Writing of Flexible Thermal Flow Sensors. *Nano Lett.* **23**, 10317–10325 (2023).

22. Tang, K. *et al.* Respiration-based human-machine interface for aphasic patients with limited physical mobility. *Chemical Engineering Journal* **487**, 150507 (2024).

23. Zhang, B. *et al.* Breath-based human–machine interaction system using triboelectric nanogenerator. *Nano Energy* **64**, 103953 (2019).

24. Kim, J.-H. & Lee, J. Controlling your contents with the breath: Interactive breath interface for VR, games, and animations. *PLOS ONE* **15**, e0241498 (2020).

25. Liu, Y. *et al.* Soft, miniaturized, wireless olfactory interface for virtual reality. *Nat Commun* **14**, 2297 (2023).